Stony Brook University

OFFICIAL COPY

The official electronic file of this thesis or dissertation is maintained by the University Libraries on behalf of The Graduate School at Stony Brook University.

© All Rights Reserved by Author.

Green Synthesis, Characterization, and Application of Metal-based Nanomaterials

A dissertation presented by

Crystal Shenandoa Lewis

to

The Graduate School

in Partial Fulfillment of the

Requirements

for the degree of

Doctor of Philosophy

in

Chemistry

Stony Brook University

August 2016

Copyright by
Crystal Shenandoa Lewis
2016

Stony Brook University

The Graduate School

Crystal Shenandoa Lewis

We, the dissertation committee for the above candidate for the

Doctor of Philosophy degree, hereby recommend

acceptance of this dissertation.

Dr. Stanislaus S. Wong – Dissertation Advisor
Professor, Chemistry

Dr. Robert Grubbs - Chairperson of Defense
Professor, Chemistry

Dr. Dale Druekhammer – Third Member
Chemistry Chair

Dr. William Moore – Outside Member

This dissertation is accepted by the Graduate School

Nancy Goroff
Interim Dean of the Graduate School

Abstract of the Dissertation

Green Synthesis, Characterization, and Application of Metal based Nanomaterials

by

Crystal Shenandoa Lewis

Doctor of Philosophy

in

Chemistry

Stony Brook University

2016

Metal-based nanomaterials have attracted significant research interest due to their unique size-dependent optical, magnetic, electronic, thermal, mechanical, and chemical properties as compared with their bulk counterparts. These advantageous and tailorable properties render these materials as ideal candidates for catalysis, photovoltaics, and even biomedical applications. However, nanomaterials are typically synthesized via chemical or physical processes, which are continuing to rise in cost, complexity, and toxicity. As a result, 'milder' and more environmentally benign nanoscale synthetic methodologies, particularly U-tube double diffusion, molten salt, and hydrothermal techniques, have been utilized to mitigate for these drawbacks. Moreover, these efficient and facile techniques coupled with the unique attributes of nanomaterials will aid in a more practical translation from the lab scale to industry with potential applications spanning from electronics, energy, to medicine.

In this thesis, we will discuss the sustainable synthesis of crystalline elemental copper (Cu), nickel (Ni), magnetic spinel ferrites (MFe_2O_4 wherein M is Co, Ni, or Zn), rare earth ion doped-calcium titanate (RE-$CaTiO_3$), and hematite (α-Fe_2O_3) as well as our ability to tailor the size and/or morphology and hence tune their properties for potential applications in solar cells and biomedicine. Specifically, for the Cu and Ni nanowires (NWs), the diameters have been dictated by the various template diameters used in the U-tube double diffusion technique. Subsequently, their photocatalytic properties were observed when coupled with TiO_2 NPs. For MFe_2O_4, RE-$CaTiO_3$, and α-Fe_2O_3 nanostructures, the hydrothermal method was employed wherein various parameters such as reaction temperature, concentration, and addition of surfactant were varied to influence their morphology and/or composition. For example, as the reaction temperature was increased, ultrasmall MFe_2O_4 particles transformed from amorphous to crystalline species, and these were subsequently investigated for their magnetic properties as well as for their potential as photocatalysts. Regarding RE-$CaTiO_3$, a comparison and correlation between their preparative synthetic techniques (i.e. hydrothermal and molten salt) and photoluminescent properties were explored. Moreover, quantum dots (QDs) were coupled onto RE-$CaTiO_3$ to observe possible charge transfer effects. Lastly for α-Fe_2O_3, microglial uptake of NPs, activation, and possible cytotoxic effects were all probed.

Dedicated in loving memory of Dr. Herbert Goulding

Table of Contents

List of Figures

List of Tables

List of Abbreviations and Symbols

DAN	2,3-diaminonaphthalene
DCF	2', 7'-dichlorofluorescein
DCFDA	2', 7'-dichlorofluorescein diacetate
MTT	3-(4,5-dimethylthiazol-2-yl)-2,5-diphenyltetrazolium bromide
MTS	3-(4,5-dimethylthiazol-2-yl)-5-(3-carboxymethoxyphenyl)-2-(4-sulfophenyl)-2H-tetrazolium
DAPI	4',6-diamidino-2-phenylindole
0D	Zero-dimensional
1D	One-dimensional
2D	Two-dimensional
3D	Three-dimensional
AP2	Adaptor protein complex
AFCs	Alkaline fuel cells
APTES	Aminopropyltriethoxysilane
AAO	Anodic alumina oxide
H	Applied field
AFM	Atomic force microscope
BAR	Bin/Amphiphysin/Rvs
$BaTiO_3$	Barium titanate
CdSe	Cadmium selenide
CaC_2O_4	Calcium oxalate
CaO	Calcium oxide
$CaTiO_3$	Calcium titanate
CRT	Cathode ray tube
CTAB	Cetyltrimethylammonium bromide
CCD	Charge-coupled device
CCV	Clathrin coated vesicle
CME	Clathrin-mediated endocytosis
CNS	Central nervous system
CVD	Chemical vapor deposition
CPZ	Chloropromazine
H_c	Coercivity
CB	Conduction band
Cu	Copper
CTCF	Corrected total cell fluorescence
Cu_2O	Cuprous oxide
Tc	Curie temperature
d	D-spacing
°	Degree
°C	Degree Celsius
DCC	Dicyclohexyl-carbodiimide
DMAB	Dimethylamine borane
DMF	Dimethyl formamide
DMSO	Dimethyl sulfoxide
DOA	Dioctylamine

DMFCs	Direct methanol fuel cells
$	Dollar
EM	Electron microscopy
EDX	Energy dispersive X-ray spectroscopy
EELS	Energy electron loss spectroscopy
eGFP	Enhanced green fluorescent protein
ΔH_f°	Enthalpy of formation
S°	Entropy
ELISA	Enzyme-linked Immuno-absorbent assay
EIA	Enzyme immunoassay
EGF	Epidermal growth factor
${}_TK^\circ$	Equilibrium constant
EG	Ethylene Glycol
fcc	Face-centered cubic
C/C_0	Final concentration over initial concentration
FT-IR	Fourier Transform Infrared
R	Gas constant
ΔG°	Gibbs free energy
GTPase	Guanosine triphosphate hydrolase
HDA	Hexadecylamine
HRTEM	High resolution transmission electron microscope
HOMO	Highest occupied molecular orbitals
N_2H_4	Hydrazine
HOR	Hydrogen oxidation reaction
H_2O_2	Hydrogen peroxide
IR	Infrared
IL1β	Interleukin 1-beta
α-Fe_2O_3	Iron oxide/ hematite
LDH	Lactate dehydrogenase
Pb	Lead
LEDs	Light emitting diodes
LPS	Lipopolysacharide
LIBs	Lithium ion batteries
LUMO	Lowest unoccupied molecular orbitals
M_r	Magnetic remnance
MRI	Magnetic Resonance Imaging
M_s	Magnetic saturation
M	Magnetization
MPA	Mercaptopropionic acid
MFe_2O_4	Metal ferrites
MOR	Methanol oxidation reaction
MO	Methyl orange
MB	Methylene blue
MIF	Microglia inhibitory factor
µg	Microgram
µL	Microliter

mL	Milliliter
M	Molar
MSS	Molten Salt Synthesis
NTs	Nanotubes
NNI	National Nanotechnology Initiative
nm	Nanometers
NWs	Nanowires
NRhomb	Nanorhombohedra
T_n	Néel temperature
T_2	Negative contrast agent
Ni	Nickel
$NiCl_2$	Nickel chloride
NO	Nitric oxide
N_2	Nitrogen
ORR	Oxygen reduction reaction
OER	Oxygen evolution reaction
PDF	Pair distribution function
PFA	Paraformaldehyde
PEMFCs	Proton exchange membrane fuel cells
min^{-1}	Per minute
ABO_3	Perovskite
PL	Photoluminescence
PV	Photovoltaics
PC	Polycarbonate
T_1	Positive contrast agent
KCl	Potassium chloride
KNO_3	Potassium nitrate
QDs	Quantum Dots
RE-$CaTiO_3$	Rare earth ion doped calcium titanate
k	Rate constant
ROS	Reactive Oxygen Species
RhB	Rhodamine B
SEM	Scanning Electron microscope
STEM	Scanning-transmission electron microscope
STM	Scanning tunneling microscope
SAED	Selected area electron diffraction
Se	Selenium
Si	Silicon
$NaBH_4$	Sodium Borohydride
NaCl	Sodium Chloride
NaOH	Sodium Hydroxide
v/v	Solvent/solvent
K_{sp}	Solubility product
$SrTiO_3$	Strontium titanate
SQUID	Superconducting quantum interference device
SPR	Surface plasmon resonance

INT	Tetrazolium salt
t	Time
TiO_2	Titanium dioxide/titania
TEM	Transmission Electron microscope
TBP	Tributylphosphine
TOPO	Trioctylphosphine
TKPR	Tuftsin
TNFα	Tumor necrosis factor alpha
UV-Vis	Ultraviolet-Visible
VB	Valence band
XRD	X-ray diffraction
XPS	X-ray photoelectron spectroscopy

Acknowledgements

There are so many individuals I would like to thank and I will do my best to thank them all.

First, I would like to thank my advisor Dr. Stanislaus S. Wong for his guidance and belief in me over the last 4 and half years of my Doctoral journey. The lessons you have taught me academically, and otherwise, have been essential to my success at Stony Brook University.

I would like to extend gratitude to Dr. Robert Grubbs and Dr. Nicole Sampson for serving as my committee members. Your insightful questions have helped me to develop my skill set as a scientist.

I would also like to thank those who have contributed to my work. In particular, I acknowledge Dr. Simon Billinge, Dr. Chenyang Shi, Dr. Luisa Torres, Dr. Stylliani-Anna Tsirka, and Dr. Georgia Papaefthymiou for their help and expertise with PDF analysis, cell culture assay experiments, and magnetic measurements, respectively.

Special thanks to the Center for Inclusive Education committee, particularly Toni Sperzel and Karian Wright, who have supported me financially through the Turner and the AGEP-T FRAME Fellowship programs, respectively. Additionally, I am thankful for your support and belief throughout this journey. I am eternally grateful for your support of my academic endeavors.

In addition, I would like to thank my fellow group members both past and present, in particular, Dr. Christopher Koenigsmann, Dr. Jonathan Patete, Dr. Amanda Tiano, Dr. Jinkyu Han, Dr. Megan Scofield, Lei Wang, Haiqing Liu, Coray McBean, Dominic Moronta, and Shiyu Yue for your support along my Doctoral journey. It is greatly appreciated.

I would be remiss if I didn't thank my professors from Oakwood University, particularly Dr. Kenneth LaiHing and Dr. Glenn Philips, who incited my passion for Chemistry. Thank you for your encouraging words and support.

I would like to thank the Goulding family, particularly Dr. Cortney Goulding and Dr. Herbert Goulding, for their belief in my father, which ultimately led to our family's immigration to the United States. Your love and support have been greatly appreciated.

Last, but certainly, not least I would like to thank God as well as my family, Nigel, Verleen, and Raynold Lewis for their love and support through the years. I can't put into words how your encouraging words have been throughout my life. You are the wind beneath my wings. I love you with all my heart.

List of Publications

1. “Synthesis, Characterization, and Formation Mechanism of Crystalline Cu and Ni Metallic Nanowires under Ambient, Seedless, Surfactantless Conditions.” **Crystal S. Lewis**, Lei Wang, Haiqing Liu, Jinkyu Han, and Stanislaus Wong. *Crystal Growth & Design*. **2014**. *14(8):* pp. 3825–3838.

2. “Correlating Size and Composition-Dependent Effects with Magnetic, Mössbauer, and PDF Measurements in a Family of Catalytically Active Ferrite Nanoparticles.” Amanda L. Tiano, Georgia C. Papaefthymiou, **Crystal S. Lewis**, Jinkyu Han, Cheng Zhang, Qiang Li, Chenyang Shi, A. M. Milinda Abeykoon, Simon J. L. Billinge, Eric Stach, Justin Thomas, Kevin Guerrero, Pablo Munayco, Jimmy Munayco, Rosa B. Scorzelli, Philip Burnham, Arthur J. Viescas, and Stanislaus S. Wong. *Chemistry of Materials.* **2015**. *27(10):* pp. 3572-3592.

3. “Correlating the chemical composition and size of various metal oxide substrates with the catalytic activity and stability of as-deposited Pt nanoparticles for the methanol oxidation reaction.” Megan E. Scofield, Christopher Koenigsmann, Dara Bobb-Semple, Jing Tao, Xiao Tong, Lei Wang, **Crystal S. Lewis**, Miomir Vukmirovic, Yimei Zhu, Radoslav R. Adzic, and Stanislaus S. Wong. *Catalysis Science & Technology.* **2016**, *6(7):* pp. 2435-2450.

4. “Probing Charge Transfer in a Novel Class of Luminescent Perovskite-Based Heterostructures Composed of Quantum Dots Bound to RE-Activated $CaTiO_3$ Phosphors.” **Crystal S. Lewis**, Haiqing Liu, Jinkyu Han, Lei Wang, Shiyu Yue, Nicholas Brennan, and Stanislaus S. Wong. *Nanoscale*, **2016**, 8(4): pp. 2129-2142.

5. “Absence of Cytotoxicity towards Microglia of Iron Oxide (Fe_2O_3) Nanorhombohedra.” **Crystal S. Lewis**, Luisa Torres, Jeremy T. Miyauchi, Cyrus Rastegar, Johnathan M. Patete, Jacqueline M. Smith, Stanislaus S. Wong, and Stella E. Tsirka. *Toxicology Research*. **2016**, *5(3):* pp. 836-847.

6. “Corrleating Titania Nanostructured Morphologies with Performance as Anode Materials for Lithium-ion Batteries.” **Crystal S. Lewis**, Yue Rue Li, Lei Wang, Jing Li, Eric Stach, Kenneth J. Takeuchi, Amy C. Marschilok, Esther S. Takeuchi, and Stanislaus S. Wong. *ACS Sustainability.* submitted for publication.

Chapter 1 - Introduction: The field of nanotechnology

1.1 What is Nano?

Nano is a unit prefix, typically used in the metric system, meaning one billionth or 10^{-9}. According to the U.S. National Nanotechnology Initiative (NNI), nanotechnology refers to any science, engineering and technology conducted at the nanoscale. The NNI further defines the nanoscale as being between 1-100 nanometers (nm). As a result, nanoscale materials, more commonly known as nanomaterials, possess at least one feature (*i.e.* length, width or height) within the 1-100 nm size regime.[1] Nanomaterials have gained widespread attention due to the unique properties derived from their small size by comparison with their respective bulk-sized structures. Hence, nanotechnology is the application of nanomaterials to technological advances.

Another way to tailor nanoscale properties is through their shape (see Figure 1.1). As a result, the morphology can be categorized by their dimensionality. For example, nanoparticles and nanorhombohedra are termed as zero-dimensional (0D) materials wherein all dimensions (*x, y, z*) are confined to the nanoscale range. As for one-dimensional (1D) materials, where at least one dimension resides within the nanoscale size regime, examples include carbon nanotubes (NTs) and DNA strands (see Figure 1.2). Two-dimensional (2D) structures such as nanoplates and nanofilms possess two dimensions in the nanoscale range (i.e. L_x, L_y). Lastly, three-dimensional (3D) motifs, an inherently more complicated material, are rather composed of either 0D nanoparticle arrays, 1D NW arrays, or porous materials, to name a few, hierarchically arranged and organized within more complex structural configurations (see Figure 1.2).

The chemical composition of these nanomaterials can also be utilized to influence their properties for various applications. In particular, metal-based nanostructures, such as titanium dioxide (TiO_2) and silver (Ag), are commonly found in cosmetics, providing UV protection, and

deodorants, allowing for longer deodorizing effects, respectively. As nanomaterial incorporation within commercial products continues to increase, so does the inherent need for efficient and environmentally safe synthetic nanomaterials as well as methods for producing them.

In this thesis, we intend to synthesize 0D and 1D metal-based nanomaterials using reasonably cost effective and relatively mild synthetic techniques. Moreover, correlations between their size, morphology, and composition with respect to their properties will be observed for potential applications in solar cells and biomedical applications. Specifically, for elemental Cu and Ni, we explore how synthesis under ambient conditions affects their overall photocatalytic properties. As for metal ferrite nanostructures, we investigate how size affects their overall magnetic properties. Lastly, for metal oxides such as calcium titanate ($CaTiO_3$) and iron oxide (Fe_2O_3), we will probe their potential applicability by analyzing for charge transfer effects within heterostructured nanocomposites as well as for possible cytotoxic effects or the lack thereof within microglia cells, respectively.

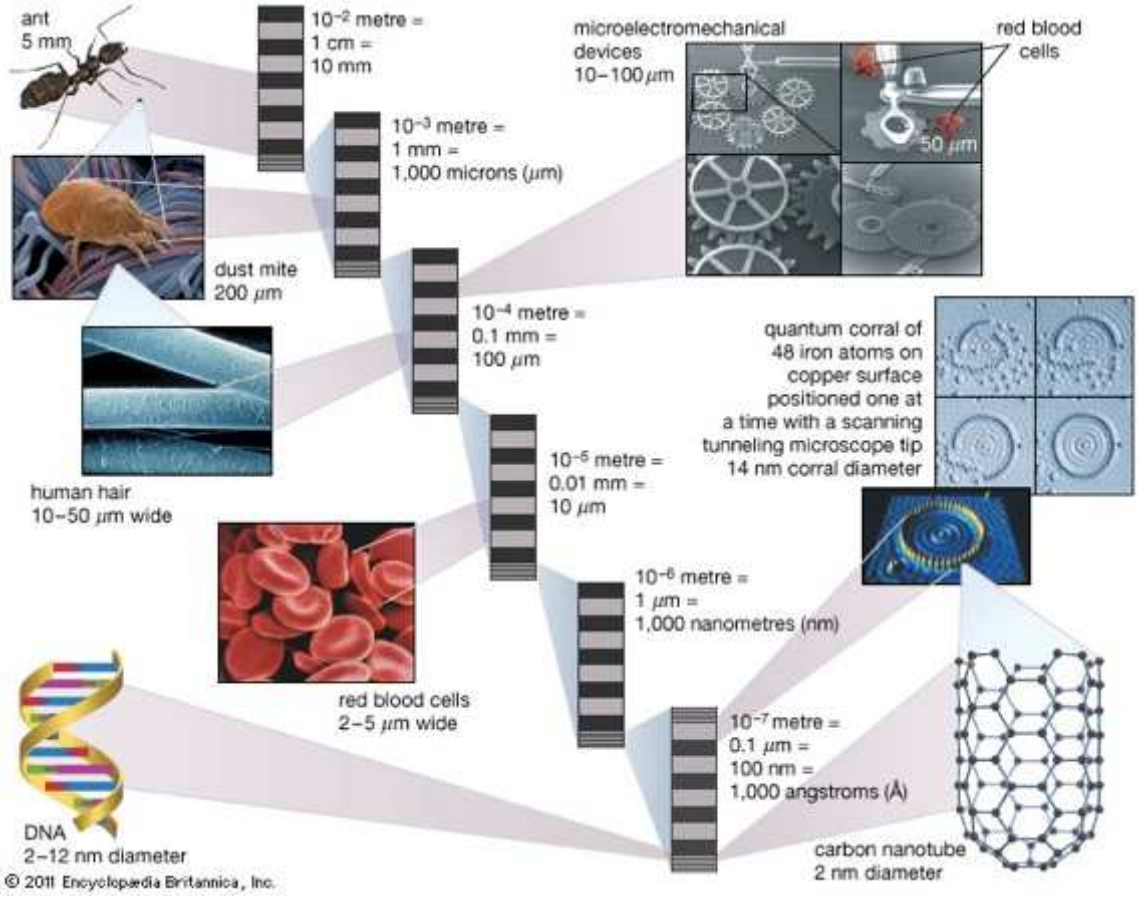

Figure 1.1: Dimensions of natural (left) and man-made (right) materials with respect to the nanoscale. Image adapted from the Encyclopedia Britannica.

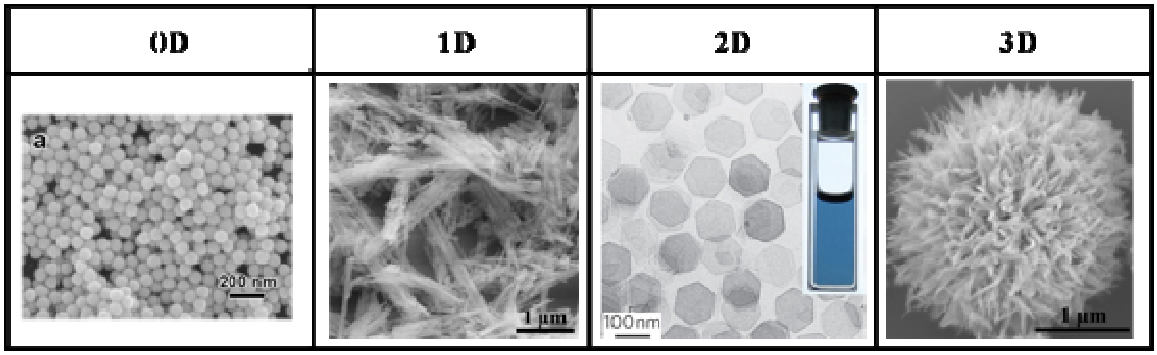

Figure 1.2: Nanoscale dimensions associated with 0D gold (Au) nanoparticles (Image adapted from Liu et al. *Sci. Rep.,* **2015**, 5: pp. 7686), as-prepared 1D titania (TiO_2) nanowires, 2D palladium hexagonal plates (Image adapted from Huang et al. *Nature Nanotech.* **2015**, 6: pp. 28-32), and as-prepared 3D TiO_2 urchins.

1.2 Nanotechnology History & Background

The use of nanotechnology began as early as the fourth century with the Roman Lycurgus cup (see Figure 1.3A), made up of a dichroic material, specifically consisting of colloidal gold and silver. Interestingly, when it is lit from the outside, it takes on an opaque green color, but becomes translucent red when illuminated on the inside.[2]

Between the fifth and sixteenth centuries, stained glassed windows, composed of nanoparticles, filled many European cathedrals. Nanowires (NWs) were employed as early as the thirteenth century in the Damascus saber (see Figure 1.3B), composed of carbon nanotubes and cementite NWs as noted by D. C. Meyer in 2006.[3] Although nanomaterials have been present within technology from centuries past, their unique properties were not formally described until 1959 by Richard Feynman in his lecture, "There's Plenty of Room at the Bottom" at an American Physical Society meeting in California.[4] It was this lecture that pioneered the quest for manipulating and controlling individual atoms, which then inspired inventions such as the scanning tunneling microscope (STM) in 1981 and the atomic force microscope (AFM) in 1986 to visualize nanoscale materials. The development of these inventions triggered an increased interest in the field of nanotechnology.

With structural characterization tools, such as AFM, continuing to evolve and with better control over nanomaterials' features and the ability to achieve unique properties, a long-term vision was implemented by the NNI in 1999.[5] This vision aimed to bridge the gap between fundamental knowledge concerning nanomaterials and the practical pursuit of novel nanotechnologies in order to further enhance existing applications.[5, 6] This passion was also echoed by Former President Bill Clinton at an NNI meeting where he said, "Imagine the possibilities: materials with ten times the strength of steel and only a small fraction of the weight

-- shrinking all the information housed at the Library of Congress into a device the size of a sugar cube -- detecting cancerous tumors when they are only a few cells in size. Some of our research goals may take 20 or more years to achieve, but that is precisely why there is an important role for the federal government."[7]

Within the past 20 years or so, nanomaterials have been utilized for a wide array of applications including but not limited to: electronic devices, photocatalysts, and drug delivery carriers as well as personal care products, food packaging, and preservatives.[1, 8, 9] Moreover, the dramatic increase in patents, publications, products and revenue, based on nanomaterials, has made it virtually impossible to truly quantify the contribution of nanotechnology to the commercial market. However, the advisory firm, Lux Research, made an attempt to quantitatively assess the estimated the global market for nano-enabled or nano-intermediate products and estimated it to be ~4.4 trillion by the year 2018.[10, 11] As a result of the growth in industrial revenue, the 2017 Federal Budget now provides approximately 1.4 billion dollars to the NNI, thereby confirming the crucial role nanomaterials are expected to continue to play in our society.[6] In light of this economic growth, the NNI's vision for nanotechnology as the next industrial revolution is likely on track to being fulfilled, or so it would seem.[7]

Figure 1.3: The Lycurgus cup at the British museum lit from the outside (A) and the inside. A Damascus Saber (B) composed of carbon nanotubes and cementite nanowires (photo by Tina Fineberg for the New York Times).

1.3 Green Synthesis Introduction

As the market for nanotechnology continues to develop and increase, so do the chemical/physical production costs associated with synthesizing these materials. Moreover, the chemical synthesis method can produce toxic byproducts that may affect the function of technological devices (i.e. solar devices), as well as impact upon human health and the environment. In an effort to address these adverse effects, in the 1990s, the U.S. Environment Protection Agency (EPA) established the field of green chemistry as a legitimate scientific field.[12, 13] In doing so, the EPA defined green chemistry as "the utilization of a set of principles

that reduces or eliminates the use or generation of hazardous substances in the design manufacture, and application of chemical products."[14, 15]

The 12 principles of green chemistry were developed in 1998 by Anastas and Warner and these ideas have aided in shaping the sustainable chemistry field.[14] These 12 principles are listed as follows: (i) minimize waste generation, (ii) increase the amount of atoms that yield the desired product vs. the amount of atoms that are considered waste, (iii) employ less hazardous synthetic methods, (iv) design chemical products that maintain their function without toxic effects, (v) employ solvents with low overall toxicity profiles within chemical reactions, (vi) enhance the use of energy efficient processes (i.e. ambient conditions if possible), (vii) synthesize future fuels and chemicals with sources that mitigate the risk of depletion, (viii) reduce the use of derivatives such as blocking groups, (ix) carefully select catalytic reagents, (x) design toxic-free, degradable chemical products, (xi) use real-time analysis to track the formation of hazardous materials produced, (xii) and reduce potential accidents through the use of safer chemistry. Herein, we aim to highlight the implementation of a few of these principles to our work within the next few chapters.

Since the publication and dissemination of these principles, green synthetic techniques have gained considerable attention as they have provided innovative alternatives for chemical and physical synthetic methods through the employment of cost-effective, environmentally friendly, and scalable techniques in the absence of either high energy or toxic chemical by-products.[1] The cost-effective nature of environmentally friendly synthetic techniques in addition to a proper control over nanomaterials' unique properties will aid in a more realistic practical translation from the lab scale to commercial applications. In particular, potential applications

include but are not limited to electronics, photovoltaics, sensing, catalysis, biology as well as medicine.

When considering a green synthetic method of inorganic materials, for example, 3 parameters must be examined: the type of capping agent, reducing agent, and solvent used. From this perspective, non-toxic capping agents (*i.e.* dextran), less hazardous reducing agents (*i.e.* sodium borohydride, $NaBH_4$), and environmentally friendly solvents (*i.e.* water) can easily aid in reducing toxic waste generated from reactions while preserving their inherent efficacy.[12] These 3 parameters are key in controlling nanostructure shape and size, facilitating overall chemical consumption, and reducing energy input involved with their production.[12] By incorporating these reaction variables, synthetic methods such as the U-tube double diffusion technique, the hydrothermal protocol, and molten salt methods can ultimately reduce the energy and temperature input significantly.

1.4 Thesis Goals & Objectives

The objective of my PhD thesis are to explore green, cost effective synthetic methods in an effort to tailor and control the chemical composition and morphology of various metal-based nanomaterials. These nanomaterials have been further characterized and studied for their individual properties such as energy transfer and cytotoxic effects for solar cell and biomedical applications, respectively. In light of this goal, my thesis is organized, according to the following themes:

1. Nanomaterials Introduction (Chapter 1)
    - Applications
    - Metal-based nanomaterials for various applications

2. Utilizing economically advantageous synthetic methods leading to reproducible, uniform composition, and morphology (Chapter 2)
    - Green Synthesis Techniques
        - The chemical reduction of metal precursors in the presence of a reducing agent sodium borohydride ($NaBH_4$) via the U-tube double diffusion technique (Chapter 3)
        - Modification of the traditional hydrothermal method to synthesize metal oxide nanomaterials (Chapter 4, 5, and 6)
        - Surfactant-assisted molten salt synthetic method to prepare metal oxides (Chapter 5)
    - Characterization techniques for metal-based nanomaterials
3. Studies observing the formation mechanism of metal derived nanomaterials and their subsequent properties
    - Monitoring the nanostructure formation process as a function of time via TEM, SEM, XRD, and other structural characterization techniques
    - Exploring their properties and potential applications

Specifically, in this thesis, elemental metals will be discussed along with both binary and ternary metal oxides. Typically, binary and ternary metal oxides possess the general formula of M_xO_y and $A_xB_yO_z$, respectively, wherein M represents a transition metal and O is oxygen.[16] The ternary metal oxides, however, are more complex, because the $A_xB_yO_z$ structure incorporates two different metals for A and B. Nonetheless, all of the previously mentioned metal-based structures may be synthesized using methodologies described in Chapter 2.

Metallic-based nanostructures are robust with stable, well-defined crystallographic structures, and exhibit either metallic, semiconducting or insulating characteristics. These advantages have led to applications wherein metal oxides are fabricated as components of either sensors, fuel cells, microelectronic circuits, or coatings against corrosion.[17-19] Herein, we have explored the optical, magnetic, and biocompatible properties of metal-based nanostructures using green synthetic techniques. Specifically, we explain the synthesis, characterization, and potential application of elemental copper, nickel, hematite, ferrites/silicates, and calcium titanate nanostructures. Based upon this work, the following scientific questions were investigated:

- As compared with bulk metals, how do nanomaterials synthesized under ambient conditions perform photocatalytically?
- What is the correlation between the composition of metal ferrites and silicates with their magnetic properties?
- What is the effect upon electron transfer within nanoscale heterostructures when preparing constituent metal oxide materials under different synthetic techniques?
- Can hematite nanorhombohedra serve as potential drug delivery carriers and treatment vehicles within microglia cells?

1.5 Applications of Metal-based Nanomaterials

As previously mentioned, nanomaterials have attracted significant research interest due to their unique size-dependent optical, magnetic, electronic, thermal, mechanical, and chemical properties as compared with those of the corresponding bulk material. Specifically, as the size decreases, the surface area of the material increases with a large percentage of the total atoms as surface atoms.

In particular, metallic nanostructures exhibit unique optical and electronic properties as a result of their strong plasmonic resonance bands in the visible region, the delocalization of conduction electrons at the nanoscale, as well as an increasing binding energy with correspondingly decreasing size regimes.[20, 21] As for magnetic and thermal properties, size-dependent effects such as superparamagnetism and melting temperatures open the way for interesting materials such as nanoscale multiferroics and their possible applications for stable electronic devices. In the following section, nanomaterials' properties and their potential applicability in photovoltaics, sensing, catalysis, biology, and medicine will be discussed in detail.

1.5.1 Photovoltaics & Optical Applications

The conversion of solar energy into electric power through the mediation of photovoltaics (PV) has gained widespread attention for several reasons. First, power generation using fossil fuel sources leads to increased greenhouse gas emission and therefore can cause significant possible damage to the environment. Second, the continuous demand for power provides additional opportunities for the introduction of other alternative renewable techniques, particularly PV or solar devices, that capitalize upon the seasonal and even daily oscillations in solar irradiance.[22, 23] There are approximately 120,000 terawatts of solar power irradiating the earth each day, but only approximately 15 terawatts are actually consumed.[24] This suggests that in order to take advantage of the beneficence and widespread abundance of solar energy, it is necessary to exploit PV technology as a practical means of energy storage and release. However, for commercial implementation on a global scale, advances in device applications and materials are needed to decrease cost and to enhance energy conversion efficiency. In particular, a replacement for a material more efficient than bulk silicon for solar panels is needed. As a result,

nanochemistry and nanomaterials have created an opportunity and motivator for developing improved energy conversion devices using cost-effective fabrication techniques.

Various nanomaterials have been utilized as constituent components for the production of photovoltaic and solar devices such as but not limited to quantum dots (QDs), plasmonic nanoparticles, and inorganic semiconductor/polymer nanocomposites.[24-28] As for QD-based solar devices, it has been well understood that tuning the size of the QDs ultimately controls the nature of the absorption spectrum. Hence, in principle, an ensemble of QD sizes can be designed to cover the solar spectrum.[29, 30] Moreover, with QDs, the possibility of multi-exciton generation (MEG) can potentially allow for the effective production of more than one electron-hole pair upon a given excitation, thereby allowing for possibly higher solar energy efficiencies and higher overall efficiencies surpassing 100%.[31, 32] Hence, due to these favorable features, in this thesis, QDs have been chemically connected onto metal oxide materials in an effort to study, observe, and potentially optimize their charge transfer properties.

1.5.2 Sensing and Catalysis

A sensor is a mechanistic device that produces measurable signals as a result of either physical, chemical, or biological stimuli or even combinations of stimuli.[33] Nanomaterials may provide for enhanced sensor capabilities due to their high surface-to-volume ratio, which allows for improved chemical reactivity, because the shape and morphology can be finely tuned. Second, their high surface area allows for the ability to functionalize the surface with specific ligands for single-molecule sensitivity and specificity.[34] As a result, many elemental metals such as Au, Pt, Pd, Cu, and Ni nanostructures have been utilized for non-enzymatic glucose sensing.[35]

A catalyst denotes any substance that can enhance the rate of a reaction, particularly either photochemical, electrochemical, or organic reactions without itself being consumed in the

process.[36, 37] Concerning catalysts, nanoscale materials provide for a series of catalytic advantages. First, nanoscale sizes offer a higher intrinsic surface area as well as the presence of active facets, particularly high-index facets, especially as compared with their bulk counterparts. This attribute can thereby enhance their catalytic activity and increase the overall reactant conversion.[38] Second, increased surface area-to-volume ratios also yield large loading capacities, thereby resulting in surface modification of various metals and ligands. Third, nanomaterials display tunable size, shape, and surface features while maintaining their chemical composition (i.e. metallic-based systems), thereby enhancing the overall conversion efficiency of the reaction. As a result of these advantages, in terms of catalytic efficiency, nanomaterials are often being synthesized with greater precision via nanotechnology-enabled processes in terms of catalytic efficiency, and these structures have been subsequently used as functional components of fuel cells, solar devices, biosensors, and photocatalysts.

The use of photocatalysts for the removal of highly toxic organic pollutants such as dyes, phenols, biphenyls, and so on has gained importance for ecological and environmental reasons. Specifically, once organic pollutants are released into the aquatic environment, various ecological issues become relevant including but not limited to clogging of sewage treatment systems as well as damage towards aquatic biota.[39, 40] However, traditional methods (*i.e.* adsorption or coagulation) for organic species removal suffer from high operating costs as well as generating secondary pollutants. Indeed, phtocatalytic degradation processes provide for suitable and effective conditions for organic pollutant conversion into less toxic byproducts. Hence, within this thesis, elemental metal nanowires (*i.e.* Cu & Ni) have been explored for their photocatalytic properties when paired with TiO_2 nanoparticles for the degradation of organic dyes.

1.5.3. Biology & Medicine

Nanomaterials have also become important to the field of biology and medicine, more commonly referred to as nanobiotechnology and nanomedicine, respectively. Similar to other applications, the nanomaterials' characteristic high surface area-to-volume ratio results in potentially large loading capacities. Hence, the nanoparticles' surface functionalization with different moieties, such as organic ligands, antibodies, DNA, and imaging agents, has become significant for the development of biosensors, cell targeting, imaging contrast enhancement, fluorescent labels, and drug delivery applications (Figure 1.4).[41, 42]

For magnetic materials, the obvious application would be Magnetic Resonance Imaging (MRI), wherein materials may be utilized as either positive (T_1) or negative (T_2) contrast agents. As a result, many structures such as magnetic metal ferrites (MFe_2O_4), MnO, Fe_3O_4, and Gd-derived nanostructures, have been probed for their contrast enhancement for MRI.[43-46] Moreover, the versatility of nanomaterials allows for the option for the use of core shell materials and other types of motifs, thereby allowing for the ability to not only control size and morphology, and, but also more importantly, to enable the possibility of multiple modes of magenetic resonance imaging. Some examples of these materials are ZnO-coated $CoFe_2O_4$, QDs immobilized onto Fe_3O_4, and upconversion-based nanoparticles comprised of Fe_3O_4 and Au seeds.[47-49]

From a medicinal standpoint, nanomaterials are commonly used as drug carriers, drug targets, and for wound healing. For infection control, as examples, engineered nanomaterials that facilitate wound healing as well as drug release can be composed of components of either natural polymers (i.e. chitosan and fibrin), synthetic polymers (i.e. PLGA and PLLA), metallic nanoparticles, or ceramic nanoparticles.[50]

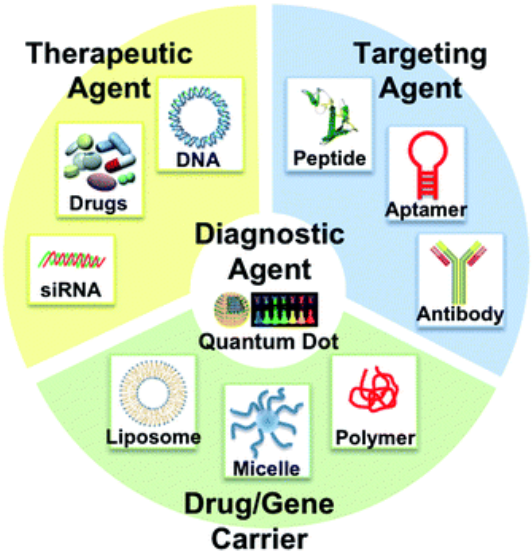

Figure 1.4. Possible construct of an all-in-one nanoplatform for imaging, drug delivery and targeting. Image adapted from Ho et al. *Nanoscale,* 2010, 2: pp. 60-68.

1.6 Toxicology

In order for these nanoscale systems to be viable agents for imaging and medicine, it is imperative to understand the relationship between the nanomaterials' physiochemical properties such as size, shape, and surface chemistry and their interaction within a cellular environment. This is a key consideration, as exposure to nanoparticles can potentially affect the cell's health, natural cell cycle & proliferation, ROS production, as well as cellular skeletal organization. [51]

Briefly, membrane trafficking encompasses all processes involving foreign objects that seek to either enter or exit the cellular membrane.[52] The internalization of these foreign materials within the plasma membrane is typically termed endocytosis. Depending upon the size, shape, and surface chemistry of the foreign materials, different uptake pathways may engulf the species. Typically, cellular uptake pathways fall under two categories: phagocytosis and pinocytosis (Figure 1.5). In the phagocytosis pathway, ingestion of microparticles measuring <0.5 μm is common, whereas smaller particles (i.e. <0.2 μm) are ingested through the pinocytosis route.[53, 54]

The pinocytosis pathway is further subdivided to include macro pinocytosis, clathrin-mediated endocytosis, caveolin-mediated endocytosis, and clathrin/caveolin-mediated endocytosis.[51, 55]

Clathrin-mediated endocytosis (CME), one of the most common forms of endocytosis, facilitates the internalization of materials of ~120 nm and below. These internalization processes include signal transduction and nutrient uptake, to name a few.[56] Unlike phagocytosis and macro pinocytosis, the CME process involves a triskelion-shaped protein, i.e. clathrin, that is composed of three heavy chains (~190 kDa) and three light chains (~25 kDa).[57-59] In particular, this mechanism proceeds within the sequence of the following steps: binding/recruitment, invagination, maturation, and scission (Figure 1.6).[60, 61]

During the binding and recruitment phases, the cargo-specific receptors (i.e. the epidermal growth factor (EGF) receptor) are bound to adaptor protein complexes (AP2, for example), subsequently capture the cargo (i.e. hormones, metabolites, nanoparticles, and etc), and thereafter become activated when the clathrin proteins begin to polymerize.[62] During the invagination step, the clathrin-coated pit (CCP) begins to internalize, in a process promoted by BAR (Bin/Amphiphysin/Rvs) domain proteins, as the clathrin proteins continue to polymerize in hexagons and pentagons to form a clathrin-coated vesicle (CCV). As the CCVs form, a range of proteins, such as actin and myosin, aid in stabilizing these vesicles.[63] After that, in the scission step, dynamin, a guanosine triphosphate hydrolase (GTPase) protein, separates the endocytotic vesicle from the plasma membrane.[61] Once the foreign materials have become engulfed, their effects within the cells can be analyzed using proliferation assays aimed at measuring lactate dehydrogenase (LDH) in addition to the production of reactive oxygen species (ROS), nitric oxide (NO) release, as well as inflammatory responses.[64, 65] Within this thesis, therefore, the effects of iron oxide engulfment within microglia cells will be further discussed in Chapter 6.

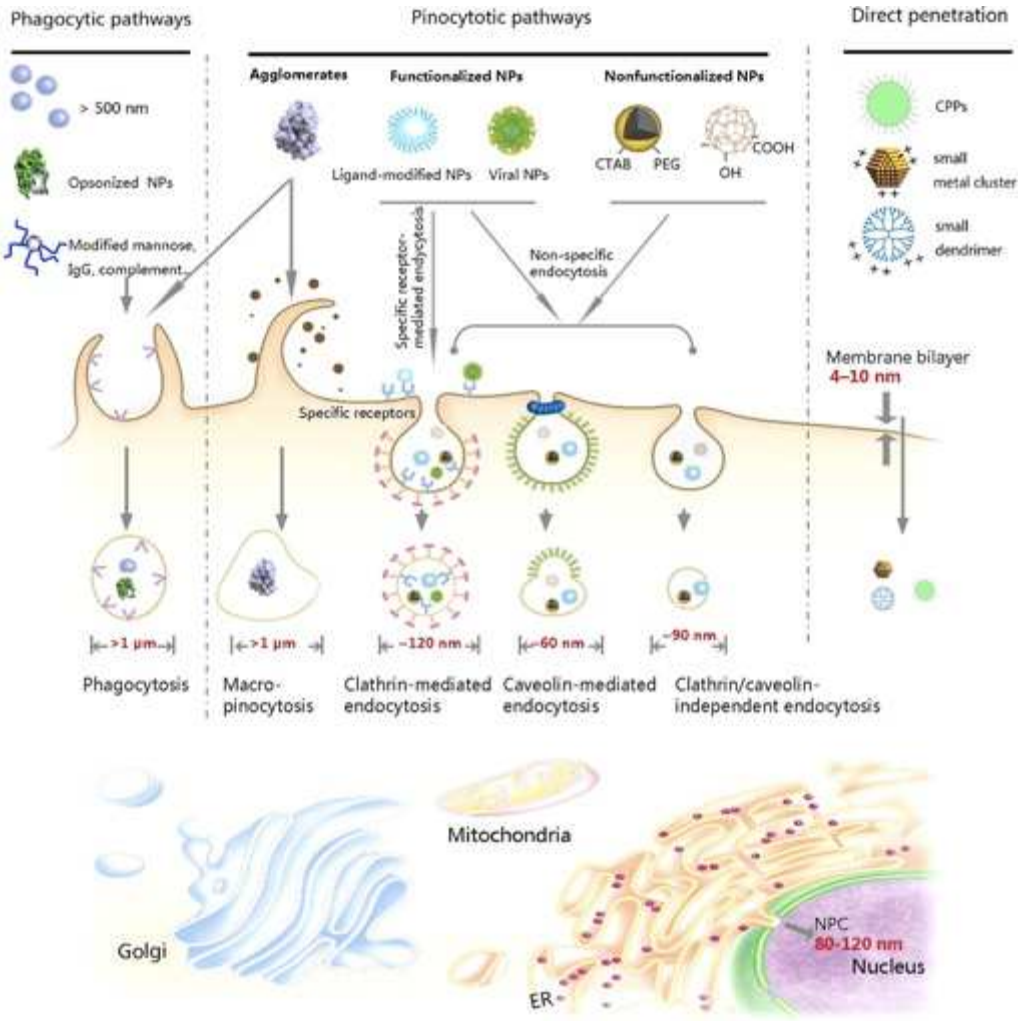

Figure 1.5. A schematic of various cellular uptake pathways associated with foreign particle incorporation. These pathways are the 'gatekeepers' within a mammalian cell and their relative success are primarily dominated by the particles' size. Image adapted from Zhu et al. *Acc. Chem. Res.*, **2013**, *46* (3): pp. 622–631.

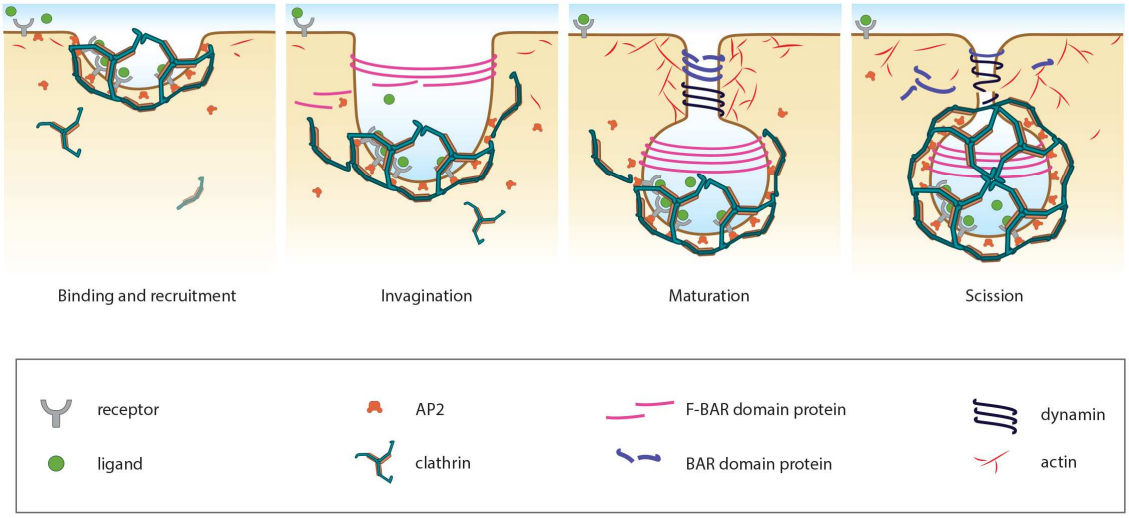

Figure 1.6. Schematic illustration of the clathrin-mediated endocytosis process. Image used by permission from MBInfo: www.mechanobio.info; Mechanobiology Institute, National University of Singapore.

1.7 Overview of Current Work

In an effort to better exploit nanomaterials' properties, we have utilized economically feasible synthetic techniques to further address their possible applications within solar and biomedicine fields. By addressing each hypothetical question, posed earlier in the Introduction, we improve the likelihood that these materials may be more readily translatable from the lab to the industry. Specifically in this thesis, we will systematically discuss the 'green' synthesis of crystalline elemental copper (Cu), and nickel (Ni), magnetic spinel ferrites (MFe_2O_4, wherein M is Co, Ni or Zn), hematite (α-Fe_2O_3), and rare earth ion-doped-calcium titanate (RE-$CaTiO_3$) using U-tube double diffusion, hydrothermal, and molten salt methods, respectively. In addition to tailoring the size and/or morphology, the possibility of using these nanomaterials for potential applications in solar cells and biomedicine was also probed. Highlights are listed below.

1.7.1 Synthesis, Characterization and Formation Mechanism of Crystalline Cu and Ni Metallic Nanowires under Ambient and Surfactantless Conditions (Chapter 3)

Crystalline elemental Cu and Ni nanowires have been successfully synthesized through a simplistic, malleable, and solution-based protocol involving the utilization of a U-tube double diffusion apparatus under ambient conditions. The nanowires prepared within the 50 and 200 nm template membrane pore channels maintain diameters ranging from ~90−230 nm with lengths attaining the micrometer scale. To mitigate for the unwanted but very facile oxidation of these nanomaterials to their oxide analogues, our synthesis mechanism relies on a carefully calibrated reaction between the corresponding metal precursor solution and an aqueous reducing agent solution, thereby resulting in the production of pure, monodisperse metallic nanostructures. These as-prepared nanowires were subsequently characterized from an applications' perspective so as to investigate their optical and photocatalytic properties.[66]

Figure 1.7. Schematic of the U-tube double diffusion technique for the synthesis of Cu and Ni NWs. Image reprinted with permission from Reference 66. Copyright 2014 American Chemical Society.

1.7.2 Correlating Composition and Morphology-Dependent Effects with Magnetic and Pair Distribution Function Measurements in a Family of Ferrite Nanoparticles and Nanowires (Chapter 4)

The magnetic spinel ferrites, MFe_2O_4 (wherein "M" = a divalent metal ion such as but not limited to Mg, Co, Zn, and Ni), represent a unique class of magnetic materials in which the rational introduction of different "M"s can yield correspondingly unique and interesting

magnetic behaviors. Herein we present a generalized hydrothermal method for the synthesis of single-crystalline ferrite nanoparticles and nanowires with M = Mg, Fe, Co, Ni, and Zn, respectively, which can be systematically and efficaciously produced simply by changing the metal precursor. Our protocol can moreover lead to reproducible size and morphology control by judicious selection of various surfactants and temperatures.

As such, nanostructures composed of M=Co, Ni, Zn particularly, have been probed for their effects of both (i) morphology and (ii) chemical composition upon the magnetic properties of these nanomaterials using complementary SQUID magnetometry. The structure of the samples was confirmed by atomic pair distribution function analysis of X-ray and electron powder diffraction data as a function of both particle size and morphology. These materials retain the bulk spinel structure to the smallest size (i.e., 3 nm).

1.7.3 Probing Charge Transfer in a Novel Class of Luminescent Perovskite-based Heterostructures Composed of Quantum Dots Bound to RE-activated $CaTiO_3$ Phosphors (Chapter 5)

Novel semiconducting heterostructures were successfully synthesized using green solution-based techniques, composed of cadmium selenide (CdSe) quantum dots (QDs) attached onto the surfaces of novel high surface area, porous rare-earth-ion doped alkaline earth titanate micron-scale spherical motifs, i.e. both Eu-doped and Pr-doped $CaTiO_3$, composed of constituent, component nanoparticles. These unique metal oxide perovskite building blocks were created using a multi-pronged synthetic strategy involving molten salt and hydrothermal protocols. Subsequently, optical characterization of these heterostructures indicated a clear behavioral dependence of charge transfer in these systems upon a number of parameters such as the nature of the dopant, the reaction temperature, and particle size. Specifically, 2.7 nm

diameter ligand-functionalized CdSe QDs were anchored onto sub-micron sized $CaTiO_3$-based spherical assemblies prepared by molten salt protocols.

We found that both the Pr- and Eu-doped $CaTiO_3$ displayed pronounced PL emissions, with maximum intensities observed using optimized lanthanide concentrations of 0.2 mol% and 6 mol%, respectively. Analogous experiments were performed on Eu-doped $BaTiO_3$ and $SrTiO_3$ motifs, but $CaTiO_3$ still proved to be the most effective host material amongst the three perovskite systems tested. Moreover, the ligand-capped CdSe QD-doped $CaTiO_3$ heterostructures exhibited effective charge transfer between the two individual constituent nanoscale components, an assertion corroborated by the corresponding quenching of their measured PL signals.[67]

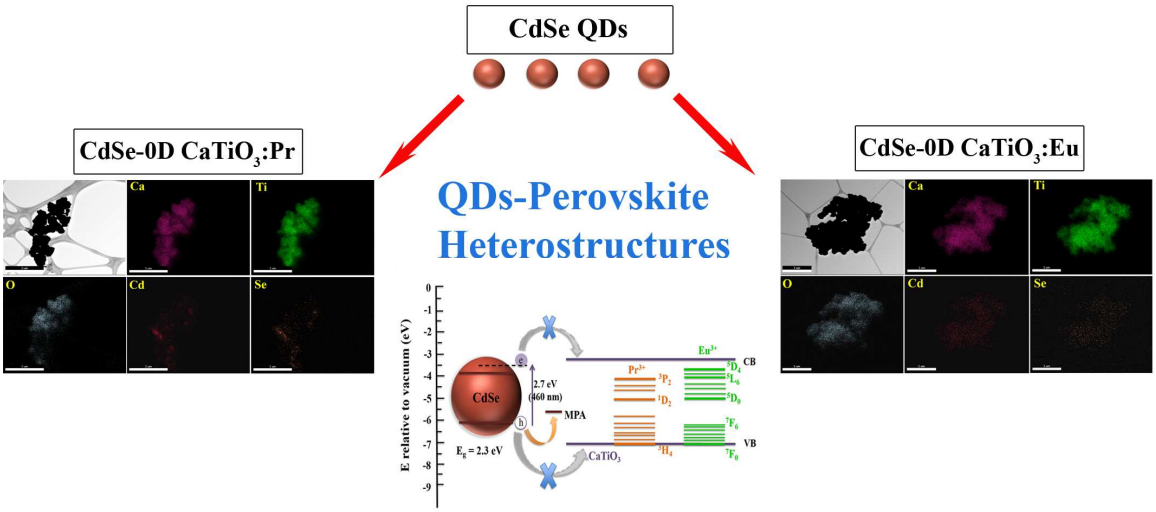

Figure 1.8. Schematic illustration of QD coupled onto RE-doped $CaTiO_3$ in order to observe their charge transfer properties. Image reproduced from Reference 67 with permission from *The Royal Society of Chemistry*.

1.7.4 Absence of Cytotoxicity towards Microglia of Iron Oxide (α-Fe_2O_3) Nanorhombohedra (Chapter 6)

Understanding the nature of interactions between nanomaterials, such as commercially ubiquitous hematite (α-Fe_2O_3) nanorhombohedra (N-Rhomb) and biological systems is of critical

importance for gaining insight into the practical applicability of nanomaterials. Microglia represent the first line of defense in the central nervous system (CNS) during severe injury or disease such as Parkinson's and Alzheimer's disease as illustrative examples.

To analyze the potential cytotoxic effect of N-Rhomb exposure in the presence of microglia, we have synthesized Rhodamine B (RhB)-labeled α-Fe_2O_3 N-Rhomb, with lengths of 47 ± 10 nm and widths of 35 ± 8 nm. Internalization of RhB-labeled α-Fe_2O_3 N-Rhomb by microglia in the mouse brain was observed, and a dose-dependent increase in the cellular iron content as probed by cellular fluorescence was detected in cultured microglia after nanoparticle exposure. The cells maintained clear functional viability, exhibiting little to no cytotoxic effects after 24 and 48 hours at acceptable physiological concentrations.

Importantly, the nanoparticle exposure did not induce microglial cells to produce either tumor necrosis factor alpha (TNFα) or interleukin 1-beta (IL1β), two pro-inflammatory cytokines, nor did exposure stimulate the production of nitrites and reactive oxygen species (ROS), which are common indicators for the onset of inflammation. Finally, we propose that under the conditions of our experiments, *i.e.* in the presence of RhB labeled-α-Fe_2O_3 N-Rhomb maintaining concentrations of up to 100 μg mL^{-1} after 48 hours of incubation, the *in vitro* and *in vivo* internalization of RhB-labeled α-Fe_2O_3 N-Rhomb are likely to be clathrin-dependent, which represents a conventional mechanistic uptake route for most cells. Given the crucial role that microglia play in many neurological disorders, understanding potential cytotoxic effects of these nanostructures is of fundamental importance if they are to be used in a therapeutic setting.[68]

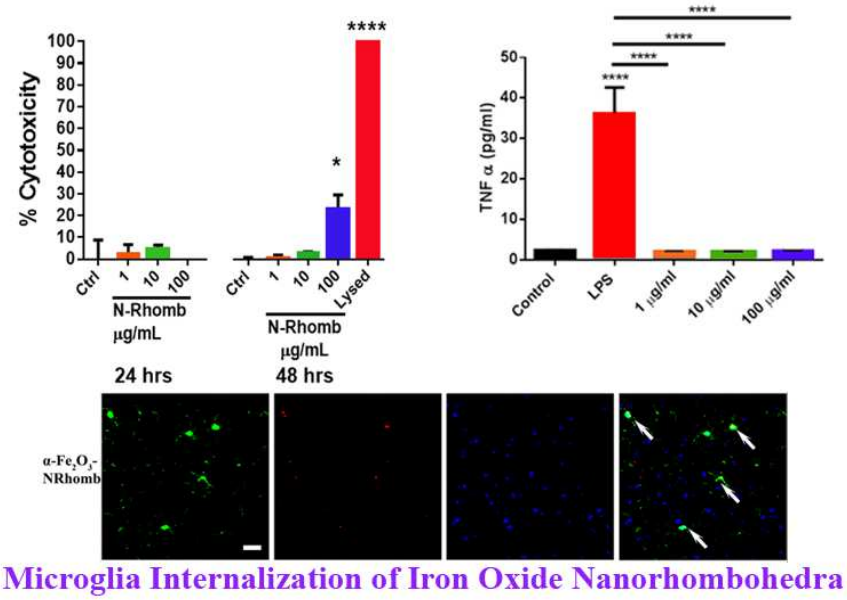

Figure 1.9. Evaluation of iron oxide cytotoxicity towards microglia cells. Image reproduced from Reference 68 with permission from *The Royal Society of Chemistry*.

1.8 References

1. J. M. Patete, X. H. Peng, C. Koenigsmann, Y. Xu, B. Karn and S. S. Wong, *Green Chemistry*, 2011, 13, 482-519.
2. I. Freestone, N. Meeks, M. Sax and C. Higgitt, *Gold Bulletin*, 2007, 40, 270-277.
3. M. Reibold, P. Paufler, A. A. Levin, W. Kochmann, N. Patzke and D. C. Meyer, *Nature*, 2006, 444, 286-286.
4. R. Feynman, *Engineering and Science*, 1960, 23, 22-36.
5. M. C. Roco, *Journal of Nanoparticle Research*, 2011, 13, 427-445.
6. National Science and Technology Council, ed. N. N. Initiative, 2016, pp. 1-112.
7. Interagency Working Group on Nanoscience Engineering and Technology, ed. N. N. Initiative, Washington, D.C. , 2000.
8. Z.-Y. Zhou, N. Tian, J.-T. Li, I. Broadwell and S.-G. Sun, *Chemical Society Reviews*, 2011, 40, 4167-4185.
9. P. G. Bruce, B. Scrosati and J.-M. Tarascon, *Angewandte Chemie*, 2008, 47, 2930-2946.
10. H. Flynn, Nanotechnology Update: Corporations Up Their Spending as Revenues for Nano-enabled Products Increase, https://portal.luxresearchinc.com/research/report_excerpt/16215, Accessed February 17, 2014, 2014.
11. W. W. I. C. f. Scholars, Project on Emerging Nanotechnologies, Inventories: Consumer Products, http://www.nanotechproject.org/, Accessed January 20, 2010, 2010.
12. H. H. Duan, D. S. Wang and Y. D. Li, *Chemical Society Reviews*, 2015, 44, 5778-5792.
13. T. J. Collins, Simon and Schuser Macmillan, New York, 1997.
14. P. T. Anastas and J. C. Warner, *Green Chemistry: Theory and Practice*, Oxford University Press, New York, 1998.
15. R. S. Varma, *Pure and Applied Chemistry*, 2013, 85, 1703-1710.
16. J. Shi and L. Guo, *Progress in Natural Science: Materials International*, 2012, 22, 592-615.
17. M. U. Din Sheikh, G. A. Naikoo, M. Thomas, M. Bano, D. Ahirwar, U. J. Pandit and F. Khan, *Rsc Advances*, 2016, 6, 42807-42818.
18. S. B. Warren, S. Vernick, E. Romano and K. L. Shepard, *Nano Lett*, 2016, 16, 2674-2679.
19. A. Aijaz, J. Masa, C. Rosler, W. Xia, P. Weide, A. J. R. Botz, R. A. Fischer, W. Schuhmann and M. Muhler, *Angewandte Chemie-International Edition*, 2016, 55, 4087-4091.
20. D. L. Feldheim and C. A. Foss, *Metal Nanoparticles: Synthesis, Characterization, and Applications*, Marcel Dekker, Inc, New York, NY, 2002.
21. S. A. Maiera and H. A. Atwater, *Journal of Applied Physics*, 2005, 98, 011101-011101 - 011101-011110.
22. A. Kudo and Y. Miseki, *Chemical Society Reviews*, 2009, 38, 253-278.
23. Y. Ma, X. Wang, Y. Jia, X. Chen, H. Han and C. Li, *Chemical Reviews*, 2014, 114, 9987-10043.
24. G. Chen, J. Seo, C. Yang and P. N. Prasad, *Chemical Society Reviews*, 2013, 42, 8304-8338.
25. A. Kongkanand, K. Tvrdy, K. Takechi, M. Kuno and P. V. Kamat, *J Am Chem Soc*, 2008, 130, 4007-4015.

26. J. M. Luther, M. Law, M. C. Beard, Q. Song, M. O. Reese, R. J. Ellingson and A. J. Nozik, *Nano Lett*, 2008, 8, 3488-3492.
27. J. Seo, M. J. Cho, D. Lee, A. N. Cartwright and P. N. Prasad, *Adv Mater*, 2011, 23, 3984-3988.
28. Y. Sun, C. J. Takacs, S. R. Cowan, J. H. Seo, X. Gong, A. Roy and A. J. Heeger, *Adv Mater*, 2011, 23, 2226-2230.
29. A. P. Alivisatos, *Science*, 1996, 271, 933-937.
30. C. B. Murray, D. J. Norris and M. G. Bawendi, *Journal of American Chemical Society*, 1993, 115, 8706-8715.
31. R. J. Ellingson, M. C. Beard, J. C. Johnson, P. Yu, O. I. Micic, A. J. Nozik, A. Shabaev and A. L. Efros, *Nano Letters*, 2005, 5, 865-871.
32. M. C. Beard, K. P. Knutsen, P. Yu, J. M. Luther, Q. Song, W. K. Metzger, R. J. Ellingson and A. J. Nozik, *Nano Letters*, 2007, 7, 2506-2512.
33. T. R. Fadel, D. F. Farrell, L. E. Friedersdorf, M. H. Griep, M. D. Hoover, M. A. Meador and M. Meyyappan, *ACS Sensors*, 2016, 1, 207-216.
34. P. Zijlstra, P. M. R. Paulo and M. Orrit, *Nature Nanotechnology*, 2012, 7, 379-382.
35. S. Y. Tee, P. T. Choon and E. Ye, *Materials Science and Engineering: C*, 2016, In Press.
36. R. Long, H. Huang, Y. P. Li, L. Song and Y. J. Xiong, *Advanced Materials*, 2015, 27, 7025-7042.
37. C. Koenigsmann, M. E. Scofield, H. Q. Liu and S. S. Wong, *Journal of Physical Chemistry Letters*, 2012, 3, 3385-3398.
38. Z. W. Quan, Y. X. Wang and J. Y. Fang, *Acc Chem Res*, 2013, 46, 191-202.
39. C.-C. Wang, J.-R. Li, X.-L. Lv, Y.-Q. Zhang and G. Guo, *Energy & Environmental Science*, 2014, 7, 2831-2867.
40. D. Lin, Q. Zhao, L. Hu and B. Xing, *Chemosphere*, 2014, 103, 188-196.
41. E. Y. Kim, D. Kumar, G. Khang and D. K. Lim, *Journal of Materials Chemistry B*, 2015, 3, 8433-8444.
42. H. Dong, S.-R. Du, X.-Y. Zheng, G.-M. Lyu, L.-D. Sun, L.-D. Li, P.-Z. Zhang, C. Zhang and C.-H. Yan, *Chem Rev*, 2015, 115, 10725-10815.
43. N. Lee, D. Yoo, D. Ling, M. H. Cho, T. Hyeon and J. Cheon, *Chem Rev*, 2015, 115, 10637-10689.
44. T. J. Kim, K. S. Chae, Y. Chang and G. H. Lee, *Current Topics in Medicinal Chemistry*, 2013, 13, 422-433.
45. H. M. Joshi, *Journal of Nanoparticle Research*, 2013, 15, 1235-(1-19).
46. P. Chevallier, A. Walter, A. Garofalo, I. Veksler, J. Lagueux, S. Begin-Colin, D. Felder-Flesch and M. A. Fortin, *Journal of Materials Chemistry B*, 2014, 2, 1779-1790.
47. T. H. Shin, Y. Choi, S. Kim and J. Cheon, *Chemical Society Reviews*, 2015, 44, 4501-4516.
48. P. Bouziotis, D. Psimadas, T. Tsotakos, D. Stamopoulos and C. Tsoukalas, *Current Topics in Medicinal Chemistry*, 2012, 12, 2694-2702.
49. N. Venkatesha, Y. Qurishi, H. S. Atreya and C. Srivastava, *Rsc Advances*, 2016, 6, 18843-18851.
50. N. Kamaly, B. Yameen, J. Wu and O. C. Farokhzad, *Chem Rev*, 2016, 116, 2602-2663.
51. Z. W. Mao, X. Y. Zhou and C. Y. Gao, *Biomaterials Science*, 2013, 1, 896-911.
52. J. M. Herrmann and A. Spang, *Methods Mol Biol*, 2015, 1270, 1-12.
53. B. D. Chithrani, A. A. Ghazani and W. C. W. Chan, *Nano Letters*, 2006, 6, 662-668.

54. H. Y. Yuan, J. Li, G. Bao and S. L. Zhang, *Phys Rev Lett*, 2010, 105.
55. M. T. Zhu, G. J. Nie, H. Meng, T. Xia, A. Nel and Y. L. Zhao, *Acc Chem Res*, 2013, 46, 622-631.
56. K. Takei and V. Haucke, *Trends Cell Biol*, 2001, 11, 385-391.
57. M. Bohdanowicz and S. Grinstein, *Physiological Reviews*, 2013, 93, 69-106.
58. T. Kirchhausen, *Trends Cell Biol*, 2009, 19, 596-605.
59. M. A. Edeling, C. Smith and D. Owen, *Nat Rev Mol Cell Biol*, 2006, 7, 32-44.
60. K. O. Schubert, M. Focking, J. H. Prehn and D. R. Cotter, *Mol Psychiatry*, 2012, 17, 669-681.
61. H. T. McMahon and E. Boucrot, *Nat Rev Mol Cell Biol*, 2011, 12, 517-533.
62. B. T. Kelly, S. C. Graham, N. Liska, P. N. Dannhauser, S. Honing, E. J. Ungewickell and D. J. Owen, *Science*, 2014, 345, 459-463.
63. M. Kaksonen, C. P. Toret and D. G. Drubin, *Cell*, 2005, 123, 305-320.
64. S. M. Smith, M. B. Wunder, D. A. Norris and Y. G. Shellman, *Plos One*, 2011, 6.
65. S. K. Choudhari, M. Chaudhary, S. Bagde, A. R. Gadbail and V. Joshi, *World Journal of Surgical Oncology*, 2013, 11.
66. C. S. Lewis, L. Wang, H. Q. Liu, J. K. Han and S. S. Wong, *Crystal Growth & Design*, 2014, 14, 3825-3838.
67. C. S. Lewis, H. Q. Liu, J. Y. Han, L. Wang, S. Y. Yue, N. A. Brennan and S. S. Wong, *Nanoscale*, 2016, 8, 2129-2142.
68. C. S. Lewis, L. Torres, J. T. Miyauchi, C. Rastegar, J. M. Patete, J. M. Smith, S. S. Wong and S. E. Tsirka, *Toxicology Research*, 2016, 5, 836-847.

Chapter 2 – Synthesis & Characterization Techniques of Metal-based Nanomaterials

2.1 Environmentally-friendly synthetic techniques

There are countless techniques for generating nanomaterials, and these methods generally fall under two categories, i.e. bottom-up and top-down approaches (see Figure 2.1).[1] In the top-down approach, bulk or macroscale materials undergo reductive chemical, electrical, or thermal processes in order to facilitate nanoscale production. A few examples of the 'top-down' method include lithography, laser ablation, and vapor condensation. By contrast, in 'bottom-up' approaches, nanostructures can be synthesized from either atomic or molecular 'building blocks', thereby allowing the precursor particles to grow in size. As such, this approach requires a deep understanding of molecular structures and assemblies, and necessitates a broad multidisciplinary approach.

Bottom-up synthetic methods include sol-gel, precipitation, self-assembly, and chemical vapor deposition protocols, to name a few. Common drawbacks for the top-down synthesis are the reliance upon expensive equipment, low throughput processes, and production of materials with surface defects. Hence, the bottom-up approach has gained significant interest, because its synthetic techniques tend to be relatively simplistic and inexpensive, and are more likely to produce defect-free materials.

Recently, the relatively sustainable environmentally friendly production of nanomaterials has become a matter of great importance for commercial and industrial applications. As such, emphasis has been placed on creating 'greener' methods using less hazardous chemicals and either reducing or completely removing toxic by-products created while synthesizing these materials. In pursuit of this goal, bottom up approaches such as wet chemical and solution-based syntheses have become popular synthetic methodologies.

As previously mentioned, the bottom up approach does not require a specialized apparatus, but rather inexpensive equipment with flexible protocols, employing a variety of chemicals such as precursors, solvents, reducing agents, oxidizing agents, and surfactants to achieve the desired end product. Similarly, manipulating various reaction parameters such as time, temperature, pH, and concentration can also allow for greater control over the resulting materials. From an applications' perspective, these synthetic routes give rise to not only effective control of the composition, size, and morphology of the nanoparticles, but also reproducible synthesis of high quality, uniform, and monodisperse nanostructures. Hence, our work focuses on green, solution-based bottom-up, synthetic approaches for metal-based nanomaterials (see Figure 2.2), and their properties for potential applications. More specifically, this thesis will discuss techniques such as wet-solution, solvothermal/hydrothermal, molten salt, template-mediated growth, and electrospinning synthetic protocols.

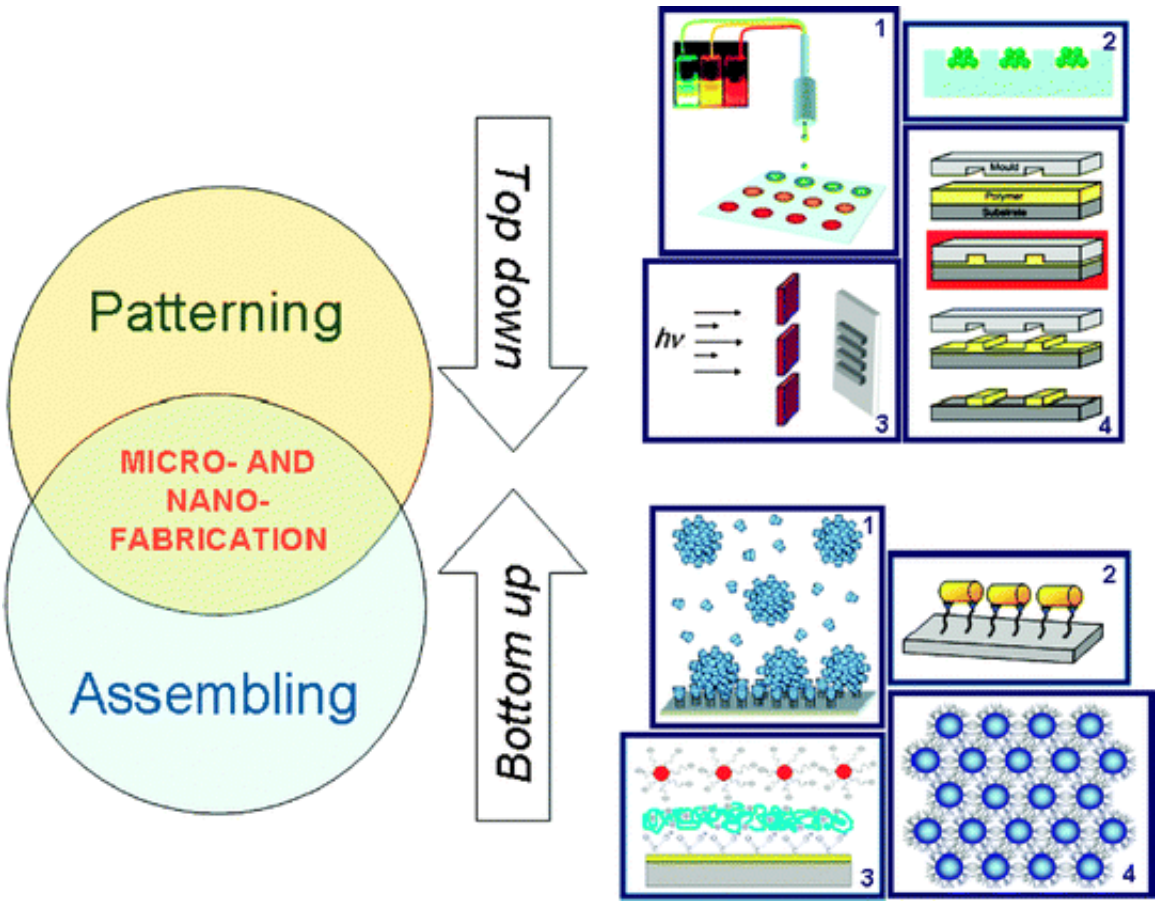

Figure 2.1: Scheme of complementary "top-down" and "bottom-up" approaches for fabrication of micro- and nano-structures. For the bottom-up strategies: examples include (1) host–guest chemistry, (2) covalent immobilization onto substrate, (3) electrostatic layer-by-layer deposition, (4) self-assembly. For the top-down strategies: examples consist of (1) ink jet printing, (2) capillary assembly, (3) photolithography, (4) nanoimprinting lithography. Image adapted from Curri et al. *Phys. Chem. Chem. Phys.* 2010, 12: pp. 11197-11207.

2.1.1 Wet Chemical Technique

Wet chemical or solution-based synthetic routes are relatively simple one-pot syntheses for the production of high-quality nanostructures. This method is particularly advantageous by comparison with the solid-state approach, as the liquid phase provides a versatile means for controlling the structural, compositional, and morphological features of the resulting nanomaterials.[2] However, this method also has limitations for the preparation of nanomaterials at the industrial stage, due to the possibility of long reaction times as well as uncontrolled nucleation and growth.[3]

To overcome these limitations, various parameters such as the choice of a stabilizer, stabilizer-to-precursor ratios, temperature, and reaction time must be implemented and rationally controlled in order to achieve uniform shape, size, and dispersion stability.[4] For this technique, stabilizers may behave as either a solvent or a reducing agent. As a result, common solvents such as dimethyl formamide (DMF), ethylene glycol (EG), benzyl-alcohol, and methyl isobutyl ketone (MIBK), can be employed for various metal-based nanostructures.[5-10] Currently, many of these solvent-mediated syntheses are assisted by microwave irradiation for enhanced nanostructure control.[11] As a result of their tunable features, many metal-based nanomaterials have been produced, including CdSe quantum dots (QDs), CdS QDs, TiO_2 nanotubes, Fe_2O_3 nanoparticles, and metal-doped MnO_2 nanoflowers.[12-15]

2.1.2 Solvothermal/Hydrothermal Technique

Solvo- and hydrothermal syntheses are techniques that utilize high temperature and pressure to induce crystallization in a sealed vessel (*i.e.* an autoclave or calorimeter-type apparatus). Specifically, with this method, as the temperature increases above the solvent's boiling point, the solvent remains in the liquid phase under pressure. This reaction would not be feasible under normal conditions, especially at low temperatures between 100- 200 °C. In most cases, the synthesis is carried out in an oven, though recently, microwave-assisted heating has become more common for relatively short reactions. The main difference between the solvothermal and hydrothermal methodologies of materials, however, is the type of solvent utilized for their synthesis. The solvothermal method incorporates organic solvents (*i.e*. non-aqueous solvents), whereas the hydrothermal method is limited to aqueous solution, particularly water.

Both synthetic techniques involve control over a wide array of experimental parameters to yield the desired product such as but not limited to reaction temperature, reaction time, pH, solvent/solvent (v/v) ratios, and various forms of surfactant. By alternating among these parameters, certain advantages such as phase purity, high crystallinity, narrow size distributions, high yield, and overall homogeneity in morphological features may be achieved. The hydrothermal/solvothermal synthetic technique is not only facile and cost-effective but also reproducible, as it yields large amounts of highly pure and crystalline materials. However, disadvantages associated with this technique includes the need for expensive autoclaves as well as the practical difficulty associated with observing in-situ growth processes without using sophisticated synchrotron techniques, such as can be found at the National Synchrotron Light Source II (NSLS II), for instance.[16] Nonetheless, this technique has resulted in the synthesis of carbonaceous species; elemental metals (*i.e.* Cu, Te, Au); metal oxides (*i.e.* SiO_2, Fe_2O_3, $SrTiO_3$, Co_3O_4); and carbon-based materials (i.e. graphene) as various morphological motifs by varying the aforementioned reaction parameters.[17-23]

2.1.3 Molten Salt Synthesis

The molten salt synthesis (MSS) is a relatively simple technique involving the use of molten salts as the reaction medium and metal precursors to synthesize complex metal oxides. This method may be easily scaled up to produce large quantities of synthetic material. Specifically, the molten salts are typically mixed with metal precursors (on occasion in the presence of a surfactant), and ground into a uniform mixture with the aid of a mortar and pestle. The mixture is then transferred into either an alumina or ceramic crucible and heated in a furnace at or above the melting temperature of the eutectic salt. At this temperature, the salt liquefies, providing a medium for the reaction to occur between the precursor ions as the product particles

begin to form. Similar to the hydro/solvothermal methods, parameters may be adjusted and tuned to yield significant changes, such as morphology, in the overall product.

The most critical parameter for the MSS method is the salt medium, which dictates the overall reaction temperature, degree of homogeneity, particle size/shape, and the degree of agglomeration.[24] Chlorides and sulfides are typically used as molten salt media, as they are stable, readily available, and easily removed with water. Sodium chloride (NaCl), potassium chloride (KCl), and potassium nitrate (KNO_3) as well as their salt mixtures including NaCl/KCl and NaOH/KOH represent very commonly used examples.[24-27] In the MSS technique, the salt must be added in excess ~80-120 wt % to adequately fill in the spaces between the reactant particles to coat the reactant's surface.[28] Upon heating, product formation takes place in two stages.

First, the reactants dissolve in the molten salt medium, and the product initially forms. Soon thereafter, the reactant seed nuclei are consumed, leading to particle growth through Ostwald ripening.[29] One of the primary advantages of this method is its high throughput of materials produced, which can provide for highly scalable technique to potentially address the demands of industry. However, even with all of the experimental parameters optimized, it is sufficiently challenging to synthesize uniform and monodisperse nanomaterials.[30] Nonetheless, due to the method's versatility, this synthesis has been adapted to facilitate the preparation of many metal-based nanostructures. For example, $BiFeO_3$, $BaTiO_3$, $CaTiO_3$, $NiFe_2O_4$, $SrTiO_3$, $SrRuO_3$ SnO_2, and $SrAl_2O_4$, $LiMn_2O_4$ of various shapes and sizes have been prepared using the MSS method for diverse applications.[25, 31-36]

2.1.4 Template-based Synthesis: U-tube Double Diffusion Technique

Nanomaterials are also commonly synthesized using electrochemical deposition and chemical vapor deposition (CVD). These methods provide another avenue for the mass

production of nanostructures, particularly particles and wires. To mediate for these reactions at a practical level often requires the use of anodic alumina oxide (AAO) membranes to typically assist in nanowire fabrication. The templates are chemically inactive; however, the membrane must first undergo the anodization process to develop well-organized pores at their surfaces for the electrochemical process.

However, there are a few drawbacks to the CVD technique, namely the creation of hazardous by-products (*i.e.* CO, HF and etc) in the CVD reaction, and moreover, these protocols require the use of volatile CVD precursors at high temperatures.[37] Furthermore, they also involve expensive equipment such as UHV chambers equipped with MBE sputtering, which can cost around $800,000 a piece, for example.[37]

A more feasible approach towards developing novel NWs is commonly known as the U-tube double diffusion technique, which involves the use of templates containing pore sizes of well defined shapes and dimensions with demonstrated size control over the resulting product dimensions and desired morphology. Specifically, the U-tube double diffusion apparatus consists of a spatially confining template membrane placed between two glass half-cells. Upon introduction of solution-based precursors within each half-cell, the mixing mild precursors nucleate within the channels to initiate localized crystal growth. As the reaction undergoes nucleation within the template pores, the generation of 1D materials takes place with little if any toxic by-products produced.

Two common forms of template materials are typically used for the formation of 1D nanowires and nanotubes, namely track-etched polycarbonate (PC) and AAO membranes, respectively. In particular, when the interactions between the metal precursor molecules in solution are greater than those between the solution and the surrounding pore walls, nucleation takes place within the pores through a homogeneous-type process, subsequently leading to

nanowire formation. This is typically the case within PC membranes, depending upon the nature of the precursor interaction. On the other hand, when interactions between the precursor molecules in solution are weaker than the corresponding interactions with the adjoining pore walls, the nucleation takes place via a heterogeneous process, resulting in the formation of nanotubes.[38] Unlike the CVD technique, the U-tube double diffusion technique represents a reasonably facile and relatively mild method, typically performed under ambient conditions without the use of toxic precursors.

It is noteworthy that such a methodology does not require either high temperatures, powered instrumentation, or the use of particularly toxic reagents/byproducts. As such, this strategy provides a cost effective, flexible, and generalizable approach for the synthesis of metal-based nanowires under ambient conditions, wherein the diameters of these nanowires may be reliably controlled by the template pore size dimension itself. Specifically, classes of elemental metals, binary metals, metal oxides, and semiconductors such as Pt, Pd, Ru, Au, Cu, Ni, Pd_9Au, PdAu, ZnO, CdS, and Tb doped $CePO_4$ have been synthesized using this technique.[39-42] The major disadvantage of the template-based methodology is in its intrinsically low yield of the desired product as compared to with other green synthetic techniques.

2.1.5 Electrostatic spinning (Electrospinning)

Electrospinning is a facile, cost effective, and reproducible technique wherein electrical charge draws polymer solutions into what is commonly known as a Taylor cone for instance, and ultimately results in the formation of a threadlike motif onto a substrate. This method can easily be applied to the fabrication of 1D nanofibers (NFs).[43] This particular method was first developed in 1934 to prepare continuous fibers for the textile industry. Since then, it has gained interest due to the versatility of the approach and its ability to produce an array of different materials such as elemental metal, metal oxide, polymers, and composites within a 1D motif. Similar to the

hydrothermal method, adjusting various experimental parameters yields fibers with diameters ranging from tens of nanometers to several micrometers. These reaction variables may be divided into classes such as solution parameters, technical parameters, and temperature conditions.[44]

Specifically, solution parameters may be further sub-divided into the following categories, such as concentration, viscosity, and molecular weight (i.e. polymers). These variables control the general morphology and uniformity of these fibers as opposed to inducing the formation of bead-like structures within the fibers. Technical parameters such as the voltage, flow rate, the collector, as well as the distance between the syringe tip and the collector are also important. Typically, longer distances between the tip and the collector give rise to thinner fibers.[45]

A general electrospinning setup consists of four essential components: a high voltage power supply, a syringe/capillary tube with a metallic needle, a syringe pump, and a ground collector or substrate. In the electrospinning process, the syringe is filled with a viscous polymer solution, the voltage is applied, and initially, elongated droplets begin to form. As the voltage increases, the electrostatic forces overcome the surface tension of the solution to form a Taylor cone. The product is then collected at the opposite end of the grounded receiving substrate.

These electrospun fibers yield highly porous features, large surface area, and good permeability, thereby becoming of interest for potential applications such as filter materials for environmental applications; wound dressing and drug delivery for biomedical purposes; as well as textile materials.[46-51] Moreover, due to the versatile nature of the electrospinning technique, many polymer-based and metal-derived nanofibers such as carbon nanotube hybrids, PVA, TiO_2, In_2O_3, MFe_2O_4, and ZnS, respectively, have been produced by this means.[52-57] However, this technique's ability to synthesize large amounts of materials in its conventional form remains inadequate in terms of transitioning from the laboratory phase to industry scale. To bridge this

divide, scientists have established different types of electrospinning approaches such as multi-needle and needle-less electrospinning techniques.[58, 59]

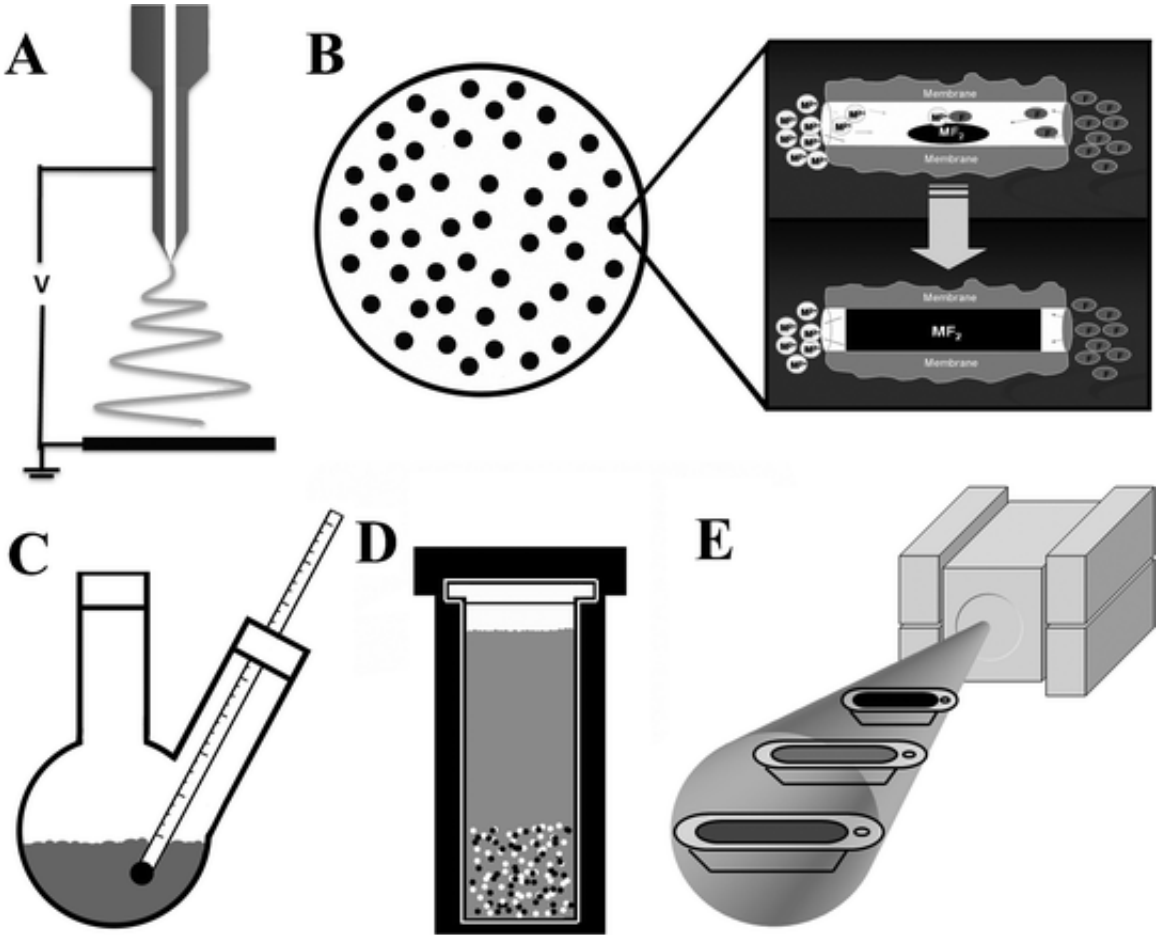

Figure 2.2: Schematic of various experimental synthetic techniques for nanoscale synthesis such as (A) electrospinning, (B) template-mediated growth, (C) wet solution methods, (D) solvo/hydrothermal protocols, and (E) molten salt methods. Image adapted from Tiano et al. *Chem. Commun.*, 2010, **46**, 8093-8130

2.1.6 Synthetic Technique Conclusions

In the previous sections, a list of reasonable environmentally suitable techniques was provided for nanomaterial synthesis. However, it is clear that each methodology has its own advantages and disadvantages and must be carefully chosen based on the applications that the nanostructures would serve. For instance, for creating uniform anisotropic structures for use in nanoelectronics, either electrospinning or template-based methods tend to better. On the other

hand, for industrial applications such as energy storage and catalysts, a larger amount of material is often necessary. As such, methodologies such as solution gelation (sol-gel), molten-salt, and hydro/solvothermal reactions would better facilitate the production of large quantities.

Hence, the cost-effective capability of these techniques in congruence with nanomaterials' unique physical properties that have rendered nanoscale materials as potentially useful for applications, including electronics, photovoltaics, sensing, catalysis, biology, as well as medicine.[53, 60, 61] Hence in this thesis, we intend to highlight green synthetic techniques, particularly the U-tube double diffusion, hydrothermal, and molten salt techniques in order to synthesize these metal-based materials, and subsequently study their properties for their potential in solar cell and biomedical applications.

2.2 Characterization Techniques

2.2.1 Overall Objectives Related to Structural Characterization

The characterization of nanomaterials is typically conducted using photons, electrons, neutrons, and ions to name a few of the most common probes. Specifically, the probing source (i.e. light) used to analyze nanostructures often varies in frequency, ranging from gamma to infrared rays. From these characterization techniques, information can be obtained regarding the structural, chemical or physical characteristics of the nanomaterial in question.

Though some characterization techniques may use a similar source, additional and diverse information can also be obtained. For instance, with X-ray diffraction and X-ray photoelectron spectroscopy, one technique confirms information about the crystal structure whereas XPS can be used to give insights into electronic effects as well as the oxidation states of the material. In this thesis, techniques such as X-ray diffraction, X-ray photoelectron spectroscopy, pair distribution function analysis, electron microscopy, Brunauer-Emmett-Teller surface area analysis, and

SQUID measurements will be employed to confirm the composition, homogeneity, morphology, surface area, and magnetic properties of as-prepared nanomaterials, respectively.

2.2.2 X-ray Analysis – Techniques to Identify Composition of Nanostructures

X-rays are high-energy electromagnetic waves with short wavelengths of ~ 1 Å, close to that of an atom. Utilizing these X-rays has enabled scientists to probe crystalline materials at the atomic scale. As a result, materials can be characterized based on their fingerprint X-ray patterns, thereby confirming their crystal structure and size. Generally, data are acquired as the X-rays interact with the sample, causing scattering effects (i.e. constructive interference) of either electrons, transmitted X-rays, or scattered X-rays depending on the instrument (*i.e.* XRD, XPS, and etc) being used.

2.2.2.1 X-Ray Diffraction

X-ray diffraction (XRD) is one of many tools that utilize scattered X-rays, particularly coherent X-rays, to provide definitive structural information as well as data on the interatomic distances of nanomaterials. The XRD setup consists of four components: an X-ray source, incident beam optics, a sample stage, and the detector. The X-ray source may be composed of either Cu, Cr, Mo, Fe, or Co as an example. In a typical XRD measurement, the X-ray source bombards the Cu target, thereby producing X-rays with electrons emanating from a hot filament typically composed of Tungsten. The X-rays are then ionized by the incident beam optic, which are composed of divergent/scattering slits, which can influence the peak intensities and resolution.

Once the X-rays strike the sample, coherent scattering of X-rays occurs and its extent/intensity is collected and recorded in the detector for further processing. The diffraction data are typically presented as scattered intensity versus the Bragg angle results. It is important to

note that in order to elucidate the crystal structure, the X-ray wavelength must be of the same order of magnitude as the interatomic distances of the material that is being characterized. For instance, the Rigaku Ultima III uses a Cu X-ray tube, which gives rise to a wavelength of ~1.54 Å, an efficient length for characterizing inorganic materials.

A conventional XRD spectrum is a plot of the signals detected (Intensity) versus the diffraction angle (2θ). Once the diffraction patterns are obtained, their peak positions and peak widths provide for relevant information about distances between crystalline planes and the crystallite size, respectively. Specifically, Bragg's Law governs the behavior of diffraction patterns through the following Bragg equation 2.1:

$$n\lambda = 2d\sin\theta \qquad (2.1)$$

Here, *d* is the lattice spacing, θ is the angle between the incident X-ray and scattering plane, 'n' is an integer, and λ is the wavelength of the incident X-ray. First, the orientation of crystalline planes is defined in terms of a notation called Miller Indices (*hkl*). According to Bragg's theory, the diffraction from a set of planes separated by an equal distance is only possible at certain specific angles. Specifically, only outgoing diffracted X-rays that are in phase will contribute to waves of constructive interference. Bragg's Law is geometrically explained in Figure 2.3. In the diffraction characterization tool, the incident X-ray beams, 1 and 2, impinge at an angle θ onto a set of planes (*hkl*). The spaces between each plane are characterized by the d-spacing (*d*) between them and the two angles from incoming and outgoing X-rays captured in the 2sinθ term.

To prepare a typical sample for XRD analysis, a fixed quantity of as-prepared nanomaterial was dispersed in ethanol, sonicated for ~1 min, and then air-dried upon deposition onto the sample holder. Diffraction patterns of the metal-based nanomaterials were subsequently obtained using a Rigaku Miniflex diffractometer, operating in the Bragg configuration using Cu

Kα radiation (1.54 Å) and 2θ lattice parameters ranging from 20 to 80° at a scanning rate of 1.0°/min.

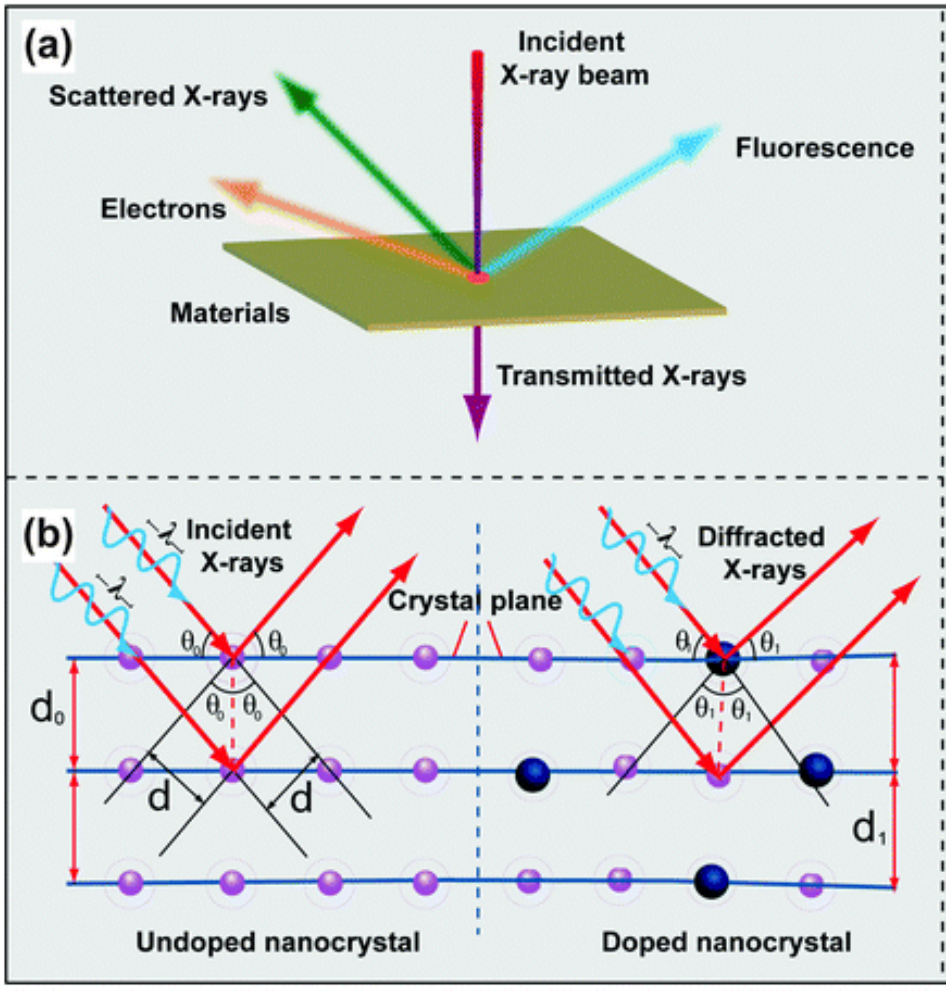

Figure 2.3: Schematic illustration of X-ray interactions with a crystalline material (A). Diffraction scattering of X-Rays in both undoped and doped atomic planes (B). Image adapted with permissions from Liu et al. *Chem. Soc. Rev.* **2015**, 44(6): pp. 1479-1508.

2.2.2.2 X-Ray Photoelectron spectroscopy

X-Ray photoelectron spectroscopy (XPS) is a surface sensitive technique used to analyze various sample characteristics such as the elemental composition, empirical formula, as well as chemical and electronic states. As a result, this method is routinely used to analyze the nature of inorganic compounds, semiconductors, metal alloys, and polymers among others. The desired sample is typically measured under a vacuum and exposed to a monochromatic X-ray source.

The incident X-rays eject core level electrons from the sample atoms, and the energy emitted from those electrons possess a binding energy (i.e. 1s, 2s, 2p, 3d peaks) characteristic of that specific element. The electron energy specific to the elements constituting the sample itself is then detected and determined as a function of the velocity, and the number of electrons is quantified, yielding a spectrum representing the surface composition (Figure 2.7). A survey spectrum of all of the elements present within the sample is commonly taken first, and then particular subsets of specific elemental surveys may be obtained within a certain binding energy region.

2.2.3 Pair Distribution Function Analysis

Atomic pair distribution function analysis (PDF) is another sensitive technique using a model free Fourier transform of X-rays or neutron diffracting data to ascertain the probability of finding two atoms within a certain interatomic distance, *r*.[62] Hence, this technique may be used for analyzing amorphous, partially crystalline, and crystalline materials. This analysis may also be used to study local disorder and the presence of inhomogeneities within crystalline magneto-resistive manganites, for instance.[63] Moreover, this technique is also sensitive to materials at the nanoscale as opposed to other conventional crystallographic methods dependent upon materials with long-range structural coherence. Specifically, the PDF can be obtained from powder diffraction data through a sinusoidal Fourier transform of the normalized scattering intensity, *S(Q),* using the PDFgetX3 program[64]:

$$G(r) = \frac{2}{\pi} \int_{Q_{min}}^{Q_{max}} Q\,[S(Q) - 1] \sin Qr\, dQ \qquad (2.2)$$

Herein, *G(r)* gives the probability of finding a pair of atoms separated by a distance of *r*, *Q* is the magnitude of the momentum transfer on scattering, and $Q = 4\pi\sin\theta/\lambda$, and *S(Q)* is the properly corrected and normalized powder diffraction intensity measured from 0 Å to 20 Å for

Q_{min} to Q_{max}, respectively.[65] In order to calibrate the sample-to-detector distance and to determine the Q_{damp} and Q_{broad}, nickel is also measured as the standard material.[66, 67] Specifically, Q_{damp} represents the PDF Gaussian dampening due to limited Q-resolution, whereas Q_{broad} is the peak broadening due to increased noise at high Q.[67] Once the refined values for Q_{damp} and Q_{broad} are acquired, these refined values, namely 0.0407 Å^{-1} and 0.0185 Å^{-1}, respectively, are then fixed and the subsequent model fits the PDF data of the diffracted samples (Figure 2.4).

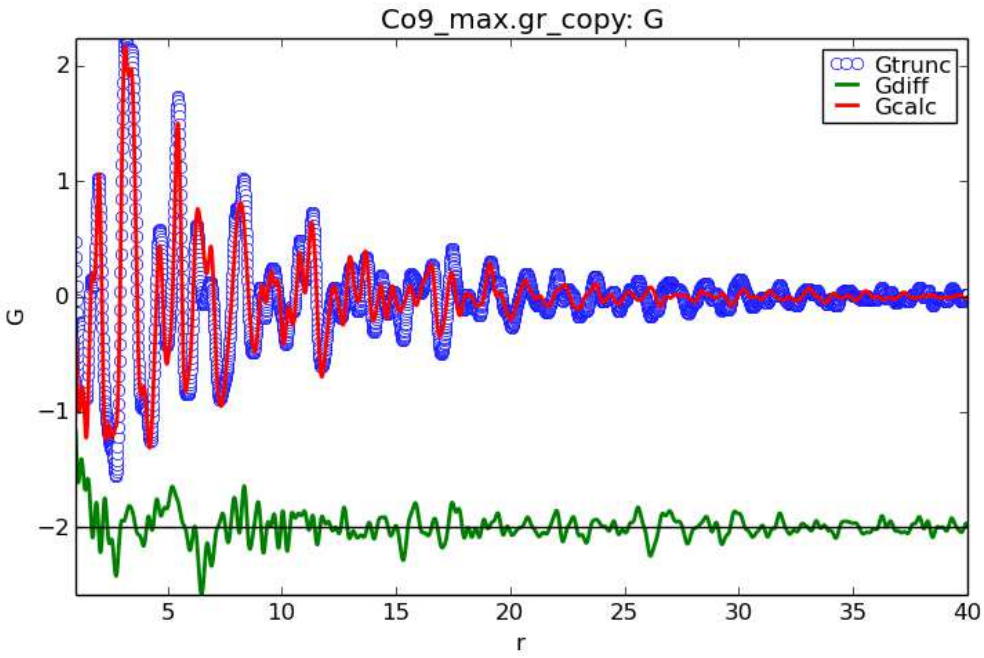

Figure 2.4: Example of PDFgui capabilities: displaying a fit on as-prepared Co ferrites

2.2.4 Microscopy – Techniques to Identify Morphological Features

Microscopy involves the use of microscopes to view and analyze objects that are too small to be seen with the naked eye. As a result, there are four classes of microscopy: *i.e.* optical, electron, fluorescence, and scanning probe microscopy. Optical or light microscopy involves passing visible light through the sample and reflecting the specimen through a single or multiple

objective lenses and capturing images with a charge-coupled device (CCD) camera. Typically, this microscope is used to magnify structural features of cells, for instance, for up to 1,000 times and to resolve details as small as 200 nm.

There are three requirements that must be fulfilled to sufficiently view the specimen for optical imaging. First, a bright light source must be focused onto a sample using lenses in a condenser. Second, the specimen must be properly prepared for microscope imaging. Third, the ability to focus on the cellular species, for instance, involves the use of objective lenses and eyepieces.

2.2.4.1 Transmission Electron Microscopy

The electron microscope uses beams of electrons as the source of illumination in order to create an image of a specimen. They are two forms of electron microscopes: transmission and scanning electron microscopes. In principle, the transmission electron microscope (TEM) is similar to the light microscope, but as opposed to glass lenses, it uses beams of electrons instead of beams of light and magnetic coils to focus the beam. This beam then passes through the sample at a high voltage, and subsequently comes into contact with a projective lenses used to generate an image (Figure 2.5).

Based upon the electronic interactions with the sample, 2 types of TEM images can be collected, namely either a ‘bright-field’ or a ‘dark-field’ image. Typically, in a bright-field image, unscattered electrons are collected, thereby resulting in a ‘darker’ image. By contrast, for dark-field images, scattered electrons are acquired, thereby yielding ‘brighter’ images (Figure 2.7). These particular bright-field or dark-field images can be ascribed to the quantitatively fewer (i.e. unscattered) electrons, reaching the image plane, versus the higher amount of scattered electrons, attaining the image plane, respectively.

With this imaging technique, cellular specimens must be stained with electron-dense heavy metals (*i.e.* uranium and lead) to introduce contrast as well as to locally absorb or scatter electrons. Inorganic samples such as either metals or metal oxides have no need for staining. For TEM viewing, the sample is typically placed onto a grid (i.e. Cu), transferred to a specimen holder under a vacuum. As previously mentioned, the electron beams pass through the sample where the image is then collected by the CCD camera. With the TEM, features as small as 50 nm or lower can be routinely imaged.

TEM also has additional capabilities allowing one to observe materials at higher magnifications for the detection of individual atoms within a sample. This type of microscopy is known as high-resolution TEM (HRTEM), wherein useful information, such as the atomic lattice parameter and the overall growth direction of an as-prepared sample, may be obtained. From an HRTEM perspective, the increased spatial resolution of sample features as small as ~ 2 nm can be visualized.

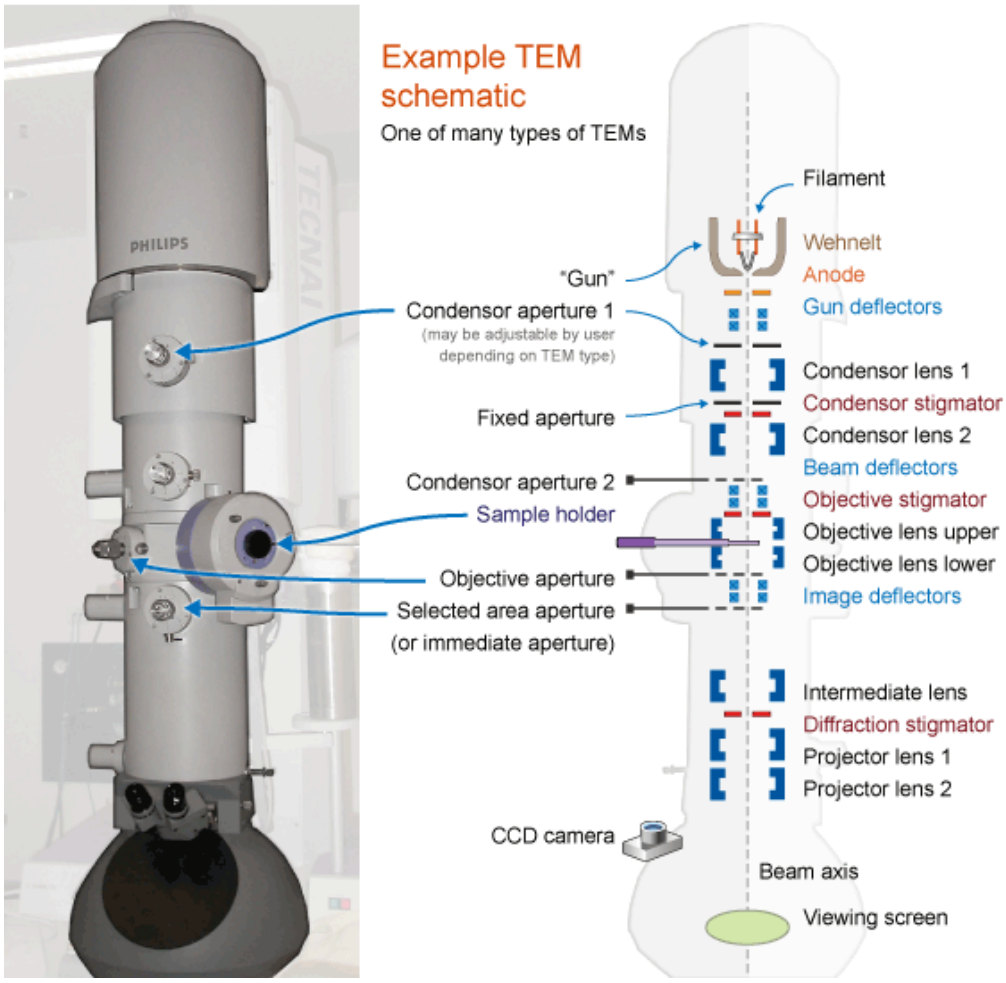

Figure 2.5: TEM schematic of transmission electron microscopy (TEM) instrument. Image adapted from www.ammrf.org.au.

2.2.4.2 Scanning Electron Microscopy

Similar to TEM, scanning electron microscopy (SEM) also utilizes electrons to form an image. In the presence of an accelerated voltage, the electrons undergo electron-sample interactions where the energy is emitted by the sample surface atoms. This energy is evolved in a variety of ways such as secondary electrons, backscattered electrons, photons, and heat. Secondary and backscattered electrons are commonly used for sample imaging. Specifically, secondary electrons are formed when the incident beam electrons collide with the sample surface electrons, removing them from their shell and re-emitting them at a relatively weak energy (~100

V). Hence, the detector must be in close proximity in order to collect the electrons and develop the SEM image (Figure 2.7).

Since the distance between the electrons and the detector is paramount for imaging, there are two types of detectors: the secondary electron detector and the back-scattering detector. The secondary electron detector collects electrons originating from elastic scattering by typically heavy atoms. This imaging mode gives insight into the composition as well as the sample's surface topography. Specifically, materials possessing heavier atoms yield greater contrast as compared with materials composed of lighter atoms. As for the sample's surface topography, depressions in the sample provide for fewer electrons and hence a 'darker' contrast, whereas protrusions in the sample allow for more electrons to be scattered off and therefore detected, hence providing for a 'brighter' image contrast.

As for the back-scattered imaging mode, the incident beam of electrons collides with the nucleus of the sample and then reflects back to the detector at high energies. Since these back-scattered electrons are more readily produced in sample with high density, this imaging mode is typically used to discern the sample's density. Unlike the TEM, larger amounts of a desired sample can be analyzed at any given time. Another difference is that these samples are transferred onto a silicon (Si) wafer rather than a metal grid.

2.2.4.3 Confocal Microscopy

Confocal microscopy has radically transformed the field of biomedical research, as this instrumentation can eliminate unnecessary background typically noted with conventional high-resolution optical microscopy, often caused by out-of-focus light and scattering effects.[68] The confocal microscope can also improve upon spatial resolution as compared with other optical techniques (i.e. wide-field fluorescence microscopy). In addition to the resolution issue, specimen

preparation is also vital as cells, either fixed or living, must be labeled with fluorescent probes for confocal imaging.

To collect confocal images, first, coherent light is introduced by the laser excitation source wherein the light passes through a light source pinhole. Subsequently, the light is reflected by dichromatic mirrors and ultimately scanned across the specimen. As the specimen is being scanned, secondary fluorescent light is emitted from the specimen through the dichromatic mirror, and later focused through the detector pinhole for imaging (Figure 2.6).

In terms of spatial resolution, conventional EM microscopes can achieve a depth of field of ~2-3 micrometers, whereas fluorescence microscopy, particularly confocal microscopy, can achieve higher spatial resolution. Specifically, the latter technique enables one to image thinner optical sections of as small as ~0.75 micrometers, thereby enhancing the detail within the image. It is for this reason that confocal microscopy can be used to view, quantify, and probe fluorescence primarily within subcellular constituents. As a result of the enhanced detail possible, many biological studies have utilized this instrument to investigate the structure and physiology of living cells in the presence of quantum dots and fluorescent-labeled nanocrystals, as examples of typical fluorophors.[69] For example, by overlaying fluorescent labels specific to the nucleus and the cellular constituents, fluorescent-labeled nanoparticles may be used to observe the exact location of nanoparticles engulfed within cells.

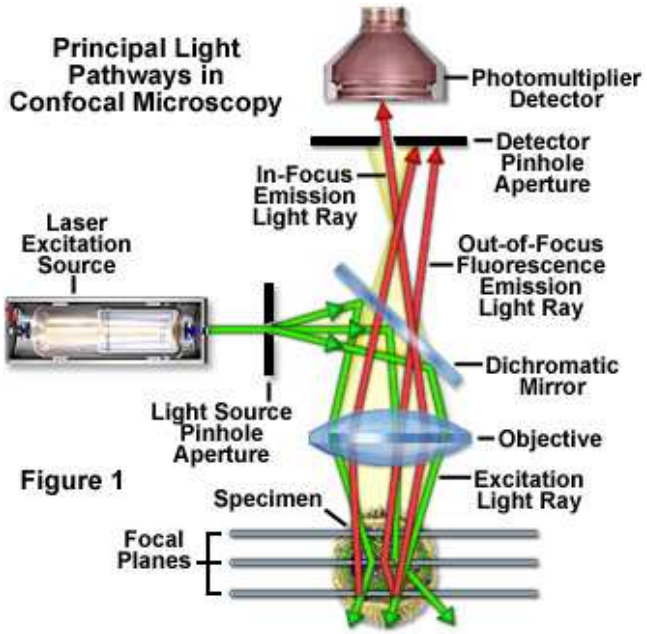

Figure 2.6: Schematic of a typical confocal microscope. Image adapted from www. Microscopyu.com.

2.2.5 Electron Microscopy – Accessory Techniques for Structural Composition

2.2.5.1 Selected Area Electron Diffraction

The ability to conduct Selected Area Electron Diffraction (SAED) is typically found within most TEM scopes. To create an SAED pattern, the desired area is focused and a strip of metal (*i.e.* SAED aperture) is placed in position to block the beam. Only a small fraction of electrons will pass through and these undergo scattering at particular angles, thereby forming a diffraction pattern. This technique is typically used to identify and differentiate polycrystalline from single crystalline materials in addition to crystalline versus amorphous materials, as well as to examine crystalline defects (Figure 2.7).

2.2.5.2 Energy Dispersive X-ray Spectroscopy

Energy dispersive X-ray spectroscopy (EDX) is a technique used to probe the elemental composition of a particular sample. A typical EDX spectrum can be collected, as the accelerating

voltage produces beams of electrons that interact and collide with an electron in the sample's inner shell (i.e. the K shell), thereby creating a vacancy. The incident beam loses energy upon collision, while the sample's outer shell (the L_3 shell, for instance) fills the vacancy, thereby emitting a X-ray energy that is characteristic of the sample's atomic number. When the X-ray is detected with EDX, it leads to a K α peak indicative of the element present in the sample. As a result, depending on where the vacancy occurs within the sample, certain peaks associated with each element are produced.

The families of peaks are Kα, Kβ, Lα, $L\beta_1$, $L\beta_2$, Mα, and Mβ, and each element may display these peaks at different signature positions if at all. Specifically, under a normal accelerating voltage, light elements (*i.e.* silicon) emit X-rays of the K-series only; intermediate-sized elements (*i.e.* copper) may give rise to either the L-series alone or a blend of K and L peaks; and heavy elements emit either M-peaks alone or a mixture of the L and M series. Hence, this technique provides for a reliable tool to distinguish and differentiate among the various elements emanating from the material.

New technologies such as EDX mapping and EDX line scans provide for other methods to yield complementary elemental information. EDX mapping is commonly used to detect elemental distribution throughout the sample. This becomes important especially for doped samples (*i.e.* rare earth ions) as well as for covalently functionalized constituents (*i.e.* heterostructures), wherein spatial resolution and elemental distribution may yield further insight into certain applications (Figure 2.7). In effect, the EDX line scan is preferred for core shell materials, as it can be used to determine elemental distributions along a line. All of these EDX features allow for information about the atomic composition of the desired material to be determined either from an overall spectrum, spatial locations, or distributions along a scanned line.

2.2.5.3 Electron Energy Loss Spectroscopy

Electron Energy Loss Spectroscopy (EELS) is a complementary technique to EDX, as they both may be used to identify the elemental composition of a given constituent. However, unlike EDX spectroscopy, this method measures the change in kinetic energy (i.e. inelastic scattering) after electron interaction with the sample. The energy distributions of inelastic scattered electrons provide important information about the local environment such as structural features, chemical bonding, electronic properties, and surface effects emanating from the sample (Figure 2.7).[70] In particular, the EELS techniques can highlight either structural features for core shell materials or the presence of an oxide on a sample's surface.

The EELS system tends to be associated with a scanning-transmission electron microscope (STEM), wherein the field emission source and electromagnetic lenses focus as-generated electrons that scan across the sample, forming a 'dark field' image.[71] In effect, a given material is exposed to beam of electrons, and depending on the nature of the material, electrons scatter inelastically and are detected through a single-prism spectrometer, according to its specific and characteristic set of kinetic energies. In particular, the measured kinetic energy of the electrons is calculated as the incident energy, E_0, minus any energy loss, E, incurred upon interaction with the sample.[71]

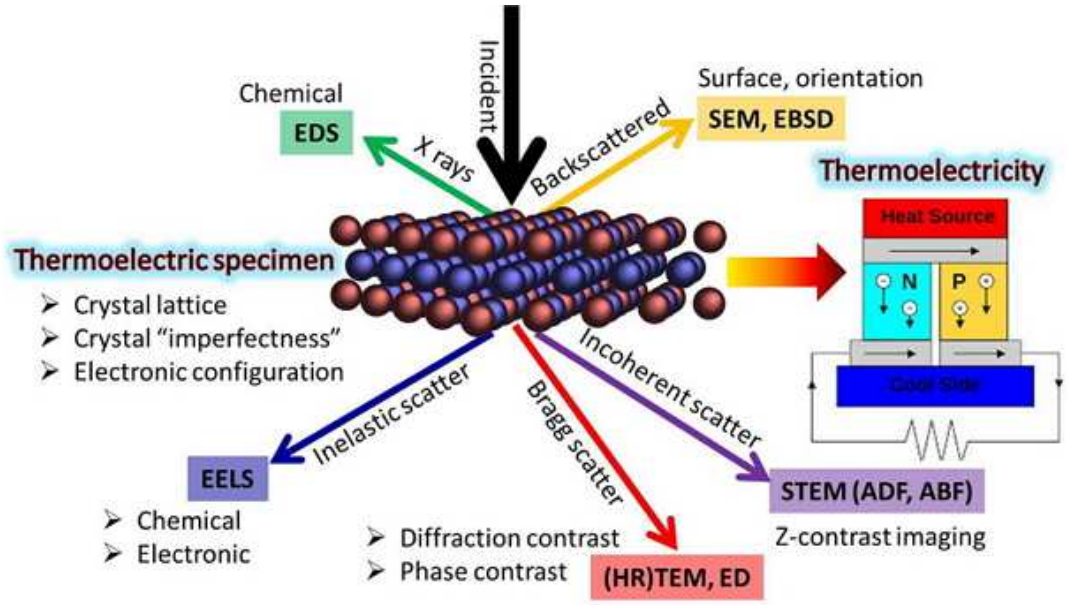

Figure 2.7: Electron interactions with either crystalline or nanoscale materials. Image adapted with permissions from Wu et al. *Nano Energy* **2015**, 13: pp. 626-650.

2.2.6 Optical Spectroscopic Techniques

Optical spectroscopy is the measurement of light interaction with a sample. The electromagnetic spectrum is not limited to visible light but rather is composed of a range spanning from long wavelength radio waves to short ultraviolet (UV) light. Generally, a sample responds to illumination in one of two ways: by absorbing some of the energy from the light or by emitting the light at a different wavelength. Depending upon either the wavelength or mode used to probe the sample, these responses may be termed absorbance spectroscopy, particularly UV-visible (UV Vis) and infrared (IR), or fluorescence spectroscopy (*i.e.* photoluminescence (PL)).

2.2.6.1. UV-Visible Spectroscopy

In absorbance spectroscopy, samples may be illuminated with either UV/Vis or infrared waves using an UV/Vis spectrometer and a Fourier transform Infrared (FT-IR) instrument,

respectively. As for the UV-Vis spectrometer (190-900 nm), its primary function is to determine the maximum absorption (λ_{max}) wavelength of a particular material, most often in an aqueous solution. Typically, the instrument is composed of a light source, monochromator, sample holder, and a light detector (Figure 2.8). The radiation source is typically a tungsten filament (300-800 nm), while the monochromator utilizes diffraction gratings in order to select for a particular wavelength of light. Briefly, the wavelength of light higher in energy than the sample's band gap (λ_{max}) can promote the sample electron from the valence band to the conduction band. The detector measures the intensity of light transmitted through the sample. What is observed on the instrumental readout is a graph defined as absorbance vs. wavelength, wherein the absorbance may be described using the Beer-Lambert equation:

$$A = \varepsilon bc \qquad (2.3)$$

wherein the measured absorbance shares a direct correlation with the concentration (c) of the sample, assuming that the path length (b) and molar absorptivity (ε) are known.

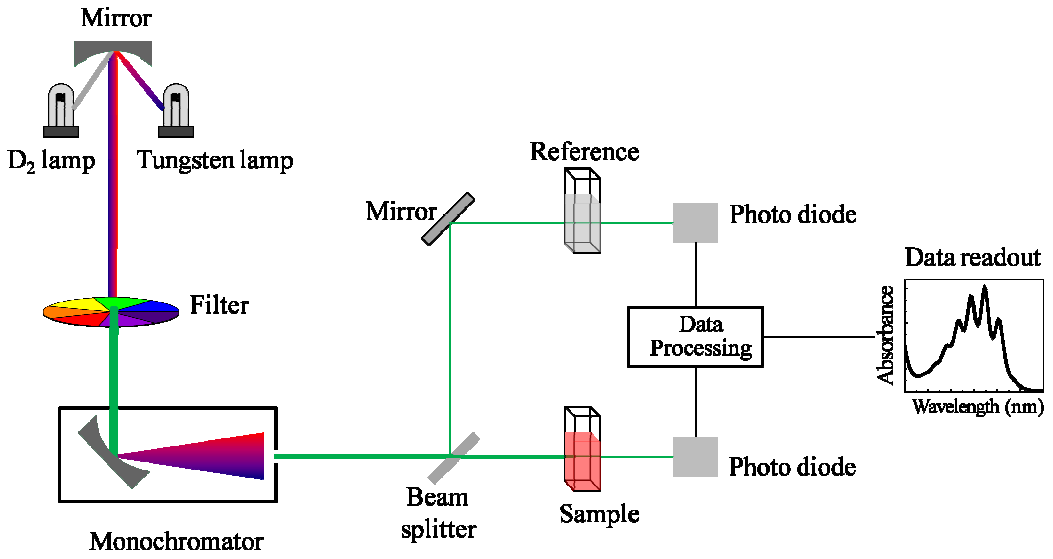

Figure 2.8: Schematic illustration of a UV-Visible spectrophotometer. Image adapted from www.chemwiki.ucdavis.edu

2.2.6.1.1 Photocatalytic experiments

As previously mentioned in Chapter 1, photocatalysts are of great importance in the removal of organic dyes within the aquatic environment. Methyl orange (MO) and methylene blue (MB) are commonly known anionic and cationic dyes, typically used in textile, printing, and research facilities.[72] As a result, in an effort to reduce adsorbent costs and to resolve disposal issues, many metal oxides have been used as platforms with which to degrade these organic dyes into less toxic molecular byproducts.

Though UV-Visible spectroscopy is typically used to confirm the band gap of a paticular material, this optical technique can also be used to monitor changes in absorbance, characteristic of the degradation of organic dyes (*i.e*. methyl orange) over a given amount of time (*i.e*. minutes). More specifically, the initial dye concentration is denoted as C_0, whereas the concentration of the dye at a given time, t, is represented as C_t. Initially, the photocatalytic degradation graph plots concentration vs. time. However, in order to understand the nature of the rate behaviors taking place, the natural logarithms (ln) of the concentration values are often plotted against time, and fits are made to denote whether the reaction is first-order by means of fitting to the following equation 2.4:

$$\ln(C_0/C_t) = kt \qquad (2.4)$$

wherein 'k' represents the reaction rate constant and 't' represent the reaction time.

2.2.6.1.2 Photodegradation Pathways of Organic Dyes

The photodegradation of MB initially starts as TiO^- sites cleave the C-S=C group within MB, thereby forming a sulfoxide (See Figure 2.9).[73] Upon irradiation, TiO_2 may also aid in catalyzing the oxidation process in water, as observed by the following reaction 2.5:

$$(H_2O \Leftrightarrow H^+ + OH^-) + h^+ \rightarrow H^+ + OH^\circ \qquad (2.5)$$

The as-generated sulfoxide group can then undergo an electrophilic attack by OH° radicals, thereby producing a sulfone moiety and also allowing for de-coupling of the two benzene rings.[73]

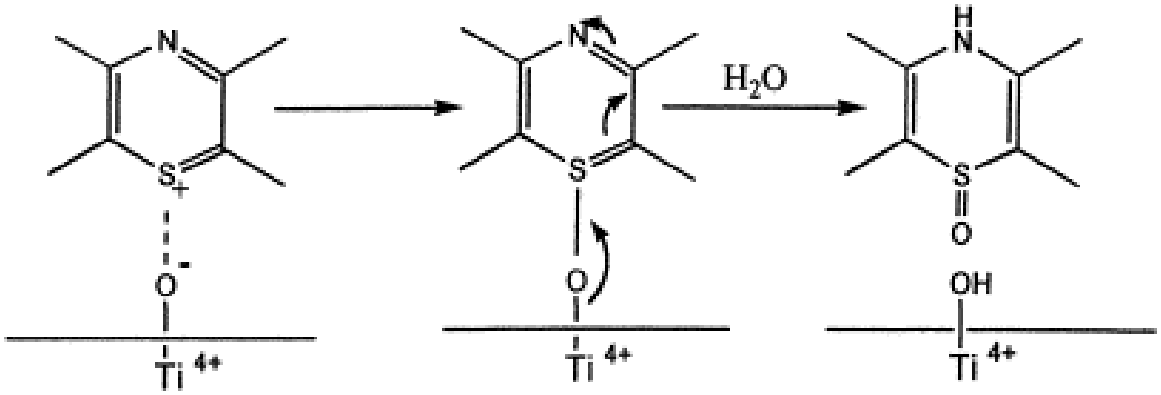

Figure 2.9. Schematic illustration of TiO interaction with MB transformed to the sulfoxide form. Image adapted with permissions from Houas et al. *Appl. Catal. B: Environ.* **2001**, 31: pp. 145-157.

As for a possible photodegradation pathway for the MO dye, either UV or Visible light irradiation should enhance the generation of electron-hole pairs within TiO_2. These electrons then can reduce the oxygen to oxygen radicals and finally to hydroxyl radicals. It is possible that the hydroxyl radicals facilitate decomposition of MO by attacking the azo group (i.e. R-N=N-R), thereby forming two less toxic molecules (Figure 2.10).[74, 75]

Mechanism of Photocatalysis:

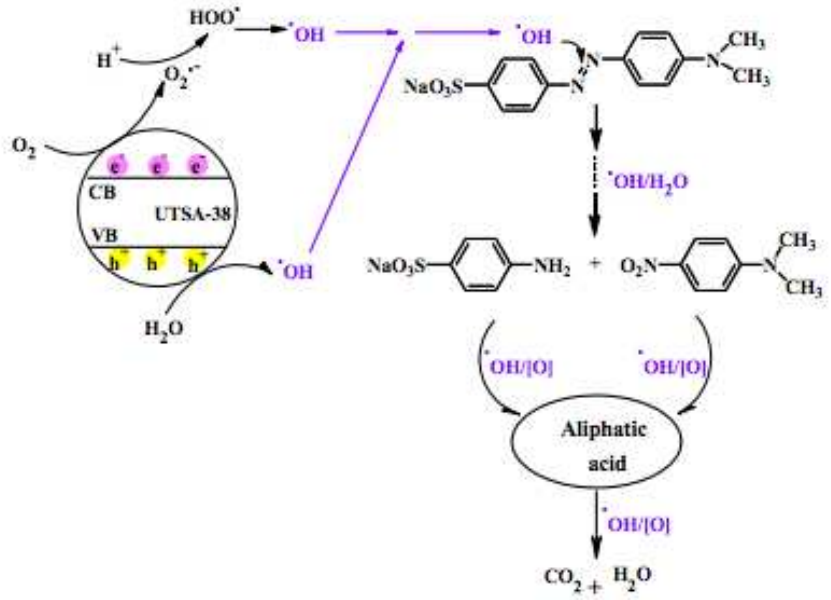

Figure 2.10. Schematic of the proposed photodegradative process of MO dye under either UV or Visible light irradiation. Image adapted with permission from Ref. 74. Copyright (2011) The Royal Society of Chemistry.

2.2.6.2. IR Spectroscopy

Another absorbance spectroscopic technique is IR spectroscopy (range of 0.78-1,000 μm), which also measures either the molecular absorption or transmission of a sample and creates its molecular fingerprint spectrum of the sample. This technique is useful for observing and identifying unknown samples, and various organic molecules, as well as determining relative amounts of each component. Specifically, FT-IR spectroscopy uses a Fourier transform to convert the data to the resulting spectrum.[76] Specifically, the FT-IR utilizes an IR source to identify what frequencies are absorbed by the sample, and the intensity of various sample frequencies are recorded, corresponding to peaks in the spectrum. Hence, being able to understand the nature of the different characteristic frequencies, particularly their stretching, and bending modes, can confirm the chemical composition of nanomaterials, and moreover, the presence of surfactants or various functional groups may also be identified. This tool is

particularly useful for identifying the binding of fluorescent moieties (*i.e.* Rhodamine B) onto nanostructures so as to confirm either the success or the failure of the binding process. More specifically, it may also confirm whether either covalent or non-covalent bonding has occurred between the two entities.

2.2.6.3 Photoluminescence Spectroscopy

Photoluminescence (PL) spectroscopy is a useful approach for probing the electronic properties of semiconducting nanomaterials. If the sample is excited by a high-energy light source whose energy is greater than its band gap, the electrons are promoted to the conduction band. During the electron-hole pair recombination, the material emits a photon. This emission is observed by the PL instrument, and is associated with not only characteristic features of the sample but also the radiative recombination processes that occur. Hence, by its very nature, PL spectroscopy can be used to determine the levels of defects, band gaps, and impurities present within these semiconductors. For example, the presence surface defects can cause shifts within the PL emission spectra, especially in the case of QDs, for instance. As for the band gap of semiconductors,[77] the following equation 2.6 may be utilized to describe its behavior:

$$E = hc/\lambda \qquad (2.6)$$

Within this equation, h is Planck's constant, c represents the speed of light, and λ denotes the wavelength of the semiconductor. In addition, the measured PL spectroscopic data also highlight PL quenching effects with respect to semiconductor combinations (i.e. QD-RE-$CaTiO_3$ heterostructures), a key indicator for efficient charge transfer as well as non-radiative transitions (Figure 2.11). Specifically, efficient charge transfer typically means electrons transferred from the host (i.e. RE-$CaTiO_3$) to the sensitizer (i.e. QDs), and vice versa.[78] Whereas a non-radiative transition refers to a process that does not necessarily involve light, it usually denotes a scenario

wherein the excess energy is dissipated in the form of interactions with phonons (*i.e.* lattice vibrations of a solid).[79] Nonetheless, PL spectra ultimately provide for useful information as to the reliability and stability of LEDs and possible applications for PV devices.[80]

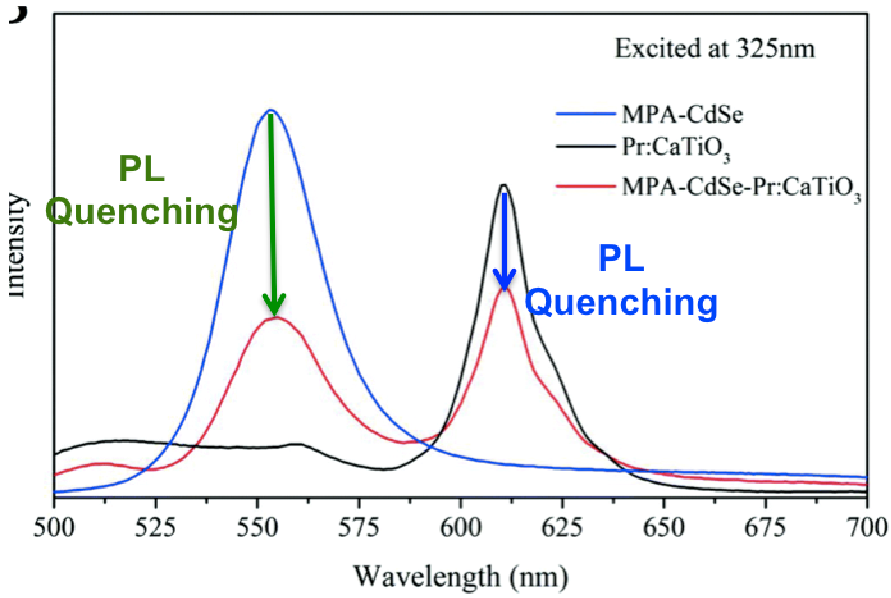

Figure 2.11: Example of a PL spectrum and associated quenching effects. Image adapted with permission from The Royal Chemistry Society.

2.2.7 Surface Area Characterization Method

2.2.7.1. Brunauer-Emmett-Teller Analysis

Brunauer-Emmett-Teller (BET) is a technique that involves physical adsorption of gases such as nitrogen, argon, carbon dioxide, and so forth, onto the material's surface to measure either the surface area or porosity of the desired material. The specific surface area is determined, based upon the theory proposed by Stephen Brunauer, Paul Hugh Emmett and Edward Teller.[81] Specifically, they posited that the volume of gas needed to form a monolayer on the surface of the sample, size, and number of adsorbed gas molecules can all be accounted for within the following equation:

$$\frac{1}{v\left[\left(P_O/_P\right)-1\right]} = \frac{c-1}{v_m c}\left(\frac{p}{p_O}\right) + \frac{1}{v_m c} \qquad (2.7)$$

wherein p and p_O are the equilibrium and saturation pressure, respectively, of the adsorbate (i.e. N_2) at the adsorption temperature. While *v* represents the volume of gas adsorbed, v_m is the gas adsorbed as a monolayer and *c* is the BET constant. This method allows for a general standard for surface area comparisons to be made between synthesized materials and materials published in literature. However, the BET method assumes not only that the gas adsorption occurs by multilayer formation as opposed to monolayer formation but also that there is an infinite number of adsorbed layers that can form when the surface is free.[82] Therefore, though this method is a great tool for comparison among samples, it is still unclear whether the absolute surface area numbers are indeed meaningful.

Nevertheless, in a typical BET analytical procedure, the physical adsorption of Nitrogen (N_2) gas at the sample surface takes place, as the amount of gas adsorbed is calculated during a multi-point measurement cycle. The calculation typically follows a modified Langmuir equation, wherein a homogeneous surface is assumed, connecting the relative pressure to the resulting BET value. Typically, the desired sample (*i.e.* ~100-200 mg) is transferred into a glass vial and heat-treated at 250°C to remove any surface species. Once placed in the BET chamber, a multi-point measurement cycle can be executed.

2.2.8 Magnetic Techniques

2.2.8.1. Superconducting Quantum Interference Device Analysis

Magnetic nanoparticles denote a class of materials that can be influenced by the presence of a magnetic field. Within this class are subclasses of magnetic materials possessing diamagnetic, paramagnetic, antiferromagnetic, ferromagnetic, and superparamagnetic properties. These magnetic nanomaterials typically consist of elements such as iron, nickel, cobalt, and manganese, as well as their respective metal-derived compounds. To determine the subtle magnetic properties of nanomaterials, superconducting quantum interference devices (SQUID)

are typically used with a specified magnetometer. With this device, information on the magnetization (M) as a function of applied field (H) can be used to distinguish among the types of magnetic behavior displayed. For example, a ferromagnetic material displays hysteresis (*i.e.* an S curve), whereas superparamagnetic materials lack this particular feature. With these traits, more information may be drawn, such as coercivity (H_c), saturation magnetization (M_s), and magnetic remnance (M_r) from the M versus H plot, which yield an indication of the type of magnets present (Figure 2.12).

For example, diamagnetic materials, particularly aluminum (Al) or copper (Cu), possess a very weak magnetic dipole moment. Paramagnetic materials, including Cu doped with iron (Fe), yield a moderate net magnetic dipole moments with their spins oriented in the direction of the applied magnetic field. Antiferromagnetic materials also have moderate magnetic dipoles oriented anti-parallel to one another; however, they also display a magnetic temperature transition from antiferromagnetism to paramagnetism known as the Néel temperature (T_N). Ferromagnetic materials, such as Fe_3O_4 or Ni, for instance, produce a large permanent magnetic dipole with a Curie temperature (T_C) and these dipoles are oriented parallel to each other.[83] The T_C represents the temperature wherein the material loses its permanent magnetic properties and is substituted for induced magnetism (*i.e.* paramagnetism). Superparamagnetism is typically observed in ferromagnetic materials at the nanoscale.[83, 84] Specifically, at this size, the magnetic ions within the nanoparticles are 'fastened' and coupled together, giving rise to a large magnetic dipole moment and high saturation magnetization but zero coercivity.

The SQUID magnetometer may also be utilized to plot magnetization as a function of temperature through zero field-cooled (ZFC) and field-cooled (FC) magnetization curves wherein the blocking temperature (T_B) of the sample and the magnetic anisotropy may also be determined.

Specifically, T_B is defined as the transition temperature from a slow magnetic moment relaxation to a rapid relaxation within a specified measurement time.

To observe the magnetic characteristics of our as-prepared metal oxides using the SQUID instrument, the materials were collected in powder form, which were subsequently encapsulated in paraffin wax within a gelatin capsule and then placed into a plastic straw in order to allow for immersion into the magnetometer. Magnetization measurements were then taken with a Quantum Design Magnetic Property Measurement System (MPMS) at fields of up to 5 T and temperatures between 2 and 300 K.

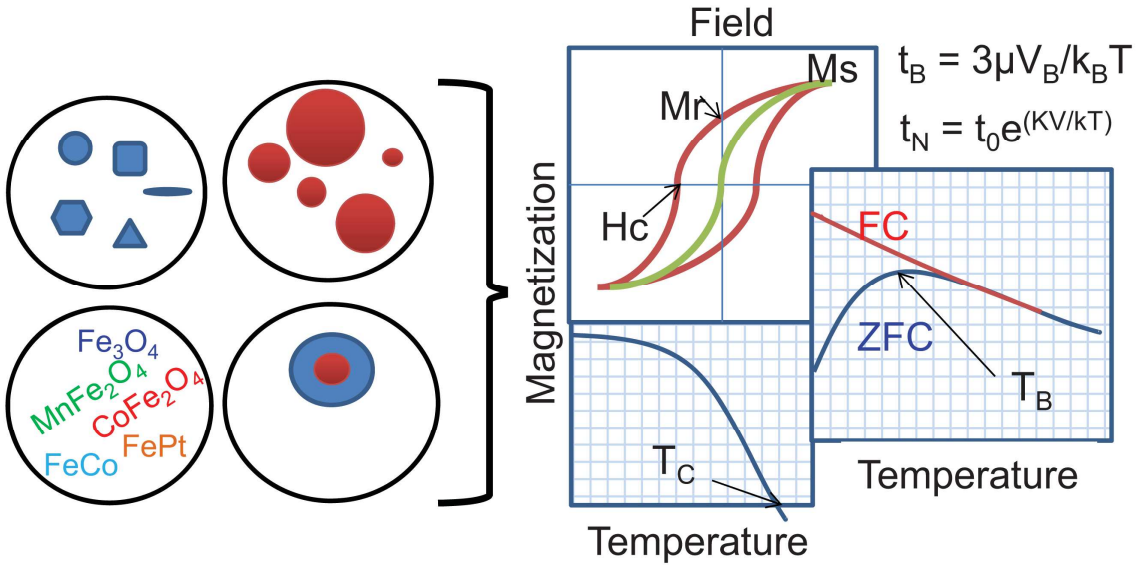

Figure 2.12: Effects of parameters such as composition, size, shape, and architecture upon magnetic properties of nanomaterials. Image adapted from Kolhatkar et al. *Int. J. Mol. Sci.* **2013**, 14(8): pp. 15977-16009.

2.2.9 Cell Culture Assays

2.2.9.1 Enzyme Linked Immuno-Absorbent Assay

The enzyme-linked immuno-absorbent assay (ELISA) or enzyme immunoassay (EIA) is a plate-based technique for the detection and quantification of antibodies, hormones, peptides or proteins based on specificity and selectivity. Typically, this procedure is performed in either a 96 or 384 well plate wherein the plate is coated with detection enzymes or other tags that bind onto

primary antibodies via a direct or indirect immobilization. Specifically, the ELISA has three types of assays: the sandwich assay, the competitive assays, and the antigen down assays. Among these assays, the sandwich assay is most commonly used due to its detection sensitivity and robust specificity (Figure 2.13).[85] This particular assay utilizes two antibodies, i.e. the capture and detection antibodies, which bind at different locations of the antigen or ligand. Specifically, the capture antibody coats the plate, the antigen binds to the capture antibody, and the detection antibody latches onto the antigen at another site, thereby creating a sandwich effect with the antigen in the middle. Subsequently, the detection antibody's affinity for the antigen is the primary determinant in terms of quantifying the presence of the antigen.

Moreover, the detection antibodies are typically tagged with reporters (i.e. fluorophores, enzymes, and etc) in order to quantify the extent of binding as it is believed that the higher the concentration of the antigen, the higher the concentration of the detection antibody. This analysis is performed using the ELISA reader. Due to the versatility of the sandwich assay, it has gained widespread attention for detection capabilities within diverse fields such as infectious diseases, allergen detection, plant pathogens, and biomarkers, to name a few.

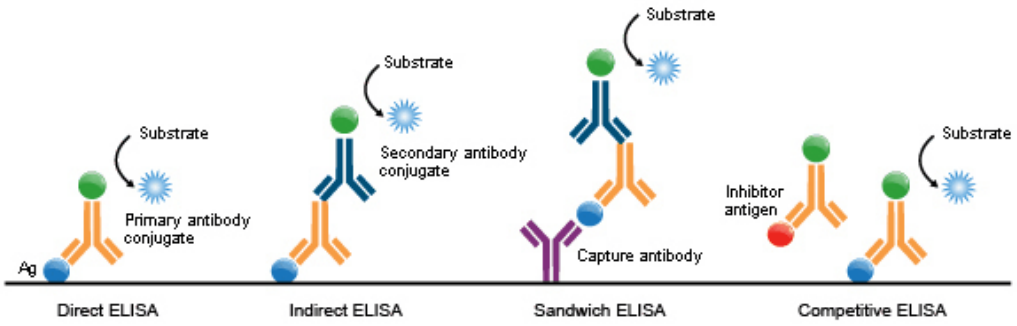

Figure 2.13: Various types of ELISA Assays. Image adapted from www.abnova.com

2.2.9.2 Lactate Dehydrogenase Assay

To analyze cellular growth inhibition or cell death (i.e. apoptosis), proliferation assays are utilized. Typically, proliferation assays such as MTT, MTS, and ATP-based assays are used for

primary screening. Lactate dehydrogenase (LDH) is an enzyme that is present in all cell types. It is rapidly released when the membranes become ruptured, a feature observed in dead cells. Hence, the LDH cytotoxicity protocol is an effective way to monitor the difference between viable and non-viable cells.

In this assay, LDH reacts with nicotinamide adenine dinucleotide (NAD^+) and reduces this to $NADH/H^+$, thereby catalyzing the conversion of pyruvate to lactate (Figure 2.14). Simultaneously, the as-generated hydrogen ions (H^+) react with a yellow-colored tetrazolium salt, added to the assay medium, which converts this into a water-soluble red pigment (formazan). The absorbance values of the cell medium were analyzed using the ELISA reader and the percentage cytotoxicity for each concentration was subsequently calculated using the following equation: Cytotoxicity (%) = (experimental reading - low control reading) / (high control reading - low control reading) x 100% (Equation 2.10).

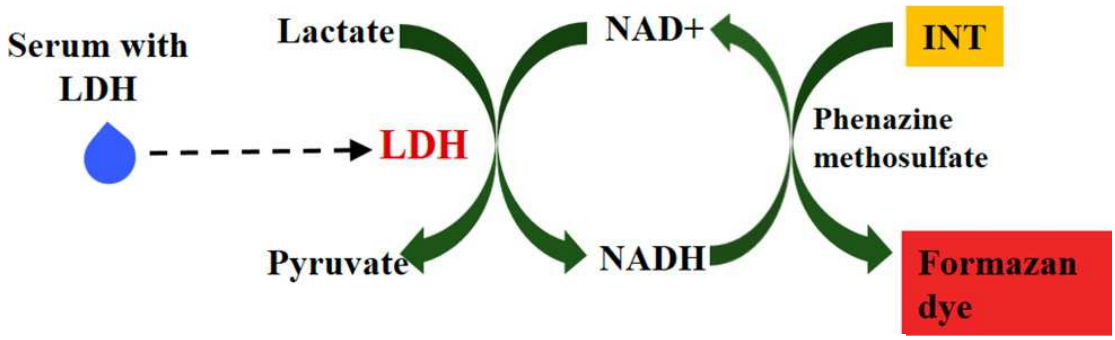

Figure 2.14: LDH Assay process. Image modified from Kannan et al. *Anal. Chem.*, **2015**, *87* (18): pp. 9288–9293

2.2.9.3 Nitric Oxide Assay

Nitric oxide (NO) is a free radical, produced by NO synthases, with a short residence time within biological systems (i.e. less than 1 second in the circulatory system). These NO synthases (NOSs) can be found in 3 forms: endothelial (eNOSs), neuronal (nNOSs), and inducible (iNOSs) each with different functions. Ultimately, the production of NO plays an important role in

regulating homeostasis within the nervous, cardiovascular, and immune systems.[86] More specifically, under normal conditions, NO is essential for the regulation of blood flow and blood pressure, for instance. It is well known that NO remains unstable and readily reacts with oxygen (O_2), thereby forming a variety of nitric oxides such as nitrogen dioxide (NO_2), dinitrogen trioxide (N_2O_3), and nitrite (NO_2^-). However, when NO is overexpressed, it leads to tumor growth and proliferation.[87] As a result, fluorescent assays have been utilized to observe NO production within cells.

Typically, the Griess reaction is used for NO assay detection within physiological fluids; however, the sensitivity limit is only 2-3 μM.[88] In an attempt to enhance the sensitivity, fluorimetric methods, involving the use of aromatic diamino compound, 2, 3-diaminonaphthalene (DAN), are often used as an indicator for NO formation. Specifically, the NO derived agent, N_2O_3, can be produced by either an acid catalyzed reaction or in the presence of O_2. The N_2O_3 then reacts with the DAN molecule to yield a fluorescent 2, 3, naphthotriazole (NAT), as shown in Figure 2.15.[88] This assay achieves sensitivities of ~10-30 nM of NAT, and can therefore be used to quantify the level of NO production.

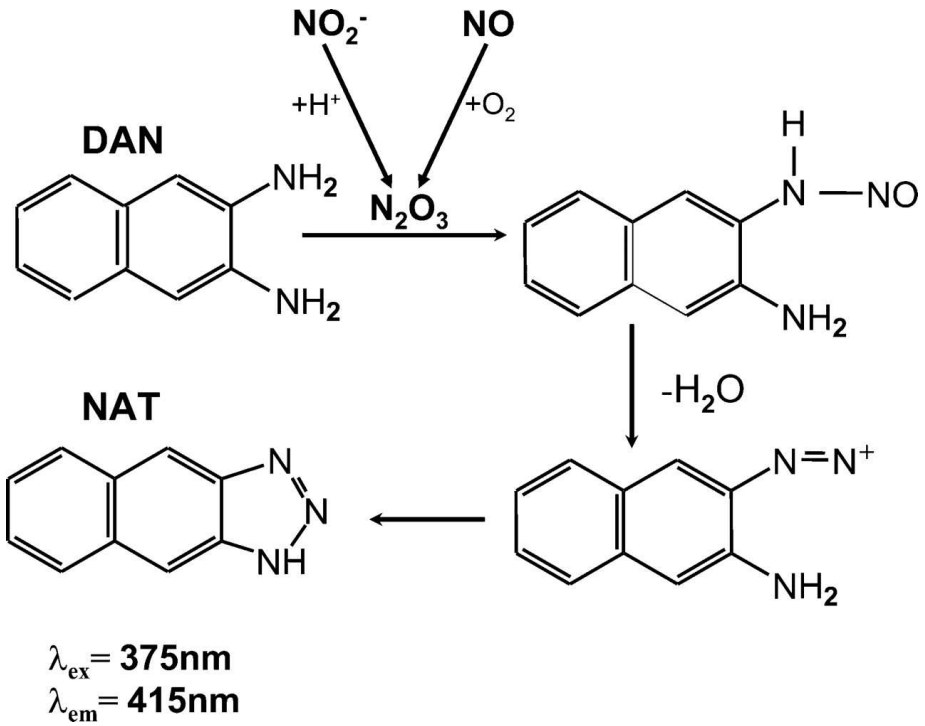

Figure 2.15: Detection of NO using diamino (DAN). The dinitrogen trioxide (N_2O_3), generated from either the autoxidation of NO or the acidification of nitrite (NO_2^-), reacts with DAN to produce a fluorescent naphthotriazole (NAT) dye that can be detected spectroscopically. Image adapted from Tarpey et al. *Am. J. Physiol. Regul. Integr. Comp. Physiol.* **2004,** 286(3): pp. R431 – R444.

2.2.9.4 - 2', 7'-Dichlorofluorescein Diacetate Assay

Reactive oxygen (RO) species, such as but not limited to peroxide, oxide anion, and hydroxyl radicals, have been known to cause DNA and RNA damage as well as oxidize proteins within cells.[89] As a result, the generation of RO species has been considered to be a known marker for the progression of diseases, such as but not limited to diabetes, cancer, and neurodegenerative diseases, to name a few.[90] Currently, there are several analytical fluorescent probes used to detect RO species; an example is dihydrorhodamine. However, the most widely used assay for RO detection is the 2', 7'-Dichlorofluorescein Diacetate Assay or otherwise commonly known as the DCFDA Assay. Initially the DCFDA is engulfed within the cells where it is then metabolized by esterases. In the presence of RO species, DCFDA is oxidized to DCF, a

fluorescent marker.[88] The fluorescence is measured to gain quantitative information regarding the existence of RO species.

2.3 Synthesis & Characterization used in this Thesis

2.3.1 U-tube Double Diffusion Synthesis of Cu and Ni nanowires

Polycarbonate (PC) membranes, maintaining pore size diameters of 50 nm and 200 nm, respectively, were immersed in distilled water and subsequently ultrasonicated to ensure removal of air bubbles either within or on the top of the surfaces of the membranes. The PC membrane was then placed between the two half-cells of a custom-made glass U-tube apparatus. To synthesize Cu NWs, a solution of freshly prepared 0.05 M $NaBH_4$ under basic conditions (i.e. 0.05 M, sodium hydroxide, NaOH) was filled in one arm of the U-tube, and a corresponding solution of 0.05 M $CuCl_2$ was inserted into the other arm, simultaneously, in order to induce Cu nanowire growth. With Cu, we expended most of our efforts on testing the effects of using different reaction variables using the smaller 50 nm templates, as these gave uniformly better results.

As for the analogous Ni NWs, corresponding solutions of 0.05 M $NaBH_4$ and 0.1M nickel chloride ($NiCl_2$) were prepared in ethanol (since most nickel nanomaterials are prepared in this solvent) and placed in the arms of the U-tubes using 50 nm template membranes to generate corresponding ~50 nm diameter nanowires.[91] With Ni, we probed the effect of varying template pore size. Hence, as for the larger nanowires prepared from 200 nm template membrane pores, solutions of 0.05 M $NiCl_2$ and 0.05 M $NaBH_4$ in ethanol were used to initiate the nanowire growth reaction.

The differences in reagent concentrations in these experiments were determined by the diffusion rates of each precursor within the PC template membrane pores themselves. The U-tube

was subsequently left undisturbed for 2 hours at room temperature. After the U-tube was dismantled, the template membrane was collected, placed onto a smoothing stone, and lubricated with mineral oil in order to ensure the physical removal of the bulk metal residual backing (i.e. a silver hue for Ni nanowires and a corresponding bronze color for Cu nanowires) on the external template surface. An image of a typical metal backing associated with Cu nanowires is shown in Figure 2.16.

Once the excess reaction residue was eliminated, the template was then dissolved in dichloromethane for an hour, washed, and centrifuged several times for further purification. After processing, both types of metallic NWs were stored in oleylamine in order to prevent oxidation and isolated using a solution containing a 3: 1 ratio of toluene and ethanol for further structural characterization. Residual salt was removed from the Ni NWs using a solution containing a 1:1 ratio of deionized water and ethanol.

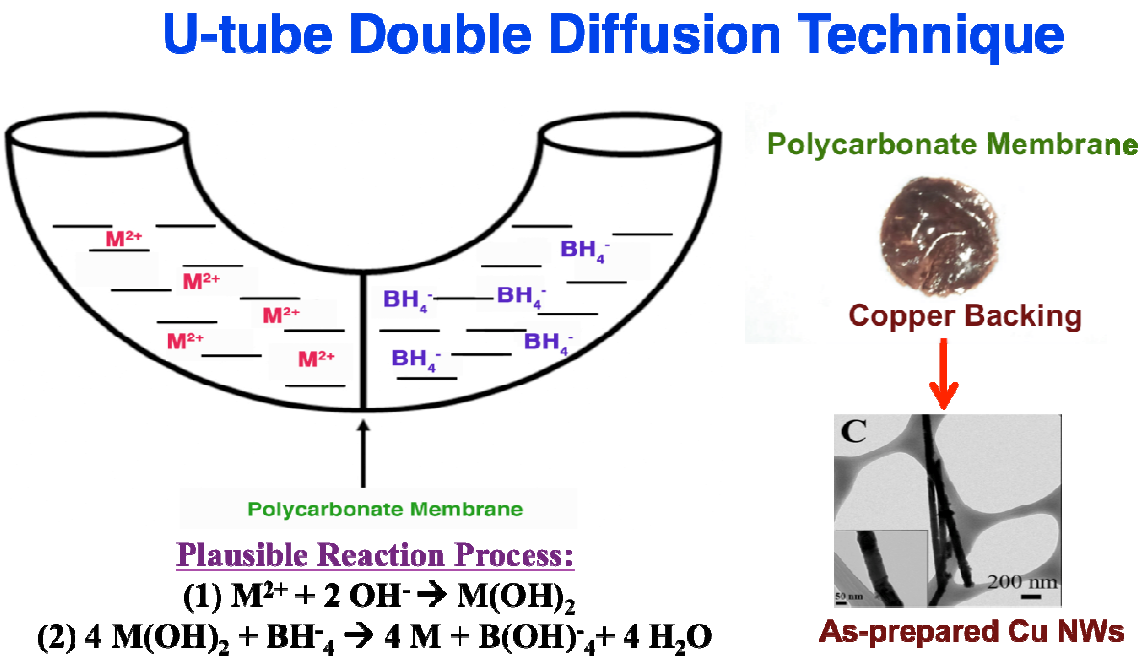

Figure 2.16: Schematic illustration of the U-tube double diffusion technique for generating as-prepared elemental Cu and Ni nanowires

2.3.2 Metal ferrite nanoparticles and nanowires using the Hydrothermal Method

MFe_2O_4 (where 'M' = Co, Ni, and Zn) nanoparticles were prepared by using a hydrothermal method, appropriately modified from previous work by Wang *et al*. which had focused on the synthesis of $MnFe_2O_4$ nanorods.[92] Briefly, 0.02 M of the desired metal precursor ($CoCl_2$, $NiSO_4$, and ZnF_2 depending on the desired ferrite composition) was dissolved in 15 mL of distilled water in a beaker and then stirred at ~300 rpm for 15 minutes. Subsequently, 0.02 M of $FeCl_3$ was also added to the beaker and dissolved in solution under continuous stirring. It is important to note that the molarities of the metal precursor solutions were calculated using the volume of the final solution, namely 18.3 mL, in order to fill up ~80% of the 23 mL autoclave (Figure 2.17). Finally, 2.3 mL of 4.4 M NaOH and 1 mL of aminotriethoxysilane (APTES) were injected into the mixture, and vigorously stirred for 30 minutes using a micro (flea) type stir bar at ~300 rpm to reduce the metals and to control the ferrites' size regime and morphology, respectively. Additionally, as per our prior experience with ferrite-based systems, we note that the role of the NaOH is to assist in the solubility of the metal precursors, thereby inducing the formation of metal ions, which can subsequently stabilize the linear silicate chains of APTES through electrostatic interactions.[93] This is important, because the selective adsorption of metal ions coupled with favorable interactions between the APTES and metal ions can collectively and synergistically impact upon the resulting nucleation process and hence, the subsequent observed morphology.

After stirring, the solution was transferred to a 23 mL Teflon-lined stainless steel autoclave (Parr Instruments) and subsequently sealed. In a typical synthesis, the autoclave was placed in an oven and heated to 220 °C for 6 - 12 hours, and then allowed to cool naturally to room temperature. The product was subsequently washed for four times with aliquots (i.e. 1 aliquot is ~10 mL) of distilled water and once with an aliquot of ethanol. It was then isolated by

centrifugation, decantation, and finally placed in a drying oven at ~80°C to remove residual solvent, thereby yielding ~150 mg of sample.

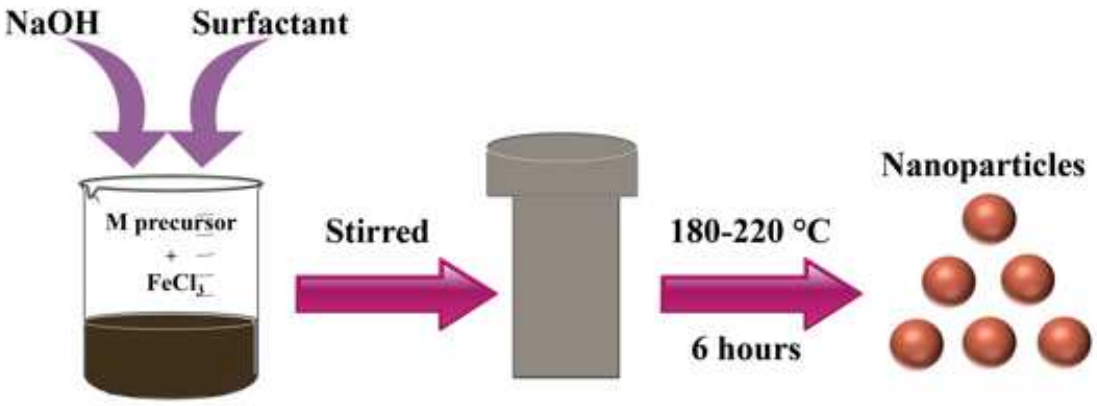

Figure 2.17: Schematic of the hydrothermal synthesis and preparation of metal ferrite nanoparticles.

2.3.3 RE:$CaTiO_3$ spheres using the Hydrothermal & Molten Salt Methods

2.3.3.1 (RE = Pr and Eu) doped $CaTiO_3$ micron-scale spheres - Molten Salt Method

To prepare RE-doped $CaTiO_3$ using a molten salt method, we followed a typical synthesis, wherein calcium oxalate, titanium dioxide (bulk TiO_2), sodium chloride (NaCl), and Triton X-100 were mixed together with an overall molar ratio of 1: 1: 20: 3, and ground for 30 minutes. Various molar dopant percentages 'x' of either praseodymium chloride ($PrCl_3$) (with 'x' = 0.05, 0.1, 0.2, and 0.5) or europium nitrate $Eu(NO_3)_3$ (with 'x'= 2, 4, and 6) were subsequently added to the slurry solution and ground for 30 minutes. Afterwards, the mixture was then placed in a quartz crucible and inserted into the muffle furnace, where it was annealed at 820°C for 3.5 h and subsequently cooled to room temperature. The sample was then collected (~200 mg), washed three times in distilled water and once in ethanol (EtOH), and finally desiccated overnight at 80°C in a drying oven.

As for comparable Eu-doped $SrTiO_3$ and $BaTiO_3$ perovskites, a previously used molten salt method was employed.[34] Briefly, strontium or barium oxalate, bulk TiO_2, NaCl, and NP-9 were mixed together with overall molar ratios of 1: 1: 20: 3, respectively. An optimal 6 mol % of Eu was added to the reaction mixture, ground for 30 minutes, and placed within the crucible. Subsequently, the crucible was transferred into the muffle furnace at 820 °C for 3.5 hours. After heat treatment, the sample was washed 3x in distilled water, once more in ethanol, and ultimately placed in a drying oven at 80 °C.

2.3.3.2 RE-doped $CaTiO_3$ porous micron-scale spheres – Hydrothermal Method

With respect to the hydrothermal method, the (RE = Pr and Eu) doped $CaTiO_3$ were prepared by placing 10 pieces of titanium (Ti) foil as the Ti precursor within a 125 mL Teflon holder. 1 M sodium hydroxide (NaOH) was subsequently added to the Teflon cup followed by the addition of 0.25 M calcium chloride ($CaCl_2$) to the mixture with stirring for 10 minutes. As an additional oxidizing agent, 7.83 mL of hydrogen peroxide (H_2O_2) was inserted with subsequent stirring for 10 more minutes. Subsequently, dopant molar percentages of either $PrCl_3$ (i.e. 'x' = 0.2) or $Eu(NO_3)_3$ (i.e. 'x' = 6) respectively, denoting optimal concentrations from the photoluminescence perspective, were added in the reaction mixture, and stirred for 15 minutes. The Teflon cup containing the reagents was then transferred into the metal autoclave and heated to 180°C for 10 hours. Once the reaction was complete, the sample was collected and washed twice with not only distilled water but also 2% hydrochloric acid (HCl) to remove calcium oxide impurities, as well as once in EtOH. The sample was subsequently dried overnight at 80°C.

2.3.4 Quantum Dot (QD) Synthesis using the Wet-solution Technique

The synthesis preparation of CdSe QDs was modified from an existing literature protocol.[94] Briefly, 0.2 mmol of CdO and 0.8 mmol of stearic acid were added to a three-necked

round bottom flask, then degassed, and ultimately heated at 150°C under an Ar atmosphere. Once the contents were dissolved, 3.88 g each of trioctylphosphine oxide (TOPO) and hexadecylamine (HDA) were added to the flask and heated to 320°C. Separately, a precursor selenium (Se) solution was prepared in an air-sensitive glovebox environment wherein the Se was dissolved in tributylphosphine (TBP) and dioctylamine (DOA). Once the solution mixture had attained 320°C within the flask, the Se precursor was injected therein, and QD growth was allowed to proceed for 15 seconds at 270°C. After growth was achieved, the mixture was later cooled to room temperature, then washed with either methanol (MeOH) or acetone, and ultimately stored in hexane.

2.3.5 Iron Oxide Nanorhombohedra (NRhomb) using the Hydrothermal Method

For the synthesis of average-sized (i.e. ~75 nm) α-Fe_2O_3 N-Rhomb, a reaction protocol from the prior literature was used.[95] Initially, a 0.04 M solution of cetyltrimethylammonium bromide (CTAB) was freshly prepared by adding in 1.458 g to 80 mL of distilled water. The solution was subsequently allowed to stir at 200 rpm for about an hour. After the CTAB was fully mixed in, a solution of 0.01 M of iron chloride ($FeCl_3$) was prepared by adding in 0.162 g of $FeCl_3$ to the CTAB solution followed by stirring for an additional 30 minutes. The solution mixture was subsequently transferred into a 100 mL volumetric flask; distilled water was then added, and the resulting solution was thoroughly shaken and mixed. 18.4 mL of the solution was later placed in a 23 mL Teflon autoclave and oven-heated to 120°C for 12 hours (Figure 2.18).[95]

The net result of this hydrothermal process enabled the hydrolysis of the iron chloride precursor and subsequent transformation to the desired Fe_2O_3. A slightly modified reaction protocol was employed for the production of smaller sized (i.e. ~47 nm) α-Fe_2O_3 N-Rhomb.

Specifically, the concentrations of both CTAB (0.02 M) and $FeCl_3$ (5 mM) were reduced by half, and the procedure described above was followed.

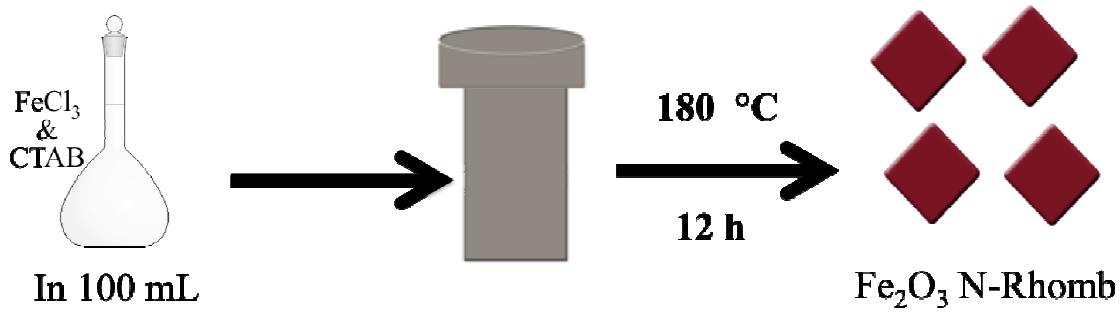

Figure 2.18: Diagram of the synthesis of iron oxide nanorhombohedra using the hydrothermal method.

2.3.6 Chemical Modification of α-Fe_2O_3 NRhomb- RhB -functionalized 47 nm α-Fe_2O_3 NRhomb

As a first, preparative step towards coating our iron oxide nanoparticles with Rhodamine, the surfaces of our 'smaller-sized' nanostructures were first chemically modified with amine-terminated groups, the source of which was derived from aminopropyl triethoxy silane (APTES) as described by a prior methodology.[96] Briefly, 0.1 g of Fe_2O_3 NRhomb and 70 mL of dimethyl sulfoxide (DMSO) were added to a 150 mL Schlenk-line flask. The flask was then de-gassed with pure nitrogen (N_2), stirred, and heated at 85°C for 26 hours. The product was subsequently washed in DMSO and heated at 120°C for 22 hours in order to thermally 'cure' it, a process which both stabilizes and strengthens the crosslinking APTES network onto the Fe_2O_3 nanostructures. The product was then collected and the APTES bound Fe_2O_3 NRhomb, with the desired pendant amine groups exposed, were used for subsequent conjugation with the Rhodamine B (RhB) dye.

Hence, to functionalize our rhombohedra with the labeled dye, 1 mg of RhB (95%, Aldrich) was dispersed in 10 ml DMSO and the exposed carboxyl groups of the RhB dye were

activated using 35 mg of 1,3-dicyclohexyl-carbodiimide (DCC), a biochemically inspired coupling agent. Subsequently, ~1.6 mg of amine-terminated, APTES modified Fe_2O_3 was added to the reaction mixture. The solution was allowed to stir for 24 hours at room temperature under dark conditions, thereby yielding the desired covalent amide bond linkages between the RhB molecules and the APTES-functionalized Fe_2O_3 NRhomb. The product was subsequently washed in water for 3 times and later dispersed in a cell culture medium at a final concentration of 1 mg/mL.

2.4 Detailed Structural Characterization Methods

2.4.1 X-ray Characterization

2.4.1.1 XRD

The crystallographic purity of as-prepared nanomaterials were confirmed using powder XRD. To prepare a typical sample for analysis, a fixed quantity of material was dispersed in ethanol and sonicated for ~1 min, prior to further air-drying upon deposition onto the sample holder. Diffraction patterns were subsequently obtained using a Rigaku Ultima III diffractometer or Scintag diffractometer, operating in the Bragg configuration using Cu Kα radiation (1.54 Å) and as a function of varying 2θ from 20 to 80° at a scanning rate of 1.0°/min for nanomaterials.

2.4.1.2 XPS for Co Ferrite Nanowires

XPS samples were prepared by initially dispersing the nanowire sample in a small amount of ethanol and then depositing multiple small aliquots onto a Si wafer (measuring 1 cm × 1 cm) followed by air drying, so as to ensure complete coverage. Samples were then transferred into the vacuum chamber of a home-built XPS surface analysis system, furnished with a model SPECS Phoibos 100 electron energy analyzer for electron detection. Once the sample was placed into the chamber, the chamber itself was evacuated to a base pressure of $\sim 2 \cdot 10^{-10}$ torr. A set of XPS

spectra were collected using an Al Kα X-ray source (hυ = 1486.6 eV) (model XR 50). For data analysis, the C 1s peak was set at a position of 284.5 eV[97] in order to subsequently calibrate the relative positions of the Fe *2p*, Co *2p*, and Si 2*p* peaks, respectively. To further analyze the nature of these peaks, the Shirley background was subsequently subtracted, and curve fitting was performed using the XPS PEAK 4.1 software. The software was able to automatically determine accurate positions for the Fe *2p*, Co *2p*, and Si *2p* peaks upon curve fitting. Finally, the processed data were plotted using the Origin 6.0 software.

2.4.2 Electron Microscopy

2.4.2.1 SEM

The morphology and size of the nanostructures were probed using a field emission SEM (FE-SEM Leo 1550) and analytical high-resolution SEM (JEOL 7600) instruments, operating at an accelerating voltage of 15 kV. Both were equipped with EDX capabilities. To prepare these samples for characterization, fixed amounts were dispersed in ethanol and sonicated for ~1 min, prior to their deposition onto the surfaces of silicon (Si) wafers.

2.4.2.2 TEM

Low magnification TEM data were generated at an accelerating voltage of 120 kV on the JEOL JEM-1400 instrument, outfitted with a 2048 x 2048 Gatan CCD digital camera. High-resolution TEM images coupled with SAED patterns were acquired at an accelerating voltage of 300 kV on a JEOL JEM-3000F and an accelerating voltage of 200 kV on a JEOL JEM-2100F microscope using a Gatan imaging filter (GIF). As prepared metal-based samples had been prepared for analysis by dispersion in ethanol followed by sonication. Subsequently, the solution was deposited drop-wise onto a 300 mesh Cu grid.

2.4.2.3 Confocal Microscopy: Quantification of Cell Fluorescence

MacGreen microglia were plated onto 24-well plates containing coverslips at a density of 15,000 cells/ml. Approximately 24 hours after plating, microglia were treated with 1 μg/mL, 10 μg/mL, and 100 μg/mL solutions of both bare RhB and RhB-labeled α-Fe_2O_3 NRhomb. After 24 hours, coverslips were fixed in 4% Paraformaldehyde (PFA) and mounted onto slides using 4',6-diamidino-2-phenylindole (DAPI) fluoromount. Five Z-Stack images were taken per cover slip at 63X magnification at a digital resolution of 1024 x 1024 with a Zeiss confocal microscope using LSM 510 Meta software. The fluorescence of each cell per image was quantified using ImageJ software. The corrected total cell fluorescence (CTCF) was calculated with the formula: CTCF = integrated density of cell – area of cell X mean gray area of a background sample. For experiments in which the mechanism of nanoparticle uptake was studied, MacGreen microglia were pre-treated with Chlorpromazine (CPZ) (Sigma- Aldrich) with a final concentration of 30 μM, approximately two hours before RhB-labeled α-Fe_2O_3 N-Rhomb exposure.

2.4.3 Optical Characterization

2.4.3.1 UV-Visible spectroscopy

To observe the nanomaterials optical properties, UV-visible spectra were obtained at high resolution with a UV1 UV-visible spectrophotometer (Thermo Scientific) using quartz cells possessing a 10 mm path length. Specifically, the metal-based nanostructures, quantum dots, and heterostructures were individually sonicated in either ethanol or methanol to yield a relatively clear (i.e. a reddish brown color for Cu NWs and a black hue for Ni NWs for those systems as examples), homogeneous mixture. The mixture was then added to the quartz cell and the subsequent UV-Visible spectra were recorded using ethanol or methanol as a blank.

2.4.3.2 FTIR Spectroscopy

FTIR spectra were collected on a Nexus 670 instrument (ThermoNicolet) equipped with a Smart Orbit diamond ATR accessory, a KBr beam splitter, and a DTGS KBr detector. Initially, a background correction in air was performed in the spectral range studied. Subsequently, as-prepared metal oxide samples were placed onto the crystal surface. FTIR data were recorded (~67 scans) over the wavenumber range of 1000–4000 cm^{-1} and evaluated in terms of expected, characteristic absorption bands. Spectra were recorded using the Omnic software with a spatial resolution of 1 cm^{-1}.

2.4.3.3 Photoluminescence (PL) Spectroscopy for CdSe QD-RE-$CaTiO_3$

Samples for PL spectra were dispersed in methanol (MeOH) for MPA-capped CdSe QDs, $CaTiO_3$: RE (RE = Eu and Pr), as well as for associated CdSe QD–$CaTiO_3$: Re heterostructures. Fluorescence data of these uniform dispersions were subsequently acquired at room temperature using a FluoroMax-4 spectrofluorimeter (Jobin Yvon) at 15 s and 5 s integration times, using excitation wavelengths of 325 nm and 399 nm for $CaTiO_3$: Pr and Eu, respectively. As for the mercaptopropionic acid (MPA)-capped QDs and the resulting CdSe QD - perovskite titanate: RE heterostructures, relevant optical data were obtained using an excitation wavelength of 375 nm.

2.5 Photocatalytic Property Measurements

2.5.1 Photocatalytic Degradation Experiments of Cu and Ni Nanowires

(a) Cu NWs. The Cu NWs were immobilized onto oleic acid capped TiO_2 NPs using a previously reported literature protocol with quantities of TiO_2 approaching 30 weight %.[98] As-prepared TiO_2 NPs were synthesized hydrothermally using an existing technique developed in our lab, and particle sample distributions measured 15 ± 7 nm.[99] For each photodegradation experiment, 10 mg of the resulting Cu NW-TiO_2 heterostructures, as-prepared TiO_2 NPs, and a

bulk Cu sample were added to aqueous solutions of Methyl Orange dye (MO, 10 mg/L) in independent runs.[98] Methyl Orange dye was preferentially chosen as a result of its resonance peak at ~450 nm, which is located near the corresponding absorption maximum of Cu NW-TiO_2 heterostructures. The mixture was subsequently stirred at room temperature and irradiated at 366 nm (~3.4 eV) excitation, using an Entela UVGL-58 Mineralight UV lamp (operating at 115 V, ~60 Hz, and 0.16 Amps). At 15 minute intervals, aliquots of the reaction mixture were removed, centrifuged, and isolated. Absorbance values were recorded in the absence of NPs at 450 nm using a UV1 UV-Visible spectrophotometer (Thermo Scientific).

(b) Ni NWs. The Ni NWs were also attached onto our hydrothermally processed TiO_2 NPs using the same literature protocol with TiO_2 quantities approaching 30 weight %.[98] For each independent photodegradation experiment, 10 mg of Ni NW-TiO_2 heterostructures, as-prepared TiO_2, and a bulk Ni sample were respectively added to aqueous solutions of Methylene Blue dye (MB, 50 mM).[100] This dye was chosen due to its absorption profile in the visible region. The mixture was subsequently stirred in the dark for 30 min and then illuminated under ambient fluorescent white light conditions for an additional 2 hours. At 30 minute intervals, aliquots of the mixture were systematically removed and centrifuged, prior to recording of the absorbance at 664 nm (1.87 eV), i.e. the dye maximum.

2.5.2 Ultrasmall Ni and Zn Ferrite Photocatalysis

First, a Beer's law plot of methylene blue was determined using aqueous solutions, ranging from 0.05 - 5 mg/L in concentration. For the photodegradation experiments, 25 mg of the desired ferrite nanoparticles have been added to a beaker containing 100 mL of a 5 mg/L aqueous solution of methylene blue, such that the ferrites maintain a concentration of 0.25 g/L. The solution was stirred magnetically at ~400 rpm in order to establish an absorption/desorption equilibrium between the dye and the nanoparticles. The solution was then irradiated at 366 nm

with an Entela UVGL-58 Mineralight UV lamp (115 V ~ 60 Hz, 0.16 Amps), placed at a distance of ~ 2 cm from the beaker. Aliquots were taken at hourly intervals, and then subjected to centrifugation at 7000 rpm in order to separate the nanoparticles from the dye. The supernatant was transferred to a quartz cell, and the optical absorbance was measured over the range of 200 - 800 nm with a UV1 UV-Visible spectrophotometer (Thermo Scientific). The absorbance at 664 nm was utilized to calculate the dye concentrations from a linear fit of the Beer's law plot. The final concentration over the initial concentration (C/C_0) was plotted with respect to time to elucidate the reaction order.

2.6 Cellular Preparations for Iron Oxide NRhomb

2.6.1 Primary neonatal microglial cell cultures

Cerebral cortices from postnatal day 1 Macgreen mice, which express enhanced green fluorescent protein (eGFP) under the control of the microglia/macrophage-specific promoter CSF1 in the C57BL/6 background,[101] were dissected, digested with trypsin (0.25% in HBSS) for 15 minutes at 37ºC, as well as mechanically dissociated and dismembered by trituration, as described previously.[102] Mixed cortical cells were plated in Dulbecco's modified eagle medium (DMEM), consisting of 10% FBS, 1% sodium pyruvate, and gentamycin on poly-D-lysine coated tissue culture plates. After 10 days, microglial cells were separated from the astrocytic monolayer by the addition of 12 mM lidocaine, and the isolated microglia were seeded onto 24 well plates at a density of 15,000 cells/mL.

2.6.2 α-Fe_2O_3 N-Rhomb preparation for Cell Culture

Due to the direct mutual attraction between nanostructures *via* either van der Waals forces or chemical bonding, some degree of aggregation is expected.[103, 104] As a result, the α-Fe_2O_3 N-

Rhomb stock solution (1 mg/mL) was prepared using a cell culture medium, containing fetal bovine serum. The solution was subsequently sonicated for 24 hours using a sonicator probe (220 - 260 V, 7.5 A, Misonix Model XL2020) in order to break up the bulkier agglomerates of nanocrystals.

2.7 Cytotoxic Analysis

2.7.1 ELISA Assay

Conditioned medium, obtained from primary cell cultures respectively treated with 1 μg/mL, 10 μg/mL, and 50 μg/mL of α-Fe_2O_3 N-Rhomb, was used for ELISA analysis. Levels of tumor necrosis factor alpha (TNFα) were determined using the eBiosciences quantitative sandwich enzyme immunoassay following the manufacturer's protocol. Briefly, 96 well plates were coated with diluted Capture antibody and incubated overnight at 4°C. The plates were blocked for one hour at room temperature followed by a two-hour incubation period with either the standard or the sample. The wells were then incubated for 1 hr with a working detector solution followed by incubation with the substrate solution for 30 min. The reaction was stopped with 50 μL of 1N H_2SO_4. The absorbance of each well was read using a 450 nm wavelength light.

2.7.2 LDH Cytotoxicity

An LDH Cytotoxicity Detection Kit (Roche Diagnostics Ltd) was used, according to the manufacturer's instructions. Briefly, primary microglia were incubated for 24 or 48 hours with different concentrations of α-Fe_2O_3 N-Rhomb. Samples were run in triplicate to determine LDH release by microglia in the presence of α-Fe_2O_3 N-Rhomb. Untreated cells served as a 'low control', whereas detergent-lysed cells served as a 'high control' for LDH release. 100 μL of the

kit 'reaction mixture' was added to the wells. The plate was then maintained in the dark for 30 minutes at room temperature, to allow for the tetrazolium salt, INT, in the presence of LDH, to become reduced to formazan. The reactions were terminated by addition of a 'stop' solution (1N HCl). Absorbance values of the formazan dye were measured at 490 nm using an ELISA plate reader. Cytotoxicity was calculated using the equation 2.10.

2.7.3 The NO Assay

The production of NO was determined by the amount of nitrite accumulated in cultured supernatant with 2,3-diaminonaphthalene (DAN). Specifically, cells were seeded in 96 well plates and exposed to the α-Fe_2O_3 N-Rhomb motifs for 24 h. The cultured supernatant was then collected and centrifuged in order to remove the N-Rhomb. In the 96 well plates, 50 µL of the Griess reagent and 50 µL of the supernatant were mixed together, and the absorbance was subsequently measured at 540 nm using an ELISA reader. The nitrite concentration was calculated based on a sodium nitrite standardization curve.

2.7.4. DCFDA Assay for the Detection of Reactive Oxygen Species

The production of reactive oxygen species (ROS) by microglia was measured using a 2', 7'-dichlorofluorescein diacetate (DCFDA) assay, as previously described.[105] Non-fluorescent DCFDA is converted to 2', 7'-dichlorofluorescein (DCF) in the presence of ROS. Briefly, microglia were plated onto a 96 well plate and incubated for 24 hours with different concentrations of N-Rhomb. After 24 hours, the media from the plates were aspirated off, and the cells were washed with 1x PBS followed by incubation with 25 µM DCFDA dissolved in 1x PBS for 30 minutes. The cells were then washed in 1x Phosphate Buffer Saline (PBS), and the amount of DCF present within the cells was quantified using a Fluoroskan Ascent Microplate Fluorimeter

(Thermo Scientific) equipped with a 485 nm excitation/ 530 nm emission filter pair. The fluorescence of treated samples was standardized, relative to untreated (i.e. negative) control cells. Cells incubated for 24 hours with 100 ng/mL lipopolysacharide (LPS) served as a positive control for the production of ROS and the subsequent oxidation of DCFDA to DCF.

2.7.5 Animal Approval

All experiments had prior approval from the Institutional Animal Care and Use Committee (IACUC) as well as the Department of Laboratory Animal Research at Stony Brook University.

2.7.6 Intrahippocampal RhB- labeled α-Fe_2O_3 N-Rhomb injection

Injections were performed bilaterally in the hippocampus. Mice were anesthetized with 1.25% Avertin and injected with 100 μg/mL of RhB-labeled α-Fe_2O_3 N-Rhomb at stereotactic coordinates -2.5 mm from Bregma and -1.7 mm lateral using a Hamilton syringe (0.485 mm I.D., Hamilton, Reno, NV) connected to a motorized stereotaxic injector (Stoelting, Wood Dale, IL). Following surgery, animals were injected intraperitoneally (i.p.) with 0.03 mg/kg of buprenorphine (Bedford labs) and left on a heating pad until they were fully recovered from anesthesia. After 24 hours post-injection, mice were anesthetized and perfused with 4% PFA. The brains were collected, post-fixed, cryoprotected, and cut into 40μm-thick sections. The sections were then mounted with DAPI fluoromount, and photographed at a digital resolution of 1024 x 1024 with a Zeiss confocal microscope using LSM 510 Meta software.

2.7.7 Statistics

All statistics were performed using either Statview (v. 4.0) or GraphPad Prism 6 for Windows. Data are presented as mean ± SEM (i.e. standard error on the mean). One-way ANOVA was used to determine the level of significance between groups in the fluorescence quantification analysis, LDH test, and TNFα ELISA, respectively. A Bonferroni post-test was used to control for multiple comparisons. Data were considered to be statistically significant, when $p < 0.05$.

2.8 References

1. P. Iqbal, J. A. Preece and P. M. Mendes, *Supramolecular Chemistry: From Molecules to Nanomaterials*, 2012, 8, 3589-3602.
2. S. Diodati, P. Dolcet, M. Casarin and S. Gross, *Chem Rev*, 2015, 115, 11449-11502.
3. A. Betke and G. Kickelbick, *Inorganics*, 2014, 2, 1-15.
4. H. Kawasaki, *Nanotechnology Reviews*, 2013, 2, 5-25.
5. K. Esumi, T. Tano and K. Meguro, *Langmuir*, 1989, 5, 268-270.
6. M. I. Dar, S. Sampath and S. A. Shivashankar, *Journal of Materials Chemistry*, 2012, 22, 22418-22423.
7. I. Pastoriza-Santos and L. M. Liz-Marzan, *Advanced Functional Materials*, 2009, 19, 679-688.
8. S. P. Xie, M. C. Paau, Y. Zhang, S. M. Shuang, W. Chan and M. M. F. Choi, *Nanoscale*, 2012, 4, 5325-5332.
9. Y. Wang, J. W. Ren, K. Deng, L. L. Gui and Y. Q. Tang, *Chemistry of Materials*, 2000, 12, 1622-1627.
10. M. Niederberger, M. H. Bartl and G. D. Stucky, *Chemistry of Materials*, 2002, 14, 4364-4370.
11. A. H. Jadhav, A. C. Lim, G. M. Thorat, H. S. Jadhav and J. G. Seo, *Rsc Advances*, 2016, 6, 31675-31686.
12. L. H. Qu and X. G. Peng, *Journal of the American Chemical Society*, 2002, 124, 2049-2055.
13. P. Lv, W. Y. Fu, Y. N. Mu, H. R. Sun, T. Liu, J. Wang, J. S. Niu, X. Li, L. Liu and H. B. Yang, *Journal of Materials Chemistry A*, 2015, 3, 16089-16096.
14. G. Ennas, G. Marongiu, A. Musinu, A. Falqui, P. Ballirano and R. Caminiti, *Journal of Materials Research*, 1999, 14, 1570-1575.
15. S. Jana, S. Pande, A. K. Sinha, S. Sarkar, M. Pradhan, M. Basu, S. Saha and T. Pal, *Journal of Physical Chemistry C*, 2009, 113, 1386-1392.
16. A. Phuruangrat, S. Thongtem and T. Thongtem, *Chalcogenide Letters*, 2013, 10, 359-365.
17. S. Xiao, P. Liu, W. Zhu, G. Li, D. Zhang and H. Li, *Nano Letters*, 2015, 15, 4853-4858.
18. C. Yan, C. M. Raghavan and D. J. Kang, *Materials Letters*, 2014, 116, 341-344.
19. T. Kita, S. Nishimoto, Y. Kameshima and M. Miyake, *Journal of the American Ceramic Society*, 2010, 93, 2427-2429.
20. D. Ding, Y. Huang, C. Zhou, Z. Liu, J. Ren, R. Zhang, J. Wang, Y. Zhang, Z. Lei, Z. Zhang and C. Zhi, *ACS Appl Mater Interfaces*, 2016, 8, 142-151.
21. P. Mukherjee, S. K. Misra, M. C. Gryka, H. H. Chang, S. Tiwari, W. L. Wilson, J. W. Scott, R. Bhargava and D. Pan, *Small*, 2015, 11, 4691-4703.
22. C. Wu, J. Cai, Q. Zhang, X. Zhou, Y. Zhu, P. K. Shen and K. Zhang, *ACS Appl Mater Interfaces*, 2015, 7, 26512-26521.
23. E. Dertli, S. Coskun and E. N. Esenturk, *Journal of Materials Research*, 2013, 28, 250-260.
24. C. Sikalidis, *Advances in Ceramics,* InTech, 2011, DOI: 10.52772/985.
25. X. Zhao, M. V. Reddy, H. X. Liu, S. Ramakrishna, G. V. S. Rao and B. V. R. Chowdari, *RSC Advances*, 2012, 2, 7462-7469.
26. D. Wang, J. L. Chu, Y. H. Liu, J. Li, T. Y. Xue, W. J. Wang and T. Qi, *Industrial & Engineering Chemistry Research*, 2013, 52, 15756-15762.
27. P. Nithyadharseni, M. V. Reddy, H. Fanny, S. Adams and B. V. R. Chowdari, *RSC Advances*, 2015, 5, 60552-60561.

28. K. H. Yoon, Y. S. Cho and D. H. Kang, *Journal of Materials Science*, 1998, 33, 2977-2984.
29. M. N. Rahaman, in *Kirk-Othmer Encyclopedia of Chemical Technology*, John Wiley & Sons, Inc., 2000, DOI: 10.1002/0471238961.0305180105231921.a01.pub2.
30. A. L. Tiano, C. Koenigsmann, A. C. Santulli and S. S. Wong, *Chemical Communications*, 2010, 46, 8093-8130.
31. X. Y. Li and Y. Q. Qu, *Crystal Growth & Design*, 2016, 16, 34-41.
32. R. E. Rojas-Hernandez, F. Rubio-Marcos, R. H. Goncalves, M. A. Rodriguez, E. Veron, M. Allix, C. Bessada and J. F. Fernandez, *Inorg Chem*, 2015, 54, 9896-9907.
33. T.-J. Park, Y. Mao and S. S. Wong, *Chemical Communications*, 2004, 23, 2708-2709.
34. S. B. Yuanbing Mao, and Stanislaus S. Wong, *Journal of the American Chemical Society*, 2003, 125, 15718-15719.
35. A. L. Tiano, A. C. Santulli, C. Koenigsmann, M. Feygenson, M. C. Aronson, R. Harrington, J. B. Parise and S. S. Wong, *Chemistry of Materials*, 2011, 23, 3277-3288.
36. G. Huang, X. C. Du, F. F. Zhang, D. M. Yin and L. M. Wang, *Chemistry-a European Journal*, 2015, 21, 14140-14145.
37. R. D. Farahani, K. Chizari and D. Therriault, *Nanoscale*, 2014, 6, 10470-10485.
38. H. Zhou and S. Wong, *American Chemistry Society Nano*, 2008, 2, 944-958.
39. H. Zhou and S. S. Wong, *ACS Nanoscience & Nanotechnology*, 2008, 2, 944-958.
40. F. Zhang and S. S. Wong, *ACS Nano*, 2010, 4, 99-112.
41. C. Koenigsmann, D. B. Semple, E. Sutter, S. E. Tobierre and S. S. Wong, *ACS Appl Mater Interfaces*, 2013, 5, 5518-5530.
42. F. Zhang and S. S. Wong, *Chemistry of Materials*, 2009, 21, 4541-4554.
43. J. Doshi and D. H. Reneker, *Journal of Electrostatics*, 1995, 35, 151-160.
44. S. De Vrieze, T. Van Camp, A. Nelvig, B. Hagstrom, P. Westbroek and K. De Clerck, *Journal of Materials Science*, 2009, 44, 1357-1362.
45. Z. Li and C. Wang, *One-Dimensional Nanostructures: Electrospinning Techniqe and Unique Nanofibers*, Springer, New York, 2013.
46. P. Peh, N. S. J. Lim, A. Blocki, S. M. L. Chee, H. C. Park, S. Liao, C. Chan and M. Raghunath, *Bioconjugate Chemistry*, 2015, 26, 1348-1358.
47. A. GhavamiNejad, A. R. K. Sasikala, A. R. Unnithan, R. G. Thomas, Y. Y. Jeong, M. Vatankhah-Varnoosfaderani, F. J. Stadler, C. H. Park and C. S. Kim, *Advanced Functional Materials*, 2015, 25, 2867-2875.
48. J. Xiao, C. Shi, H. Zheng, Z. Shi, D. Jiang, Y. Li and Q. Huang, *J Agric Food Chem*, 2016, 64, 3226-3233.
49. S. Padmakumar, J. Joseph, M. H. Neppalli, S. E. Mathew, S. V. Nair, S. A. Shankarappa and D. Menon, *ACS Appl Mater Interfaces*, 2016, 8, 6925-6934.
50. X. Zhao, Z. M. Yuan, L. Yildirimer, J. W. Zhao, Z. Y. Lin, Z. Cao, G. Q. Pan and W. G. Cui, *Small*, 2015, 11, 4284-4291.
51. J. J. Alcaraz-Espinoza, A. E. Chavez-Guajardo, J. C. Medina-Llamas, C. A. S. Andrade and C. P. de Melo, *ACS Appl Mater Interfaces*, 2015, 7, 7231-7240.
52. T. Krishnamoorthy, V. Thavasi, M. Subodh G and S. Ramakrishna, *Energy & Environmental Science*, 2011, 4, 2807-2812.
53. L. Xu, H. Song, B. Dong, Y. Wang, J. Chen and X. Bai, *Inorg Chem*, 2010, 49, 10590-10597.
54. O. Yildiz, K. Stano, S. Faraji, C. Stone, C. Willis, X. W. Zhang, J. S. Jur and P. D. Bradford, *Nanoscale*, 2015, 7, 16744-16754.

55. F. Y. Zhai, W. Huang, G. Wu, X. K. Jing, M. J. Wang, S. C. Chen, Y. Z. Wang, I. J. Chin and Y. Liu, *ACS Nano*, 2013, 7, 4892-4901.
56. M. Li, Y. P. Xiong, X. T. Liu, X. J. Bo, Y. F. Zhang, C. Han and L. P. Guo, *Nanoscale*, 2015, 7, 8920-8930.
57. L. J. Chen, C. R. Lee, Y. J. Chuang, Z. H. Wu and C. Y. Chen, *Crystengcomm*, 2015, 17, 4434-4438.
58. Y. Liu and L. Guo, *J Nanosci Nanotechnol*, 2013, 13, 843-847.
59. M. A. Alamein, S. Stephens, Q. Liu, S. Skabo and P. H. Warnke, *Tissue Eng Part C Methods*, 2013, 19, 458-472.
60. E. Y. Kim, D. Kumar, G. Khang and D. K. Lim, *Journal of Materials Chemistry B*, 2015, 3, 8433-8444.
61. G. Chen, J. Seo, C. Yang and P. N. Prasad, *Chemical Society Reviews*, 2013, 42, 8304-8338.
62. T. Proffen, S. J. L. Billinge, T. Egami and D. Louca, *Zeitschrift Fur Kristallographie*, 2003, 218, 132-143.
63. S. J. L. Billinge, R. G. DiFrancesco, G. H. Kwei, J. J. Neumeier and J. D. Thompson, *Physical Review Letters*, 1996, 77, 715-718.
64. P. Juhas, T. Davis, C. L. Farrow and S. J. L. Billinge, *Journal of Applied Crystallography*, 2013, 46, 560-566.
65. T. Egami and S. J. L. Billinge, *Underneath the Bragg peaks: structural analysis of complex materials*, Elsevier, Amsterdam, 2nd. edn., 2012.
66. T. Proffen and S. J. L. Billinge, *Journal of Applied Crystallography*, 1999, 32, 572-575.
67. C. L. Farrow, P. Juhas, J. Liu, D. Bryndin, E. S. Bozin, J. Bloch, T. Pro and S. J. L. Billinge, *Journal of Physics: Condensed Matter*, 2007, 19, 335219.
68. J.-A. Conchello and J. W. Lichtman, *Nature Methods*, 2005, 2, 920-931.
69. J. H. Liu, L. Cao, G. E. LeCroy, P. Wang, M. J. Meziani, Y. Y. Dong, Y. F. Liu, P. J. G. Luo and Y. P. Sun, *ACS Appl Mater Interfaces*, 2015, 7, 19439-19445.
70. R. F. Egerton, *Electron energy-loss spectroscopy in the electron microscope*, Springer, New York-Dordrecht-Heidelberg-London, 3rd edn., 2011.
71. R. F. Egerton, *Reports on Progress in Physics*, 2009, 72.
72. J. Ma, F. Yu, L. Zhou, L. Jin, M. Yang, J. Luan, Y. Tang, H. Fan, Z. Yuan and J. Chen, *ACS Appl Mater Interfaces*, 2012, 4, 5749-5760.
73. A. Houas, H. Lachheb, M. Ksibi, E. Elaloui, C. Guillard and J.-M. Herrmann, *Applied Catalysis, B: Environmental*, 2001, 31, 145-157.
74. C.-C. Wang, J.-R. Li, X.-L. Lv, Y.-Q. Zhang and G. Guo, *Energy & Environmental Science*, 2014, 7, 2831-2867.
75. M. C. Das, H. Xu, Z. Wang, G. Srinivas, W. Zhou, Y.-F. Yue, V. N. Nesterov, G. Qian and B. Chen, *Chemical Communications*, 2011, 47, 11715-11717.
76. P. R. Griffiths and J. A. De Haseth, *Fourier Transform Infrared Spectrometry*, A John Wiley & Sons, Inc., Hoboken, New Jersey, 2nd edn., 2007.
77. B. Ketterer, M. Heiss, M. J. Livrozet, A. Rudolph, E. Reiger and A. F. I. Morral, *Physical Review B*, 2011, 83.
78. D. L. Dexter and J. H. Schulman, *Journal of Chemical Physics*, 1954, 22, 1063-1070.
79. Z. Burshtein, *Optical Engineering*, 2010, 49, 091005/091001-091005/091019.
80. M. S. Mehata, *Applied Physics Letters*, 2012, 100, 151908-151908-4.
81. S. Brunauer, P. H. Emmett and E. Teller, *Journal of the American Chemical Society*, 1938, 60, 309-319.

82. K. S. Walton and R. Q. Snurr, *Journal of the American Chemical Society*, 2007, 129, 8552-8556.
83. A. G. Kolhatkar, A. C. Jamison, D. Litvinov, R. C. Willson and T. R. Lee, *International Journal of Molecular Sciences*, 2013, 14, 15977-16009.
84. G. C. Papaefthymiou, *Nano Today*, 2009, 4, 438-447.
85. K. L. Cox, V. Devanarayan, A. Kriauciunas, J. Manetta, C. Montrose and S. Sittampalam, in *Assay Guidance Manual*, eds. G. S. Sittampalam, N. P. Coussens, H. Nelson, M. Arkin, D. Auld, C. Austin, B. Bejcek, M. Glicksman, J. Inglese, P. W. Iversen, Z. Li, J. McGee, O. McManus, L. Minor, A. Napper, J. M. Peltier, T. Riss, O. J. Trask, Jr. and J. Weidner, Bethesda (MD), 2004.
86. N. S. Bryan and M. B. Grisham, *Free Radic Biol Med*, 2007, 43, 645-657.
87. S. K. Choudhari, M. Chaudhary, S. Bagde, A. R. Gadbail and V. Joshi, *World Journal of Surgical Oncology*, 2013, 11, 118/1-11.
88. M. M. Tarpey, D. A. Wink and M. B. Grisham, *American Journal of Physiology-Regulatory Integrative and Comparative Physiology*, 2004, 286, R431-R444.
89. T. J. Guzik, R. Korbut and T. Adamek-Guzik, *Journal of Physiology and Pharmacology*, 2003, 54, 469-487.
90. W. Droge, *Physiological Reviews*, 2002, 82, 47-95.
91. X. Guo, F. Zheng, M. Guo, M. Zhang and K.-C. Chou, *Rare Metals (Beijing, China)*, 2013, 32, 179-185.
92. J. Wang, Q. Chen, B. Hou and Z. Peng, *European Journal of Inorganic Chemistry*, 2004, 2004, 1165-1168.
93. A. L. Tiano, G. C. Papaefthymiou, C. S. Lewis, J. Han, C. Zhang, Q. Li, C. Shi, A. M. M. Abeykoon, S. J. L. Billinge, E. Stach, J. Thomas, K. Guerrero, P. Munayco, J. Munayco, R. B. Scorzelli, P. Burnham, A. J. Viescas and S. S. Wong, *Chemistry of Materials*, 2015, 27, 3572–3592.
94. L. Qu and X. Peng, *Journal of the American Chemical Society*, 2002, 124, 2049-2055.
95. Z. Pu, M. Cao, J. Yang, K. Huang and C. Hu, *Nanotechnology*, 2006, 17, 799-804.
96. L. Ye, R. Pelton and M. A. Brook, *Langmuir*, 2007, 23, 5630-5637.
97. S. Chen, Z. Wei, L. Guo, W. Ding, L. Dong, P. Shen, X. Qi and L. Li, *Chem Commun (Camb)*, 2011, 47, 10984-10986.
98. Y. Zhang, M. Huang, F. Li, H. Zhao and Z. Wen, *Journal of Materials Science*, 2013, 48, 6728-6736.
99. Y. Mao and S. S. Wong, *Journal of the American Chemical Society*, 2006, 128, 8217-8226.
100. G. G. Nakhate, V. S. Nikam, K. G. Kanade, S. Arbuj, B. B. Kale and J. O. Baeg, *Materials Chemistry and Physics*, 2010, 124, 976-981.
101. R. T. Sasmono, A. Ehrnsperger, S. L. Cronau, T. Ravasi, R. Kandane, M. J. Hickey, A. D. Cook, S. R. Himes, J. A. Hamilton and D. A. Hume, *J Leukoc Biol*, 2007, 82, 111-123.
102. R. Bronstein, L. Torres, J. C. Nissen and S. E. Tsirka, *J Vis Exp*, 2013, DOI: 10.3791/50647.
103. R. J. Hunter, *Foundations of Colloid Science*, Oxford University Press, New York, 1987.
104. D. Li and R. B. Kaner, *Journal of the American Chemical Society*, 2006, 128, 968-975.
105. A. D. Harrington, S. E. Tsirka and M. A. A. Schoonen, *Chemosphere*, 2013, 93, 1216-1221.

Chapter 3 - Synthesis, Characterization, and Formation Mechanism of Crystalline Cu and Ni Metallic Nanowires under Ambient, Seedless, Surfactantless Conditions

3.1 Introduction

The use of metal nanomaterials in catalysis research has grown rapidly, due to progress in material science. In particular, the reduced sizes of nanoparticles introduce unique characteristics such as varying the electronic structure of the metal nanoparticles, meaning that the Fermi level is increased, thereby causing lower reduction potentials at the surface.[1] Moreover, the nanoparticle size also increases the amount of high-energy surface atoms, thereby leading to enhanced catalysis. In addition to these properties, certain metallic nanoparticles (*i.e.* Ag, Au, Cu, Pt) also display optical properties with small imaginary dielectric constants over a wide range of wavelengths in order to ultimately facilitate surface plasmon resonance (SPR) upon either UV, visible, or near infrared (NIR) irradiation.[2] As a result of metal NPs' unique electronic and optical properties, their applications range from biosensors, electronic devices, to catalysts for applications such as photoreactions or fuel cell reactions.

Of these metals, copper (Cu) has been universally used in practical products, such as electrical devices, water pipes, roofing materials, and brass furnishings. Moreover, copper for electronics has made a huge impact upon technology, since it is an excellent conductor for heat and electricity. Cu-containing nanostructures have generated significant interest, due to the metal's earth abundance, and have been extensively analyzed at the nanoscale in order to probe their potentially game-changing thermal and electrical conductivities.[3, 4] Cu is also known to promote reactions when doped onto metal oxides, such as zinc oxide (ZnO), cerium oxide (CeO_2), and iron oxide (Fe_2O_3) due to its strong metal-support interactions.[5] These reactions include methanol production and water gas shift reactions, respectively.[5-7] Moreover, the

incorporation of Cu, with other elemental metals such as platinum (Pt), can lead to the formation of highly active catalysts for the methanol oxidation reaction (MOR), a reaction used in direct methanol fuel cells (DMFCs). Specifically, PtCu can achieve an activity of ~1.26 mA/cm^2, which far surpasses that of its commercial Pt-Ru counterparts by more than 2 fold.[8]

As for 1D materials, currently films derived from Cu NWs produced from aqueous solution-based protocols have achieved respectable optoelectronic performance, characterized by a sheet resistance of 61 Ohm/cm^2 and 67% transmittance.[9] It was found that this device performance could be tuned by varying the concentration of the Cu NW ink. Corresponding films composed of electrospun Cu NWs have been shown to possess very low resistance and high transmittance, while maintaining mechanical flexibility.[10] Not surprisingly, research has been initiated on Cu NWs for a variety of applications including but not limited to solar cells,[11,12] touch screens, and light-emitting diodes (LED).[13,14-16]

Similarly, nickel (Ni) is commonly used for the production of stainless steel, due to the metal's favorable resistance to high temperature and corrosion.[17] It also has been used in the past as rechargeable batteries and as catalysts.[18-20] Specifically, for rechargeable batteries, due to the low solubility product ($K_{sp} = 10^{-35}$) of its hydroxide form, nickel oxide-based batteries are able to hold more energy and maintain stability under commercial cycle durability conditions, ranging from 500-1,000 cycles.[21, 22] Ni NWs are also widely known for their electrical transport properties, and have been found to evince a similar but larger magnitude of temperature-dependent resistivity as compared with bulk Ni. This observation may potentially be ascribed to the presence of either grain boundary scattering or defects within the crystal structure at the nanoscale.[23]

Recently, high-quality metal 1D nanostructures, such as nanowires or nanotubes, have been considered as novel systems for their potential applications in sensing, electronic, and

optical devices due to their high surface area-to-volume ratio.[24] Many different approaches for the preparation of these coinage metal nanomaterials (such as Cu and Ni) include but are not limited to electrospinning, electrochemical deposition, UV photolithography, hydrothermal processes, liquid phase reduction, and CVD methods.[3, 25-43] However, while these techniques can successfully generate these nanomaterials, a step forward synthetically speaking would be to possibly mitigate for the use of either specialized instrumentation (*i.e.* lithography), high energy processing (*i.e.* CVD), or the use of potentially toxic precursors (*i.e.* hydrazine in conventional wet chemistry protocols) in order to synthesize pure, monodisperse, and crystalline Cu or Ni nanostructures.

In other words, it would be desirable if these nanostructures could be produced in as little as a few hours under ambient temperature and pressure conditions, using only relatively mild precursors that would react completely without the need for any extraneous reagents or catalysts, thereby fulfilling green chemistry principles III, V, and VI (see Chapter 1). In this context, our lab has successfully adhered to these principles for the synthesis of various 1D NW materials using the U-tbue double diffusion technique, including metal oxides (i.e. ZnO, CuO, Fe_2O_3, $BaCrO_4$, $CaWO_4$, $SrWO_4$, $MnWO_4$, and $BaWO_4$ as well as their doped analogues), metal sulfides (i.e. CdS, PbS, and CuS), metal fluorides (i.e. BaF_2, CaF_2, SrF_2, $KMnF_3$, and NH_4MnF_3), metal phosphates (i.e. Tb-doped $CePO_4$), pure elemental metals (i.e. Au, Ag, Pt, and Pd), as well as homogeneous segmented binary materials (i.e. Pd/Au and Pd/Pt) using a reasonably simple protocol.[44-53]

Over the years, we have noted that such a methodology does not require either (1) high temperatures or high-energy inputs, (2) powered instrumentation, or (3) an association with particularly toxic reagents/byproducts. For metal nanowires (i.e. Cu and Ni, in particular), which (i) tend to oxidize relatively easily, (ii) are difficult to form as a purified motif, and (iii) are

therefore particularly sensitive to the reaction conditions used to create them, we note that the same solution-based template methodology can be applied with the use of commercially available and relatively inexpensive sodium borohydride ($NaBH_4$) as the reducing agent, due to its standard potential value (-1.24 V), which is capable of readily reducing Cu^{2+} (0.34 V) and Ni^{2+} (-0.25 V) at room temperature.[54] Such a strategy therefore provides for a relatively low cost, flexible, and generalizable approach for synthesizing these nanowires under ambient conditions. The size and morphology regime of these nanomaterials can be reliably varied and altered by controlling the template pore size and thickness from whence these nanowires are ultimately isolated.

In addition to synthesizing these nanowires, their photocalalytic capabilities will be explored in an attempt to answer whether elemental nanowires can enhance photocatalytic reactions at a greater rate than their bulk counterparts.

3.2 Results & Discussion

3.2.1. X-ray Diffraction.

The purity and crystallinity of our as-prepared NWs were characterized using XRD, as shown in Figure 3.1A and B for the Cu and Ni samples, respectively. All diffraction peaks present could be readily indexed to the JCPDS 04-0836 for face centered cubic (*fcc*) crystalline Cu; there are only additional 2 minute peaks, situated at 2θ values of 38° and 39°, respectively, consistent with the formation of copper (I) oxide (Cu_2O), as described by JCPDS #33-0451. This impurity may be ascribed to the exposure of the NWs to oxygen during the 4-hour scanning time, a hypothesis which is also consistent with the prior literature in that it is well known that Cu readily oxidizes in air.[55]

With respect to the Ni NWs, most diffraction peaks could be ascribed to the JCPDS #04-0850 for crystalline *fcc* Ni. We should also note that the actual amount of Ni NWs we obtained in

our synthetic protocols is not as quantitatively substantial as that of Cu NWs, perhaps due to the lower diffusion rate for Ni as compared with Cu. Hence, not surprisingly, higher background peaks and lower signal-to-noise ratios were observed in Figure 3.1B. It is important to note that no 'expected' impurity peaks, including nickel oxide, nickel hydroxide, and analogous metal oxides, were observed. Since Ni does not oxidize as easily as Cu (based on known oxidation potentials, i.e. E° = -0.34 V and + 0.25 V for Cu and Ni, respectively), since the oxidized form is relatively more stable for Cu, it is reasonable that these oxide peaks are not actually observed under these relatively mild reaction conditions.

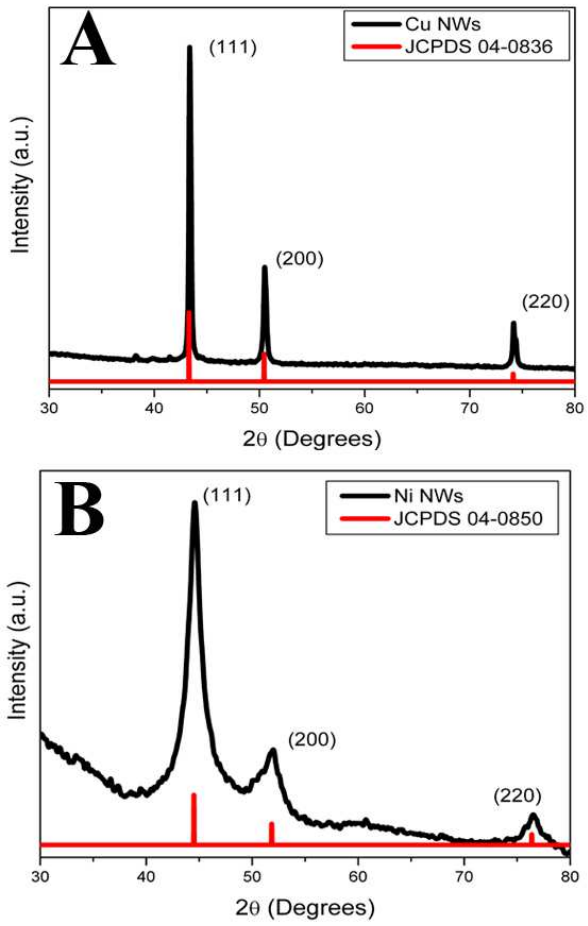

Figure 3.1. XRD patterns from (A) as-prepared Cu Nanowires (top curve in black) and the corresponding JCPDS standard for Cu (bottom curve in red); (B) as-prepared NWs (top curve in black) and the corresponding JCPDS standard for Ni (bottom curve in red). Reprinted with permission from Ref. 53. Copyright 2014 American Chemical Society.

3.2.2. Electron Microscopy.

3.2.2.1 Cu NWs

The size and morphology of the NW samples were observed using FE-SEM, TEM, and HR-TEM. Figure 3.2A, C, and inset to C highlight SEM and TEM images of the Cu NWs, respectively, prepared within the pores of a 50 nm polycarbonate template membrane. These images demonstrate the presence of crystalline nanorods with a roughened surface morphology throughout their entire length with an average diameter of 100 ± 13 nm. These TEM images are representative of an overall distribution of not only dispersed but also aggregated nanowire bundles. EDS analysis (Figure 3.2B) suggests that we formed elemental Cu, though some degree of oxygen and carbon was also noted, an observation which may originate from either the NW sample itself, the sampling environment, or the presence of some degree of oxidation, possibly ascribed to the nanowire surface species as well as to any residual polycarbonate template. The noticeable Si peak can be attributed to the underlying silicon wafer.

To further analyze Cu nanowires (lower left inset to Figure 3.2D), a single arbitrary nanowire structure was probed at the atomic scale using HR-TEM analysis. Based on the HR-TEM results (Figure 3.2D), the measured interplanar distance of 0.203 nm was consistent with the (111) plane of the face-centered cubic (*fcc*) phase of crystalline Cu. Complementary SAED (Figure 2E) analysis shows that the diffraction patterns highlighting the 111, 200, 220, and 311 planes, respectively, can be indexed to crystalline Cu and are in reasonable agreement with the complementary XRD data.

As for the analogous Cu NWs, prepared using complementary 200 nm templates, Figures 3.3A and C illustrate representative SEM and TEM images of the Cu NWs. The images also demonstrate the presence of roughened NWs with an average diameter of 233 ± 19 nm and an average length of ~1.5 μm. Based on EDS analysis (Figure 3.3B), we note that Cu is certainly

present within the sample. Peaks corresponding to carbon and oxygen can be ascribed to residual impurities arising from the template, the sampling environment, and possibly some level of oxidation. The noticeable Si peak can be attributed to the underlying silicon wafer.

Based upon the HR-TEM results (Figure 3.3D), the Cu NWs (upper lefthand inset to Figure 3D) were found to be polycrystalline in nature, analogous to what we have noted for other types of nanowires in prior reports under similar reaction conditions.[45, 49] Measured interplanar distances of 0.202 nm and 0.187 nm are consistent with the expected (111) and (200) planes, respectively. All of these data point to the formation of the *fcc* phase of crystalline Cu. Complementary SAED (Figure 3.3E) analysis shows that the diffraction patterns, possessing features associated with the 111, 200, 220, and 311 planes, respectively, can be indexed to crystalline Cu and are consistent with the complementary XRD data.

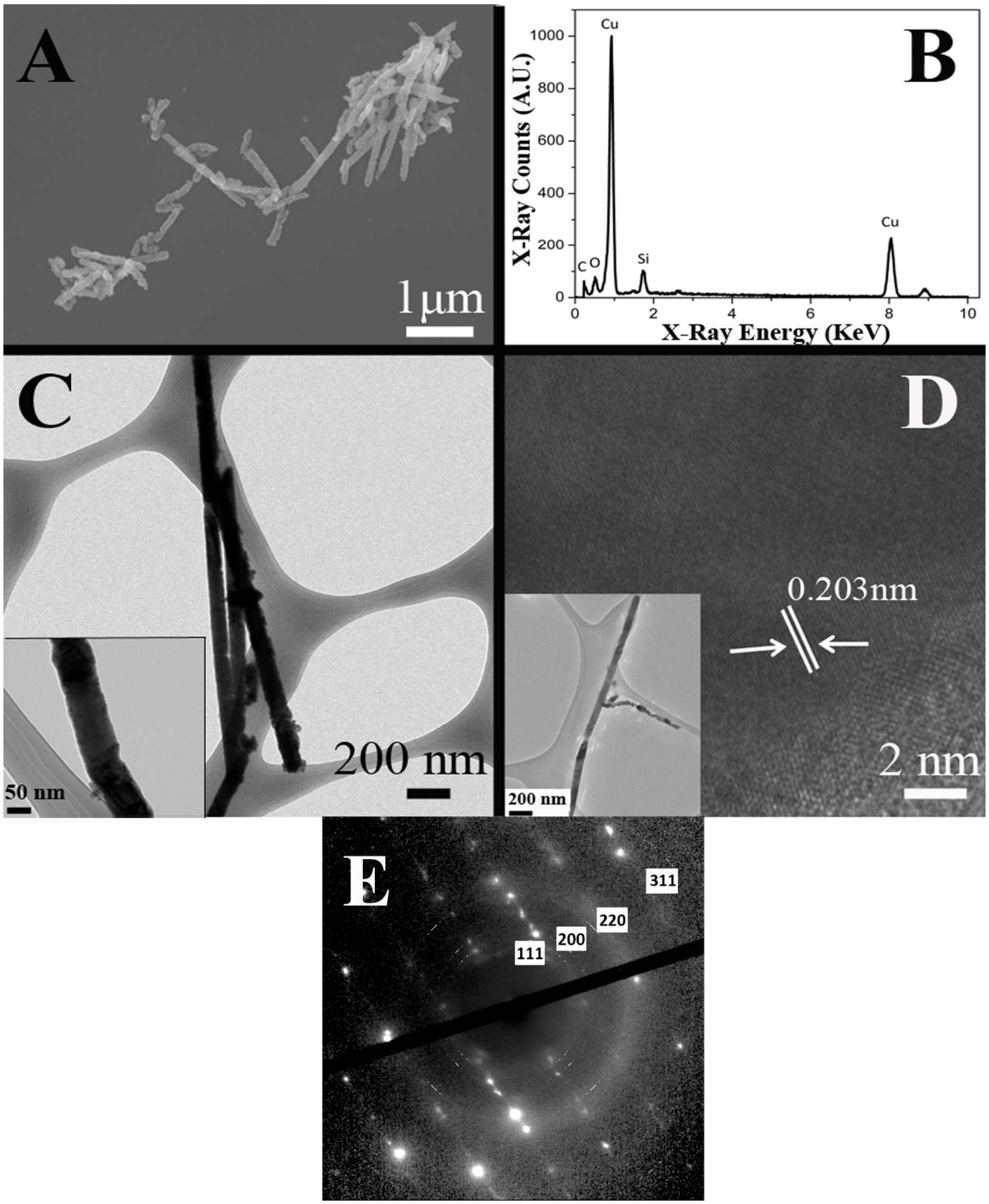

Figure 3.2. TEM and SEM images of isolated Cu NWs (A, C, higher magnification image as inset to (C)) prepared using template membranes possessing 50 nm pore diameters. EDS spectrum of as-prepared Cu NWs (B). The Si peak is associated with the silicon wafer. The higher magnification TEM image (D) denotes a localized area of a typical nanowire (lower resolution image in the lower lefthand inset to (D)). Selected area electron diffraction pattern with assigned diffraction spots is shown in (E). Reprinted with permission from Ref. 53. Copyright 2014 American Chemical Society.

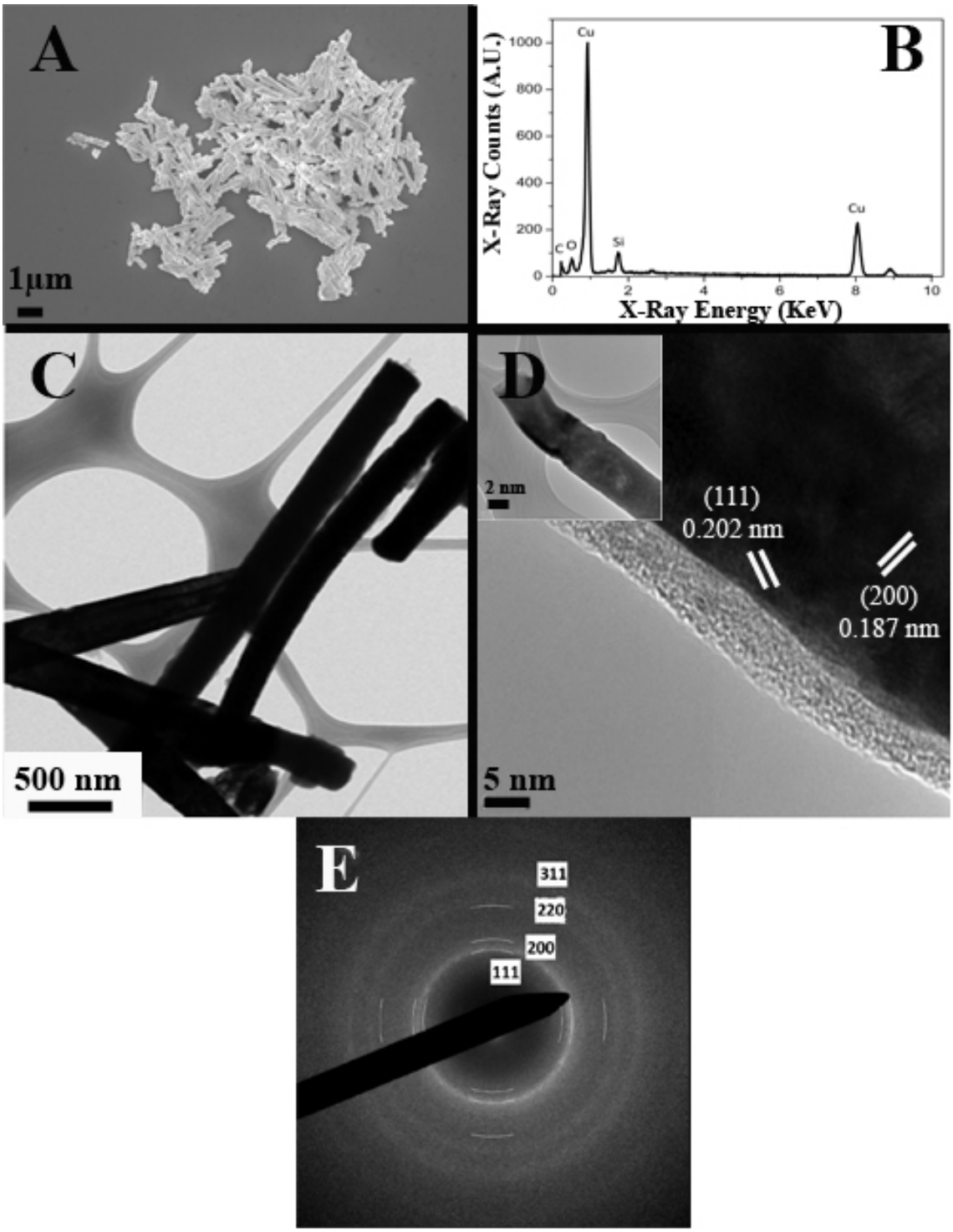

Figure 3.3. TEM and SEM images of isolated ~200 nm Cu NWs (A, C). EDS spectrum of as-prepared Cu NWs (B). The Si peak is associated with the silicon wafer. The TEM image (upper lefthand inset in D) denotes the region where a higher resolution image (D) was obtained. Selected area electron diffraction pattern is presented in (E). Reprinted with permission from Ref. 53. Copyright 2014 American Chemical Society.

3.2.2.2 Ni NWs

The size and morphology of the NW samples were also observed using FE-SEM, TEM, and HR-TEM analysis. Figure 3.4A and C show SEM and TEM images of the Ni NWs, respectively, using a 50 nm polycarbonate template. These images are consistent with the presence of crystalline, homogeneous, and uniform nanorods throughout their entire length, possessing an average diameter of 92 ± 10 nm. The TEM images show both dispersed as well as aggregated nanowire bundles. The EDS analysis (Figure 3.4B) is indicative of the presence of elemental Ni as well as of some degree of oxygen and carbon present. The latter contamination may likewise be ascribed to the NW sample, the sampling environment, as well as the presence of oxidation emanating from the nanowire surface and/or from the residual polycarbonate template, respectively. The presence of the silicon (Si) peak can be attributed to the silicon wafer.

To further study typical Ni nanowires (lower righthand inset to Figure 3.4D), an arbitrary individual structure was analyzed at the atomic scale using HR-TEM. Based on the HR-TEM image (Figure 3.4D), the observed, measured interplanar distance of 0.201 nm was consistent with the (111) plane of the face-centered-cubic (*fcc*) phase of the crystalline Ni observed. Complementary SAED data (Figure 3.4E) underscore a diffraction pattern, composed of diffuse rings, which can be indexed to the 111, 200, and 220 planes, respectively, of polycrystalline Ni, a scenario in good agreement with prior XRD results.

As for the analogous Ni NWs, prepared using complementary 200 nm templates, Figures 3.5A and C show representative SEM and TEM images of these nanostructures. These images demonstrate the formation of smooth NWs possessing average diameters of 225 ± 33 nm with average lengths of a micron. We note that some of the nanowires appeared to be noticeably bent and evince mechanical flexibility, an observation which has been ascribed to sample processing effects. Nonetheless, prior literature has shown that at room temperature, Ni NWs are often

elastic up to a threshold of 7.5% strain at different strain rates with a yield stress of 5.5 GPa,[56] a value comparable with that of Nylon (~2-4 GPa).[57] Based on EDS analysis (Figure 3.5B), we note that Ni is present within the sample. Peaks corresponding to carbon and oxygen likely can be ascribed to factors associated with the presence of residual template, an impure sampling environment, and possible oxidation effects. The apparent Si peak can be attributed to the underlying silicon wafer.

The NWs were also further probed at higher resolution. Specifically, based on HR-TEM results (Figure 3.5D), the Ni NWs (lower right inset to Figure 3.5D) were found to be crystalline in nature with a measured interplanar distance of 0.206 nm, data which are consistent with the presence of the (111) plane, corresponding to the *fcc* phase of crystalline Ni. Complementary SAED (Figure 3.5E) analysis suggests that the diffraction patterns associated with the 111, 200, and 220 planes, respectively, can be ascribed to crystalline Ni, and our results are also in reasonable agreement with the complementary XRD data.

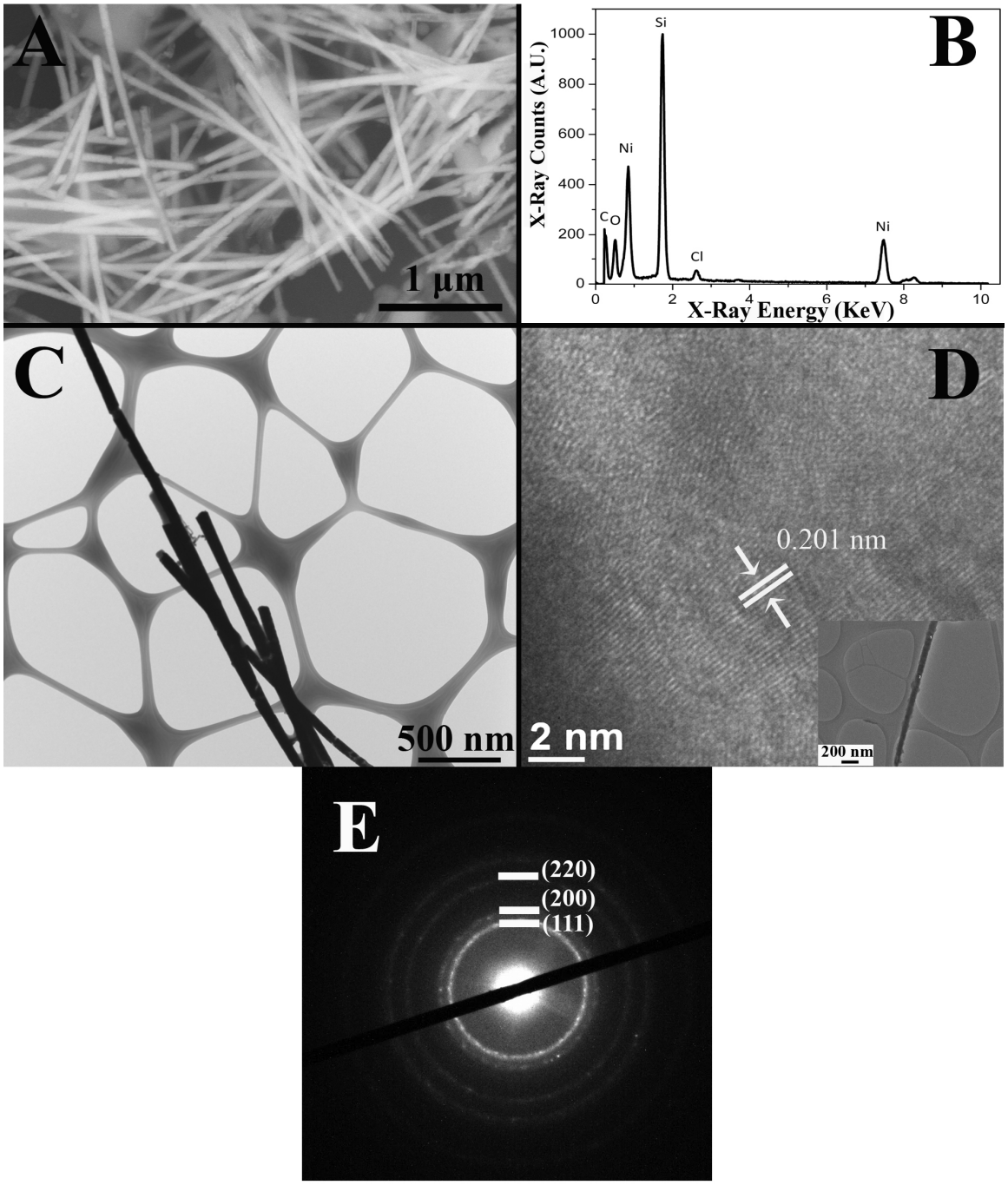

Figure 3.4. TEM and SEM images of as-prepared Ni NWs (A and C) prepared using template membranes possessing 50 nm pore diameters. EDS spectrum of the isolated Ni NWs (B) with the Si peak correlated with the presence of the underlying silicon wafer. The TEM image (lower right inset to D) denotes the region where the higher resolution TEM image (D) was taken as well as the SAED pattern (E). Reprinted with permission from Ref. 53. Copyright 2014 American Chemical Society.

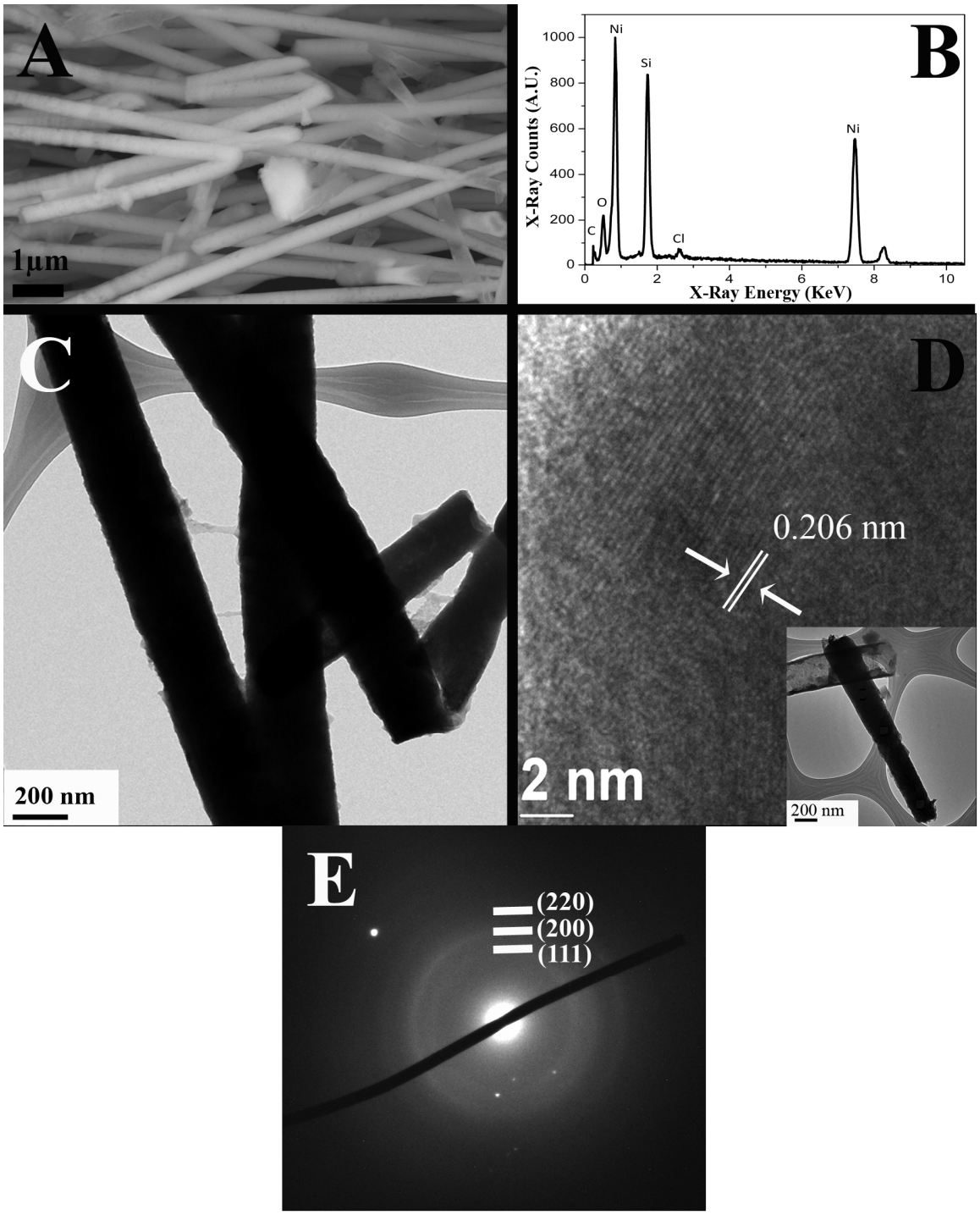

Figure 3.5. TEM and SEM images of as-prepared ~200 nm Ni NWs (A and C). EDS spectrum of the isolated Ni NWs (B) with the Si peak correlated with the presence of the underlying silicon wafer. The lower magnification image (lower righthand inset to D) denotes the nanowire where the HRTEM image (D) was taken as well as the SAED pattern (E). Reprinted with permission from Ref. 53. Copyright 2014 American Chemical Society.

3.2.3. UV-Visible Spectroscopy

Figure 3.6A and B feature UV-visible spectra of Cu and Ni NWs produced under ambient conditions. The absorption spectrum for Cu highlights a surface plasmon peak centered at ~594 nm, which is somewhat red-shifted from what has been previously shown in the literature, but this observation may possibly be due to an increase in diameter and aspect ratio as well as to a higher degree of aggregation by comparison with conventional Cu nanoparticles previously studied.[58-62] The absence of a peak near 370 nm, normally ascribed to Cu_2O, indicates that there is no observable sign of widespread sample oxidation, although we cannot rule out the presence of localized oxidation upon air exposure, evident from the XRD data. Figure 3.6B highlights the presence of UV-visible absorption spectra of Ni NWs with an absorbance peak of ~387 nm, which is in good agreement with the literature.[36, 63]

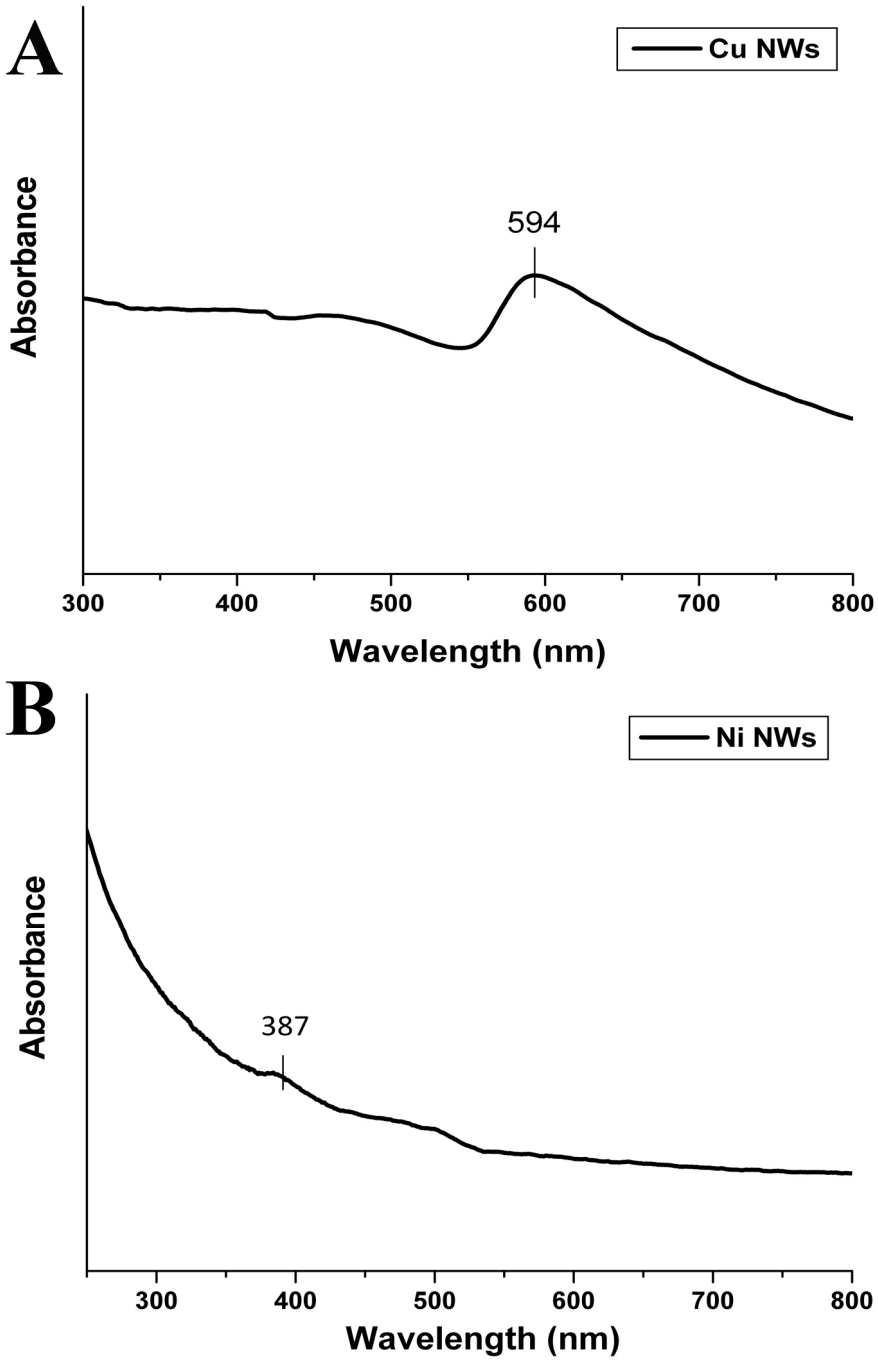

Figure 3.6. UV-Visible absorption spectra of Cu NWs (A) and Ni NWs (B). Reprinted with permission from Ref. 53. Copyright 2014 American Chemical Society.

3.2.4. Electron Energy Loss Spectroscopy (EELS) Cross Sectional Analysis.

Cross-sectional line scans were collected on selected metal NWs in order to observe the thickness of the oxide layers on these nanomaterials. It is evident that we form a primary central 'core' of elemental Cu and Ni NWs, respectively, with a very thin outer oxide 'shell'. For the Cu NWs, based on spatially resolved EELS spectra (Figure 3.7A and B), it is apparent that the nanostructure surface has circumferentially oxidized with a thin outer oxide layer possessing a thickness of ~30 nm (based on full width at half-maximum measurements, FWHM). This observation may be due in part to exposure to air during processes associated with characterization, such as sample preparation and image acquisition. As for the Ni NWs, based on spatially resolved EELS spectra (Figure 3.8A and B), the corresponding thin outer oxide layer appears to be roughly ~20 nm in thickness, based on FWHM measurements, as evidenced by the magnitude and spatial breadth of the elemental oxygen signal on the nanowire perimeter. The intensity and uniformity of the Ni peak are consistent with a reasonably homogeneous elemental nickel nanostructure as a result of the room-temperature synthesis process. In effect, the oxygen peak distribution is strongest at the circumferential edges, consistent with the formation of a narrow outer surface oxide layer, measuring between 20-30 nm. Moreover, the oxygen signal diminishes in intensity within the interior of the wire structure itself.

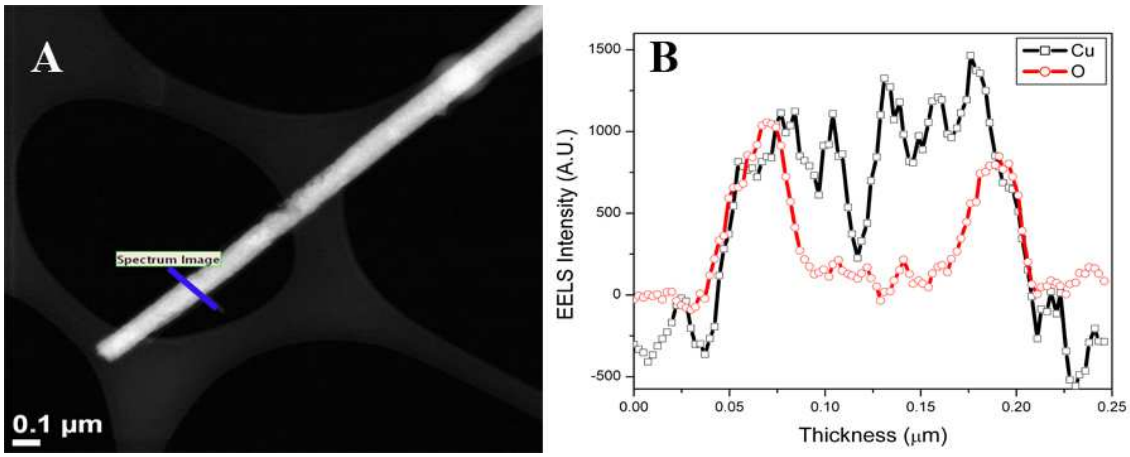

Figure 3.7. Electron energy loss spectroscopy (EELS) cross-sectional analysis of an as-prepared copper nanowire. Signal intensities for copper and oxygen (B) correspond to the blue slice in the survey image, highlighted in (A). Reprinted with permission from Ref. 53. Copyright 2014 American Chemical Society.

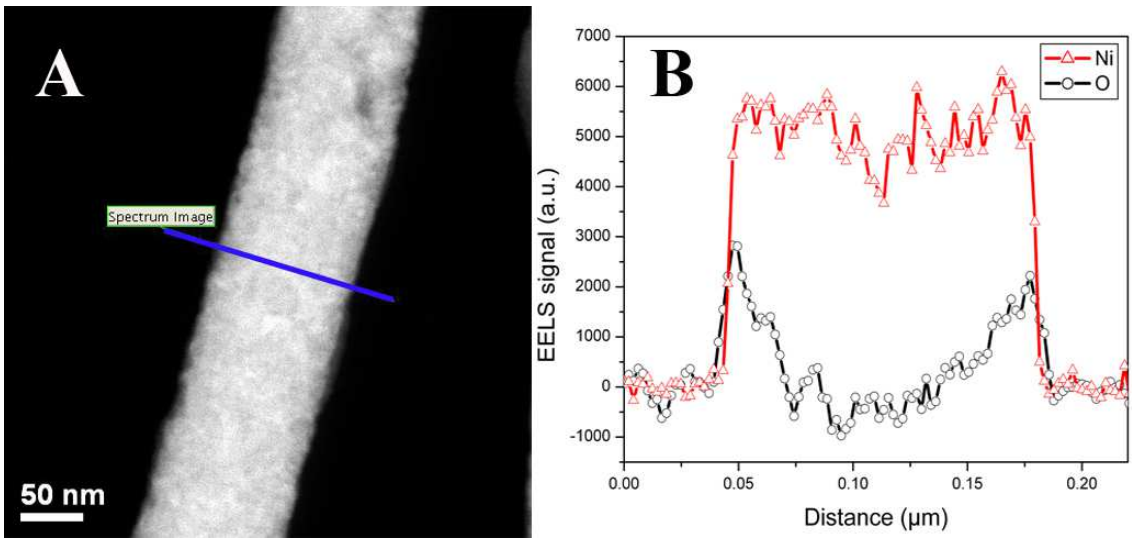

Figure 3.8. Electron energy loss spectroscopy (EELS) cross-sectional analysis of an as-prepared nickel nanowire. Signal intensities for nickel and oxygen (B) correspond to the blue slice in the survey image highlighted in (A). Reprinted with permission from Ref. 53. Copyright 2014 American Chemical Society.

3.2.5. Photocatalytic Degradation Results

3.2.5.1 Cu NWs

In Figure 3.9A, C_0 represents the initial concentration of MO and C denotes the time-dependent concentration, reflecting a time-dependent decoloration in this case, of MO, after UV irradiation. Under UV irradiation illumination (λ_{ex} = 366 nm (3.4 eV)), electrons are excited from a filled valence band to an empty conduction band, thereby generating electron-hole pairs in wide band gap (i.e. 3.2 eV) TiO_2 NPs. Hence, photodegradation occurs[64] as a result of the interaction of dye molecules with reactive oxidizing species generated on the nanoparticulate metal oxide surface when either (i) the holes react with adsorbed OH^- to produce hydroxyl radicals or (ii) electrons combine with adsorbed electron acceptors such as oxygen to create O_2^-, for instance.[65] Not surprisingly, our TiO_2 NPs evinced a ~50% reduction in MO dye absorption after 1 hour of reaction.

By contrast, the composite containing Cu NWs coupled with TiO_2 gave rise to a sizeable ~90% decrease in the absorption level of MO, after an hour of reaction. This observation may have potentially been due to a number of reasons. First, because the surface potential of Cu-TiO_2 composites is much less than that of pure TiO_2 during UV illumination, the composite surface possesses abundant electronic traps (such as oxygen vacancies and Cu^{+2} species), which can intrinsically decrease the recombination rate of photoinduced charge carriers including electron-hole pairs,[66, 67] thereby leading to enhanced photocatalytic efficiency.[68, 69] Second, the interfacial charge transfer from the photoexcited TiO_2 to the proximal, coupled Cu generates reactive radical species such as $^{\bullet}OH$.[54, 70] Third, Cu^{2+} may reduce to Cu^{1+} in the presence of a photogenerated electron, which can subsequently react with H_2O_2 to create larger quantities of reactive and ultimately destructive surface radical species, including primarily $^{\bullet}OH$, all of which are ultimately responsible for the high oxidant activity that results in the organic dye compound degradation in

these photocatalytic reactions.[66, 67, 70, 71] Fourth, the composite provides for a moderate specific surface area for more abundant reaction sites as compared with their elemental analogues.[72] By contrast, bulk Cu exhibited relatively poor performance for the degradation of MO, approximately after an hour of reaction activity.

3.2.5.2 Ni NWs

In Figure 3.9B, C_0 denotes the initial concentration of MB and C is the corresponding time-dependent concentration, manifested as a signal decrease associated with the decoloration of MB under ambient fluorescent white light exposure. Based upon the photodegradation results (Figure 3.9B), TiO_2 NPs evinced a ~50% reduction in Methylene Blue absorption after 3 hours of reaction. This result is consistent with previous literature, as TiO_2 is photoactive in the UV region.[65, 73, 74] By comparison, use of the corresponding composites composed of Ni NWs associated with TiO_2 led to a greater than 60% decrease in the absorption value of MB over 3 hours as compared with bulk Ni.

This observed increased degradation activity is likely caused by the enhanced activity of more readily produced photogenerated electrons and corresponding hole pairs, a process which occurs relatively more quickly based on the reduced band gap of the Ni-TiO_2 composite (2.28 eV)[73] as compared with bare, undoped TiO_2 (3.2 eV)[73] with the decrease in bandgap for the composite attributable to the 'electron acceptor' character of Ni.[72] These photogenerated electrons can either assist in the reduction of the MB dye directly or react with either O_2, OH^-, or H_2O to generate radicals (such as $O_2^{\bullet-}$) that are known to be powerful oxidizing agents.[75] We should note that, based on existing literature, when Ni NPs were incorporated with TiO_2, photodegradation results of ~50% were recorded; these data are comparable to what we have observed herein.

We should note that the photodegradation ability of TiO_2 in MO is relatively greater than and evinces different kinetic behavior as compared with TiO_2 in the presence of MB (i.e. blue curves in Figure 3.9A and 9B, respectively). That experimental observation can mainly be attributed to differential adsorption efficiencies of MO and MB onto the surfaces of TiO_2 NPs.[74] Specifically, MO, an anionic dye, preferentially and more efficiently adsorbs onto the TiO_2 surface through favorable electrostatic interactions as compared with MB, a cationic dye, thereby resulting in a more effective photocatalytic reaction of TiO_2 NPs with MO as compared with MB.

Moreover, both reactions (i.e. for Cu and Ni-incorporated TiO_2 composites) were calculated to be first-order reactions, following the $\ln(C_0/C)$ vs. irradiation time plots (Figure 3.10 A and B, respectively), from whence we were able to derive associated reaction rate constants (Table 2.1). Specifically, the kinetics are governed by the equation $\ln(C_0/C) = kt$ wherein C_0 is the initial dye concentration and C represents the concentration of either (i) MB for Ni or of (ii) MO for Cu at a given reaction time 't'. The reaction rate constant, 'k', is derived from the slopes of the 'best' fit lines. From our analysis, we were able to calculate the first-order reaction rate constants for dye photodegradation reactions, involving Cu-TiO_2 and Ni-TiO_2 composites, to be 0.0358 and 0.0077 min^{-1}, respectively. Indeed, the rate constants were computed to be 3.6×10^{-2} min^{-1} for Cu NW-TiO_2 and 7.7×10^{-3} min^{-1} Ni NW-TiO_2 heterostructures, respectively, suggestive of a faster degradation potential as compared with either bare TiO_2 NPs or analogous heterostructures (i.e. 4.2×10^{-3} min^{-1} for Cu-TiO_2 composites) previously reported.[72] Overall, we note herein that when a metal nanowire (i.e. Cu & Ni) is bound in combination with TiO_2, such a composite evinces greater photocatalytic performance and activity as compared with as-prepared TiO_2 nanoparticles.

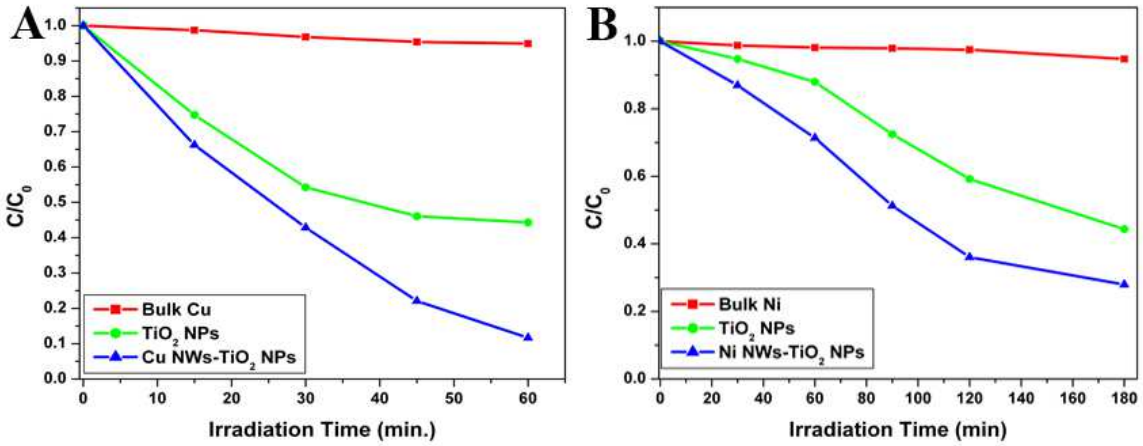

Figure 3.9. Photocatalytic activities of composites of (A) TiO_2 coupled with Cu NWs for the degradation of Methyl Orange as well as of (B) TiO_2 coupled with Ni NWs for Methylene Blue degradation. Analogous, comparative photodegradation data with control samples consisting of (i) bulk metal (i.e. Cu and Ni) and (ii) TiO_2 NPs are also shown. Reprinted with permission from Ref. 53. Copyright 2014 American Chemical Society.

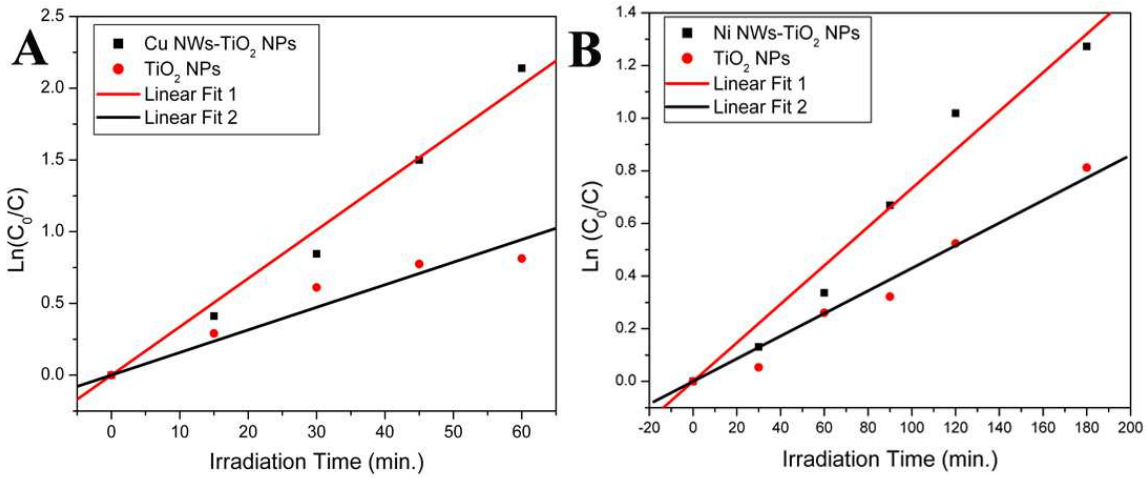

Figure 3.10. First order linear fits of the **(A)** photodegradation of MO in the presence of Cu NW-TiO_2 NP heterostructures as well as of bare TiO_2 NPs as a function of irradiation time. **(B)** Photodegradation of MB in the presence of Ni NW-TiO_2 NP heterostructures as well as TiO_2 NPs as a function of irradiation time. Supplemental Information image reprinted with permission from Ref. 53. Copyright 2014 American Chemical Society.

	Sample	k (min^{-1})	R^2
Data for First-Order Reactions	Cu-TiO_2 heterostructures (Figure 3.10A)	0.036	0.9878
	TiO_2 NPs (Figure 3.10A)	0.0158	0.9634
	Ni-TiO_2 heterostructures (Figure 3.10B)	0.0077	0.9716
	TiO_2 NPs (Figure 3.10B)	0.0043	0.9918

Table 3.1. Table of calculated '*k*' values for metal nanowire-metal oxide composite and corresponding control samples from the slopes of the logarithmic concentration versus irradiation time plots, assuming first-order kinetics. Supplemental information image reprinted with permission from Ref. 53. Copyright 2014 American Chemical Society.

3.3. Reaction Parameters

3.3.1. Metal NWs Summary

In order to induce Cu/Ni nanowire growth, a full summary of all reactions used to generate as-prepared Cu/Ni nanowires, including an accompanying description of the results of a systematic parameter variation, is described in Tables 2.2 & 2.3 and Figures 3.11 through 3.16 inclusively. Specifically, reaction times were varied from 15 min to 4 hours, wherein it was found that the minimum time needed to produce homogeneous and smooth nanowires was ~2 hours. Shorter time periods yielded short, partially filled wires likely due to the finite diffusion rates of the precursor solutions within the template pores (Figure 3.11).

Copper Nanowires							
#	*Cu Conc.* *	*Reducing Agent*	*Solvent*	*Template Pore Size*	*Length*	*Width*	*Description of Results*
1	50 mM	$NaBH_4$	EtOH	**(A)**50 nm	*1.6* ± 0.27 μm	65 ± 12 nm	Long partially filled wires
				(B)200 nm	0.9 ± 0.2 μm	184 ± 25 nm	Fragmented nanowires
2	200 mM	$NaBH_4$	EtOH	50 nm	n/a	n/a	No wires produced
3	50 mM	$NaBH_4$/ HCl	EtOH : H_2O**	50 nm	3.2 ± 1.9 μm	58 ± 18 nm	Longer and more filled nanowires
4	50 mM	$NaBH_4$/ HCl	H_2O	50 nm	n/a	n/a	No wires produced
5	**50 mM : 75 mM (of reducing agent)**	**$NaBH_4$/ HCl**	**H_2O**	**50 nm**	**1.5 ± 0.92 μm**	**92 ± 15 nm**	**Filled nanowires**
6	**50 mM**	**$NaBH_4$/ NaOH**	**H_2O**	**50 nm**	**2 ± 0.76 μm**	**85 ± 27 nm**	**Filled nanowires**
7	50 mM	Hydrazine	EtOH	50 nm	n/a	n/a	Template decom-posed
8	Various concen-trations	Dimethyl-amine-borane	EtOH	50 nm	n/a	n/a	No nanowires formed

Table 3.2. Summary of reactions used to generate as-prepared Cu nanowires, subsequently isolated after systematic parameter variation. The results of sample # 5 and 6, highlighted in bold, consisted of solid, filled nanowires. Supplemental information table reprinted with permission from Ref. 53. Copyright 2014 American Chemical Society.

*Note: All NWs were prepared using copper chloride ($CuCl_2$) as the copper-containing precursor. The molar ratio of precursor to reducing agent was 1: 1, unless otherwise noted. **$CuCl_2$ was dispersed in Ethanol as well as in $NaBH_4$/HCl, solubilized in H_2O.

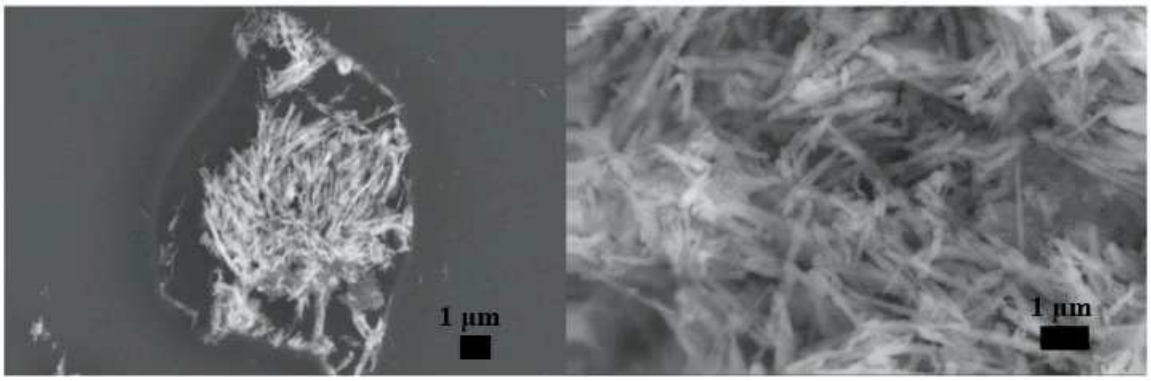

Figure 3.11. SEM images of as-synthesized Cu NWs obtained using 50 mM $NaBH_4$ and 50 mM $CuCl_2$ with 50 nm template pores. Results of sample #1A (See Table 2.2). Supplemental information image reprinted with permission from Ref. 53. Copyright 2014 American Chemical Society.

3.3.2. Under Basic Conditions

Unlike the case for Co nanoparticles, we observed that the Cu nanowires form upon reaction with $NaBH_4$ instead of the boride, as confirmed by the absence of the boron Kα emission peak from EDS spectra for both the ~90 nm and the ~200 nm wires, respectively (Figures 3.2 & 3.3). This observation may be possibly attributed to the more negative redox potential of Co.[76] In addition to Cu's evident reactivity with the reducing agent, we note that the role of the NaOH is to adjust the pH as well as to enhance the reduction process in water by generating metal hydroxides within the template pores.[3, 4, 77] Consequently, we expect that the NW growth can be rationalized in terms of redox reactions, given in Equations (3.1) and (3.2) under basic conditions at room temperature.[78, 79]

$$Cu^{2+} + 2\ OH^- \rightarrow Cu(OH)_2 \qquad (3.1)$$

$$4\ Cu(OH)_2 + BH^-_4 \rightarrow 4\ Cu + B(OH)^-_4 + 4\ H_2O \qquad (3.2)$$

The use of NaOH to aid in the reduction of metals is not entirely new, as metal nanoparticles such as bimetallic Pt-Ni as well as elemental Co, Cu, Fe, and Ni have been prepared under these types of conditions.[80] However, these reaction typically require the presence of

surfactants/polymers as well as consistent stirring.[80, 81] As a result, our devised method reported herein requires neither surfactants nor stirring but rather a template and a minimum reaction duration of ~2 hours to prepare uniform nanorods.

3.3.3. Under Acidic Conditions

Additional experiments were conducted under acidic conditions. In a typical example, 50 mM of HCl solution was prepared separately in water, and then added to the $NaBH_4$ solution (in water) in one side arm with 50 mM $CuCl_2$ precursor solution on the other half cell of the U-tube. HCl was used, because it is known to enhance the hydride generation associated with $NaBH_4$, and as a result, may help to increase the rate of the reaction.[82] Nanowire growth did in fact take place.

From the XRD data, it was determined that elemental crystalline copper (Cu^0) is present within the nanowires, as the observed peaks are in good agreement with the JCPDS #08-0836 database standard. However, there are also additional peaks (2θ values of ~36° and ~62°) that correspond to the cuprous oxide (Cu_2O), i.e. JCPDS #05-0667 database standard (Figure 3.12B). UV-visible analysis also confirmed the presence of Cu_2O at a peak location of 378 nm,[58] which is distinctive from the corresponding peak associated with Cu^0 nanowires, analogously located at ~607 nm (Figure 3.12D). The Cu^0 nanowire peak is slightly red shifted from what has been previously found in the literature, but this observation may be potentially due to increased nanowire diameters, possible aggregation effects, as well as to the intrinsically higher aspect ratio of these nanowires.[59, 83] The peak located in the 230-250 nm range may also be attributed to not only amorphous copper chloride but also the $CuCl_2$ solution itself.

Due to the overwhelming presence of Cu_2O, a second reduction step from previous literature,[84] had to be incorporated in order to generate elemental Cu NWs. Based on HR-TEM data, after an additional reduction purification process, the nanowires displayed a *d*-spacing of

~2.23 Å, which is representative of elemental Cu (Figure 3.13B). Unfortunately, this process also yielded highly fragmented nanowires (lower left inset of Figure 3.13B).

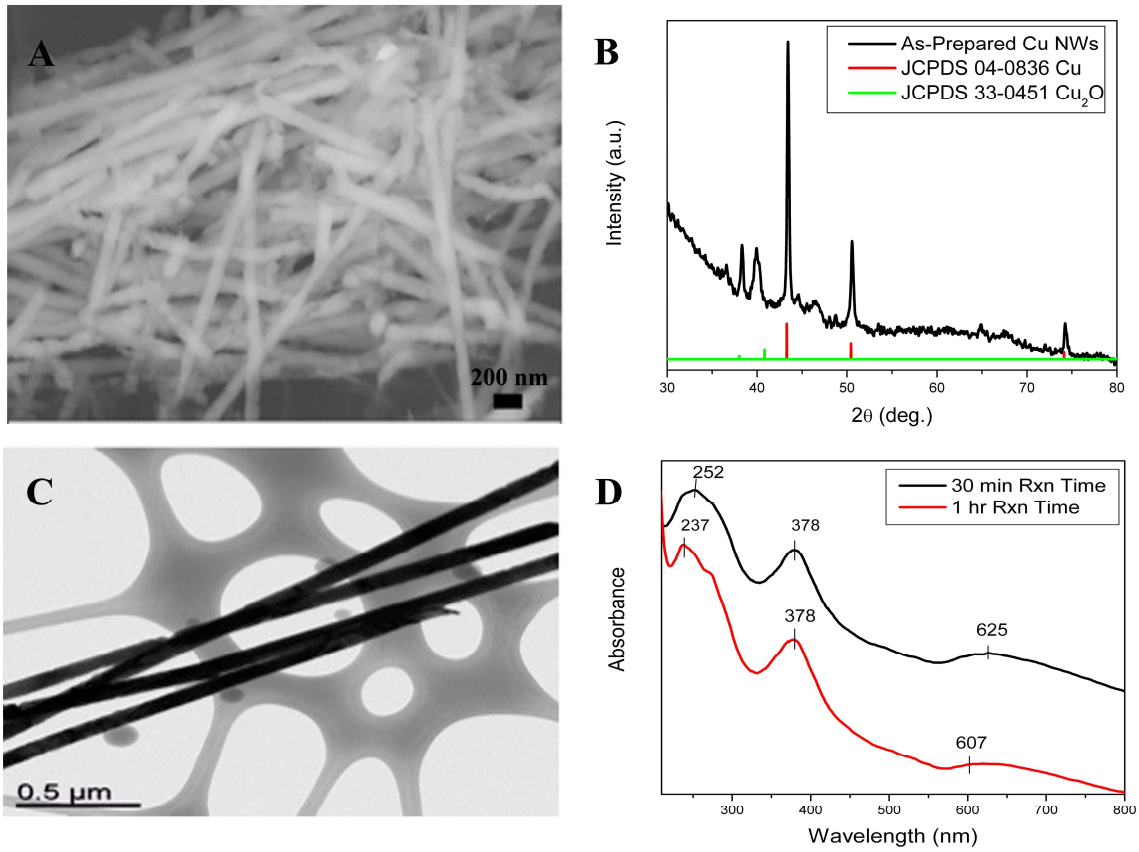

Figure 3.12. SEM image (A), XRD pattern (B), TEM image (C), and UV-visible spectra (D) of as-prepared Cu NWs, synthesized under acidic conditions (i.e. 50 mM : 50 mM concentrations of $CuCl_2$: $NaBH_4$ in 50 mM HCl). Results of sample #6. Supplemental information image reprinted with permission from Ref. 53. Copyright 2014 American Chemical Society.

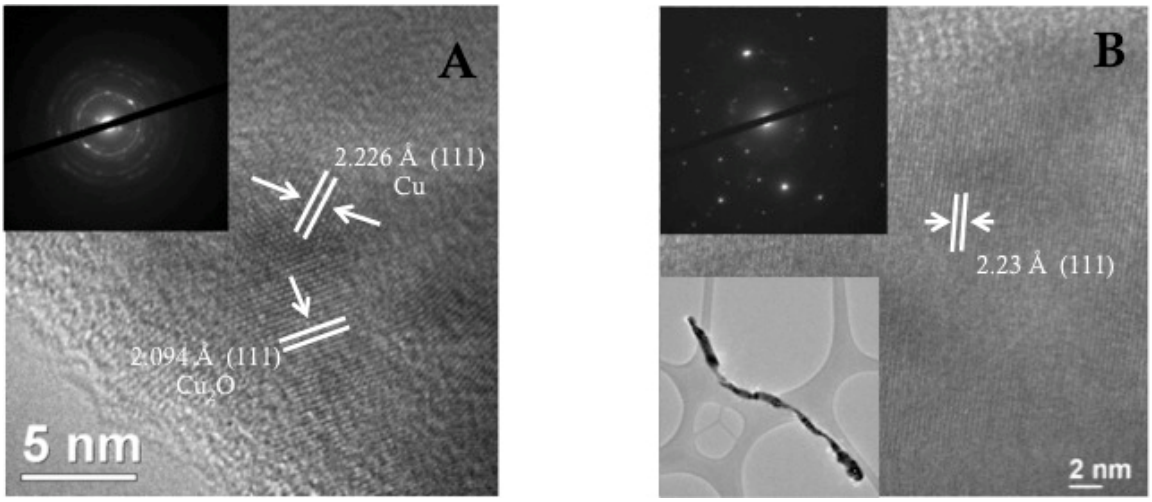

Figure 3.13. Results of sample #6 after the second reduction step. Before (A) and after (B) the reduction step, observed using HR-TEM analysis. Supplemental information image reprinted with permission from Ref. 53. Copyright 2014 American Chemical Society.

3.3.4 Varying the Reducing Agent

As mentioned previously, based upon the standard potentials of $NaBH_4$ ($E° = -1.24$ V) with respect to Cu ($E° = 0.34$ V) and Ni ($E° = -0.257$ V), a spontaneous reduction reaction would occur under ambient conditions, as confirmed by the formation of as-prepared elemental nanowires. Nonetheless, other reducing agents have also been employed for our nanowire synthesis, such as hydrazine (N_2H_4, $E° = -0.33$ V) and dimethylamine borane ($(CH_3)_2NH{\cdot}BH_3$, DMAB). In a typical reaction, ethanolic solutions of hydrazine and $CuCl_2$ were added simultaneously. Instantaneously, the solutions turned cloudy, and then, a darker hued impurity started to form. As a result, the reaction was stopped, the template was removed, and it was found that the hydrazine had been dissolving the template itself, thereby forming black copper particles, whereas the creamy residue likely represented the remnant template (Figure 3.14). Regarding DMAB, its reducing solution seemed to migrate and diffuse through the template pores slightly faster than the corresponding $CuCl_2$ solution. This observation indicated that the local DMAB concentration was likely reduced to be less than 50 mM, which might conceivably have lowered the nanowire yield as a result. Not surprisingly, no crystalline nanowires were produced with

DMAB. From our study of the use of different reducing agents, we noted that $NaBH_4$ is an excellent reducing agent of choice for our template-based co-precipitation method under ambient conditions.

Figure 3.14. Image of as-prepared Cu NWs formed using a U-tube double diffusion device under ambient conditions. Nanowires were prepared using $CuCl_2$ in EtOH and a reducing agent, i.e. hydrazine, dispersed in EtOH. Supplemental information image reprinted with permission from Ref. 53. Copyright 2014 American Chemical Society.

Nickel Nanowires							
#	*Nickel Conc.**	*Reducing Agent*	*Solvent*	*Template Pore Size*	*Average Length*	*Average Width*	*Description of Results*
A	25 mM	$NaBH_4$	EtOH	50 nm	N/A	N/A	No wires produced
B	50 mM	$NaBH_4$	EtOH	50 nm	N/A	N/A	No wires produced
C	75 mM	$NaBH_4$	EtOH	50 nm	1.8 ± 0.7 μm	89 ± 10 nm	Filled nanowires
D	**100 mM**	**$NaBH_4$**	**EtOH**	**50 nm**	**2.4 ± 1.1 μm**	**92 ± 10 nm**	**Filled nanowires**
E	25 mM	$NaBH_4$	EtOH	200 nm	1.2 ± 0.7 μm	209 ± 17 nm	Hollow Nanotubes
F	**50 mM**	**$NaBH_4$**	**EtOH**	**200 nm**	**4.7 ± 1.9 μm**	**215 ± 22 nm**	**Filled nanowires & some nanotubes**
G	75 mM	$NaBH_4$	EtOH	200 nm	N/A	N/A	No wires produced
H	100 mM	$NaBH_4$	EtOH	200 nm	N/A	N/A	No wires produced

Table 3.3. Summary of reactions used to generate as-prepared Ni nanowires, subsequently isolated after systematic parameter variation. Samples D and F, highlighted in bold, yielded the best results. Supplemental Information table reprinted with permission from Ref. 53. Copyright 2014 American Chemical Society.

*Note: All NWs were prepared using nickel chloride ($NiCl_2$) as the nickel-containing precursor. The molar concentration of the sodium borohydride reducing agent precursor was maintained at 50 mM, unless otherwise specified.

3.3.5. Ni NWs

In the context of reactions using templates possessing 50 nm pore sizes, with the reducing agent concentration set at a relatively constant concentration of 0.05 M, nickel precursor concentrations of 0.025 M and 0.05 M produced no Ni NWs, presumably due to a lack of a sufficient probability of necessary nucleation events within the template pores within a set time period. As a result, slightly higher, i.e. 0.075 M and 0.1 M, Ni concentrations were used and did in fact produce uniform, ~50 nm diameter wires (Figure 3.4). A reasonable reaction mechanism

to explain our observations is described as follows, in Equations (3.3) and (3.4), under basic conditions:

$$Ni^{2+} + 2\ OH^- \rightarrow Ni(OH)_2 \quad (3.3)$$

$$4\ Ni(OH)_2 + BH^-_4 \rightarrow 4\ Ni + B(OH)^-_4 + 4\ H_2O \quad (3.4)$$

As for reactions within the larger 200 nm-diameter template pores giving rise to ~200 nm diameter wires (Figure 3.5), the previously mentioned Ni concentrations (i.e. 0.075 M (Figure 3.15) and 0.1 M, respectively) were also tested, but these reaction conditions yielded either hollow nanotubes or essentially nothing of interest, i.e. no nanowires. As a result, the $NaBH_4$ concentration was maintained at 0.05 M, while the metal precursor concentration was systematically varied from 0.025 M to 0.1 M. We noted that as the reducing agent concentration was increased from 0.025 M (Figure 3.16) to 0.05 M, uniform filled wires were more likely to form. This observation may possibly be due to increasingly favorable intramolecular interactions between reagent molecules (i.e. homogeneous nucleation) versus less favorable intermolecular interactions with the pore walls (i.e. heterogeneous nucleation), as the reducing agent concentration increases.[45] However, as the reducing agent concentration was increased even further (i.e. 0.075 and 0.1 M), no wires were produced in these larger sized template membranes, suggesting a narrow parameter window for reaction optimization.

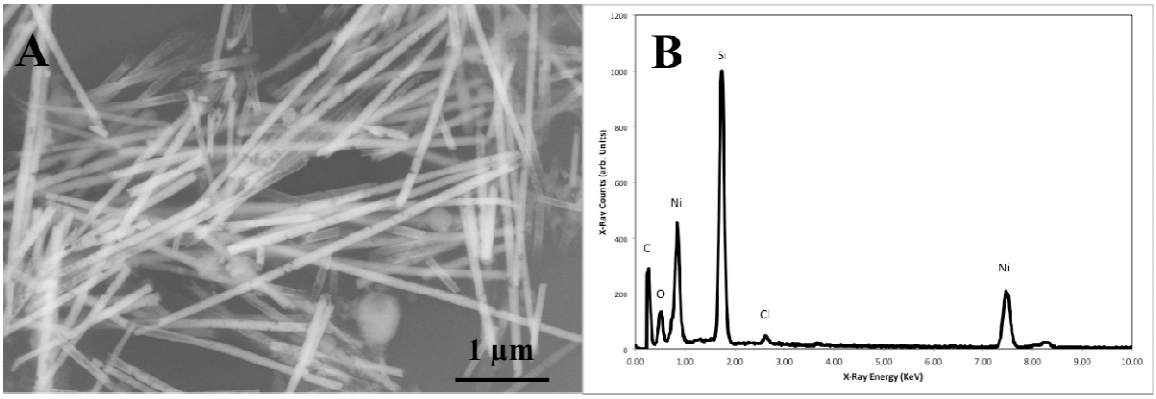

Figure 3.15. SEM image (A) and EDS analysis (B) of as-synthesized Ni NWs obtained using 50 mM $NaBH_4$ and 75 mM of $NiCl_2$ in ethanol (EtOH) with 50 nm template pores. Results of sample C. Supplemental Information image reprinted with permission from Ref. 53. Copyright 2014 American Chemical Society.

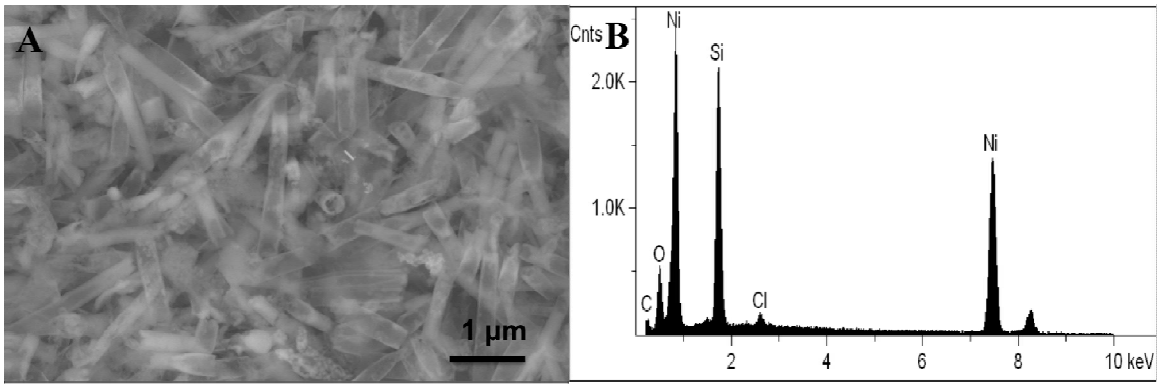

Figure 3.16. SEM image (A) and EDS analysis (B) of as-synthesized Ni NWs obtained using 50 mM $NaBH_4$ and 25 mM of $NiCl_2$ in ethanol (EtOH) with 200 nm template pores. Results of sample E. Supplemental Information image reprinted with permission from Ref. 53. Copyright 2014 American Chemical Society.

3.4. Plausible Growth Mechanism

Plausible growth mechanisms for the metal nanowires and nanotubes are shown in Figure 3.17. Based upon our previous work,[48] we believe that the growth of the NWs within the PC templates follows a two-step process. In the *first step*, the precursor and the reducing agent

diffuse into the pore space and inevitably, the diffusion fronts intersect, resulting in the reduction of the metallic precursor and formation of metal seed nuclei. This initial rapid reduction followed by a nucleation process yields both a short polycrystalline NW segment within the template pore and a thin layer of metallic material on the outer surfaces of the template within the reducing agent half-cell. In fact, the formation of the metallic layer on the surface of the template facing towards and thereby exposed to the reducing agent half-cell can be observed visually within the initial stages of the reaction. In the case of Cu, we noted a red color, whereas for Ni, it was black in hue. In the *second step*, these isolated, disparate nucleation sites grow by extension throughout the porous template network. In a homogeneous nucleation scenario, as-formed metal nuclei preferentially self-assemble with each other into either filled wire-like or rod-like motifs, whereas in the analogous heterogeneous nucleation scenario, preferred confinement of growth along the pore walls themselves can therefore lead to the generation of primarily hollow tube-like motifs upon the elongation and self-assembly of the as-formed nuclei.

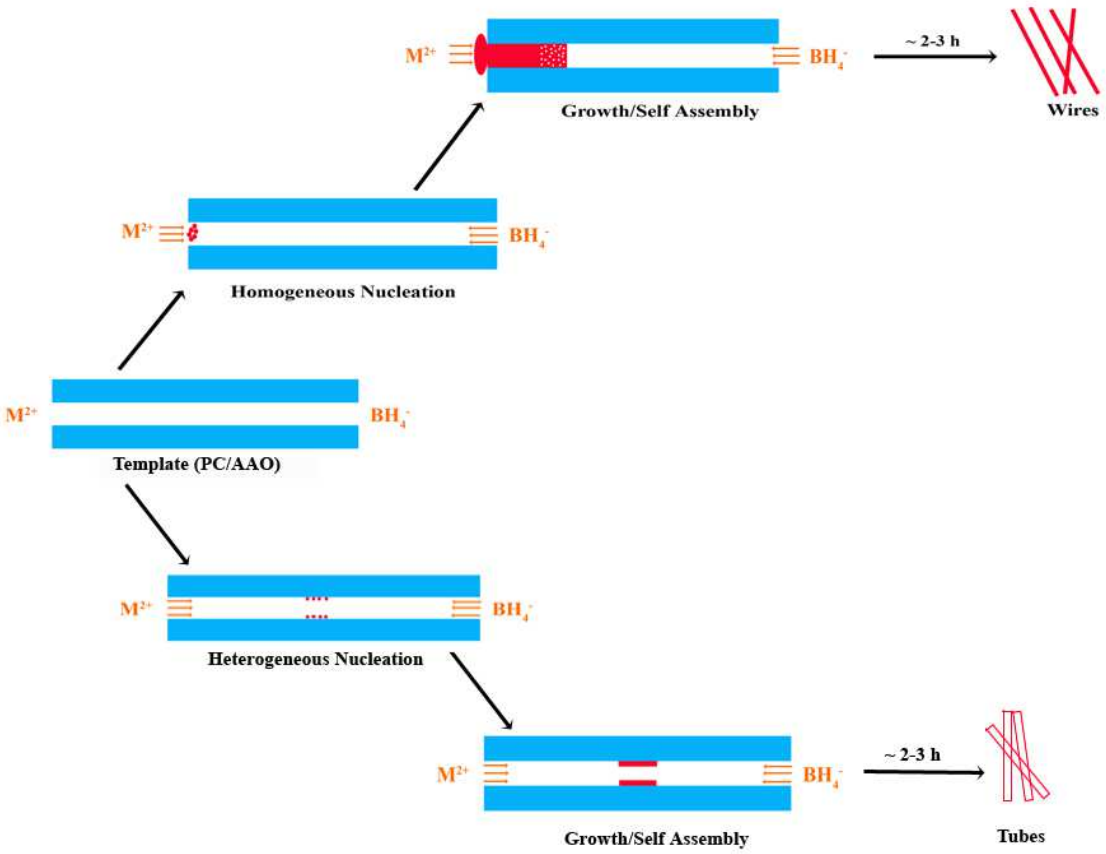

Figure 3.17. Plausible growth mechanism for Cu and Ni Nanowires (NWs) and Nanotubes (NTs) under room temperature conditions. Reprinted with permission from Ref. 53. Copyright 2014 American Chemical Society.

3.5 Conclusions

Our lab has reported on a reliable, reproducible, and seedless growth under ambient conditions using a solution-based template methodology of difficult-to-isolate, crystalline, homogeneous elemental Cu and Ni nanowires with a plausible growth mechanism. Moreover, we have fulfilled some of the requirements of various green chemistry protocols, such as the use of relatively mild chemicals (*i.e.* metal chlorides & $NaBH_4$), the incorporation of a non-hazardous and energy efficient synthetic technique (*i.e.* U-tube double diffusion), as well as the utilization of aqueous solvents (*i.e.* water). The porous polycarbonate templates we have used have enabled us

not only to control size but also to direct nanowire growth and morphology within the membrane channels. These nanowires have been extensively characterized using complementary optical spectroscopy, electron microscopy, as well as diffraction techniques. Moreover, the degree of oxidation of these nanowires was probed both qualitatively and quantitatively using both EDX and EELS.

Additionally, parameters such as the reaction time, solvent, pH, and reducing agents were employed and confirmed that the reaction time must be at least 2 hours and that solvents such as water and ethanol may be used. As for pH, for Cu nanowires, under basic conditions, homogeneous nanowires formed. By contrast, under acidic conditions a second reduction step was needed to remove the presence of Cu_2O within the nanowires. Lastly, by comparison with analogous reducing agents, DMAB and N_2H_4, $NaBH_4$ remained the best for nanowire growth within the PC membrane.

Moreover, an enhanced photocatalytic activity of metallic Cu and Ni nanowires (deliberately coupled with TiO_2) was observed as compared with both bulk and commercial TiO_2 nanoparticulate control samples in the presence of two different and distinctive dyes, namely Methyl Orange and Methylene Blue, respectively. Both Cu-TiO_2 and Ni-TiO_2 composites, incorporating metallic NWs, gave rise to first order rate reactions for their respective dyes, implying comparable behavior with what had been previously observed in the literature. Overall, these functional improvements in performance could be primarily ascribed to active surface area and electronic enhancement effects associated with the composites as compared with TiO_2 itself.

3.6 Future Work

3.6.1 Metal-catalyzed Organic Reactions

Metal-mediated reactions have been recognized as powerful tools in several industrial processes such as phenol plymerization and Glaser-Hay alkyne coupling, to name a few.[85] Particularly, Cu-based catalysts remain rich in chemistry as it can easily act through one-electron or two-electron processes due to its different oxidation states (Cu, Cu^{+}, Cu^{2+}, and Cu^{3+}).[85] As a result, Cu catalysts enhance redox chemistry in a highly site-selective and stereoselective manner on either simple or complex molecules (i.e. hightly functionalized).[86] Therefore, as an extension of our work, we plan to observe these as-synthesized Cu NWs as they catalyze various oxidation reactions such as benzylic oxidation, oxidation of hydrocarbons and alkanes to name a few. Moreover, these Cu NWs will also be applied to catalyze the metal-mediated amination reaction.

3.6.2 Fuel Cell Application

As mentioned in the introduction, Cu has been extensively incorporated as catalysts for proton exchange membrane fuel cell (PEMFCs) reactions such as MOR and oxygen reduction reaction (ORR), due to its high catalytic activity and low cost.[87, 88] Specifically, PEMFCs contain electrolyte that allows for protons to exchange from the anode (i.e. MOR reaction) to the cathode (i.e. ORR reaction) of the cell. These processes are further described in the following reaction equations (3.5-3.7):

Anode: $H_2 \rightarrow 2H^+ + 2e^-$	E^0 (V) = 0.00	(3.5)
Cathode: $1/2\ O_2 + 2H^+ + 2e^- \rightarrow 2\ H_2O$	E^0 (V) = 0.1.229	(3.6)
Overall: $H_2 + 1/2\ O_2 \rightarrow H_2O$ + Energy	E^0 (V) = 0.1.229	(3.7)

Though elements such as Cu have been immobilized onto Pt in order to enhance these reactions, most of these nanomaterials have been produced using high-energy protocols such as electrodeposition, high temperature wet solution methods, and heat treatments, to name a few.[89-91]

In using an ambient, surfactantless U-tube technique to produce Cu/Ni nanowires, the amount of expensive metals such as Pt can ultimately be reduced. The goal herein, is to utilize the U-tube method to synthesize M (M=Cu, Ni, Co, and Fe) NWs, and subsequently deposit Pt NPs to create heterostructured motifs and tested for their applications as catalysts for the ORR fuel cell reaction.[92] Moreover, using the U-tube method may also aid in the generation of alloyed PtM NWs materials for these reactions as well. The goal here would be to investigate whether either a core shell configuration or an alloyed composition would generate the highest activity. Once the activities are observed, the aim would be to understand the underlying mechanistic interactions that are responsible for enhancing the activity.

Currently, alkaline fuel cells (AFCs) have also gained popularity they do not display the water management issues typically associated with the use of PEMFCs.[93, 94] As a result, of alkaline electrolyte use, some major advantages include: 1) an increase in ORR activity, due to the kinetically favored and much faster reduction of oxygen to OH^- as compared with its acidic equivalent, 2) the circumvention of the corrosive acidic environment, and 3) the generation of comparable overall current densities to that of their acidic counterparts.[94-96]

In AFCs, electricity can be generated through two reactions: the ORR at the cathode and the hydrogen oxidation reaction (HOR) at the anode through the following equations 1 & 2.

Overall: $2H_2O + 2e^- \rightarrow H_2 + 4OH^-$ (3.8)

Anode: $H_2 + 2OH^- + 2e^- \rightarrow 2H_2O$ (3.9)

Cathode: $O_2 + 2H_2O + 4e^- \rightarrow 4OH^-$ (3.10)

By analogy with PEMFCs, the use of AFCs broadens the scope to potentially more plentiful and less expensive metals that could be applied as catalysts. Metals such as Ni and Cu provide for cost effective and highly active catalysts to help replace expensive metals like Pt.

However, for the HOR reaction, Pt catalysts are generally not as good in alkaline electrolyte by comparison with their acidic counterparts. Specifically, Pt catalysts in alkaline media normally suffer from decreased kinetics with almost 2 orders of magnitude slower rates of reaction than in acid.[95, 96]

Though Pt coupled with Ru, Au, Ag, and Cu have been tested for HOR, there has yet to be a systematic study utilizing only cost efficient metals such as Cu (as a reference), Ni, Co, and Fe NWs.[97-100] Herein, the goal would be to again correlate the composition of either a core shell or alloyed motif of PtM NWs with their respective HOR activity in AFCs as well as to understand the underlying effects that influence their activities.

3.7 References

1. M. A. Mahmoud, R. Narayanan and M. A. El-Sayed, *Acc Chem Res*, 2013, 46, 1795-1805.
2. A. I. Henry, J. M. Bingham, E. Ringe, L. D. Marks, G. C. Schatz and R. P. Van Duyne, *Journal of Physical Chemistry C*, 2011, 115, 9291-9305.
3. T. M. D. Dang, T. T. T. Le, E. Fribourg-Blanc and M. C. Dang, *Advances in Natural Sciences: Nanoscience and Nanotechnology*, 2011, 2, 150091-150096.
4. Y. Wang, A. V. Biradar, G. Wang, K. K. Sharma, C. Duncan, S. Rangan and T. Asefa, *Chemistry - A European Journal*, 2010, 16, 10735-107343.
5. S. Kuld, M. Thorhauge, H. Falsig, C. F. Elkjaer, S. Helveg, I. Chorkendorff and J. Sehested, *Science*, 2016, 352, 969-974.
6. S. D. Senanayake, P. J. Ramirez, I. Waluyo, S. Kundu, K. Mudiyanselage, Z. Y. Liu, Z. Liu, S. Axnanda, D. J. Stacchiola, J. Evans and J. A. Rodriguez, *Journal of Physical Chemistry C*, 2016, 120, 1778-1784.
7. M. Zhu, T. C. R. Rocha, T. Lunkenbein, A. Knop-Gericke, R. Schlögl and I. E. Wachs, *ACS Catalysis*, 2016, DOI: 10.1021/acscatal.6b00698, 4455-4464.
8. Y. Cao, Y. Yang, Y. Shan and Z. Huang, *ACS Appl Mater Interfaces*, 2016, 8, 5998-6003.
9. A. R. Rathmell, S. M. Bergin, Y.-L. Hua, Z.-Y. Li and B. J. Wiley, *Advanced Materials*, 2010, 22, 3558-3563.
10. H. Wu, D. Kong, Z. Ruan, P.-C. Hsu, S. Wang, Z. Yu, T. J. Carney, L. F. Hu, S. an and Y. Cui, *Nature Nanotechnology*, 2013, 8, 421-425.
11. Y. Zhao, Y. Zhang, Y. Li, Z. He and Z. Yan, *RSC Advances*, 2012, 2, 11544-11551.
12. M.-G. Kang, H. J. Park, S. H. Ahn and L. J. Guo, *Sol. Energy Mater. Sol. Cells*, 2010, 94, 1179-1184.
13. S. Ye, A. R. Rathmell, I. E. Stewart, Y.-C. Ha, A. R. Wilson, Z. Chen, *Chemical Communications*, 2014, 50, 2562-2564.
14. O. Lupan, T. Pauporte, B. Viana and P. Aschehoug, *Electrochim. Acta*, 2011, 56, 10543-10549.
15. I. Halaciuga, S. LaPlante and D. Goia, *Rapid Communications*, 2009, 24, 3237-3240.
16. Y. Zhao, Y. Zhang, Y. Li, Z. He and Z. Yan, *Royal Society of Chemistry Advances*, 2012, 2, 11544-11551.
17. M. Cempel and G. Nikel, *Polish Journal of Environmental Studies*, 2006, 15, 375-382.
18. S. B. Sapkal, K. F. Shelke, B. B. Shingate and M. S. Shingare, *Bulletin of the Korean Chemical Society*, 2010, 31, 351-354.
19. D. Ai and S. Kang, *Materials Transactions*, 2006, 47, 1056-2059.
20. A. K. Shukla, S. Venugopalan and B. Hariprakash, *Journal of Power Sources*, 2001, 100, 125-148.
21. V. Pokropivny, R. Lohmus, I. Hussainova, A. Pokropivny and S. Vlassov, *Introduction to Nanomaterials and Nanotechnology*, Tartu University Press, Ukraine, 2007.
22. K. Hasegawa, M. Ohnishi, M. Oshitani, K. Takeshima, Y. Matsumaru and K. Tamura, *Zeitschrift für Physikalische Chemie*, 1994, 183, 325-331.
23. M. N. Ou, T. J. Yang, S. R. Harutyunyan, Y. Y. Chen and C. D. Chen, *Applied Physics Letters*, 2008, 92, 63101-63104.
24. H.-W. Liang, J.-W. Liu, H.-S. Qian and S.-H. Yu, *Acc Chem Res*, 2013, 46, 1450-1461.
25. Q.-C. Chen, *Jingxi Huagong*, 2005, 22, 417-419.
26. A. Khalil, R. Hashaikeh and M. Jouiad, *J. Mater. Sci.*, 2014, 49, 3052-3065.

27. X.-h. Wang, G. Chen, C.-y. Li, L. Yang, H. Cao and W.-m. Zhou, *Cailiao Gongcheng*, 2010, 20-23.
28. X. Sun and F. Xu, *Adv. Mater. Res. (Durnten-Zurich, Switz.)*, 2011, 335-336, 429-432.
29. X. Liu, X. She, G. Song, X. Sun and S. Wang, *Dianzi Yuanjian Yu Cailiao*, 2008, 27, 51-53.
30. L. Qingming, Z. Debi, Y. Yamamoto, R. Ichino and M. Okido, *Transactions of Nonferrous Metals Society of China*, 2012, 22, 117-123.
31. H. Choi and S.-H. Park, *Journal of American Chemistry Society*, 2004, 126, 6248-6249.
32. G. Yue, Q. Xu, G. Meng, X. He, F. Han and L. Zhang, *Journal of Alloys and Compounds*, 2009, 477, L30-L34.
33. N. V. Surmawar, S. R. Thakare and N. T. Khaty, *International Journal of Green Nanotechnology*, 2011, 3, 302-308.
34. X. Li, Y. Wang, G. Song, X. She, Z. Peng, S. Wang and J. Li, *J. Nanosci. Nanotechnol.*, 2010, 10, 4363-4367.
35. Y.-Q Liu, M. Zheng, F.-X. Wang, and G.-B. Pan, *RSC Advances*, 2012, 2, 11235-11237.
36. X. Guo, F. Zheng, M. Guo, M. Zhang and K.-C. Chou, *Rare Metals (Beijing, China)*, 2013, 32, 179-185.
37. Y. Zhao, Y. Zhang, Y. Li and Z. Yan, *New Journal of Chemistry*, 2012, 36, 130-138.
38. A. Roy, V. Srinivas, S. Ram, J. A. De Toro and U. Mizutani, *Physical Review B*, 2005, 71, 188443-(1-10).
39. M. R. Knecht, J. C. Garcia-Martinez and R. M. Crooks, *Chemical Materials*, 2006, 18, 5039-5044.
40. Y. Chang, M. L. Lye and H. C. Zeng, *Langmuir*, 2005, 21, 3746-3748.
41. A. R. Rathmell and B. J. Wiley, *Advanced Materials*, 2011, 23, 4798-4803.
42. D. Zhang, R. Wang, M. Wen, D. Weng, X. Cui, J. Sun, H. Li and Y. Lu, *Journal of American Chemical Society*, 2012, 134, 14283-14286.
43. K. R. Krishnadas, P. R. Sajanlal and T. Pradeep, *Journal of Physical Chemistry C*, 2011, 115, 4483-4490.
44. F. Zhang, Y. Yiu, M. Aronson and S. Wong, *Journal of Physical Chemistry C*, 2008, 38, 14816-14824.
45. H. Zhou and S. Wong, *American Chemistry Society Nano*, 2008, 2, 944-958.
46. C. Koenigsmann, E. Sutter, T. A. Chiesa, R. R. Adzic and S. S. Wong, *Nano Letters*, 2012, 12, 2013-2020.
47. C. Koenigsmann, Z. Tan, H. Peng, E. Sutter, J. Jacobskind and S. Wong, *Israel Journal of Chemistry*, 2012, 52, 1090-1103.
48. C. Koenigsmann, A. Santulli, E. Sutter and S. Wong, *American Chemistry Society Nano*, 2011, 5, 7471-7487.
49. F. Zhang and S. S. Wong, *Chemistry of Materials*, 2009, 21, 4541-4554.
50. F. Zhang and S. S. Wong, *American Chemistry Society Nano*, 2010, 4, 99-112.
51. Y. Mao, F. Zhang and S. S. Wong, *Advanced Materials*, 2006, 18, 1895-1899.
52. H. Zhou, W.-p. Zhou, R. R. Adzic and S. S. Wong, *Journal of Physical Chemistry C*, 2009, 113, 5460-5466.
53. C. S. Lewis, L. Wang, H. Q. Liu, J. K. Han and S. S. Wong, *Crystal Growth & Design*, 2014, 14, 3825-3838.
54. D. Bu and H. Zhuang, *Appl. Surf. Sci.*, 2013, 265, 677-685.
55. P. K. Khanna, S. Gaikwad, P. V. Adhyapak, N. Singh and R. Marimuthu, *Materials Letters*, 2007, 61, 4711-4714.

56. H. Ikeda, Y. Qi, T. Cagin, K. Samwer, W. L. Johnson and W. A. Goddard, *Phys Rev Lett*, 1999, 82, 2900-2903.
57. K. Rajagopal, *Engineering Physics*, PHI Learning Private Limited, New Dehli, Second Edition edn., 2011.
58. M. Salavati-Niasari and F. Davar, *Materials Letters*, 2009, 63, 441-443.
59. J. L. Cuya Huaman, K. Sato, S. Kurita, T. Matsumoto and B. Jeyadevan, *Journal of Materials Chemistry*, 2011, 21, 7062-7069.
60. A. Ghaddar, J. Gieraltowski and F. Gloaguen, *J. Appl. Electrochem.*, 2009, 39, 719-725.
61. P. Pootawang, N. Saito and S. Lee, *Nanotechnology*, 2013, 24, 55604-55613.
62. J.-L. Duan, J. Liu, H.-J. Yao, D. Mo, M.-D. Hou, Y.-M. Sun, Y.-F. Chen and L. Zhang, *Mater. Sci. Eng., B*, 2008, 147, 57-62.
63. M. Vishlaghi, M. Tabriz and O. Moradi, *Materials Research Bulletin*, 2012, 47, 1666-1669.
64. Y. Su, Y. Yang, H. Zhang, Y. Xie, Z. Wu, Y. Jiang, N. Fukata, Y. Bando and Z. L. Wang, *Nanotechnology*, 2013, 24, 295401: 295401-295406.
65. X. H. Wang, J.-G. Li, H. Kamiyama, Y. Moriyoshi and T. Ishigaki, *Journal of Physical Chemistry B*, 2006, 110, 6804-6809.
66. A. Zaleska, *Recent Patents on Engineering*, 2008, 2, 157-164.
67. K.-i. Yamanaka, T. Ohwaki and T. Morikawa, *Journal of Physical Chemistry C*, 2013, 117, 16448-165456.
68. K. Song, J. Zhou, J. Bao and Y. Feng, *Journal of the American Ceramic Society*, 2008, 91, 1369-1371.
69. B. Xin, P. Wang, D. Ding, J. Liu, Z. Ren and H. Fu, *Applied Surface Science*, 2008, 254, 2569-2574.
70. M. Sahu, B. Wu, L. Zhu, C. Jacobson, W.-N. Wang, K. Jones, Y. Goyal, Y. J. Tang and P. Biswas, *Nanotechnology*, 2011, 22, 415704- (415701-415709).
71. G. Mele, R. Del Sole, G. Vasapollo, E. Garcia-Lopez, L. Palmisano and M. Schiavello, *Journal of Catalysis*, 2003, 217, 334-342.
72. Y. Zhang, M. Huang, F. Li, H. Zhao and Z. Wen, *Journal of Materials Science*, 2013, 48, 6728-6736.
73. G. G. Nakhate, V. S. Nikam, K. G. Kanade, S. Arbuj, B. B. Kale and J. O. Baeg, *Materials Chemistry and Physics*, 2010, 124, 976-981.
74. M. Zeng, *Bulletin of the Korean Chemical Society*, 2013, 34, 953-956.
75. M. Kemmell, V. Pore, J. Tupala, M. Ritala and M. Leskela, *Chemistry of Materials*, 2007, 19, 1816-1820.
76. G. N. Glavee, K. J. Klabunde, C. M. Sorensen and G. C. Hadjipanayis, *Langmuir*, 1994, 10, 4726-4730.
77. Z. Ding, W. Wang, S. Z. Wu and J. P. Liu, *Ieee Transactions on Magnetics*, 2015, 51.
78. K. J. Ziegler, R. C. Doty, K. P. Johnston and B. A. Korgel, *Journal of the American Chemical Society*, 2001, 123, 7797-7803.
79. Q. M. Liu, D. B. Zhou, Y. Yamamoto, R. Ichino and M. Okido, *Transactions of Nonferrous Metals Society of China*, 2012, 22, 117-123.
80. A. K. Singh and Q. Xu, *International Journal of Hydrogen Energy*, 2014, 39, 9128-9134.
81. N. Sahiner, S. Butun, O. Ozay and B. Dibek, *Journal of Colloid and Interface Science*, 2012, 373, 122-128.
82. M. B. B. Guerra, R. Carapelli, K. Miranda, A. R. A. Nogueira and E. R. Pereira-Filho, *Analytical Methods*, 2011, 3, 599-605.
83. A. Ghaddar, J. Gieraltowski and F. Gloaguen, *J. Appl. Electrochem.*, 2009, 39, 719-725.

84. W.-r. Lee, Y. S. Lim, S. Kim, J. Jung, Y.-K. Han, S. Yoon, L. Piao and S.-H. Kim, *Journal of Materials Chemistry*, 2011, 21, 6928-6933.
85. S. E. Allen, R. R. Walvoord, R. Padilla-Salinas and M. C. Kozlowski, *Chem Rev*, 2013, 113, 6234-6458.
86. T. Punniyamurthy, S. Velusamy and J. Iqbal, *Chem Rev*, 2005, 105, 2329-2363.
87. Y. Liao, G. Yu, Y. Zhang, T. T. Guo, F. F. Chang and C. J. Zhong, *Journal of Physical Chemistry C*, 2016, 120, 10476-10484.
88. K. W. Lux and K. J. Rodriguez, *Nano Letters*, 2006, 6, 288-295.
89. K. Jayasayee, J. A. R. Van Veen, T. G. Manivasagam, S. Celebi, E. J. M. Hensen and F. A. de Bruijn, *Applied Catalysis B-Environmental*, 2012, 111, 515-526.
90. M. Oezaslan, F. Hasche and P. Strasser, *Polymer Electrolyte Fuel Cells 10, Pts 1 and 2*, 2010, 33, 333-341.
91. X. W. Du, S. P. Luo, H. Y. Du, M. Tang, X. D. Huang and P. K. Shen, *Journal of Materials Chemistry A*, 2016, 4, 1579-1585.
92. M. E. Scofield, H. Q. Liu and S. S. Wong, *Chemical Society Reviews*, 2015, 44, 5836-5860.
93. M. T. Koper, *Nat Chem*, 2013, 5, 255-256.
94. E. Antolini and E. R. Gonzalez, *Journal of Power Sources*, 2010, 195, 3431-3450.
95. J. Durst, A. Siebel, C. Simon, F. Hasche, J. Herranz and H. A. Gasteiger, *Energy & Environmental Science*, 2014, 7, 2255-2260.
96. W. C. Sheng, H. A. Gasteiger and Y. Shao-Horn, *Journal of the Electrochemical Society*, 2010, 157, B1529-B1536.
97. E. G. Mahoney, W. C. Sheng, Y. S. Yan and J. G. G. Chen, *Chemelectrochem*, 2014, 1, 2058-2063.
98. Y. Wang, G. W. Wang, G. W. Li, B. Huang, J. Pan, Q. Liu, J. J. Han, L. Xiao, J. T. Lu and L. Zhuang, *Energy & Environmental Science*, 2015, 8, 177-181.
99. M. A. Montero, M. R. G. de Chialvo and A. C. Chialvo, *International Journal of Hydrogen Energy*, 2011, 36, 3811-3816.
100. S. M. Alia, B. S. Pivovar and Y. S. Yan, *Journal of the American Chemical Society*, 2013, 135, 13473-13478.

Chapter 4 - Correlating Size and Composition-Dependent Effects with Magnetic, Mössbauer, and PDF Measurements in a Family of Catalytically Active Ferrite Nanoparticles and Nanowires

4.1 Introduction

Nanomaterials denote structures with at least one feature size in the range between 1 and 100 nm. As such, these structures have attracted significant research interest, due to their unique size-dependent optical, magnetic, electronic, thermal, and chemical properties as compared with those of the corresponding bulk. Specifically, one-dimensional (1D) nanomaterials, including but not limited to nanowires, nano-whiskers, and nanorods, have generated widespread attention, as they give rise to distinctive chemical and physical properties by comparison with their bulk counterparts.

In particular, 1D nanomaterials can give rise to thermodynamic stability, physiochemical properties, and magnetic properties (i.e. hysteresis and Curie temperature) that are inherently dependent upon the nanowires' length, diameter, inter-wire coupling, and chemical composition.[1-3] Hence, due to these properties, magnetic 1D materials have been extensively probed for their potential use as viable components of spintronic devices, data storage media, and MRI contrast agents.[4, 5] For example, ferromagnetic nanowires have recently been fabricated as building blocks for nanoscale magnetic logic junctions.[6, 7] Hence, the flexibility and versatility of magnetic nanostructures are potentially of significant interest for various types of applications.

Our lab has successfully synthesized a variety of magnetic materials such as various morphological manifestations of bismuth ferrite ($Bi_2Fe_4O_9$ and $BiFeO_3$), hematite (Fe_2O_3), yttrium manganese oxide ($YMnO_3$), as well as a class of spinel ferrite (MFe_2O_4) nanoparticles using facile, generalizable, and relatively simplistic sol-gel template, molten salt, and hydrothermal syntheses, respectively.[8-11] The resulting materials have been finely tuned for the

generation of a number of motifs, sizes, and shapes ranging from 1D nanowires, zero-dimensional nanocubes, bulk sized materials (~100 nm nanoparticles), to ultra-small ~2 nm MFe_2O_4 particles, using controlled reaction parameters and thus finely tuning their magnetic properties.

Of these magnetic materials, MFe_2O_4 (M= Co, Zn, Ni) nanostructures display superparamagnetic behavior coupled with high stability, which are particularly useful attributes for MRI and hyperthermia applications.[4, 12, 13] In this thesis, the effects of chemical composition and size upon the magnetic properties of our as-prepared ferrites were probed using pair distribution function (PDF) analysis, electron microscopy, and SQUID magnetometry, respectively. Specifically, in terms of size, the structure maintained its spinel structure until it attained the ultra-small size regime (i.e. ~3 nm). Moreover, when the overall size decreased to ultra-small particles, superparamagnetic behavior was observed. Hence as an extension of this work, the focus of this thesis herein has been to confirm the overall structure of these Co-based ultrathin (i.e.~2 nm in diameter), superparamagnetic nanowires and to correlate their structure to that of the ultra-small, as-prepared Ni and Zn ferrite nanoparticles.

Similarly, all ultra-small motifs (i.e. nanowires and particles) were prepared in the presence of 3-aminopropyltriethoxysilane (APTES) a molecule not typically used to control size. We consider that APTES may mimics the role and function of a surfactant. It is well known that the presence of surfactants can potentially alter the particle size of nanostructures by creating a barrier for mass transfer, modulating the surface energy and thus prevent nanoparticle agglomeration. However, our work has highlighted metal ion interactions between the APTES under basic environments as the primary reason for the resulting ultra-small particles. Hence, in an effort to further probe the synergistic effects that surfactant and base play on nanostructured

growth, a systematic study will be employed to confirm if indeed both entities aid in the overall morphology.

As a result, our contribution has been to use a generalized method for reproducibly synthesizing crystalline cobalt ferrite ($CoFe_2O_4$) nanowires of definable morphology and motif, while exhibiting chemical control over the metal ions within the spinel crystal structure. In so doing, we have attempted to correlate both morphology and chemical composition with the resulting magnetic properties of these nanowires by using SQUID magnetometry. Furthermore, we have also proposed a growth mechanism for the formation of these nanowire bundles by systematically varying the time, temperature, and surfactant used in the hydrothermal reaction in an effort to more precisely understand the role of each parameter in determining the resulting 1D anisotropic growth of these metal ferrite. Through these systematic variations, it is clear that the base (i.e. NaOH) as well as the surfactant/templating agent (i.e. APTES) play an inherent role in the growth of these nanowire bundles.

4.2 Results & Disscusion

4.2.1 Product Characterization

TEM and HRTEM images of our crystalline ultra-small Zn (Zn2), Ni (Ni3), and Co (Co3) ferrites prepared in the presence of APTES at higher reaction temperatures (220°C) as opposed to the conventional temperature (190 °C) are shown in Figure 4.1A-C and Figure 4.1D-F, respectively (see Table 3.1). At the conventional temperature, all other ferrites such as Co1 (~23.5 nm), Co2 (~14.9 nm), Ni1 (~87.3 nm), and Zn1 (~7.8 nm) were prepared in the absence of APTES as the surfactant.[14] Nonetheless, on the basis of statistical measurements of several tens of nanoparticles, pertaining to each sample analyzed, the average diameters of our crystalline as-prepared Zn and Ni, ferrites, i.e. the so-called “ultra-small nanoparticles”, were noted to be 3.1 ±

0.7 nm and 3.0 ± 0.6 nm, respectively. Upon extension of the reaction time to 6 hours, the presence of smooth nanowire bundles for the Co-based ferrite was observed, possessing an average length of 5 ± 0.25 μm and an overall width of 250 ± 23 nm. These bundles consist of individual nanowires characterized by widths of 2 ± 0.5 nm.

Moreover, the crystallinity of our ultra-small nanoparticles and nanowires were further confirmed by HRTEM and SAED patterns (Figure 4.1D-F and respective insets). HRTEM images in particular revealed interlayer spacings, corresponding to the expected lattice parameters associated with the spinel cubic structure of Zn and Ni ferrites, respectively. Interplanar spacings were estimated to be ~0.253 nm and 0.249 nm, respectively, corresponding to the (211) planes. In addition, the associated SAED patterns shown in the insets could be indexed to the reflection of a pure, crystalline spinel cubic structure according to their respective JCPDS standards. Furthermore, we should note that the expected spinel crystal structure of these ultrathin NW and ultra-small nanoparticulate metal ferrite samples was confirmed by XRD, and these data are shown in the Figure 4.2.

Table 4.1. Reaction specifics, product characterization data, and surface area for MFe_2O_4 nanoparticles. All other ferrite reactions were conducted at 190°C for 12 hours without the presence of surfactant, unless explicitly specified under 'Additional Notes'. APTES= 3-aminopropyltriethoxysilane

'M'	Sample #	Product Characterization (morphology and size)	Additional Notes	Surface area (m^2/g)
Ni	3	Particles; 3.0 ± 0.6 nm	$NiSO_4$ precursor, 1 mL of APTES used; run at 220°C	345.4
Zn	2	Particles 3.1 ± 0.7 nm	$ZnCl_2$ precursor, 1 mL of APTES used; run at 220°C	239.2
Co	3	Nanowires Avg. Length: 5 ± 0.25 μm Overall diam: 250 ± 23 nm Individual Wire diam.: 2 ± 0.5 nm	$CoCl_2$ precursor, 1 mL of APTES used; run at 220°C	52.79

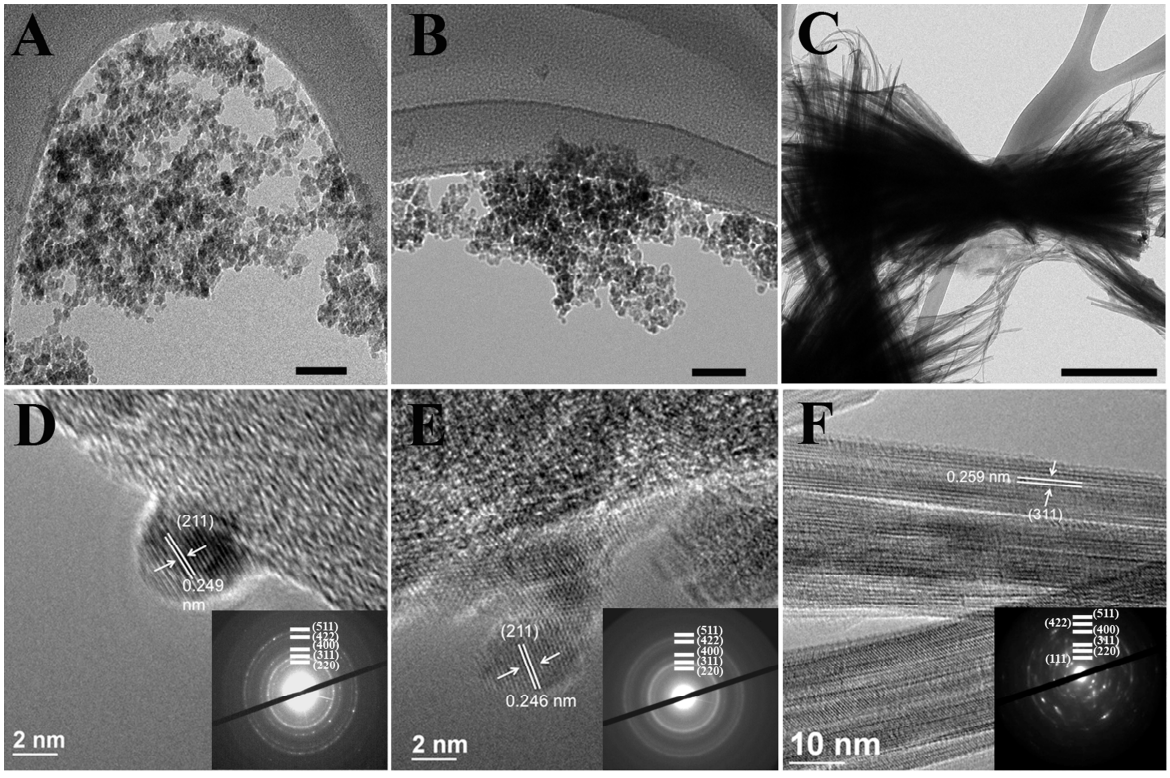

Figure 4.1. TEM images of nickel (A, Ni3), zinc (B, Zn2) and cobalt (C, Co3) metal ferrites prepared at 220˚C. High-resolution TEM images of single-crystalline nanostructures of nickel (D, sample Ni3), zinc (E, sample Zn2), and cobalt (F, Co3) metal ferrite samples. All scale bars for the low resolution TEM are either 40 nm (A and B) or 250 nm (C). Selected-area electron diffraction patterns (D-F insets) can be indexed to the cubic spinel structure ferrites. Images A-B and D-E reprinted with permission from Ref. 14. Copyright 2015 American Chemical Society.

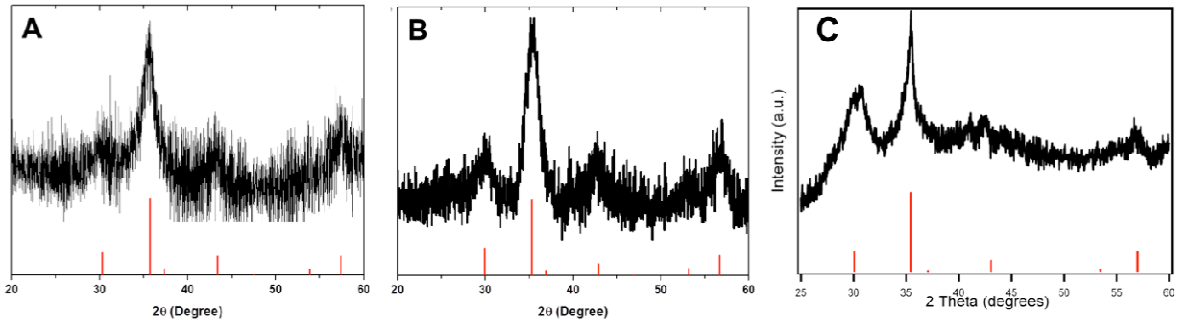

Figure 4.2. XRD patterns of ultra-small nanostructures of (A) Ni (Ni3), (B) Zn (Zn2), and (C) Co (Co3) ferrite, respectively. The JCPDS standards (red line) used to index the ferrite are numbers 74-2081, 821049, and 22-1086 for Ni, Zn, and Co ferrites, respectively. Supplementary images A-B reprinted with permissions from Ref. 14 Copyright 2015 American Chemical Society.

4.2.2 Magnetic Measurements

In terms of the ultra-small nanoparticles, particularly the Zn2, the ZFC-FC curves of these samples are dominated by interparticle magnetic interactions, as evinced by the broad maxima of the ZFC curves and flattened ZF-curve below T_{max}. Moreover, the 3 nm Zn ferrite posess M_S values of ~7/5 emu/g and ~6.4 emu/g at 5 K and 300 K, respectively. As for the 3 nm Ni ferrite, the presence of a slight hysteresis was observed at 300 K with a small coercivity of 17 Oe. These ultra-small particles also evinced relatively low M_S values (i.e. 12.1 emu g^{-1}), as opposed to bulk $NiFe_2O_4$ (i.e. M_S = 55 emu/g).[15] This observation overall may be potentially attributed to superparamagnetism at the nanoscale.

It is important to note that for the Co NW bundles, the magnetization of the samples did not completely saturate, even in the presence of the largest applied magnetic field of 5 T. This effect is very pronounced for our ultrathin superparamagnetic silicate-coated Co ferrite nanowires, which also exhibit a large depression in their M_S, i.e. ~3.6 emu/g, due to reduced interparticle dipole-dipole interactions (Figure 4.3E). Moreover, this is also a characteristic sign

of nanoscale magnetism, which can be attributed to spin canting at the nanowire surface,[16] meaning that the spins are not perfectly aligned. In addition to the low saturation magnetization, the low remnance M_r/M_s present at 5 K suggests the presence of the supporting silicate within the nanowires themselves. Previous studies have shown that larger sized SiO_2-$CoFe_2O_4$ core-shell structures gave rise to a similar trend in both the saturation magnetization and the coercivity (H_c), an observation which was attributed to their small nanoparticle size of ~11 nm.[17, 18]

Based upon previous ZFC-FC curves of these metal ferrite materials, particularly the Co series, it was observed that as the particle size decreased, the temperature at which the ZFC and FC curves diverged, i.e. the blocking temperature, T_B,[11] also diminished in magnitude. With the amorphous ultra-small 2.6 nm particles yielding a T_B of ~45 K,[14] by contrast, our ~2.0 nm crystalline individual NW bundles gave rise to a T_B of ~15 K, above which superparamagnetic behavior is expected (Figure 4.3F).

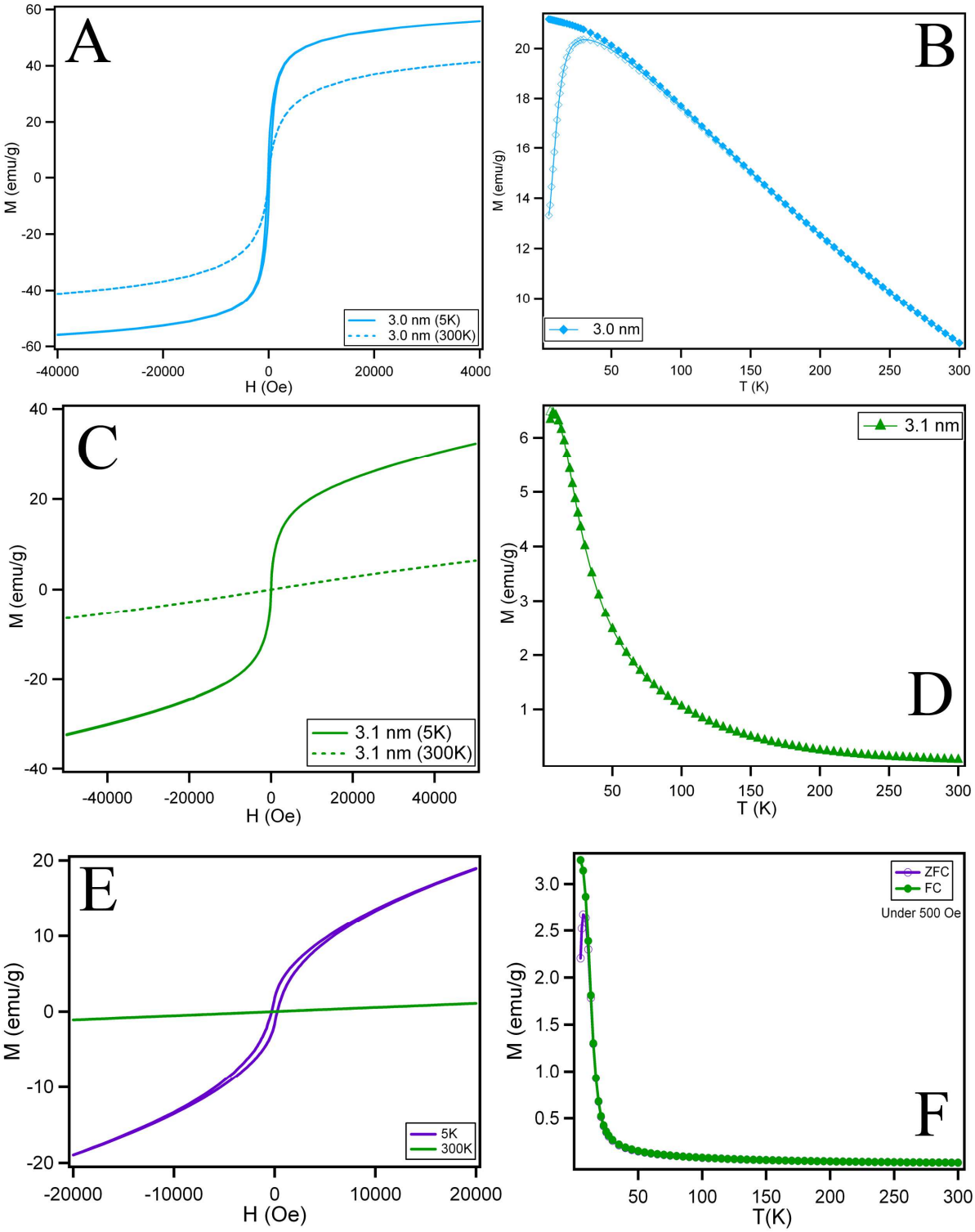

Figure 4.3. M versus H curves (A, C, E) at 5 K and 300 K with ZFC-FC curves (B, D, F) with an applied field of 500 Oe for the Ni3, Zn2, and Co3 ferrites. Images A-D reprinted with permissions from Ref. 14 Copyright 2015 American Chemical Society.

Table 4.2. Magnetic characterization and surface area of Ni3, Zn2, and Co3. Magnetic characterization data were obtained from M versus H curves at 5 K and 300 K, along with ZFC-FC curves at an applied field of 500 Oe. Note the unit (emu/g) is calculated for the total mass of the material.

Name	**T (K)**	**H_c (Oe)**	**M_S (emu/g)**	**M_R (emu/g)**	**M_r/M_s**	**T_{max}/T_B (K)**	**BET surface area (m^2/g)**
Ni3	5 300	160 17	40.8 12.1	8.69 0.19	0.21 0.01	29	345.4
Zn2	5 300	18.3 -	7.5 6.4	0.59 -	0.08 -	6	239.2
Co3	5 300	330 -	16.5 2.7	1.8 -	9.1 -	15	52.79

4.2.3. PDF Analysis on Magnetic Ferrite Nanoparticles.

The premise of using the pair distribution function (PDF) is that materials are made of multiple elements, have large unit cells, and are often low dimensional or incommensurate structures.[19] Increasingly also, they have aperiodic disorder with some aspect of the structure that is clearly different from the average crystal structure. In the case of nanoparticles, the very concept of a crystal is invalid, as the approximation of infinite periodicity is no longer a good one. Hence, the value added of a 'total scattering' experiment generating PDF data over a conventional powder diffraction analysis is the inclusion of diffuse scattering as well as Bragg peak intensities in the analysis, and the wide range of Q (the magnitude of the scattering vector) over which data are measured. 'Total scattering' data can be analyzed by fitting models directly in reciprocal-space.[20]

Hence, in light of the extensive magnetization data collected and interpreted,[14] we attempted to further understand and refine the crystal structure of the ferrite samples using PDF

analysis, which has already been previously applied to systems ranging from ultra-small CdSe quantum dots, with diameters of 2 nm to 4 nm, as well as to existing metal oxide systems, such as $YMnO_3$ particles, measuring from 10 nm to ~467 nm.[21, 22] However, though $MgFe_2O_4$ and $CoFe_2O_4$ have been analyzed in the past[23-25] using PDF, the size regime of these specific particles was nominally 6 nm or higher, and these ferrite materials conserved their cubic spinel structure. Herein, we are currently the first to report on a PDF analysis of a range of variously-sized nanoparticulate metal oxide samples.

For illustrative purposes, Co, Zn, and Ni ferrites with various size regimes were rigorously analyzed (Table 4.2 as well as Figures 4.6 and 4.7). The PDFs of all the ferrite nanoparticles are plotted in the *r*-range up to 40 Å in Figure 4.4. The PDF peaks for Co1, Co2, Ni1, and Ni2 samples are still strong at 40 Å where the end point is designated, indicating well-ordered local structures in these materials. By contrast, the PDF peak intensities in Zn1, Zn2, and Ni3 samples diminish more quickly with increasing *r* values, indicating a smaller structural coherence for these samples. The PDFs with a high degree of structural coherence (i.e. Co1, Co2, Ni1, and Ni2) are very similar, suggesting these samples share the same structure with each other. However, apart from the reduced size of the particles, PDF patterns of Ni3, Zn1, and Zn2 are similar to the well-ordered Ni and cobalt PDFs, indicating that the underlying structure is the same.

In order to extract more quantitative structural information, we carried out PDF model fits, using the structural model for the cubic spinel space group $Fd\bar{3}m$ (No. 227), and calculated reasonable agreement values with the experimental Synchrotron Light Source XRD and electron microscopy diffraction data (R_w) as shown in Figure 4.5, with the fit results summarized in Table 4.2. We should note that due to similar scattering potentials of the Co and Ni samples, the degrees of inversion (DOIs) were derived from previous Mössbauer experiments and were used in the

model fits.[14] By an inspection of the fits, we observe a good agreement between the measured data and the simulated models for Co1, Co2, Ni1, and Ni2 with an R_w value of ~0.1. The structural features of these larger particles are well described by the cubic spinel model. As the particle size decreases, the fits become worse, being in the vicinity of $R_w = 0.4 – 0.5$. This indicates that there is some 'unfit' component in the signal which may originate from ligand effects, for example, of the small nanoparticles. In the ePDFs of Zn2 and Ni3, there is also a residual signal from the carbon grid that supported the nanoparticles, which was not completely subtracted during the background correction. Nonetheless, it is clear that the best-fit PDFs from the models explain the structure well, with calculated peaks lining up well with the measured PDF. We therefore trust the refinements quite well and the poor R_w can be attributed to signals from impurity components as opposed to a poor fit to the nanoparticle structures. The refined parameters show good agreement between the ultra-small and the larger nanoparticles.

The range of signal in the PDF, which indicates the range of structural coherence, is comparable to the physical size of the particles observed in the TEM. Both of these observations suggest that the degree of structural order in the ultra-small nanoparticles is actually rather small. In effect, they appear to be very small chunks of well-defined spinel material. Notably, all the samples, especially the Ni and Zn, exhibit a very high degree of inversion between the tetrahedral and octahedral sites. Initially, there appears to be no clear structural explanation for the different magnetic response of the ultra-small nanoparticles. As a result, to solve the crystal structure of these nanoparticles, the $CoFe_2O_4$ (Co3) nanowires were systematically probed by varying reaction time, temperature, surfactant, as well as control experiments in order to ascertain what other structures may be present within the material.

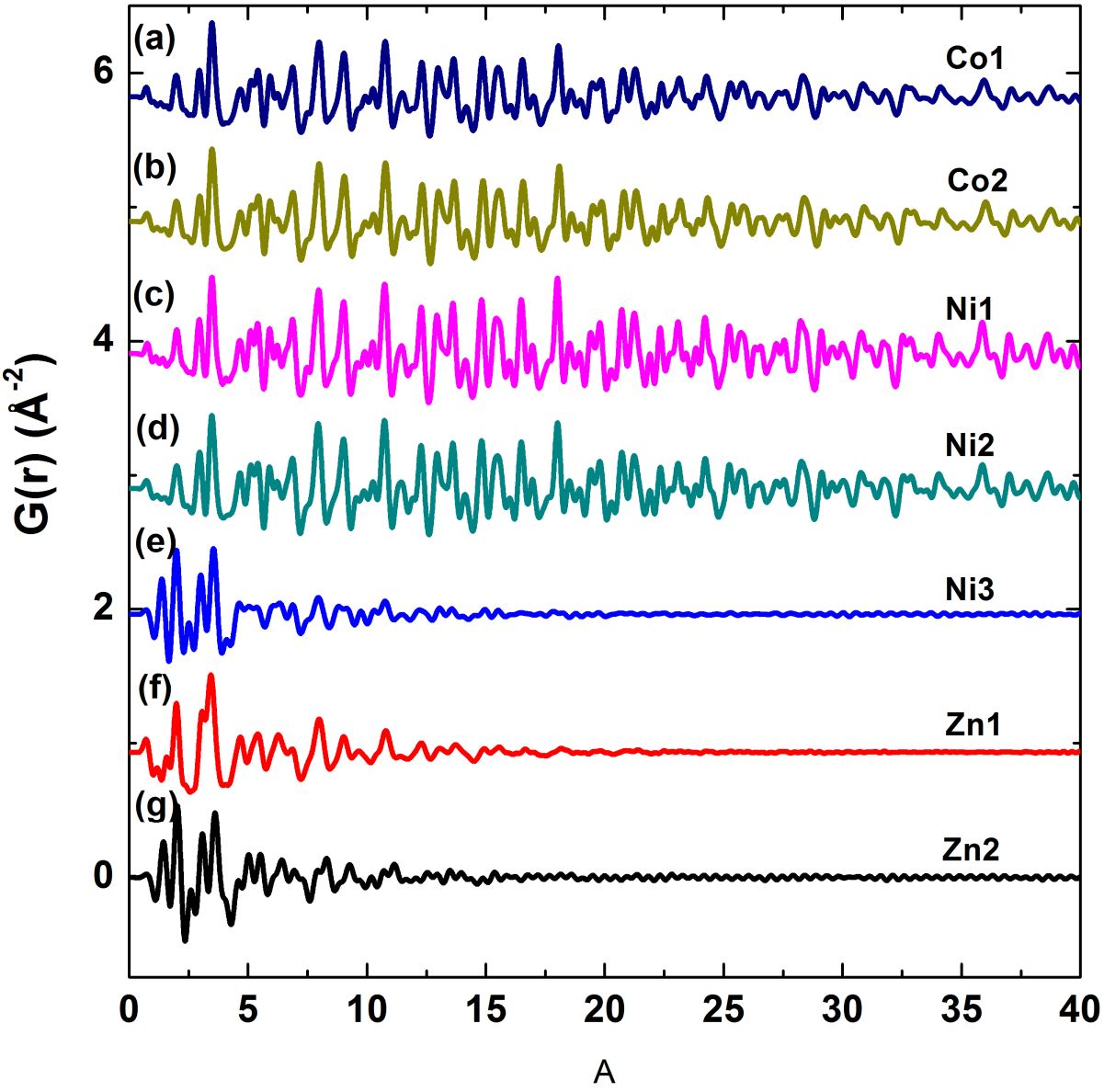

Figure 4.4. Measured PDFs for Co, Ni, and Zn ferrite nanoparticles of various sizes plotted in a *r*-range up to 40 Å. Image reprinted with permissions from Ref. 14. Copyright 2015 American Chemical Society.

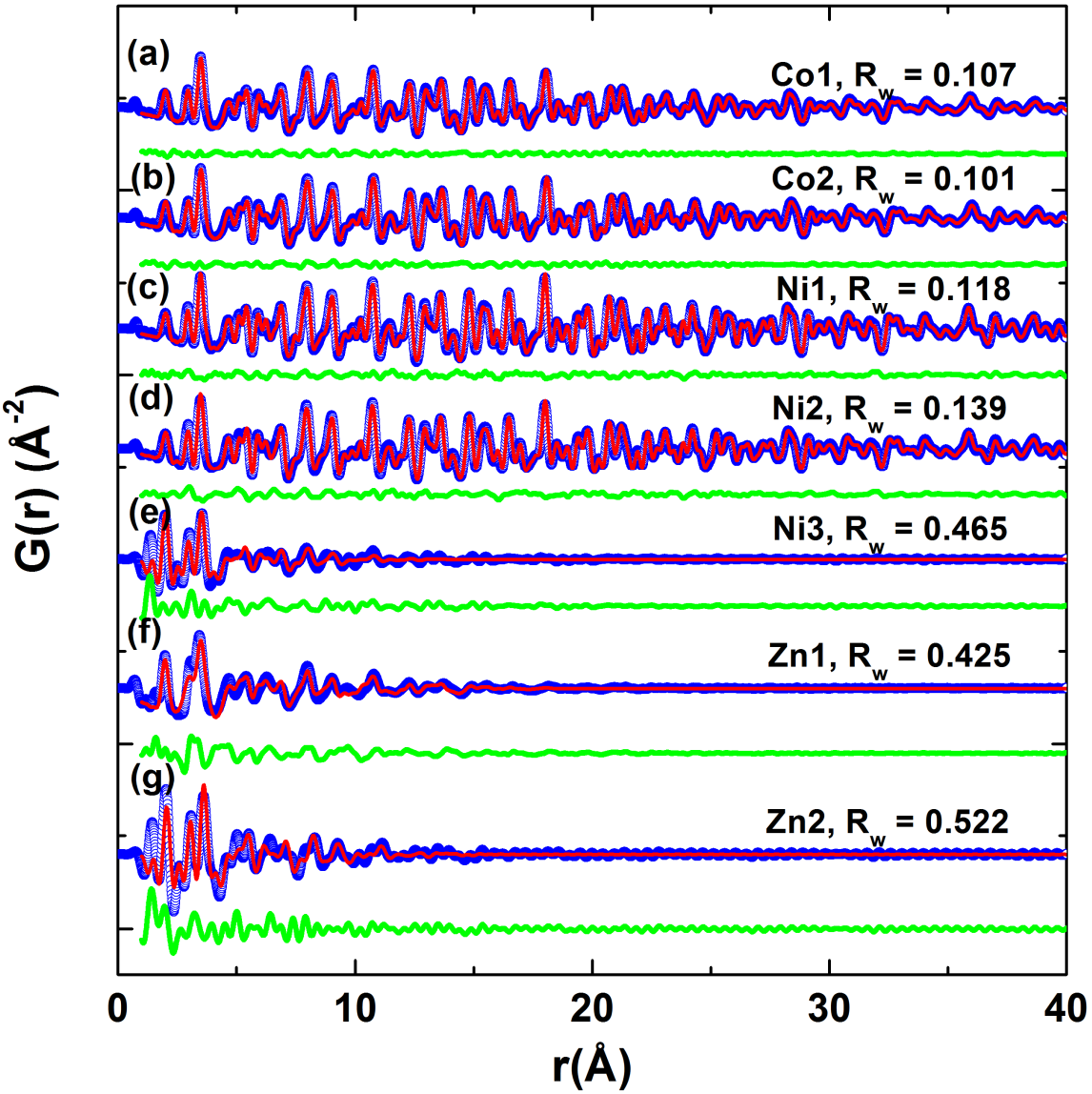

Figure 4.5. PDF fits for as-prepared Co, Ni, and Zn ferrite NPs in an 'r-range' from 1 Å to 40 Å. The blue circles and red solid lines correspond to measured and simulated PDFs, respectively. The green solid lines offset below are the difference curves. Agreement factors, R_w, are displayed beside each model fit. Image reprinted with permissions from Ref. 14. Copyright 2015 American Chemical Society.

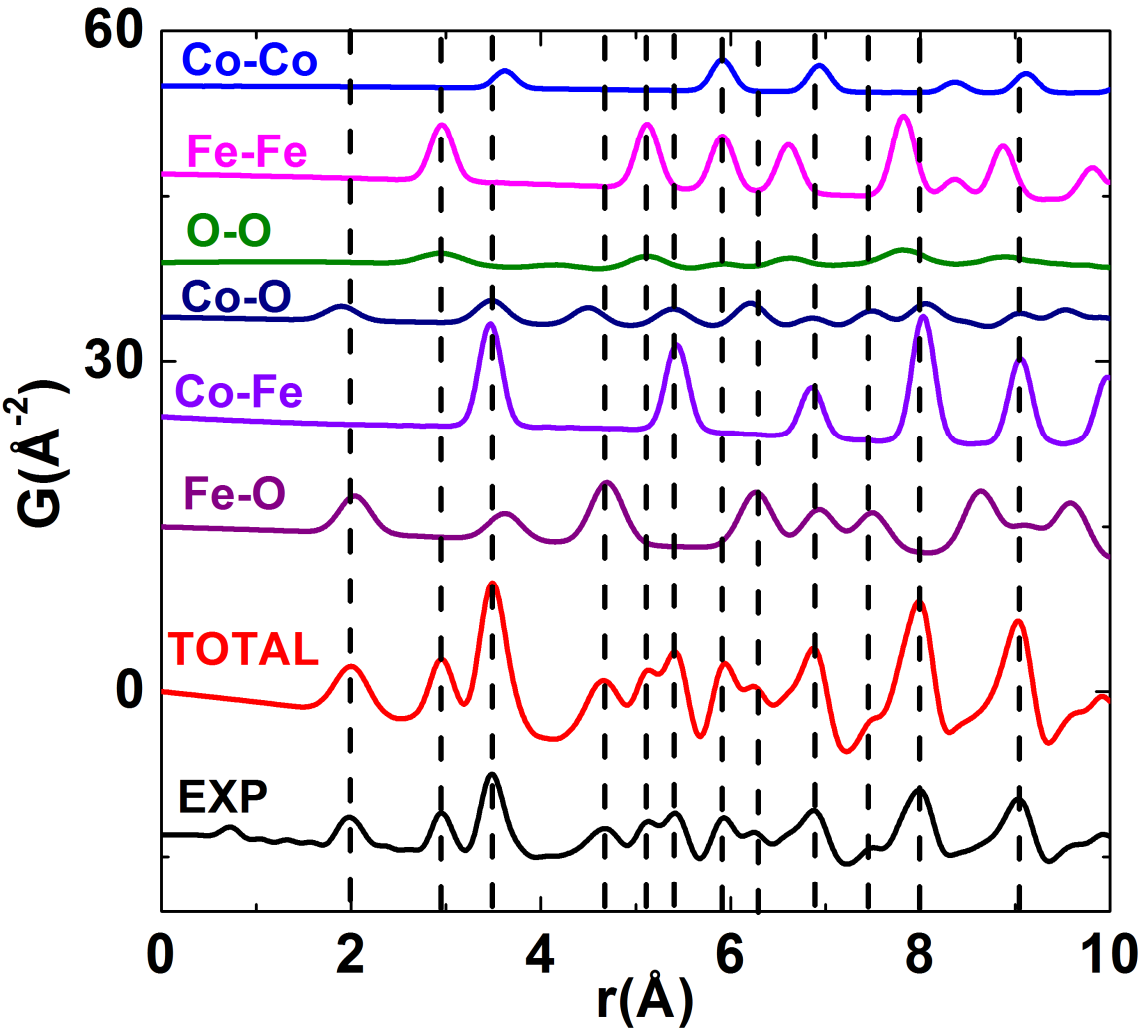

Figure 4.6. A comparison between the calculated and measured PDF profiles of the Co1 sample together with the contribution from each atomic pairs. The vertical dashed lines mark the peak positions. Supplementary image reprinted with permissions from Ref. 14. Copyright 2015 American Chemical Society.

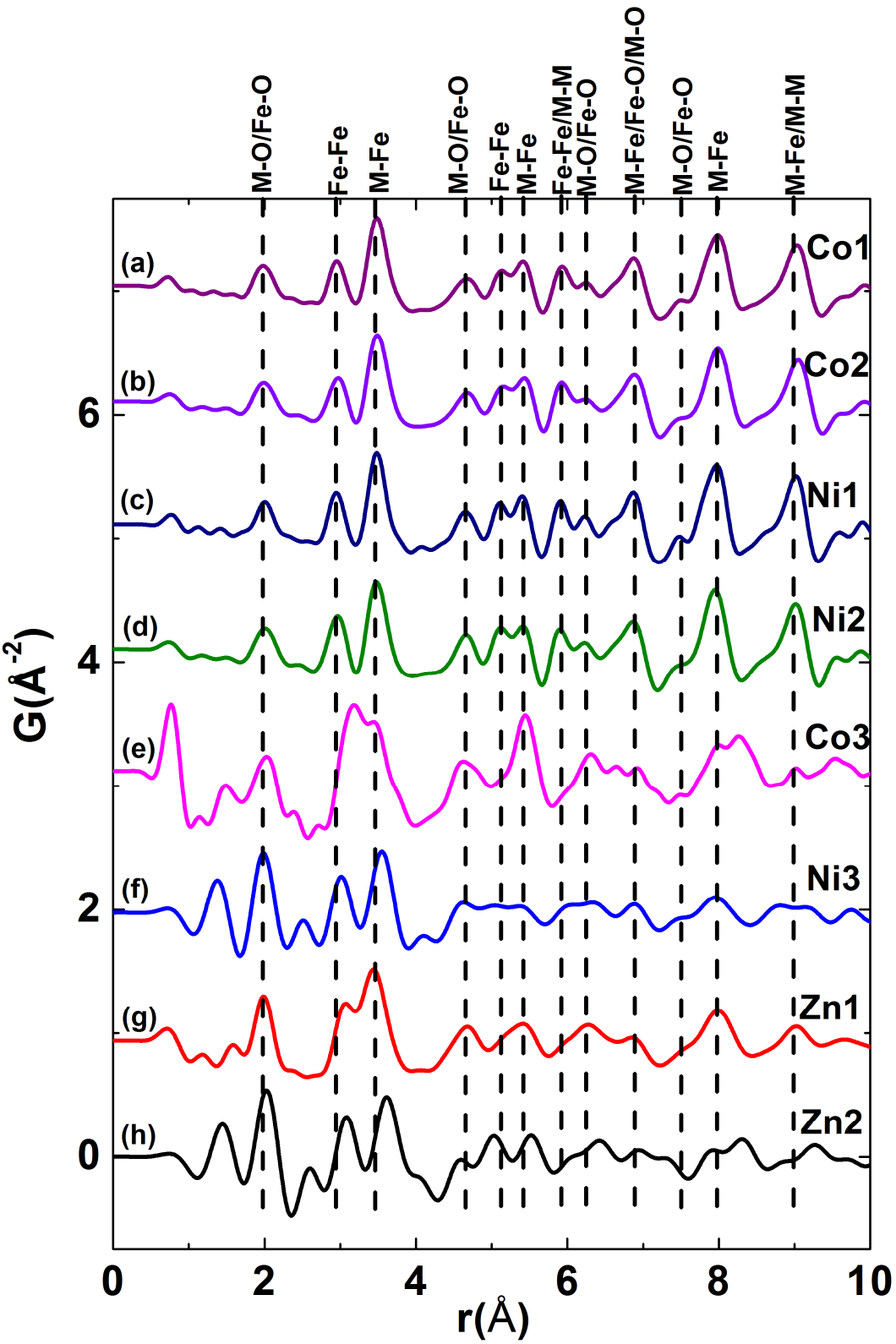

Figure 4.7. A stack of PDFs of all samples in a **r**-range up to 10 Å with vertical dashed lines, indicating the specific atom pairs in the cubic spinel structure, as demonstrated by the Co1 sample. Supplementary image reprinted with permissions from Ref. 14. Copyright 2015 American Chemical Society.

4.2.4 Investigation of the Co Ferrite Nanowire Bundles

4.2.4.1 X-ray Photoelectron Spectrscopy

The Co NW bundles were further investigated using XPS in order to more accurately determine their precise chemical composition of crystalline and amorphous materials. Specifically, spectra were collected at binding energies associated with Fe 2*p*, Co 2*p*, and Si 2*p* transitions, respectively. The accumulated spectra were corrected for charge effects, normalized, and finally subjected to background subtraction. Deconvolution of these spectral features was achieved using the XPS PEAK 4.1 software. From the XPS spectra of $CoFe_2O_4$@$MSiO_4$, Fe $2p^{3/2}$ peaks located at ~ 725 eV and 714 eV can be identified with Fe^{2+} obtained from iron silicate.[26] As for the Co spectra (Figure 4.8B), the presence of Co (II) $2p^{3/2}$ & $2p^{1/2}$ peaks centered at ~795 and ~779 eV, respectively, is indicative of $CoFe_2O_4$. In addition, the presence of Co (III) $2p^{1/2}$ peak at higher binding energies, ~802 eV, is suggestive of the formation of Co silicates localized within an octahedral symmetry.[27,28,29] Finally, the Si 2*p* peak located at ~99 eV can be ascribed to the formation of SiO_4^{4+}.[28] The chemical composition of the sample was further quantified using the XPS software, wherein the ratio of $CoFe_2O_4$: $FeSiO_4$: $CoSiO_4$ was 3.1: 1: 1.6. From these data, it is probable that APTES indeed interacts with the metal ions forming amorphous metal silicates. The ratio information, generated by the XPS software, was later used as an input parameter for pair distribution function analysis, as explained in upcoming sections.

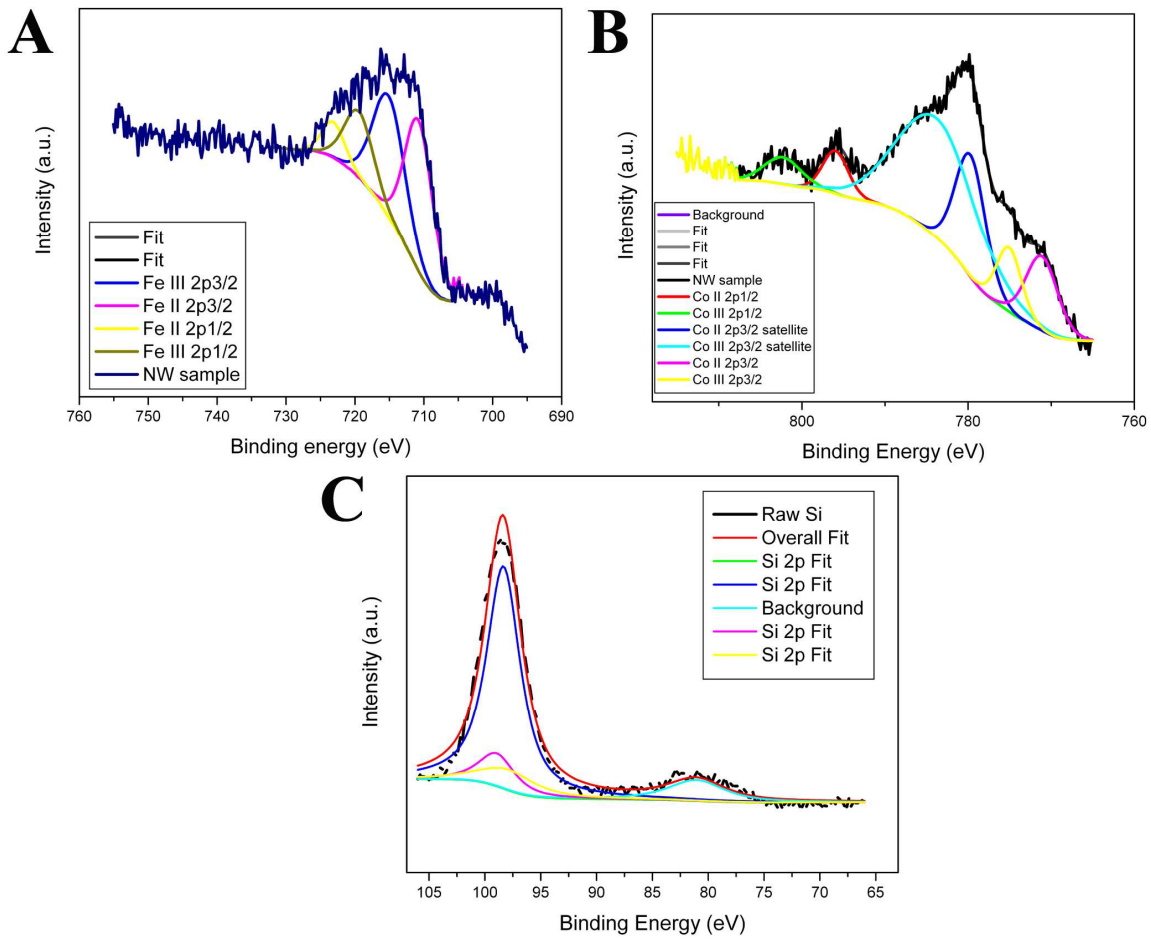

Figure 4.8. X-ray photoelectron spectroscopy data for Co NW bundles (Co3) highlighting (A) iron $2p^{3/2}$ and $2p^{1/2}$, (B) cobalt $2p^{3/2}$, and (C) silicon (Si) 2p transitions, respectively. Deconvolution of each of the accumulated spectra imply the presence of Fe silicates, Co silicates, and the silicate group SiO_4 itself, respectively.

4.2.4.2 PDF Analysis

As previously mentioned, the quantitative ratios obtained from the XPS data were used for pdf analysis. Initially, when the spinel structure was used within the pdfGui software, the R_w value was ~0.8, which was similar to the Ni and Zn ultra-small nanoparticles. However, when the XPS ratios were input into the algorithm, the R_w value reduced from 0.8 to 0.2, as confirmed by the PDF fit (Figure 4.9). As a result, we can confidently state that we indeed possess constituents of both $CoFe_2O_4$ and metal silicates ($MSiO_4$) within the Co NW bundles. This particular composition more than likely emanates from a synergistic interaction between the metal ions and the APTES surfactant, and will be further discussed in later sections.

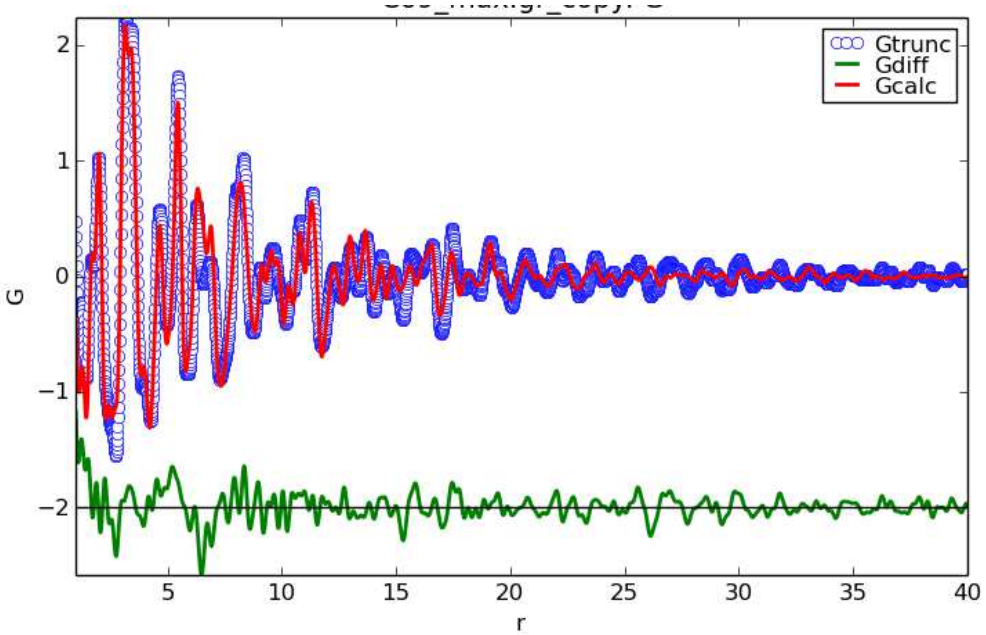

Figure 4.9. PDF fits for as-prepared Co ferrite NWs (Co3) in an 'r-range' from 1 Å to 40 Å. The blue circles and red solid lines correspond to measured and simulated PDFs, respectively. The green solid lines offset below are the difference curves.

4.2.4.3. Plausible Growth Mechanism

Temperature Dependent Study

Systematic variations in a number of reaction parameters such as temperature and time were employed in order to better understand the growth formation of ferrite nanowire bundles. For example, for the temperature-dependent study of $CoFe_2O_4@MSiO_4$ bundles, the reaction time was increased in 20-degree intervals to a nominal reaction time of 6 hours, shown in Figure 4.1C. From this study, it was observed that at 180 °C (Figure 4.10A), a nebulous strand-like APTES coating surrounded and coated the as-prepared, ultra-small amorphous nanoparticles. Generally at this temperature, adsorption of APTES takes place through a dehydration process, wherein water molecules present in the reaction medium react with the ethoxy groups forming either silanols or linear silicate chains sharing oxygen atoms.[30] As the temperature is increased to 200 °C, as shown in Figure 4.10B, nanoparticle aggregation and accompanying nanoscale strands were observed, features which could be potentially ascribed to the formation of metal ion seeds (i.e. Co, and Fe ions) and linear silicate chains, respectively. Nonetheless, these processes are suggestive of the occurrence of initial seed nucleation followed by particulate fusion into 1D strands.

It is plausible to hypothesize that the negatively charged silicate strands are electrostatically stabilized by the combination of positively charged Na^+ and metal cations in solution, associated with NaOH and the relevant transition metal precursors.[31] As the temperature was further increased to 220 °C (Figure 4.10C), well-defined, crystalline nanowire bundles of presumably ferrites were observed. Moreover, residual

silicate remained present within the reaction medium so as to facilitate the formation of nanowire bundles.

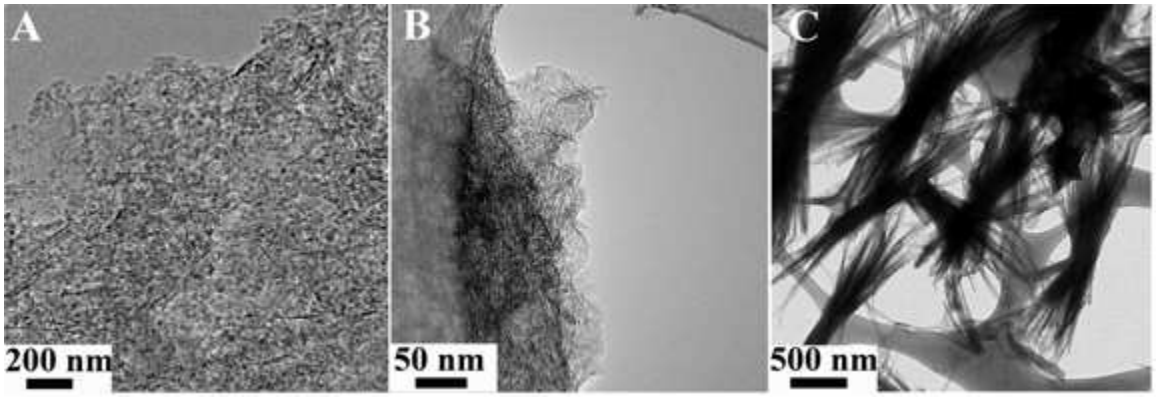

Figure 4.10. Representative TEM images of $CoFe_2O_4$@$MSiO_4$ NWs bundles synthesized at 180°C (A), 200°C (B), and 220°C (C), respectively.

Time-Dependent Study

In parallel, a reaction time-dependent study was conducted at a fixed temperature of 220 °C. These efforts focused on further understanding the role of sodium hydroxide and APTES in enabling and facilitating the transformation of nanoparticles to nanowire bundles for the $CoFe_2O_4$@$MSiO_4$. Hence, the concept was that the presence of sodium hydroxide would assist in the eventual synthesis of $CoFe_2O_4$@$MSiO_4$ NW bundles. The time-dependent study began at 3 h, as crystalline materials were initially created at that time. After 3 hours at 220°C, nanoparticle aggregates were observed for $CoFe_2O_4$ as shown in Figure 4.11A. As the reaction time was additionally increased to 4 hours, the initial formation of nanoparticle aggregates evolved into the production of increased numbers of nanoscale strands (Figure 4.11B). Finally by 5 h of reaction time, as shown in Figure 4.11C and F, these nanoparticles had transformed and coalesced into more ordered and structured nanostrands of ferrites, assembled within a perceptible framework. This

degree of organization increased with ever greater reaction times, i.e. 6 h, resulting in the formation of recognizable NW bundles.

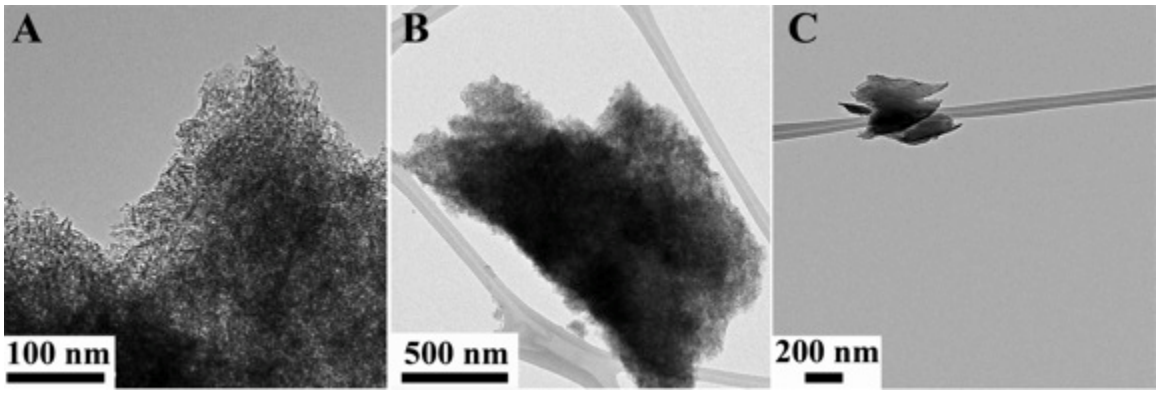

Figure 4.11. Representative images concerning the time evolution of the (A, B, and C) Co ferrite nanostructures, associated with reaction time intervals of 3 h (A), 4 h (B), and 5 h (C), respectively.

Reaction Schematic

Hence, based upon the combined temperature and time-dependent reaction studies, we can reasonably postulate that the predominant reaction mechanism herein involves an initial nucleation followed by aggregation and subsequently recrystallization to yield the resulting nanowires. That is, first, the bulky precipitate from the metal and surfactant precursors dissolve in water, forming smaller, more numerous and discrete, and relatively homogeneous metal silicate seeds (Figure 4.12A). These individual seeds then cluster, coalesce, and undergo an oriented attachment mechanism to form sheets (Figure 4.12B).[32] This process presumably occurs through an oriented attachment mechanism, which would account for the formation of smaller particles to form larger structures as a result of favorable crystallographic or surface orientations.[32]

Subsequently, the silicate seeds may form straight chain-like structures of repeating silicate molecules, wherein dangling oxygen atoms undergoes charge

compensation by surrounding sodium and metal ions. It is also worth mentioning that the existence of ionic channels for sodium has been demonstrated by using inelastic neutron scattering within sodium silicate structures and that furthermore, the Si-O network remains otherwise inert.[33] Hence, this ionic and relatively conducting oxide 'supporting framework' may enable the local inclusion of transition metal cations, i.e. Co and Fe; it is plausible therefore that the presence of adjacent vacancies may thereby favorably facilate the formation of interfacial phases, such as $CoFe_2O_4$.

Specifically, positively charged Na^+ and transition metal cations can cluster together, and electrostatically neutralize negatively-charged linear silicate chains, thereby stabilizing them and facilitating the formation of strand-like structures of repeating silicate molecules (Figure 4.12C).[33] It is then presumed that the simultaneous presence of APTES within the reaction medium assists in the stabilization of the nanostrands, enables their further anisotropic growth, and thereby eases their transformation into clusters of 1D NWs, stacked into bundle configurations (Figure 4.12D).[34]

A similar behavior was observed by Manjunatha *et al.,* associated with the preparation of $CdSiO_3$ nanobelts via a hydrothermal method.[31] Specifically, both the $CdSiO_3$ and $CoFe_2O_4$ nanowires employ the silicate precursor as a template to yield a linear straight chain with metal ions stabilizing this chain thereby forming 'sandwich structures' composed of alternating silicate and metal layers stacked one above the other.[31] However, Manjunatha *et al.* did not observe a synergistic interaction between the silicate and Na^+ ions nor did they attribute the presence of Na^+ ions to the possibility of influencing the observed nanowire morphology, even though the silica source for the $CdSiO_3$ nanobelts was indeed sodium metasilicate (Na_2SiO_3). Nevertheless, based upon

the observations of previous literature as well as from our own insights collected herein, a time evolution of nanowire formation is highlighted and summarized in our growth schematic, as depicted in Figure 4.12.

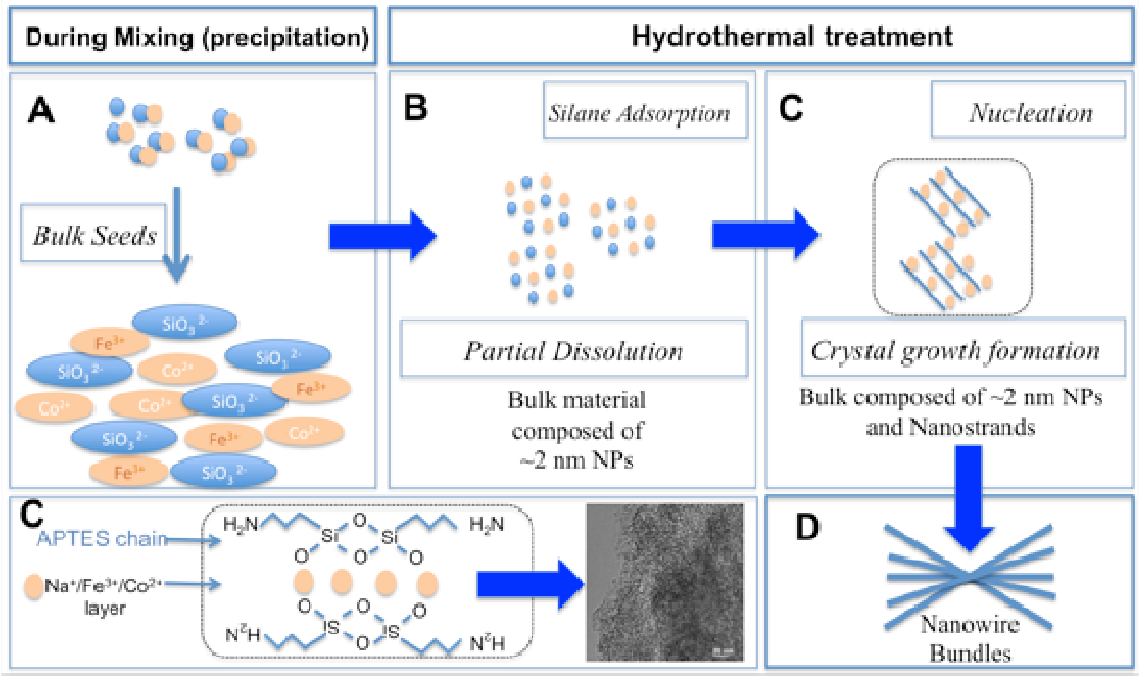

Figure 4.12. A modified schematic representation of the proposed growth mechanism of metal ferrite nanowire bundles from Manjunatha et al. *J. Mater. Chem*. **2012**, 22: pp. 22392-22397.

Control Experiments

What is unique about our proposed formation mechanism is that we highlight the constructive and synergistic role of NaOH in terms of favorably promoting nanowire growth. Specifically, to further confirm our hypothesis concerning the synergistic effects of APTES and NaOH for nanowire growth, control experiments were performed in the absence of either APTES or NaOH precursors. These runs yielded primarily nanoparticles. Specifically, control experiments in the absence of NaOH were performed exclusively in water as well as in mixed water: ethanol (1:1 v/v) solutions. Interestingly,

after 6 hours in aqueous solution, nanowires began to form from the bulk-like precursors. Nevertheless, as the reaction time progressed from 6 to 24 hours, these Fe_3O_4 nanowires began to degrade into ultra-small nanoparticles (Figure 4.13A-C).

Indeed, the implication is that APTES can induce the formation of linear chains, but in the absence of basic conditions, induced by the presence of Na^+ ions for example, this linear template is not stabilized and the metal precursor seeds end up forming nanoparticles. This type of scenario ended up playing out in an aqueous water-ethanol solution, because initially after 6 hours, the Co ferrites had formed small but discernible 1D building blocks circumferentially coated with ultra-small nanoparticles. Though it is certainly possible that crystal splitting of these rectangular blocks into nanowires could occur at longer reaction times, we instead observed the formation of discrete nanoparticles (Figure 4.13 D-F). These observations confirm the significance and the necessity of the simultaneous presence of both APTES and NaOH in bringing about the growth of anisotropic nanowires of $CoFe_2O_4@MSiO_4$ in our systems.

Surfactant-assisted growth protocols are common in the context of 1D materials, and are well understood.[35-39] However, it is worth reinforcing that although APTES as the surfactant is definitely a major contributor to our nanowire bundle motif, we consider the presence of ionic species to be equally important determinants of the resulting morphology as well. Indeed, previous reports have indicated that Na^+ ions can preferentially adsorb onto a particular facet and thereby promote[40-42] one-dimensional growth within metal oxide systems.[15,16] Herein, we propose constructive and beneficial synergistic interactions between the APTES surfactant and the Na^+ metal cation, as essential and critical factors driving nanowire growth of $CoFe_2O_4@MSiO_4$.

This concept of positive synergy between surfactants and metal ions and its resulting directing influence upon crystal growth has been previously documented. For example, the simultaneous presence of both cetyltrimethylammonium bromide (CTAB) and Ag^+ ions enabled Au nanorod growth,[43] whereas the concurrence of both Ca^{2+} and CTAB allowed for the generation of highly faceted iron oxides.[44] From our control experiments, given the introduction of Na^+ ions from the basic solution used, it is therefore feasible to envision a mutually complementary and synergistic interaction between APTES and the ions in solution with respect to nanowire formation.

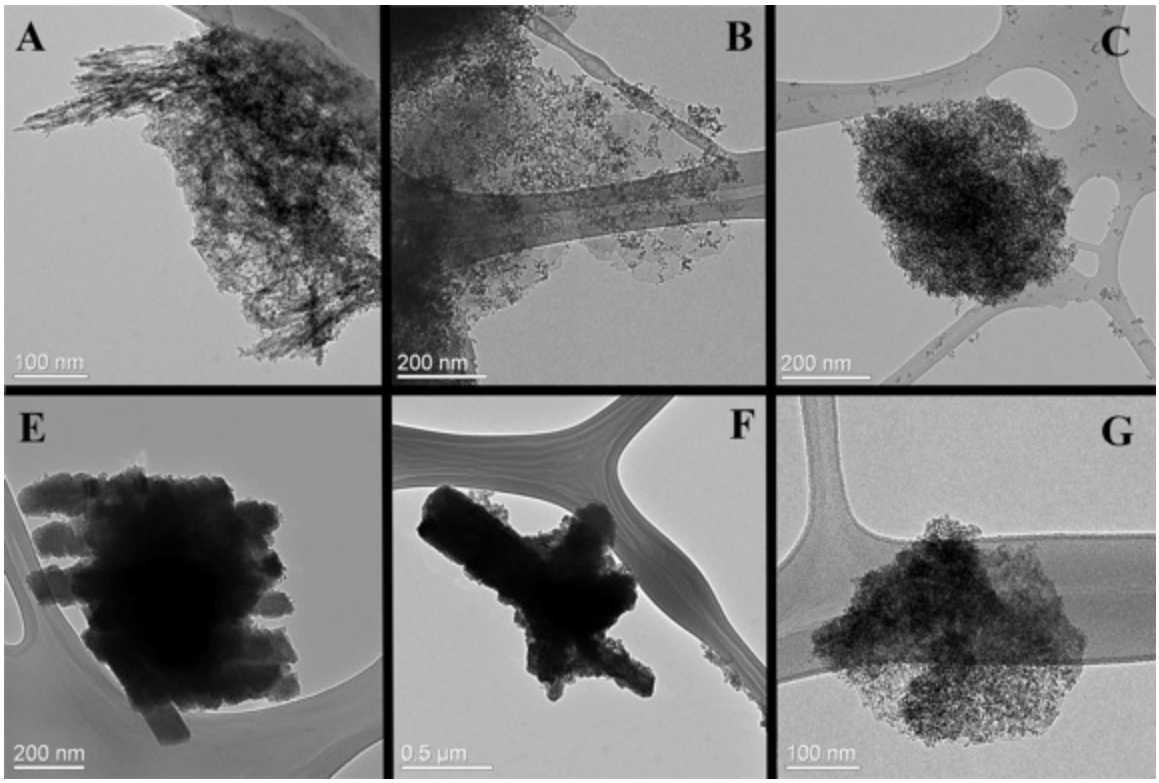

Figure 4.13. Control experiments for the synthesis of $CoFe_2O_4$@$MSiO_4$ nanostructures in the absence of NaOH. Reactions were run either in water (A-C) or in 1:1 volume ratios of H_2O/EtOH (E-F) for 6, 12, and 24 hours, respectively.

Role of Silicate Derivatives

To gain further mechanistic insights, we varied the identity of the surfactant used. Specifically, we sought alternatives to APTES, such as tetraethoxysilane (TEOS) and tetramethoxysilane (TMOS) possessing similar silicate groups in order to confirm the role of this particular surfactant in the observed nanowire growth. APTES is a surfactant-like molecule possessing a silicate SiO_3^{2-} head group in addition to an amine-terminated functional group, which can exist as a positively charged species under lower pH conditions. Our high pH, basic reaction conditions likely rule out that there are charged amines that may be either contributing to the formation of either electrostatic complexes

or acting as facet capping agents. Hence, we hypothesize that the silicate head group within APTES plays a role in directing morphology.

To further rule out the effect of the amine functional group, 'amine-less' species, i.e. TEOS and TMOS, were substituted for APTES. The net result of these experiments was that we observed similar wire-like bundle morphologies by TEM (Figures 4.14B and 4.14C). These results corroborate the role of the silicate functional groups in directing the resulting overall crystal growth.

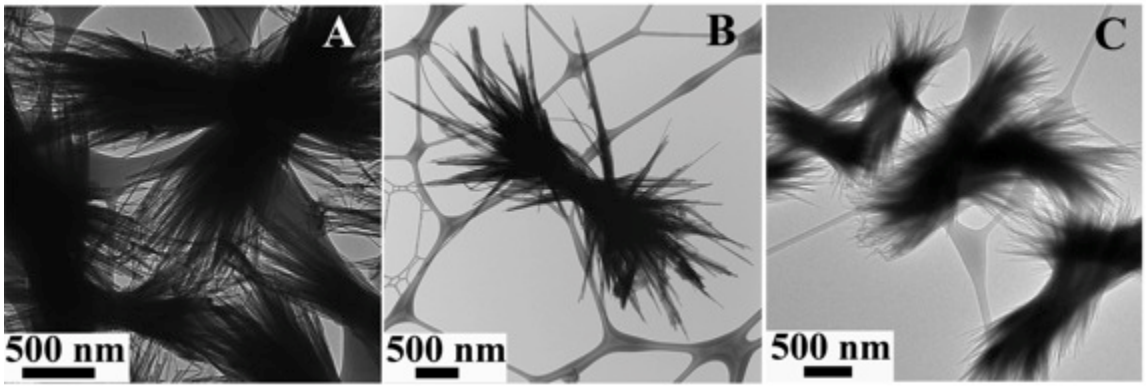

Figure 4.14. As-prepared Co ferrite nanowire bundles, created using various surfactants such as (A) aminopropyltriethoxy silane (APTES), (B) tetraethyl orthosilicate (TEOS), and (C) tetramethyl orthosilicate (TMOS), respectively.

4.3. Conclusions

We have developed a simple and efficient hydrothermal method for the synthesis of large quantities of single-crystalline MFe_2O_4 (where 'M' = Co, Ni, and Zn) nanoparticles and nanowires. We have explored a variety of experimental parameters in order to reliably tailor our synthesis in order to generate different chemical compositions, sizes, and morphologies. Of the parameters investigated, the nature of the precursors as well as the inclusion of surfactant represented the most critical factors to consider in terms of 'selecting' for a specific chemical composition and particle size.

Indeed, by including APTES into the reaction solution, we could generate reasonably monodisperse, ultra-small nanoparticles and nanowires. Structural PDF analysis was performed on a series of MFe_2O_4 nanoparticles of various sizes, where the spinel structure was no longer maintained in the ultra-small size regime. Initially these ultra-small nanoparticles were thought to be MFe_2O_4, however upon closer analysis of the Co NW bundles, interactions between the metal ions and the APTES lead to the formation of another phase comprised of metal silicates under high temperatures and pressures. The presence of this additional phase was further corroborated by PDF analysis of the Co NW bundles.

In an effort to understand their function in nanowire growth of the Co sample, the roles of various precursors were probed. Hence, based on control experiments, such as (i) the absence of either APTES or NaOH precursors, as well as (ii) the substitution of APTES with TEOS and TMOS silicate derivatives, we conclude that the simultaneous presence of both APTES surfactant and NaOH is critical for enabling nanowire bundle growth. Hence it is reasonable to presume that a positive and constructive synergistic effect exists between APTES and NaOH and that favorable interactions between the two can favorably control nanowire growth.

As for the magnetic measurements, we discovered that superparamagnetism is only present in the ultra-small nanoparticles ($\leq$ 4.0 nm) as well as the nanowires with very magnetic low saturation values. The presence of spin canting, uncompensated surface spins and magnetic anisotropy was observed for a majority of our samples; blocking temperatures associated with these systems were also discussed. Moreover, our data are consistent with prior observations reported by other groups[45, 46, 47] who have

noted that (a) differential ligand-surface interactions may be responsible for altering the observed surface spin-canting disorder and that (b) T_B as well as M_r/M_s and H_c values generally increase with increasing nanoparticle size.

4.4 References

1. J. L. Moran-Lopez, R. A. Guirado-Lopez, J. M. Montejano-Carrizalez, F. Aguilera-Granja, R. Rodriguez-Alba, J. Mejia-Lopez, A. H. Romero and M. E. Garcia, *Current Science*, 2008, 95, 1177-1201.
2. A. K. M. Bantu, J. Rivas, G. Zaragoza, M. A. López-Quintela and M. C. Blanco, *Journal of Applied Physics*, 2001, 89, 3393-3397.
3. J. P. Pierce, E. W. Plummer and J. Shen, *Journal of Applied Physics Letters*, 2002, 81, 1890-1892.
4. M. Ravichandran, G. Oza, S. Velumani, J. T. Ramirez, F. Garcia-Sierra, N. B. Andrade, M. A. Garza-Navarro, D. I. Garcia-Gutierrez, R. Lara-Estrada, E. Sacristán-Rockf and J. Yig, *RSC Advances*, 2015, 5, 17223-17227.
5. S. Zeng, D. Baillargeat, H.-P. Ho and K.-T. Yong, *Chemical Society Reviews*, 2014, 43, 3426-3452.
6. Z. Wang, X. Liu, M. Lv, P. Chai, Y. Liu, X. Zhou and J. Meng, *The Journal of Physical Chemistry C*, 2008, 112, 15171-15175.
7. D. A. Allwood, G. Xiong, M. D. Cooke, C. C. Faulkner, D. Atkinson, N. Vernier and R. P. Cowburn, *Science*, 2002, 296, 2003-2006.
8. J. M. Patete, J. Han, A. L. Tiano, H. Liu, M.-G. Han, J. W. Simonson, Y. Li, A. C. Santulli, M. C. Aronson, A. I. Frenkel, Y. Zhu and S. S. Wong, *Journal of Physical Chemistry C*, 2014, 118, 21695-21705.
9. T.-J. Park, G. C. Papaefthymiou, A. J. Viescas, A. R. Moodenbaugh and S. S. Wong, 2007, 7, 766-772.
10. T.-J. Park and S. S. Wong, 2006, 18, 5289-5296.
11. A. L. Tiano, G. C. Papaefthymiou, C. S. Lewis, J. Han, C. Zhang, Q. Li, C. Shi, A. M. M. Abeykoon, S. J. L. Billinge, E. Stach, J. Thomas, K. Guerrero, P. Munayco, J. Munayco, R. B. Scorzelli, P. Burnham, A. J. Viescas and S. S. Wong, *Chemistry of Materials*, 2015, 27, 3572–3592.
12. E.-K. Lim, Y.-M. Huh, J. Yang, K. Lee, J.-S. Suh and S. Haam, *Advanced Materials*, 2011, 23, 2436-2442.
13. J.-T. Jang, H. Nah, J.-H. Lee, S. H. Moon, M. G. Kim and J. Cheon, *Angewandte Chemie*, 2009, 121, 1260-1264.
14. A. L. Tiano, G. C. Papaefthymiou, C. S. Lewis, J. Han, C. Zhang, Q. Li, C. Shi, A. M. M. Abeykoon, S. J. L. Billinge, E. Stach, J. Thomas, K. Guerrero, P. Munayco, J. Munayco, R. B. Scorzelli, P. Burnham, A. J. Viescas and S. S. Wong, *Chemistry of Materials*, 2015, 27, 3572-3592.
15. A. Kale, S. Gubbala and R. D. K. Misra, *Journal of Magnetism and Magnetic Materials*, 2004, 277, 350-358.
16. G. C. Papaefthymiou, *Nano Today*, 2009, 4, 438-447.
17. T. Tago, T. Hatsuta, K. Miyajima, M. Kishida, S. Tashiro and K. Wakabayashi, *Journal of American Ceramics Society*, 2002, 85, 2188-2194.
18. A. Casu, M. F. Casula, A. Corrias, A. Falqui, D. Loche and S. Marras, *The Journal of Physical Chemistry C*, 2007, 111, 916-922.
19. S. J. L. Billinge and I. Levin, *Science*, 2007, 316, 561-565.
20. R. E. Dinnebier and S. J. L. Billinge, *Powder Diffraction: Theory and Practice*, Royal Society of Chemistry Cambridge, UK, 1 edn., 2008.

21. S. Tripathi, V. Petkov, S. M. Selbach, K. Bergum, M.-A. Einarsrud, T. Grande and Y. Ren, *Physical Review B*, 2012, 86, 094101/094101-094101/094108.
22. A. S. Masadeh, E. S. Bozin, C. L. Farrow, G. Paglia, P. Juhas, A. Karkamkar, M. G. Kanatzidis and S. J. L. Billinge, *Physical Review B*, 2007, 76, 115413/115411 - 115413/115411.
23. N. G. Jovic, A. S. Masadeh, A. S. Kremenovic, B. V. Antic, J. L. Blanusa, N. D. Cvjeticanin, G. F. Goya, M. V. Antisari and E. S. Bozin, *Journal of Physical Chemistry C*, 2009, 113, 20559-20567.
24. L. Kumar, P. Kumar, A. Narayan and M. Kar, *International Nano Letters*, 2013, 3, 8(1)-(8)12.
25. M. Gateshki, V. Petkov, S. K. Pradhan and T. Vogt, *Journal of Applied Crystallography*, 2005, 38, 772-779.
26. T. Yamashita and P. Hayes, *Applied Surface Science*, 2008, 254, 2441-2449.
27. R. D. Desautels, M. P. Rowe, M. Jones, A. Whallen and J. van Lierop, *Langmuir*, 2015, 31, 2879-2884.
28. P. S. Guo and C. X. Wang, *RSC Advances*, 2015, 5, 70661-70667.
29. R. D. Desautels, J. W. Freeland, M. P. Rowe and J. van Lierop, *Journal of Applied Physics*, 2015, 117, 17C728-(1-4).
30. Z. Liu, X. Duan, G. Qian, X. Zhou and W. Yuan, 2013, 24, 045609/045601-045609/045606.
31. C. Manjunatha, B. M. Nagabhushana, H. Nagabhushana and R. P. S. Chakradhar, *Journal of Materials Chemistry*, 2012, 22, 22392-22397.
32. E. J. H. Lee, C. Ribeiro, E. Longo and E. R. Leite, *Journal of Physical Chemistry B*, 2005, 109, 20842-20846.
33. B. Miao, W. Zeng, S. Hussain, Q. Mei, S. Xu, H. Zhang, Y. Li and T. Li, *Materials Letters*, 2015, 147, 12-15.
34. Z.-x. Yang, W. Zhong, Y.-x. Yin, X. Du, Y. Deng, C. Au and Y.-w. Du, *Nanoscale Research Letters*, 2010, 5, 961-965.
35. L. Hou, H. Hua, S. Liu, G. Pang and C. Yuan, *New J. Chem.*, 2015, 39, 5507-5512.
36. L. Liu, H. Z. Kou, W. Mo, H. Liu and Y. Wang, *Journal of Physical Chemistry B*, 2006, 110, 15218-15223.
37. D. Qin, J. Zhou, C. Luo, Y. Liu, L. Han and Y. Cao, *Nanotechnology*, 2006, 17, 674-679.
38. C. Bao, M. Jin, R. Lu, P. Xue, Q. Zhang, D. Wang and Y. Zhao, *Journal of Solid State Chemistry*, 2003, 175, 322-327.
39. X. Shi, M. Li, H. Yang, S. Chen, L. Yuan, K. Zhang and J. Sun, *Materials Research Bulletin*, 2007, 42, 1649-1656.
40. R. Liu, Y. Jiang, H. Fan, Q. Lu, W. Du and F. Gao, *Chemistry*, 2012, 18, 8957-8963.
41. C. Z. Wen, H. B. Jiang, S. Z. Qiao, H. G. Yang and G. Q. Lu, *Journal of Materials Chemistry*, 2011, 21, 7052.
42. X. Han, M. Jin, S. Xie, Q. Kuang, Z. Jiang, Y. Jiang, Z. Xie and L. Zheng, *Angew Chem Int Ed Engl*, 2009, 48, 9180-9183.
43. Q. Zhang, L. Han, H. Jing, D. A. Blom, Y. Lin, H. L. Xin and H. Wang, *ACS Nano*, 2016, 10, 2960-2974.

44. M. Mohapatra, D. Behera, S. Layek, S. Anand, H. C. Verma and B. K. Mishra, *Crystal Growth & Design*, 2012, 12, 18-28.
45. C. Pereira, A. M. Pereira, C. Fernandes, M. Rocha, R. Mendes, M. P. Fernández-García, A. Guedes, P. B. Tavares, J.-M. Grenèche, J. P. Araújo and C. Freire, *Chemistry of Materials*, 2012, 24, 1496-1504.
46. C. Liu and Z. J. Zhang, *Chemistry of Materials*, 2001, 13, 2092-2096.
47. N. Moumen and M. P. Pileni, *Chemistry of Materials*, 1996, 8, 1128-1134.

Chapter 5 – Synthesis and Charge Transfer in a Novel Class of Luminescent Perovskite-based Heterostructures Composed of Quantum Dots Bound to RE-Activated $CaTiO_3$ Phosphors

5.1 Introduction

In recent years, ternary metal oxides, including either ABO_3 or ABO_4 compositions, have been extensively investigated as a result of their exceptional dielectric, ferroelectric, pyroelectric, piezoelectric, magnetic, and semiconducting properties with possible applications as components in solid oxide fuel cells, gas sensors, steam electrolysis units, and photocatalysts for water splitting.[1, 2] In particular, within the ABO_3 perovskite structure, the A site cation is located in a 12-coordinated cubic octahedral geometry, while the B site cation is 6-fold coordinated with oxygen anions positioned within an octahedral geometry. Typically the larger cation resides in the A site, whereas the smaller cation is located in the center of the octahedra as the B site.[3, 4]

Various techniques, such as co-precipitation, impregnation, in situ preparation methods, microwave, sol-gel, solvothermal, hydrothermal, molten salt, and solid state-based syntheses have been employed to synthesize a number of classes of perovskites.[5-9] In particular, our lab has successfully achieved the generation of various motifs (i.e. nanotubes, nanowires, nanocubes, and nanoparticles) of the ABO_3 perovskite system, including $BiFeO_3$, $LiNbO_3$, $BaZrO_3$, $BaTiO_3$, $SrTiO_3$, and $SrRuO_3$ using facile and readily scalable techniques such as but not limited to sol-gel, hydrothermal, and molten salt type reactions as well as a combination thereof.[10-14]

Among these ABO_3 systems is the orthorhombic phase of calcium titanate ($CaTiO_3$), possessing a space group of *Pnma*. $CaTiO_3$ is a particularly important perovskite, due to its biocompatibility, and has been used for example as a coating for Ti

implants.[15, 16] Moreover, as a result of its wide band gap energy of ~3.7 eV,[16, 17] it has also been incorporated as a component of functional electronic devices.[18] In addition, it is also a key constituent of a synthetic rock known as Synroc, which is used to immobilize nuclear waste.[19, 20] Furthermore, it is a typical incipient ferroelectric whose dielectric constant increases with decreasing temperatures, i.e. from $\varepsilon_r \approx 170$ at 300 K to $\varepsilon_r \approx 330$ at 4.2 K, thereby leading to possible, potential applications in microwave devices.[20, 21]

Though these perovskite structures are relatively stable, the A and/or B site cation may undergo lattice substitution with foreign cations maintaining either a distinctive oxidation state or a singular ionic radius, while preserving its inherent crystalline structure.[5] Not surprisingly, a number of perovskite-type oxides, i.e. ABO_3 (with 'A'= Ca, Sr, or Ba; 'B' = Ti, Zr, or Si), have served as the host material for rare-earth-ion (Re) activators, such as Pr^{3+}, Eu^{3+}, and Tb^{3+}, and have evinced intense red and blue-green luminescent properties, depending on the identity of the dopant itself.[17, 18, 22-24] Specifically, red-emitting phosphors, incorporating Pr^{3+} and Eu^{3+}, are being explored for their applications in cathode ray tube (CRT) television displays.[25] Moreover, $CaTiO_3$ has also operated as a potential host lattice for large to medium-sized Re ions (i.e. La to Eu), which either selectively dope at the Ca-site via a Ca vacancy incorporation mechanism or integrate via a charge compensation mechanism when Re ions replace both the Ca and Ti site within the $CaTiO_3$ lattice structure, according to theoretical calculations.[20]

Similar perovskite systems, such as Eu-doped $BaTiO_3$, have also yielded a correlation between the europium ion dopant concentration and the corresponding luminescence, as measured via pair distribution function analysis coupled with steady state photoluminescence (PL). Indeed, as the lattice underwent expansion with an

increasing mol % of Eu (i.e. 1-3 mol %), there was a direct impact upon luminescence.[26] However, no substantive explanation has been put forward to explain the nature of how either A-site or A/B-site localization affects the magnitude of the resulting observed PL enhancements.

In general, the enhanced luminescent properties, observed within the combined host-rare earth ion dopant system, originates from the UV light-mediated promotion of an electron from the ground state of the host to the excited *5d* state of the Re ion, which overlaps with the conduction band of the host. As a result, the electron can completely delocalize within the conduction band and auto-ionize (or emission of the outer shell electrons), thereby giving rise to a state involving the simultaneous generation of Ln^{3+}, h^{+}, and free e^{-}. The capture of the free electron results in an energy emission due to excitonic recombination with some of the energy transferred to the re-emitting lanthanide *4f* state.[6, 27]

In an effort to potentially control and further enhance these desirable luminescent properties, studies have sought to alter the concentration of the rare earth ion, to vary the synthesis reaction temperature, as well as to add in co-dopant species (such as Bi^{3+}).[6,28] However, direct correlations between the synthesis technique and the resulting luminescence have yet to be thoroughly explored. The closest analogue to the current study in terms of intellectual direction and stated objectives is a recent work on calcium apatite nanoparticles (~50 nm) which had been either electrostatically adsorbed or grown in situ onto ~ 200 nm silica particles. Interpretation of the optical data on these systems did not yield any perceptible difference in the luminescence behavior either in the presence or absence of the silica spheres.[29]

As a result, our study is significant for three main reasons. *First*, to highlight the robustness and relative ease of formation of our heterostructures, we have focused on creating well defined and previously unreported motifs of RE (RE = Eu and Pr)-doped $CaTiO_3$ prepared using two distinctive and complementary potentially milder synthetic methodologies, i.e. molten salt and hydrothermal syntheses. Interestingly, each methodology possesses its own advantages and disadvantages. For the molten salt method, it is a simple, cost-effective, and readily scalable technique, that uses salt as the reaction medium itself for reagent dissolution and product precipitation. Moreover, this synthetic technique generates relatively high yields of products (minimum of ~200 mg per run), and enables the production of highly crystalline materials.[6] However, this method also gives rise to disadvantages such as insufficient size control and high nucleation rates, thereby resulting in agglomeration. By contrast, the hydrothermal method can lead to the production of crystalline, phase pure materials with little if any perceptible defects as well as to the fabrication of novel size-controlled morphologies. Nonetheless, at times, the size and shape distribution of materials prepared hydrothermally may be somewhat polydisperse.[2]

Second, we have synthesized novel heterostructures, comprised of cadmium selenide (CdSe) quantum dots (QDs) immobilized onto porous RE-doped $CaTiO_3$ micron-scale structures, the last of which have been fabricated using the molten salt technique. Based on our previous investigations, particularly with QDs attached onto carbon nanotubes (CNTs), we have observed that coupling constituent moieties with unique size and composition-dependent properties can yield products with unforeseen characteristics as compared with their individual components.[30, 31] This observation has

been the underlying theme of our systematic efforts to create novel and optically intriguing heterostructures created by attaching CdSe and CdS QDs onto various nanoscale motifs of (a) $CePO_4$, (b) $LaPO_4$, (c) $CaWO_4$ as well as (d) calcium tungstate/molybdate-based systems, which had been doped with RE (with RE = Eu, Ce, and/or Tb).[32-35] In that series of studies, we independently probed the effects of chemical composition, dopant identity, coverage, and morphology upon the resulting optical behavior.

Therefore, of relevance for the current study, we noted that not only charge transfer from CdSe to $LaPO_4$: Eu but also energy transfer from $LaPO_4$: Eu to CdSe QDs were substantially more efficient processes with 3D as compared with 1D (i.e. one-dimensional) heterostructures, possibly due to the nearly 3 times higher coverage density of QDs on the surfaces of the underlying 3D $LaPO_4$ motif, thereby contributing to its more effective absorption capability of $LaPO_4$: Eu emission.[32] Moreover, to further emphasize the significance of morphology, we noted that the observed PL quenching of 0D $CaWO_4$ is greater than that of 1D $CaWO_4$ within as-synthesized $CaWO_4$ – MPA-capped CdSe QD heterostructures, despite the slightly lower coverage and quantity of CdSe QDs attached and bound onto the underlying 0D versus 1D $CaWO_4$ templates. We ascribed such unexpected behavior mainly to the higher PL output and PL quantum yield (QY) associated with the larger crystallite size of 0D $CaWO_4$, which in turn generated more photoinduced charge carriers, thereby resulting in greater PL quenching as compared with the 1D $CaWO_4$ motif.[34] This finding is significant as it forms the basis of our study with 0D CdSe QDs on 0D $CaTiO_3$, Moreover, it begs the question of whether a

porous host material will experience the presence of heightened numbers of photoinduced charge carriers as well.

Third, it is worth mentioning that there have been only two prior reports on heterostructures, composed of as-prepared QDs coupled with perovskites, and these had been tailored for water splitting applications. Specifically, CdSe-$SrTiO_3$ and CdS-$BaSnO_3$ composite heterostructures gave rise to improved photoelectrochemical performances with photocurrent densities of ~5 mA/cm^2 and ~4.8 mA/cm^2 at 0 V, respectively.[36, 37] Herein, our emphasis is different and distinctive in that we have (i) purposely generated novel, previously unreported, crystalline, and porous spherical motifs of $CaTiO_3$ and (ii) subsequently taken advantage of the favorable luminescent characteristics of their doped analogues to create unusual perovskite-based heterostructures with unique optoelectronic properties. Moreover, we have sought to more precisely understand the nature of the charge transfer properties within these systems.

Specifically, with the addition of rare earth ion dopants, such as Pr^{3+} and Eu^{3+}, within the perovskite structure, it is expected that luminescence will be observed. In fact, with Eu as the main dopant, the red emission intensity upon excitation at 330 nm has been found to be ~2x greater than the corresponding intensity of structures that had been excited using either near UV-visible (i.e. 395 nm) or blue visible (i.e. 467 nm) wavelengths, thereby implying an efficient energy transfer from the host material to the dopant ions.[38, 39] By contrast, this wavelength-dependent excitation behavior, apparent with Eu, has not been definitively observed with Pr-doped materials. With the addition of an extra luminescent component, i.e. quantum dots, the recombination mechanisms will

be clearly affected, and it is therefore important to understand charge transfer in the underlying metal oxides incorporated within these heterostructures.

Therefore, herein, previously unreported porous spherical motifs of Eu and Pr-doped $CaTiO_3$ micron-scale structures have been prepared using both customized molten salt as well as modified hydrothermal methods. The photoluminescent properties of these materials were separately measured and compared. We found that the molten salt method gave rise to metal oxides characterized by clearly superior photoluminescence performance as compared with hydrothermally derived samples. Therefore, for our subsequent photophysical studies, CdSe QDs were coupled onto the outer surfaces of these RE-doped $CaTiO_3$ motifs, prepared via the molten salt method, so as to correlate luminescence as well as electron and/or charge transfer behavior with structure and morphology within these systems.

5. 2. Results & Discussion

5.2.1. Investigation of the Reaction Mechanism: Molten Salt

As previously discussed in Chapter 2, the MS method generally relies upon the choice of the salt medium to dictate the reaction temperature as well as chemical reactivity. Consequently, NaCl was chosen due to its melting point of ~ 801°C, yielding an excellent solvent at lower temperatures (~820 °C) with respect to conventional solid-state reactions (i.e. 1,000 °C to 1200 °C). For our MS synthesis, the salt was added in excess (~80 wt %), and the temperature was increased above its melting point to ensure uniform size distributions and morphologies for the RE-$CaTiO_3$ systems.[40]

In addition to the salt, the metal precursors' intrinsic solubility enhances material transport within the salt medium.[40] Though this type of information is not heavily documented in literature, it is clear that for the calcium oxalate precursor, it is indeed highly soluble with a solubility of ~2.03 x10^4 mol/dm^3 in NaCl.[41, 42] In order to gain some insight to the plausible reaction formation of $CaTiO_3$ nanostructures therefore, we propose a potential synthesis reaction defined by the following Equations 5.1 and 5.2:

$$CaC_2O_4 \rightarrow CaO + CO_{2\,(g)} + CO_{(g)} \qquad (5.1)$$

$$CaO + TiO_2 \rightarrow CaTiO_3 \qquad (5.2)$$

First, the calcium oxalate (CaC_2O_4) undergoes thermal decomposition, thereby forming carbonaceous species and calcium oxide (CaO). Subsequently after CaO production, the CaO and TiO_2 nucleate and undergo Ostwald ripening to from $CaTiO_3$.[40]

In an effort to determine whether this reaction is indeed viable under these temperature conditions, Gibbs free energy values were calculated at the precise reaction temperature of ~820 °C. To ascertain the reaction characteristics of our process (i.e. whether it be spontaneous or non-spontaneous), thermodynamic values (Table 5.1) for the metal precursors and the desired products, in the absence of the molten salt, were applied to the Gibbs free energy equation. From these calculations, it was observed that Equation 5.1 is indeed a non-spontaneous reaction with $\mathbf{\Delta G^\circ}$ = ~215.45 kJ/mol, wherein energy is needed to overcome the activation barrier and ultimately favor product formation. However, once the intermediate species, CaO, is formed, the subsequent reaction (Eqn. 5.2) is spontaneous and favorable at 820°C with $\mathbf{\Delta G^\circ}$ = -338.07 kJ/mol, thereby producing the perovskite material.[43]

Compound	ΔH_f° (kJ mol^{-1})	S° (J K^{-1} mol^{-1})
CaC_2O_4	-1674.9	156.5
CaO	-635.1	38.21
TiO_2	-938.7	49.9
$CaTiO_3$	-1661.4 ± 1.5[43 44]	317.7[43]
$CO_{2\,(g)}$	-393.52	213.80
$CO_{(g)}$	-110.53	197.65

Table 5.1. Thermodynamic parameters associated with possible intermediate species in the formation of $CaTiO_3$. The parameters were obtained from Lange's Handbook of Chemistry,[45] unless otherwise noted.

Initially, there should be cause for concern as thermal decomposition of CaC_2O_4 is generally an unfavorable reaction, thereby possibly preventing perovskite synthesis. However, it is commonly known that the calcium precursor undergoes thermal decomposition wherein the carbon species are burned off between 400 – 600 °C and CaO begins to form.[46] Moreover, based upon previous reports, calcium oxalate decomposition is predicted to follow a 3-step process (Eqns. 5.3 to 5.5):

Step I: $CaC_2O_4\,H_2O \rightarrow H_2O + CaC_2O_4$ (5.3)

Step II: $CaC_2O_4 \rightarrow CO_{(g)} + CaCO_3$ (5.4)

Step III: $CaCO_3 \rightarrow CO_{2\,(g)} + CaO$ (5.5)

These steps include a series of dehydration, decarbonylation, and decarboxylation processes, with the rate limiting step being the decarbonylation process (Step II).[47] In the work by *Zadykowicz et al.,* the thermal reactivity of CaC_2O_4 was investigated by plotting the temperature dependence of the Gibbs free energy, i.e., $\mathbf{\Delta_{r,\,T}G^\circ}$ in particular.

Specifically, $\mathbf{\Delta_{r,\,T}G^\circ}$ may be calculated using the following equation:

$$\mathbf{\Delta_{r,\,T}G^{\circ}} = -RT\ln {}_{T}K^{\circ} \quad (5.6)$$

wherein $\mathbf{\Delta_{r,\,T}G^{\circ}}$ is directly related to the equilibrium constant (${}_{T}K^{\circ}$), R represents the gas constant, and T is indicative of the temperature.

From these studies, the temperatures needed to decompose CaC_2O_4 in the form of dehydration, decarbonylation, and decarboxylation processes were ~353 K, ~435 K, and ~1,083 K, respectively.[47] We can confirm therefore that our reaction temperature herein of ~820 °C is indeed a favorable one for all decomposition steps to occur.

In addition to investigating the reaction mechanisms, we also carefully tested and varied a number of reaction parameters such as the molar ratios of titanium precursors, the nature of the surfactants, as well as the reaction times themselves in an effort to generate pure, homogeneous, and uniform RE-doped $CaTiO_3$, in terms of size, shape, and morphology. A summary of our data from these collective runs as well as from complementary XRD results is presented in both Table 5.2 as well as in Figure 5.1, respectively.

#	Precursors (Ratio is 1: 1 unless otherwise noted)	Titanium Precursor	Temp (ºC)	Surfactant (mL)	Time (h)	Cooling Rate (ºC/min)	Product (composition, morphology, size)
Molten Salt Method							
(Titanium precursor): Pr doped sample							
A	Calcium Oxalate and TiO_2	P25 TiO_2	820	No surfactant	3.5	Natural cooling	Average Diameter: 65 ± 9 nm 50% cubes vs 50% particles– Pure $CaTiO_3$
B	Calcium Oxalate and TiO_2	P25 TiO_2	820	No surfactant	3.5	**Quenched**	Average Diameter: 65 ± 9 nm 60% cubes vs 40% particles– Pure $CaTiO_3$
C	Calcium Oxalate and TiO_2	P25 TiO_2	820	NP-9 (1.75 mL)	3.5	Natural cooling	Average Diameter: 58 ± 20 nm 30% cubes vs. 70% spheres – Pure $CaTiO_3$
D	Calcium Oxalate and TiO_2	P25 TiO_2	820	NP-9 (2.33 mL)	3.5	Natural cooling	Average Diameter: 76 ± 22 nm 100% particles - Pure $CaTiO_3$
E	Calcium Oxalate and TiO_2	P25 TiO_2	820	Triton X-100	3.5	Natural cooling	Pure $CaTiO_3$
F	**Calcium Oxalate and Bulk TiO_2**	**Bulk TiO_2**	**820**	**Triton X-100**	**3.5**	**Natural cooling**	**Average Diameter: 210 ± 22 nm 100% Roughened particles – Pure $CaTiO_3$**
G	Calcium oxalate and TiO_2	P25 TiO_2	820	Triton X-100	3.5	Natural cooling	Average Diameter: 54 ± 13 nm 50% cubes vs. 50% particles - Pure $CaTiO_3$
H	Calcium Oxalate and TiO_2	5 nm TiO_2 NPs	820	NP-9	3.5	Natural cooling	Avg. Diameter: 56 ± 33 nm 30% cubes vs. 70% particles – Pure $CaTiO_3$
Eu doped sample							
1	Calcium Oxalate and 2% Europium Nitrate	Bulk TiO_2	820	Triton X-100	3.5	Natural cooling	Average Diameter: 210 ± 32 nm 100% Roughened particles –Pure $CaTiO_3$
2	Calcium Oxalate and 4% Europium Nitrate	Bulk TiO_2	820	Triton X-100	3.5	Natural cooling	Average Diameter: 220 ± 26 nm 100% Roughened particles –Pure $CaTiO_3$
3	Calcium Oxalate and 6% Europium Nitrate	Bulk TiO_2	820	Triton X-100	3.5	Natural cooling	Average Diameter: 290 ± 35 nm 100% Roughened particles –Pure $CaTiO_3$

Table 5.2. Detailed Reaction parameters and product description for all reactions conducted using the molten salt method preparing either Eu or Pr-doped $CaTiO_3$.

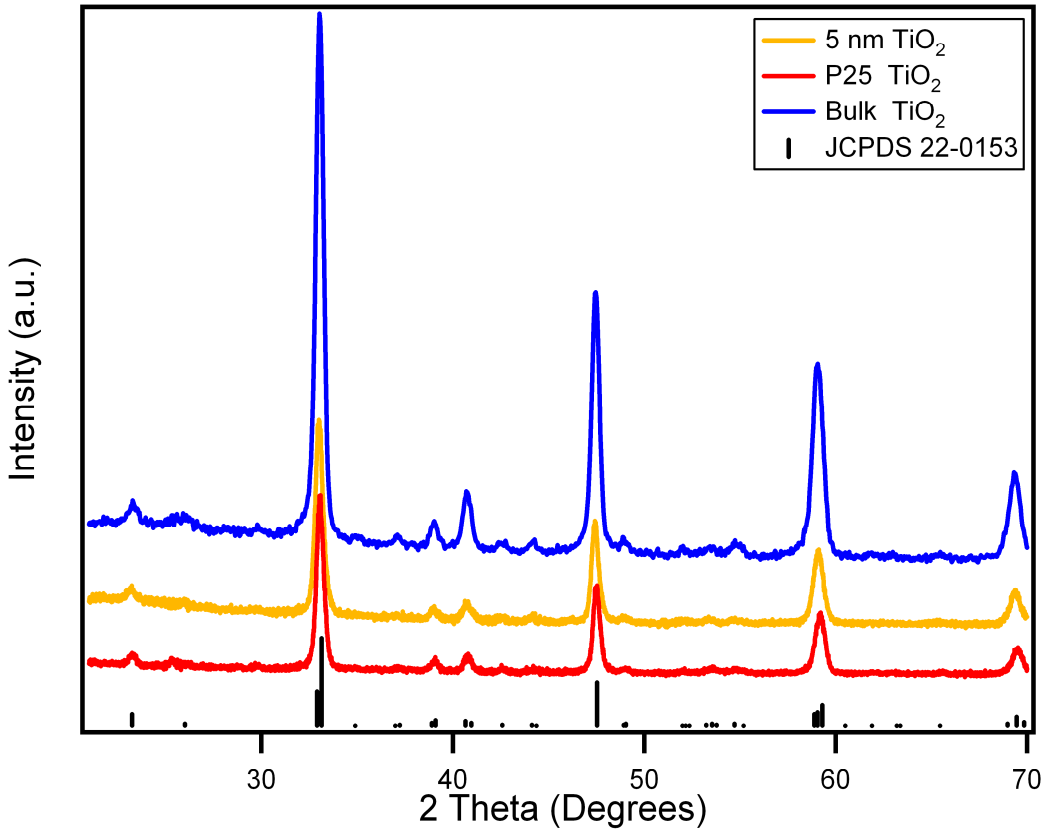

Figure 5.1. XRD results for samples, prepared using the molten salt method with various titanium precursors. Supplemental image reproduced from Ref. 74 with permission from The Royal Society of Chemistry.

5.2.1.1. Selection of the TiO_2 Precursor

From the TEM and XRD (Figure 5.1) results, it is clear that the size of the titanium precursor source dictates the corresponding size of the desired perovskite product. Specifically, when using either 5 nm as-prepared TiO_2 or commercially available (~25 nm) P25 TiO_2, the resulting perovskite materials were formed with average diameters of ~ 54 nm and ~56 nm, respectively. However, upon inclusion of bulk TiO_2 precursor, nanostructures possessing an average diameters of ~ 226 nm are produced. Additionally, the perovskite materials produced using bulk TiO_2 precursor

yielded a more uniform morphology (i.e. micron spheres) by comparison with that generated using smaller sized Ti precursors. However, in terms of composition, no matter what the Ti source used, all products yielded a phase pure $CaTiO_3$ in accordance with the JCPDS #22-0153 (Figure 5.1).

5.2.1.2. Inclusion of Surfactant

Inspired by the goal and objective of achieving uniform and homogeneous particle control, surfactants were also investigated for improvements in this area. First, within a surfactant-free control experiment, various different types of morphologies were observed, such as cubes and particles (Sample B, Table 5.2). A similar trend was also noted upon inclusion of a nonionic surfactant (i.e. Triton X-100 or NP-9), depending upon the Ti source (Sample D and F). Ultimately, we found that Triton X-100 exhibited a significant degree of control and led to the production of uniform and monodisperse $CaTiO_3$ microspheres in the presence of bulk TiO_2 precursor.

Interestingly, the nature of the interaction of surfactants with bulk material could be dependent upon the surfactant's ability to form "reverse micelle" networks, in which the distances between the reactive metal ion species could be controlled with potential consequences for the resulting homogeneity of the desired product.[48] Additionally, from a morphological standpoint, the presence of surfactant more specifically assists in the ability to generate fine precursor particles during the mechanical grinding process, thereby inhibiting aggregation and subsequently allowing for discrete nanostructure formation.[49] Furthermore, surfactants may also play a role in terms of catalyzing the reaction process.[48, 50]

In spite of the potential role provided by surfactant inclusion, it is clear that surfactant decomposition takes place between 400-600°C. As a result, the question is: what then is the role of surfactant upon the overall morphology? This answer under molten salt conditions has still yet to be determined since the high molten salt reaction temperatures render it unlikely for surfactants to remain as intact and discrete entities within the molten flux.[10] Nonetheless, though the actual function of the surfactant within the molten salt synthesis process is still debatable, we note that many different types of nanostructures have been synthesized under such conditions including but not limited to barium ferrite ($BaFe_{12}O_{19}$) nanoparticles, bismuth ferrite ($Bi_2Fe_4O_9$) nanocubes, Eu-doped yttrium oxide (Y_2O_3), ytterbium silicate, and sodium titanate ($Na_2Ti_3O_7$ & $Na_2Ti_6O_{13}$) nanowires.[12, 48, 49, 51, 52]

5.2.2. Investigation of the Reaction Mechanism: Hydrothermal

For the hydrothermal method, initially a stock solution of calcium hydroxide ($Ca(OH)_2$) was used as the calcium precursor. However, the precursor would precipitate out of solution, thereby leading to increases in the amount of TiO_2 and CaO impurities. As a result, calcium chloride ($CaCl_2$) was used in the presence of a base (*i.e.* NaOH), a Ti source (*i.e.* Ti foil), as well as an oxidizing agent (*i.e.* H_2O_2). The reaction proceeded as follows, as described by Eqns 5.7 to 5.9:

$$CaCl_2 + 2NaOH \rightarrow Ca(OH)_2 + 2NaCl \quad (5.7)$$

$$Ca(OH)_2 \rightarrow CaO + H_2O \quad (5.8)$$

$$CaO + 2H_2O_2 + Ti + \rightarrow CaTiO_3 + 2H_2O \quad (5.9)$$

In these reactions, the calcium chloride first reacted with the base to form a more soluble $Ca(OH)_2$ solution. Subsequently, thereafter, the $Ca(OH)_2$ underwent dehydration to form CaO. Based upon previous reports, the H_2O_2 is also responsible for etching the Ti foil, thereby producing spherical Ti, which then reacts with CaO to ultimately form the perovskite, $CaTiO_3$. Moreover, with this relatively simple straightforward reaction, we can also negate the possibility for competing reactions. In particular, we note the potential for Ti to interact with NaOH and H_2O_2 thereby forming $Na_2Ti_3O_7$. However, this reaction would most certainly lead to the formation of residual sodium titanate species within the desired product. We hypothesize that with our method, the initial reaction with $CaCl_2$ and NaOH prevents Ti-associated competing side reactions from occurring. For additional information concerning hydrothermal reaction parameters, a summary of our data from these collective runs is recorded in Table 5.3.

#	Precursor Ratios (1M NaOH unless otherwise noted)	Ti Precursor	Temp. (ºC)	Surfactant (mL)	Time (hr)	Cooling Rate (ºC/min)	Product (composition, morphology, size)
Hydrothermal Method							
F	0.25 $Ca(OH)_2$ Stock Solution	Ti foil	130	No surfactant	**4**	Natural cooling	Avg. Diameters: 278 ± 87 nm Large aggregates- $CaTiO_3$-- with TiO_2 and CaO impurities
G	0.5 M $CaCl_2$ – 30 mL	Ti foil	180	No surfactant	4	Natural cooling	Avg. Diameters: 178 ± 87 nm Cubes - No $CaTiO_3$-- with TiO_2 and CaO impurities – Irreproducible
H	0.5M $CaCl_2$ – 10 mL	Ti foil	180	No surfactant	4	Natural cooling	Avg. Diam.: 500 ± 154 nm Microspheres with CaO_4 impurity-- without HCl wash
I	0.25 $CaCl_2$ – 10 mL	Ti foil	180	No surfactant	4	Natural cooling	Avg. Diam.: 380 ± 140 nm Microspheres with a reduced intensity of CaO impurities – **without HCl wash**
J	**0.25 $CaCl_2$ – 10 mL**	**Ti foil**	**180**	**No surfactant**	**4**	**Natural cooling**	**Avg. Diam.: 330 ± 97 nm Microspheres – with HCl wash**
K	0.25 $CaCl_2$ – 10 mL	Ti foil	180	No surfactant	10	Natural cooling	Avg. Diam.: 500 ± 45 nm Microspheres with a reduced intensity of CaO impurities – **without HCl wash**

Table 5.3. Detailed reaction parameters and product descriptions for all reactions conducted using the hydrothermal method involved with preparing Pr-$CaTiO_3$ microspheres. Table reproduced from Ref. 74 with permission from The Royal Society of Chemistry.

5.3. Structural Characterization

5.3.1. Optimized Pr-doped $CaTiO_3$

In effect, we were able to successfully demonstrate the synthesis of pure Pr doped $CaTiO_3$ using both the molten salt (MS) and hydrothermal methodologies. The corresponding XRD patterns, shown in Figures 5.2A and B and associated with both synthetic techniques, unequivocally reveal that our as-prepared samples evinced a pure cubic perovskite structure, possessing a space group of *Pnma*. These findings agree with the JCPDS standard #22-0153 with little if any detectable impurities observed in either sample. Additionally, the crystallite sizes for both hydrothermal and molten salt-prepared perovskites were calculated using the Debye-Scherrer Equation, and these data yielded crystallite domain size dimensions of ~29.9 and ~38.1 nm, respectively. Upon closer analysis of the XRD spectra (Figure 5.3), it is evident that for both the molten salt and hydrothermally prepared samples, the Pr replaces the underlying Ca ions, constrains the lattice and results in a peak, which is upshifted to ~33°.

Moreover, the sizes and morphologies of both molten salt and hydrothermally prepared Pr-doped $CaTiO_3$ motifs were investigated using a combination of TEM and SEM. With respect to the SEM analysis, representative images are shown in Figures 5.4A and B. Specifically, Figure 5.4A can be ascribed to the molten salt-prepared Pr-doped $CaTiO_3$ micron-scale spheres, possessing average diameters of 226 ± 30 nm. Analysis of the corresponding TEM image in the inset to Figure 5.4A yielded average diameters of 210 ± 22 nm, which are consistent with the SEM data. Based upon XRD, it is clear that these structures are composed of constituent ~38.1 nm particles closely fused within a spherical motif. From both electron microscopy images, it is moreover clear that the

external surfaces of the micron-scale spheres appear to be slightly roughened and corrugated with a surface area of ~ 8.7 m^2/g (Table 5.4). This magnitude of surface area is comparable to previous literature reports on perovskites that had been previously prepared at similar reaction temperatures.[53]

As for the hydrothermally synthesized Pr-doped $CaTiO_3$ samples, the representative SEM image in Figure 5.4B confirms the formation of porous micron-scale spheres with average diameters of 330 ± 97 nm. The TEM image in the inset to Figure 5.4B gives forth similar morphologies maintaining average diameters of 304 ± 85 nm. From these images, it is apparent that the resulting porous micron-scale spheres likely are composed of high-surface-area aggregates, characterized by smaller constituent nanoparticulate units, measuring ~29.9 nm, concentrically arranged and assembled. This observation was corroborated by our BET data, wherein our as-prepared perovskites exhibited a relatively large specific surface area of ~ 51.9 m^2/g (Table 5.4), a finding consistent with the intrinsically porous nature of our $CaTiO_3$ perovskite structures.[54]

In addition, a series of high-resolution TEM (HRTEM) images for both molten salt prepared and hydrothermal treated perovskite samples (i.e. Figures 5.5B & E) revealed expected interlayer *d*-spacings, corresponding to the orthorhombic phase of the host material, $CaTiO_3$. Specifically, the measured *d*-spacings of 0.278 nm and 0.279 nm, respectively, were consistent with the anticipated (112) lattice plane within $CaTiO_3$. Complementary SAED patterns (Figures 5.5C & F) highlight the presence of distorted diffraction spots, which can be potentially attributed to the overall polycrystallinity of the micron-scale structures. Nevertheless, careful analysis of the diffraction patterns indicates that the data are consistent with the expected perovskite host material, i.e. $CaTiO_3$.

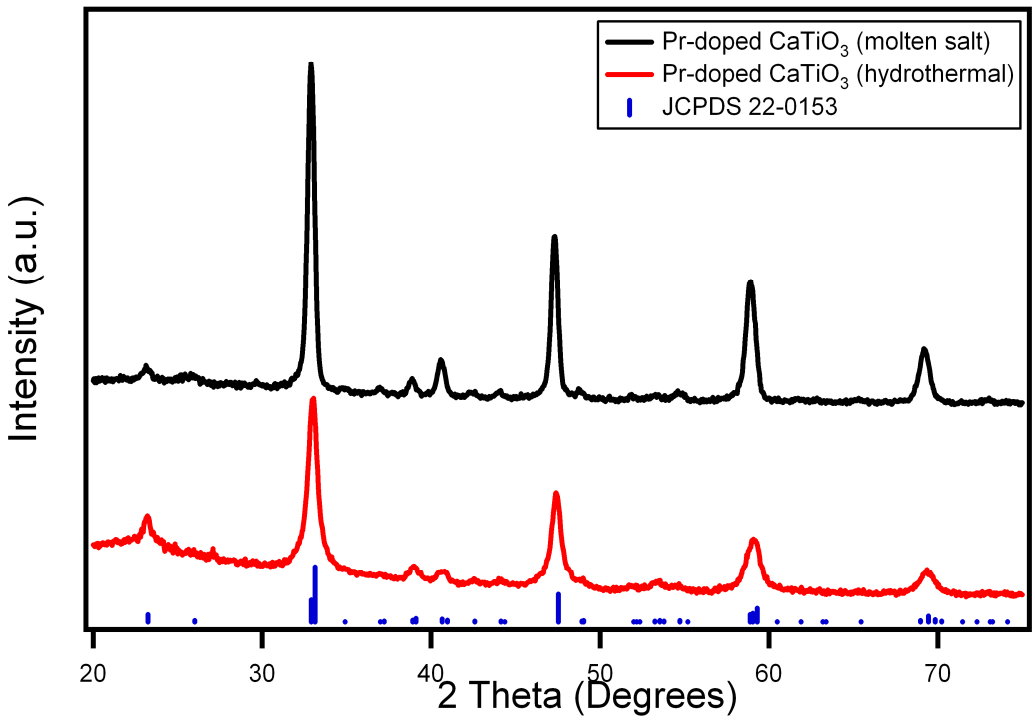

Figure 5.2. XRD patterns of as-prepared, luminescently desirable 0.2 molar percent Pr-doped $CaTiO_3$ microspheres, generated via molten salt (top, black) and hydrothermal (middle, red) methodologies. The JCPDS no. 22-0153 database standard is shown for the bulk orthorhombic perovskite, $CaTiO_3$ (bottom, blue). Image reproduced from Ref. 74 with permission from The Royal Society of Chemistry.

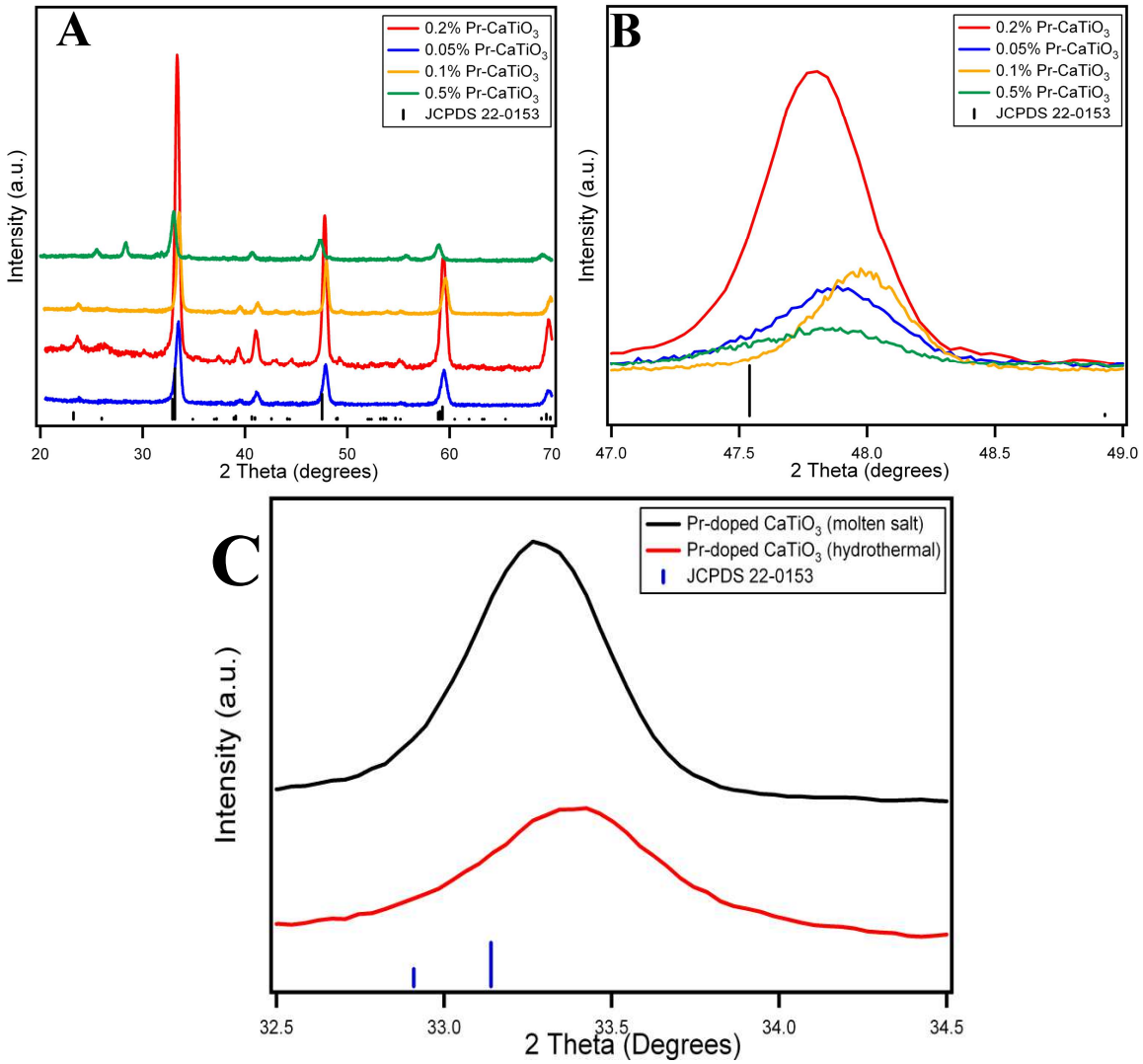

Figure 5.3. X-Ray Diffraction patterns of (A) 0.2%, 0.05%, 0.1%, and 0.5% Pr-doped $CaTiO_3$; associated peak shifts (B) for a signal centered at a 2θ value of ~47 degrees; as well as peaks shifts (C) for the molten salt-prepared (black) and hydrothermally-generated (red) 0.2% Pr-doped $CaTiO_3$ samples, centered at a 2θ value of ~33 degrees. Supplemental image reproduced from Ref. 74 with permission from The Royal Society of Chemistry.

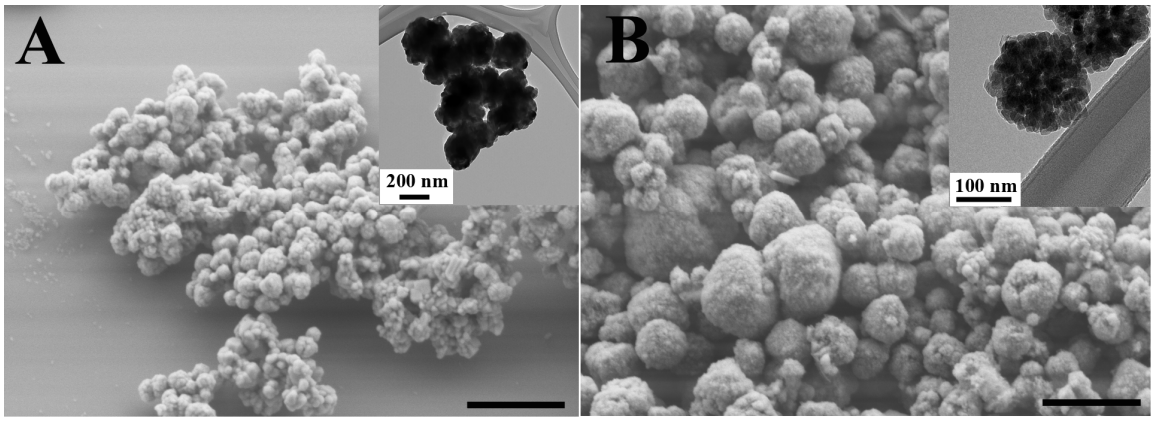

Figure 5.4. Representative SEM images of (A) molten salt-derived Pr-doped $CaTiO_3$ and (B) hydrothermally-treated Pr-doped $CaTiO_3$ with the corresponding TEM images highlighted in the insets to (A) and (B). Scale bar is 1 μm for each SEM image shown. Image reproduced from Ref. 74 with permission from The Royal Society of Chemistry.

Name	Surface Area (m^2/g)
Pr-doped $CaTiO_3$: MSS (molten salt syn.) method	8.79
Pr-doped $CaTiO_3$: Hydrothermal method	51.9
Eu-doped $CaTiO_3$: MSS (molten salt syn.) method	9.56

Table 5.4. BET surface area analysis of as-prepared samples of lanthanide ion-doped $CaTiO_3$. Table reproduced from Ref. 74 with permission from The Royal Society of Chemistry.

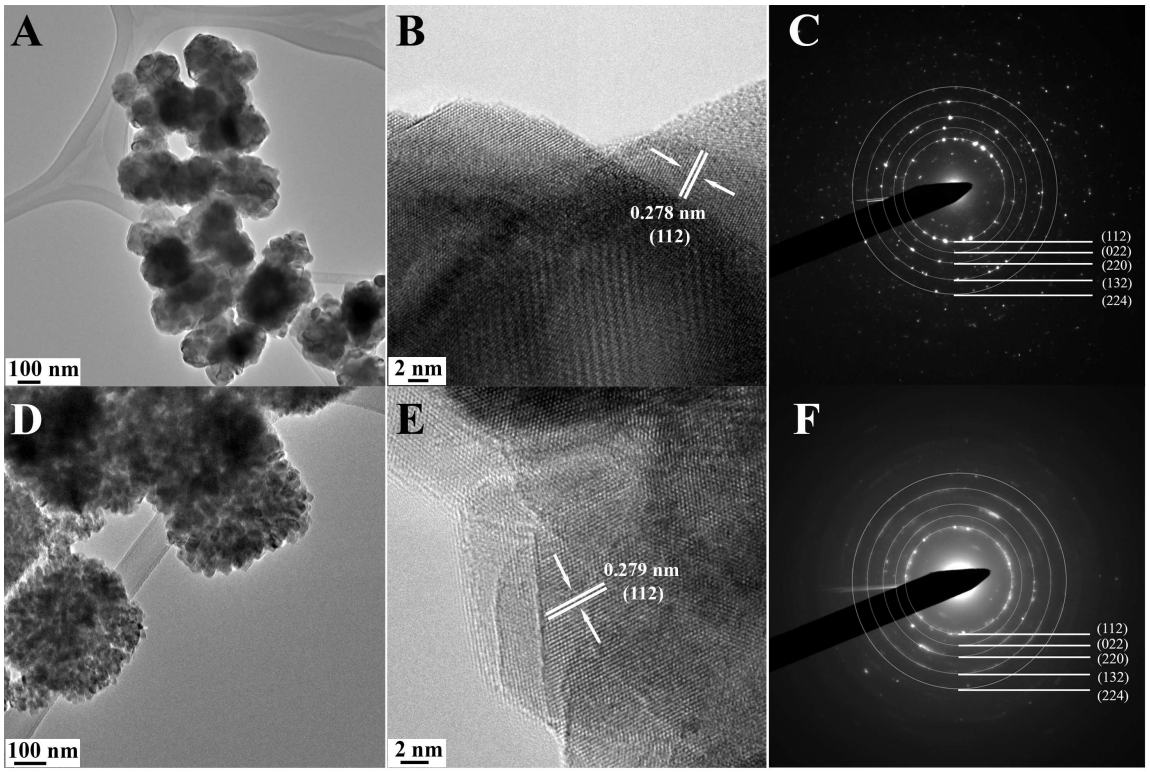

Figure 5.5. Representative (A and D) TEM and (B and E) HR-TEM images, as well as the corresponding SAED (C and F) patterns, associated with bare Pr-doped $CaTiO_3$ prepared using both molten salt and hydrothermal methods, respectively. Image reproduced from Ref. 74 with permission from The Royal Society of Chemistry.

5.3.2. Eu-doped $CaTiO_3$

To deal with the issue of possible dopant-induced structural distortions, we should note that the Eu-doped $CaTiO_3$ also evinced a pure cubic perovskite structure itself, and that the structural characterization data agreed with the JCPDS standard without the presence of any detectable impurities (Figure 5.6A). By analogy with the Pr-doped sample, the XRD spectra highlights a upshifted peak position centered at a 2θ value of ~33°, indicative of a lattice expansion wherein the Eu (~109 pm) ion substitutes for the larger Ca (~140 pm) ion at the A site. Various molar concentrations of Eu^{3+} have been successfully incorporated within the $CaTiO_3$ lattice. Based on the XRD data (Figure 5.7),

for all of the molar % concentrations probed, the crystal lattice becomes more spatially constrained, through the preferential replacement of the Ca ion with Eu at the A site.[55-57]

The size and morphology of our molten salt-prepared Eu-doped $CaTiO_3$ motifs were investigated using a combination of TEM and SEM data. With respect to the SEM (Figure 4B), the roughened spherical motifs averaged ~290 ± 35 nm in diameter, whereas with TEM (inset of Figure 5.6B), the structures measured ~315 ± 27 nm in diameter. Additionally, the SEM analysis (Figure 5.8A and C) of a series of analogous Eu-doped $SrTiO_3$ and $BaTiO_3$ microspheres revealed similar size dimensions to that of $CaTiO_3$–based motifs, with overall diameters noted to be ~262 ± 37 nm and ~243 ± 32 nm, respectively. The corresponding XRD patterns, shown in Figures 5.8B and D, reveal that the chemical compositions of our as-prepared samples agree with the JCPDS standards #73-0661 and #31-0174 with little if any detectable unforeseen impurities observed in either sample analyzed, i.e. Eu-doped $SrTiO_3$ and $BaTiO_3$, respectively.

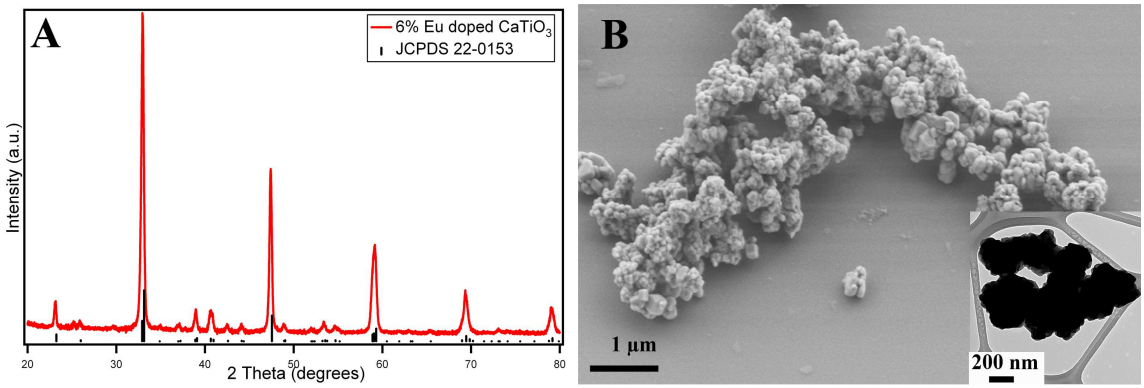

Figure 5.6. Representative (A) XRD pattern, as well as (B) SEM and (inset of B) TEM images of Eu-doped $CaTiO_3$, prepared using the molten salt technique. Image reproduced from Ref. 74 with permission from The Royal Society of Chemistry.

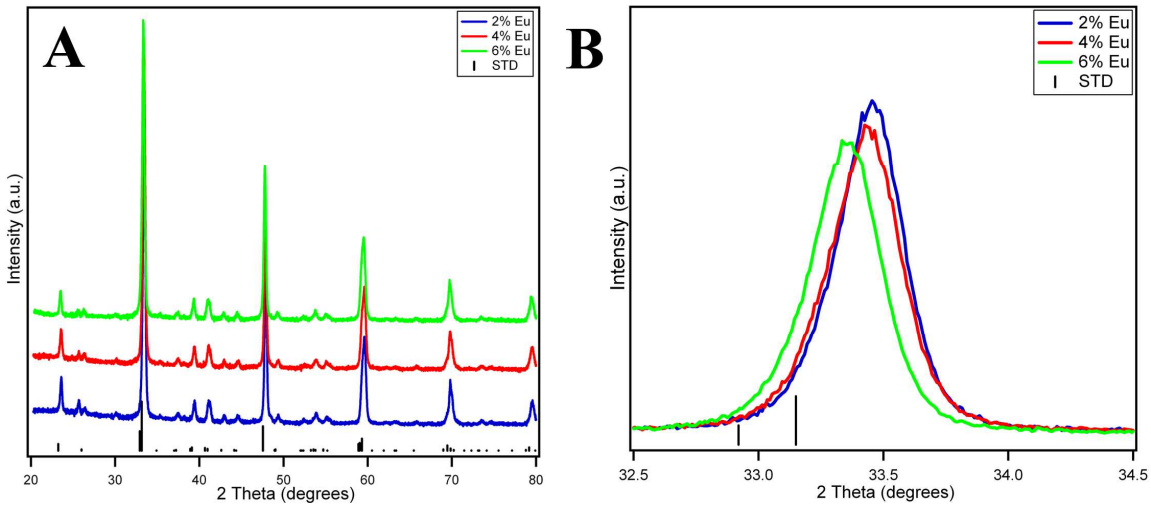

Figure 5.7. X-Ray Diffraction patterns of (A) 0.2%, 0.05%, 0.1%, and 0.5% Eu-doped $CaTiO_3$ and associated peak shifts for a signal centered at a 2θ of ~33 degrees. Supplemental image (SI) reproduced from Ref. 74 with permission from The Royal Society of Chemistry.

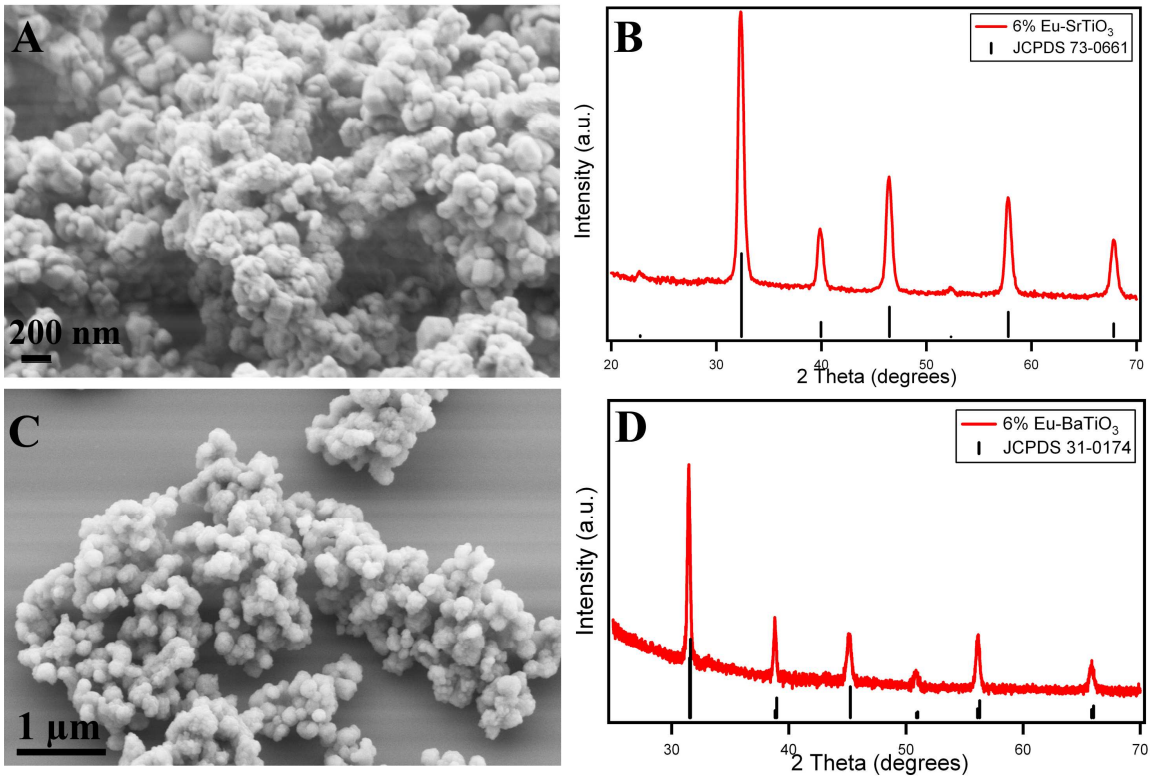

Figure 5.8. Representative SEM (A and C) and XRD patterns (B and D) of Eu-doped $SrTiO_3$ and $BaTiO_3$, respectively, using the molten salt synthesis technique. Image reproduced from Ref. 74 with permission from The Royal Society of Chemistry.

5.3.3. CdSe QD - Perovskite Heterostructures

Both of the Pr: $CaTiO_3$ - CdSe and Eu: $CaTiO_3$ - CdSe heterostructures were formed using a procedure developed by our group and which has been previously utilized and reported for the creation of composite-based systems.[32, 33, 35, 58] According to Figure 5.9, the CdSe quantum dots immobilized onto the outer surfaces of the $CaTiO_3$ exist as either small aggregates or clusters of several dots, as opposed to individual QDs. This phenomenon has also been observed in our previous studies, involving ligand exchange and the formation of associated heterostructures. This observation has been attributed to QD aggregation during the ligand exchange process.[32] High-resolution TEM images have demonstrated that the *d*-spacing of the underlying material, i.e. 0.385 nm, can be well correlated with the (101) lattice plane of $CaTiO_3$, while the measured *d*-spacings of individual dots within the group of particles can be ascribed to the CdSe (100) lattice plane. Additionally, the indexed selected area electron diffraction (SAED) pattern is consistent with the presence of both $CaTiO_3$ and CdSe.

STEM images along with their corresponding elemental maps are highlighted in Figures 5.10A-E and 5.11A-E, wherein we find an even, uniform, and homogeneous spatial distribution of the various constituent elements (i.e. not only Ca, Ti, and O but also Cd and Se) within the CdSe-modified, Pr and Eu-doped $CaTiO_3$ heterostructures, which is, as expected. We note that a reduced Cd and Se intensity would likely be indicative of the lower overall concentration of quantum dots and suggestive of a quantitatively decreased particulate coverage onto the underlying titanate motifs. Nevertheless, our data are supportive of a fairly even and spatially uniform distribution of

this element within the $CaTiO_3$ host. Indeed, results on the presence and localization of Pr and Eu elements can be found in particular with Figures 5.12 and 5.13, respectively.

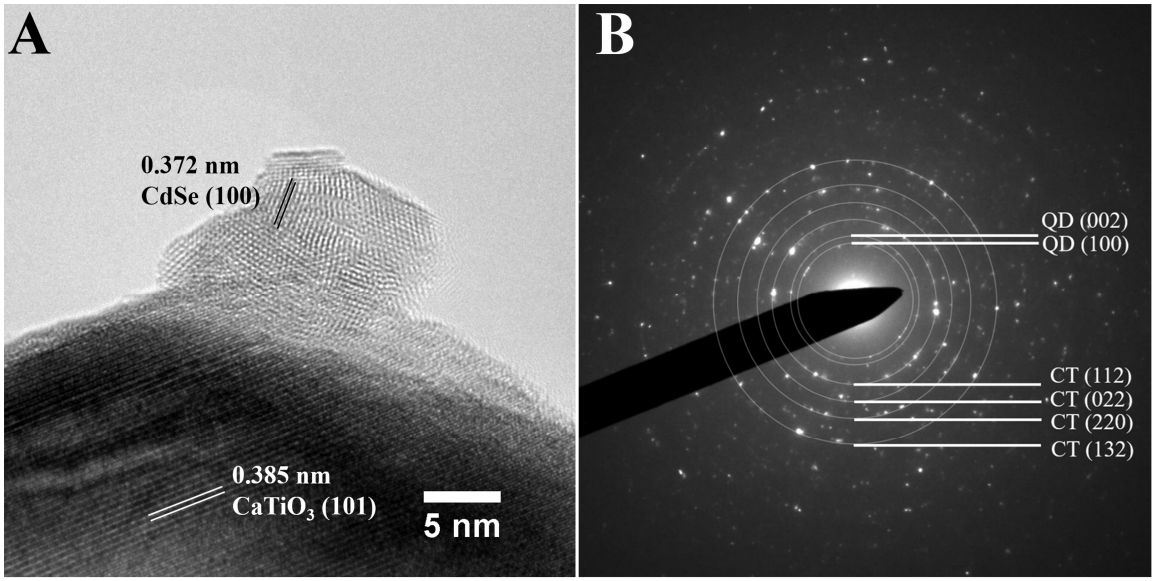

Figure 5.9. Representative (A) HR-TEM image as well as the corresponding SAED (B) pattern, associated with heterostructures composed of CdSe QD attached onto Pr-doped $CaTiO_3$ porous spherical motifs. Image reproduced from Ref. 74 with permission from The Royal Society of Chemistry.

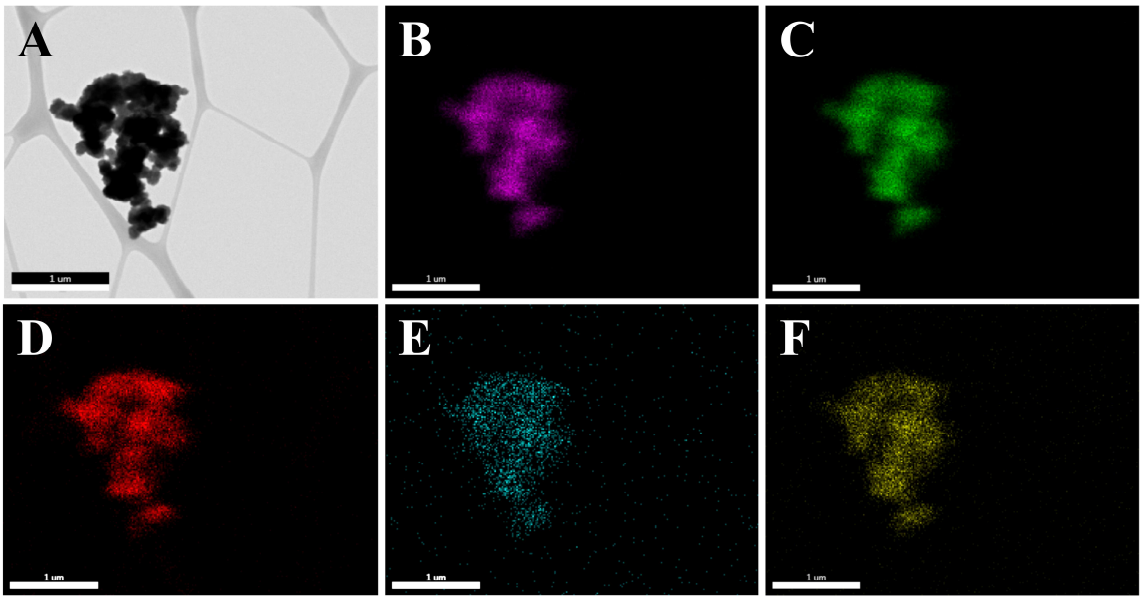

Figure 5.10. (A) Dark-field STEM image of CdSe QDs anchored onto Pr-$CaTiO_3$ heterostructures. Elemental mapping of the same region as measured by energy dispersive X-ray spectroscopy, highlighting the spatial elemental distribution of (B) Ca, (C) Ti, (D) O, (E) Cd, and (F) Se, respectively. Scale bar is 1 μm for each image. Image reproduced from Ref. 74 with permission from The Royal Society of Chemistry.

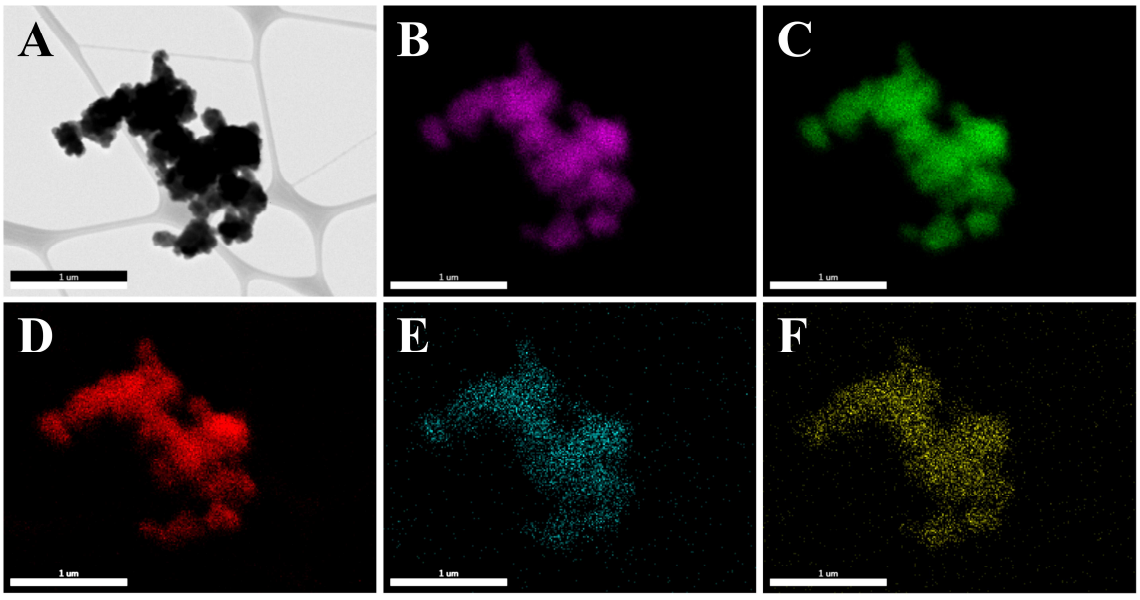

Figure 5.11. (A) Dark-field STEM image of CdSe QDs anchored onto Eu-doped $CaTiO_3$ heterostructures. Elemental mapping of the same region as measured by energy dispersive X-ray spectroscopy, highlighting the spatial elemental distribution of (B) Ca, (C) Ti, (D) O, (E) Cd, and (F) Se, respectively. Scale bar is 1 μm for each image. Image reproduced from Ref. 74 with permission from The Royal Society of Chemistry.

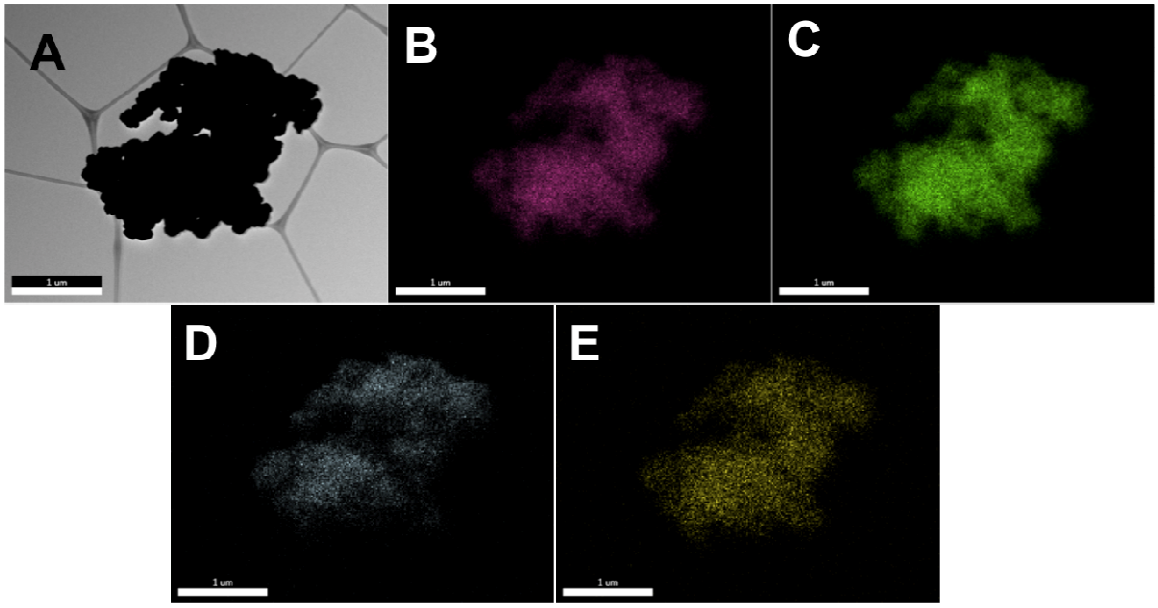

Figure 5.12. (A) Dark-field STEM image of CdSe QDs anchored onto Pr-doped $CaTiO_3$ heterostructures. Elemental mapping of the same region, as measured by energy dispersive X-ray spectroscopy, highlighting the spatial elemental distribution of (B) Ca, (C) Ti, (D) O, and (E) Pr, respectively. Scale bar is 1 μm for each image. SI image reproduced from Ref. 74 with permission from The Royal Society of Chemistry.

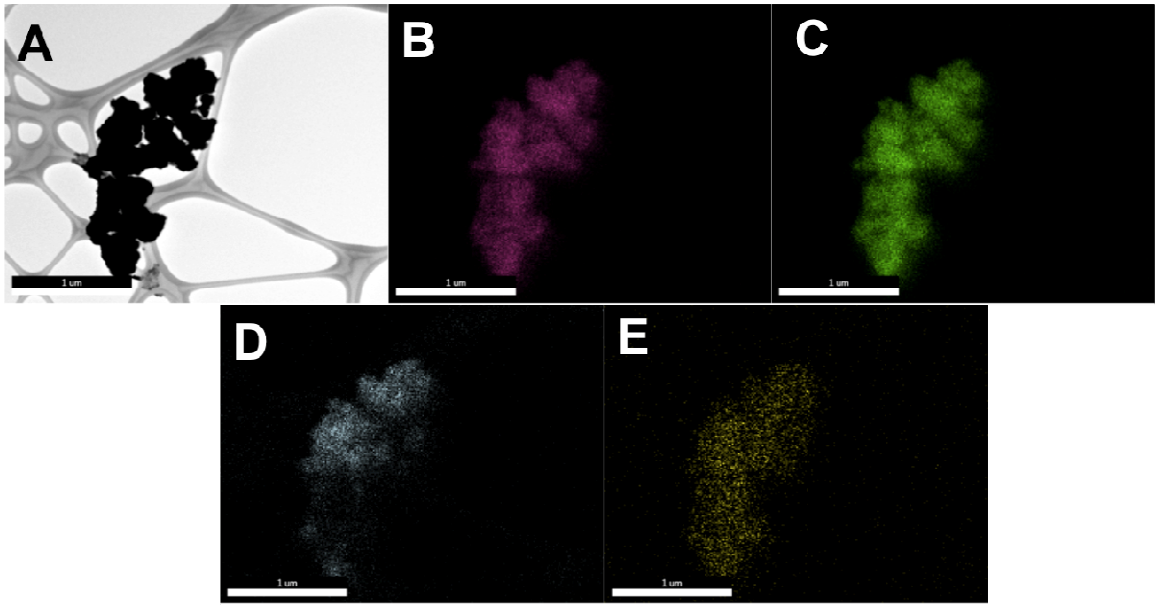

Figure 5.13. (A) Dark-field STEM image of CdSe QDs -Eu-doped $CaTiO_3$ heterostructures. Elemental mapping of the same region highlighting the spatial elemental distribution of (B) Ca, (C) Ti, (D) O, and (E) Eu, respectively. Scale bar is 1 μm for each image. SI image reproduced from Ref. 74 with permission from The Royal Society of Chemistry.

5.3.4. Optical data collected on Pr-doped $CaTiO_3$ and Corresponding Heterostructures

The incorporation of Pr^{3+} ions within $CaTiO_3$ microspheres was further confirmed via PL measurements for samples prepared by both molten salt and hydrothermal methods. Indeed, both spectra (Figure 5.14) display red emission peaks, located at ~611 nm, corresponding to the $^1D_2$ to $^4H_3$ transitions of the Pr^{3+} ion.[59-61] However, the PL emission intensity associated with the molten salt sample appears to be approximately three times greater than that observed for the corresponding hydrothermally prepared perovskite counterpart. This finding may be possibly related to inherent structural differences of the perovskite products themselves, such as variations in the inherent constituent crystallite domain size (i.e. ~38 nm versus 29.9 nm, respectively) for instance, associated with the disparate reaction temperatures used to prepare these 2 different samples, namely 820 °C versus 180 °C for the molten salt versus hydrothermal reactions respectively.

Upon closer analysis of the relevant XRD data and specifically of the peak positioned at ~33°, there appears to be a more dramatic upshift associated with the hydrothermal sample as compared with its molten salt-prepared counterpart. These results are consistent with a relatively higher degree of substitution (i.e. 0.2 mol % concentration) of Pr for the underlying Ca framework ions associated with the hydrothermal sample as compared with its molten salt derived analogue (Figure 5.2). Though each synthesis technique uses the same amount of Pr precursor, it can be inferred based on the XRD peaks, that a decreased Pr concentration is integrated within the molten salt prepared perovskite sample.

Hence, the quantity of Pr in and of itself is insufficient to explain the dramatic increase in the red luminescence. A more plausible explanation for this observed difference in the red emission intensity can be put forth, based upon cumulative XRD and BET analysis. Specifically, we note that the hydrothermally-derived sample maintained a high surface area, a large degree of polycrystallinity, as well as the presence of multiple facets, which may have introduced surface defects, such as oxygen vacancies, that could have acted as surface trap sites for excited electrons within the Pr-doped $CaTiO_3$ itself, thereby potentially inducing unfavorable PL quenching.[62] Therefore, based on this insight into sample quality, in order to facilitate our optical data interpretation and analysis, the CdSe QDs were subsequently attached onto pure and crystalline molten salt-prepared samples so as to better understand the nature of potential energy and charge transfer within the resulting heterostructures.

Nonetheless, for both synthesis techniques developed, another PL emission peak was observed at ~563 nm (Figure 5.14), and this signal could be attributed to electron-hole recombination by energetic defects within the $CaTiO_3$ matrix. These surface defects (i.e. indicative of structural disorder induced at either a short or intermediate range) are primarily caused by the presence of titanium (Ti^{3+}) *d*-orbital surface states appearing at relatively higher oxygen vacancy concentrations.[63, 64] Moreover, the PL emission peak of the bare $CaTiO_3$ was observed at ~561 nm (Figure 5.15), again further confirming the expected identity of the peak profile associated with Pr-doped $CaTiO_3$ samples.[63]

Additionally, PL emission spectra were collected on various mole percent concentrations (i.e. 'x' = 0.05, 0.1, 0.2, and 0.5) of Pr-doped $CaTiO_3$ materials, obtained using an excitation wavelength of 325 nm, as shown in Figure 5.16. By analogy with

previous Pr-doped $CaTiO_3$ samples analyzed in the literature, the PL emission resulted in peaks positioned at ~563 and ~611 nm, corresponding to the intrinsic $CaTiO_3$ perovskite structure and to the $^1D_2$ to $^3H_4$ transition of Pr^{3+}, respectively. As expected, the measured PL intensity increased with increasing dopant molar percent concentrations, i.e. from 0.05 to 0.2 mol%, with 0.2 mol % evincing the highest PL red emission intensity observed. It is noteworthy that when the concentration was further increased to ~0.5 mol %, the PL signal apparently decreased, possibly due to a concentration quenching effect, wherein the Pr^{3+} acted as a trapping center and consequently, the excess energy dissipated non-radiatively.[27, 65] As a result, in order to maximize signal-to-noise ratios and therefore to acquire quantitative insights into as-obtained data, the acceptably performing 0.2 mol % Pr doped $CaTiO_3$ was used as the model system with which to subsequently attach MPA-capped CdSe QDs in order to observe potential charge and/or energy transfer behavior.

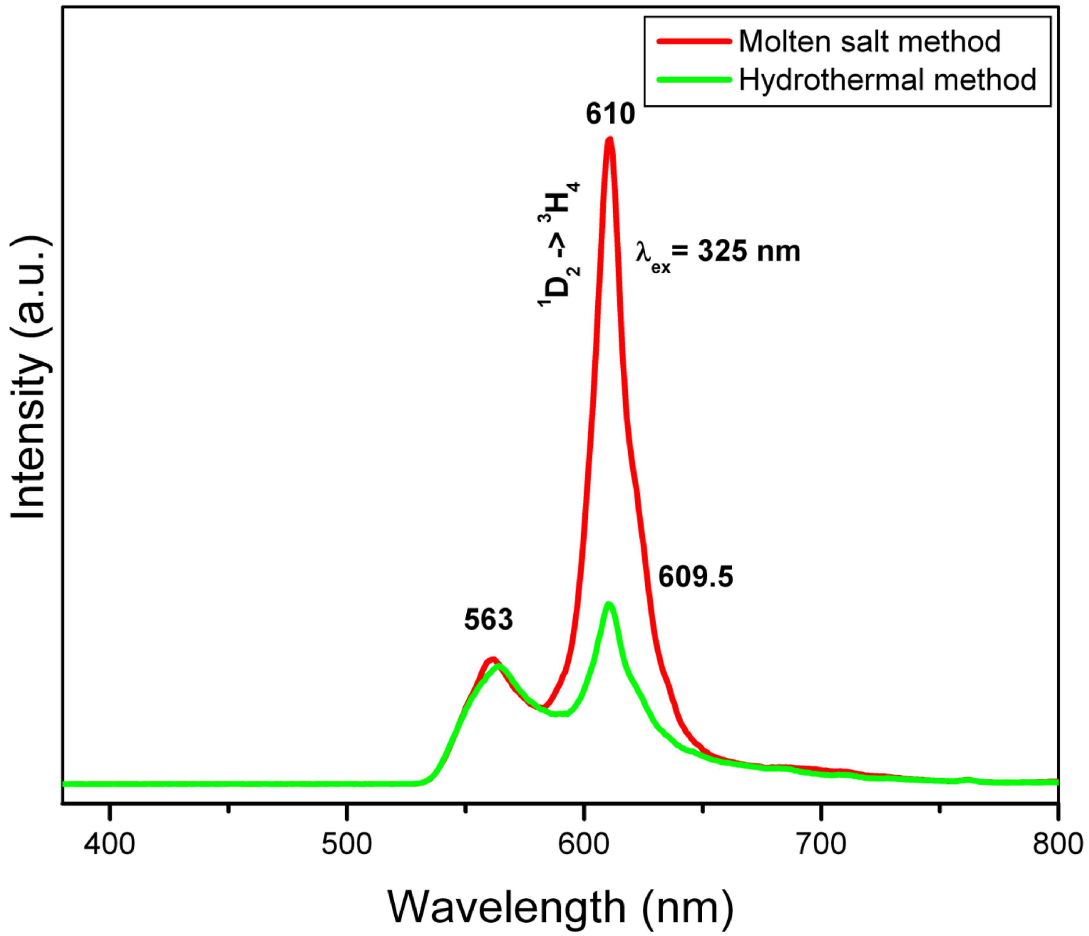

Figure 5.14. Photoluminescence emission of 0.2 mol % Pr-doped $CaTiO_3$ prepared by molten salt and hydrothermal methods, respectively, and collected at an excitation wavelength of 325 nm. Image reproduced from Ref. 74 with permission from The Royal Society of Chemistry.

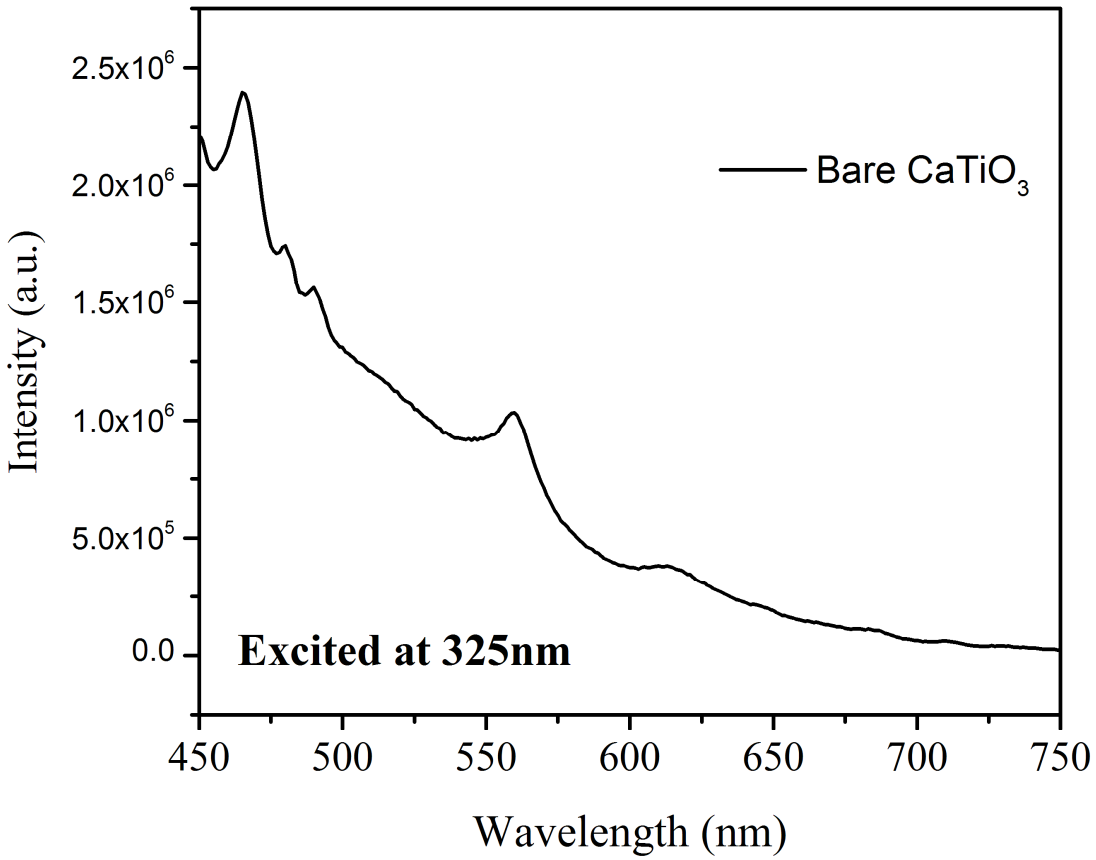

Figure 5.15. Photoluminescence emission profile of bare $CaTiO_3$. SI image reproduced from Ref. 74 with permission from The Royal Society of Chemistry.

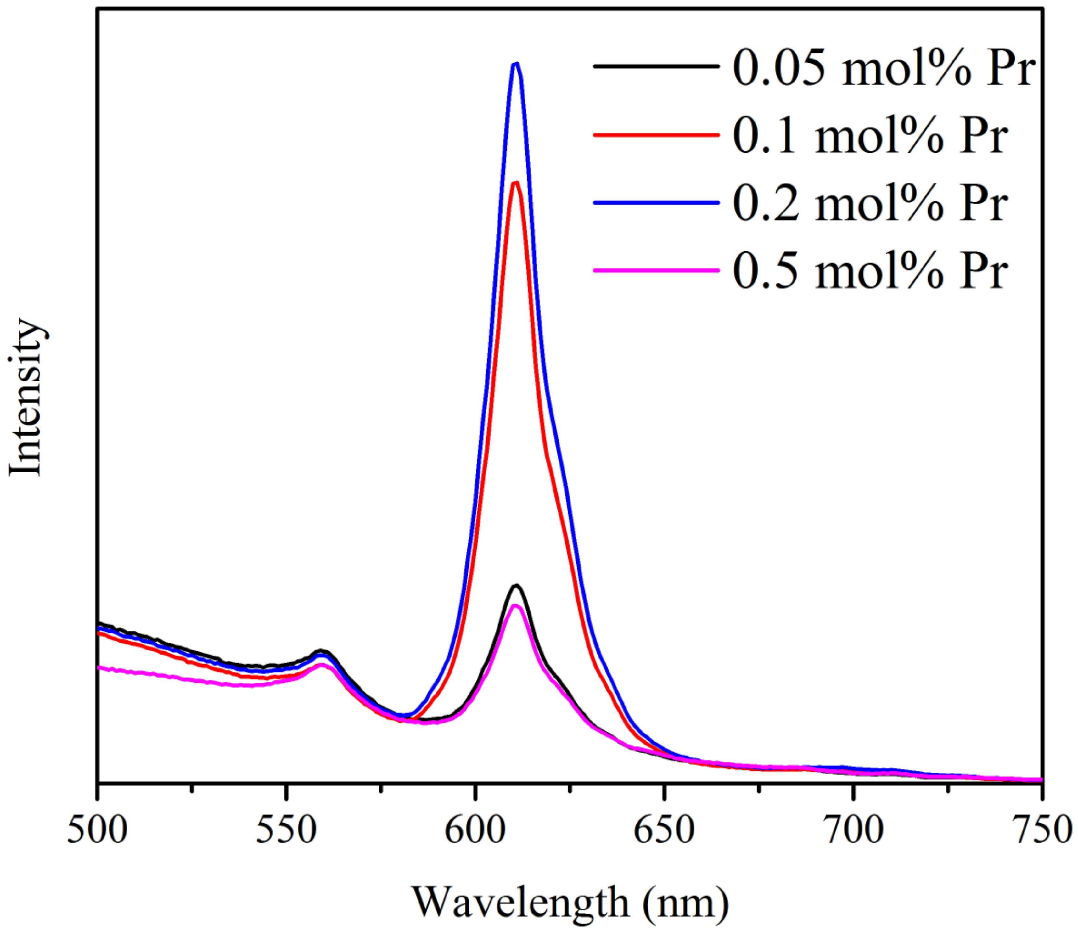

Figure 5.16. Photoluminescence emission data collected with various concentrations of Pr-doped $CaTiO_3$ prepared using the molten salt reaction protocol with data acquired at an excitation wavelength of 325 nm. Image reproduced from Ref. 74 with permission from The Royal Society of Chemistry.

The steady state PL of MPA-capped CdSe QDs and of the complementary MPA-capped CdSe QD-porous Pr-doped $CaTiO_3$ heterostructures were collected upon excitation at 460 nm, shown in Figure 5.17A, a wavelength chosen in order to induce QD emission. This specific wavelength was primarily used to obtain the emission profile of only CdSe QDs themselves. At this wavelength, the absorption of $CaTiO_3$ is negligible, because the excitation energy at 460 nm is significantly lower than that needed to properly excite Pr-doped $CaTiO_3$ itself (i.e. 325 nm). According to Figure 5.17A, within

experimental error, the PL intensity and position of the MPA-capped CdSe QD -Pr-doped $CaTiO_3$ heterostructures are similar to that of the MPA-capped CdSe QDs alone. Analogous optical behavior has been observed with our prior work on comparable MPA-capped CdSe QD - $CaWO_4$ heterostructures.[58]

Upon excitation at 325 nm (Figure 5.17B), the as-obtained PL spectrum of the composite heterostructure exhibits a pair of emission peaks localized at 553 nm and 611 nm that can be ascribed to contributions from CdSe QDs and Pr-doped $CaTiO_3$. It is evident that the PL spectrum of the composite heterostructure incorporates a convolution of signals derived from both constituent components. Moreover, when compared with the PL emission profile of each individual component subunit, namely CdSe QDs and $CaTiO_3$ themselves, it is apparent that the PL intensities of all of the observed peaks within the heterostructure have been quenched to some extent. Comparable behavior has been previously observed with our analogous QD-$CePO_4$: Tb systems in which we attributed the 'quenching' effect to charge transfer between CdSe and $CePO_4$: Tb. By analogy, under 325 nm irradiation, it is plausible to postulate that the excited electrons within the CB of Pr-doped $CaTiO_3$ are transferred and favorably donated to the corresponding CB of CdSe QDs, thereby resulting in a reduction in the $CaTiO_3$: Pr^{3+} emission intensity within the resulting heterostructures themselves, since the CB of $CaTiO_3$ is higher in energy than the analogous CB of CdSe, as shown in Figure 5.24A.

Nonetheless, by contrast with the case of $CePO_4$ attached to QDs, the possibility of hole transfer from CdSe QDs to Pr-doped $CaTiO_3$ in our current system herein is rather low, because the VB of our QDs is higher than that of the corresponding VB of Pr-doped $CaTiO_3$ (Figure 5.23). Therefore, any observed quenching phenomena associated

with our CdSe QDs upon 325 nm excitation would likely arise from either (i) an electron transfer (as opposed to a hole transfer) process emanating from CdSe QDs to Pr-doped $CaTiO_3$ or (ii) the possibility of a higher fraction of increased non-radiative decay processes. As highlighted in Figure 5.24A, the photo-generated electrons within CdSe QDs most likely possess a higher intrinsic energy as compared with the conduction band of $CaTiO_3$, a scenario which should give rise to plausible electron transfer.

It is worth mentioning that we have ruled out large and significant contributions from any possible energy transfer between CdSe and $CaTiO_3$. Indeed, as evinced by previous report[66], in heterostructures incorporating either luminescent organic dyes or a bound system of inorganic materials and quantum dots, CdSe QDs nominally act as the energy transfer donors, if such a process is favored to occur at all. However, in our specific case, the spectral overlap between the emission spectra of CdSe QDs (λ_{em} = 553 nm) and the corresponding absorption spectra of Pr-doped $CaTiO_3$ (λ_{abs} ~ 325 nm) is in fact rather minimal, and in effect, there is little if any overlap. Therefore, the energy transfer process in and of itself is unlikely to be a major contributor to the PL quenching within these heterostructures.

In order to better support our assertion that only charge transfer occurs within our composite system, excitation spectra of all the individual components of these heterostructures were collected. As we have observed in Figures 5.18 and 5.19C, the CdSe quantum dots do not appear to give rise to absorption at either 611 nm or 613 nm, namely the specific emission peak positions of Pr-doped $CaTiO_3$ and Eu-doped $CaTiO_3$, respectively. Similarly, neither Pr-doped $CaTiO_3$ nor Eu-doped $CaTiO_3$ can be excited by the absorption of light centered at 553 nm, which denotes the emission peak position of

MPA-capped CdSe quantum dots. Because these 2 materials are excited at essentially very different wavelengths, it is likely that there is a lack of a spectral overlap (and hence, substantive interaction) between the underlying $CaTiO_3$ host and the immobilized CdSe QDs, thereby essentially ruling out the likelihood of energy transfer. We believe this assertion corroborates our overall narrative, and highlights the relatively greater role and importance of charge transfer herein.

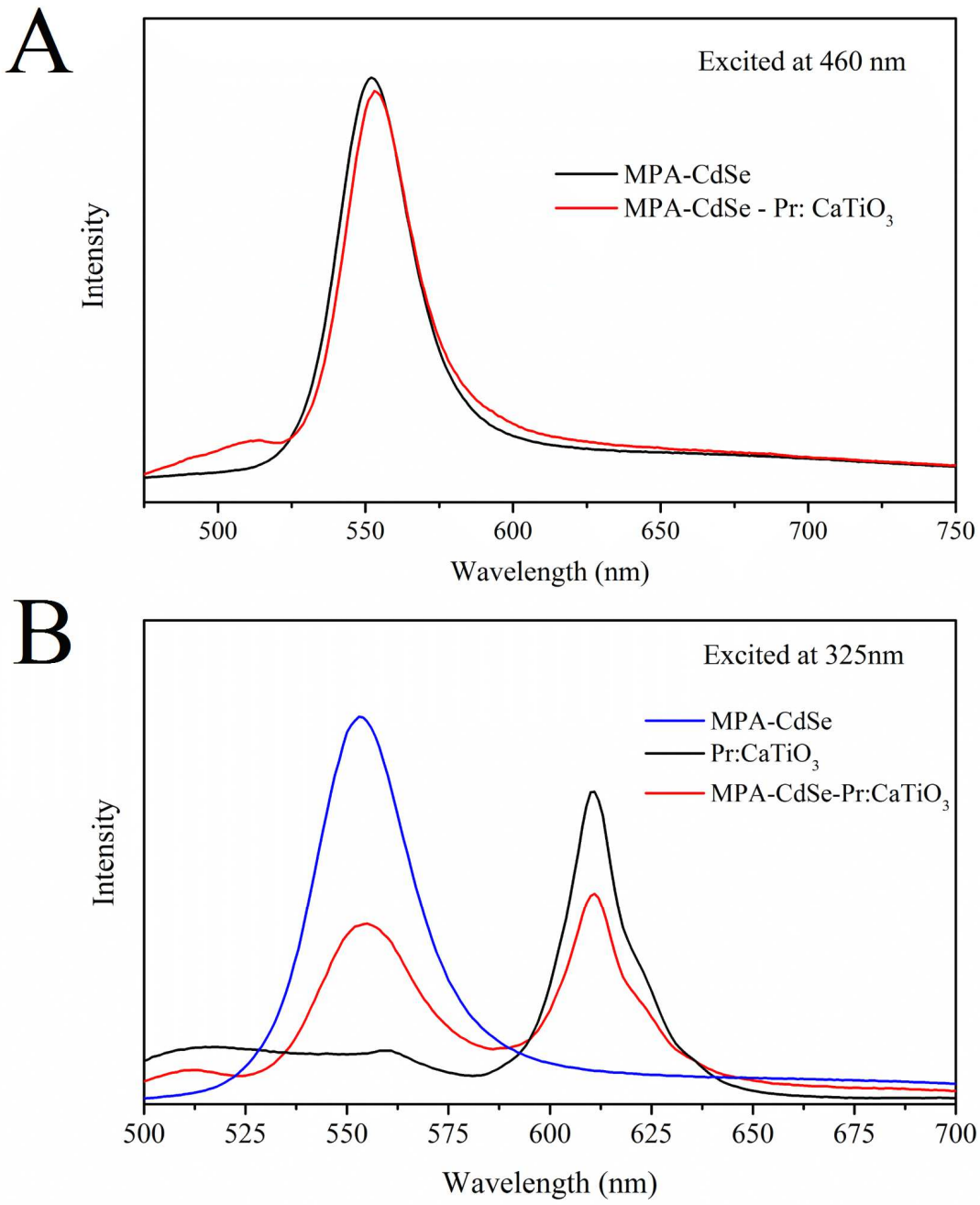

Figure 5.17. PL emission spectra of MPA-capped CdSe QDs, Pr-doped $CaTiO_3$, as well as MPA-capped CdSe QD –Pr-doped $CaTiO_3$ heterostructures under (A) 460 and (B) 325 nm excitation, respectively. Image reproduced from Ref. 74 with permission from The Royal Society of Chemistry.

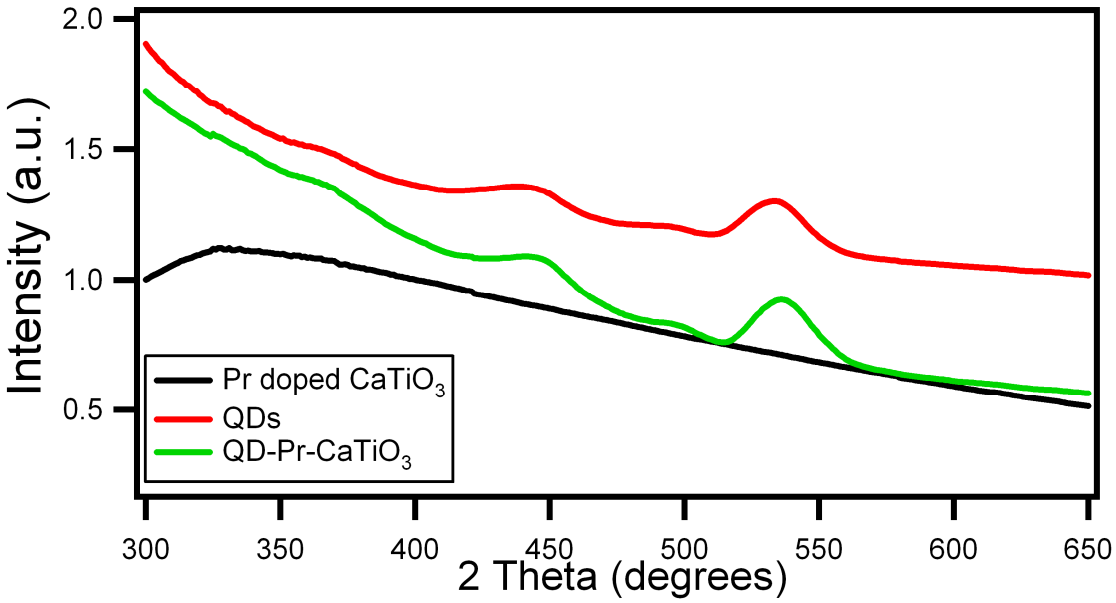

Figure 5.18. UV-Visible spectra of Pr-doped $CaTiO_3$, bare CdSe QDs, as well as Pr-doped $CaTiO_3$ structures, decorated with CdSe QDs. SI image reproduced from Ref. 74 with permission from The Royal Society of Chemistry.

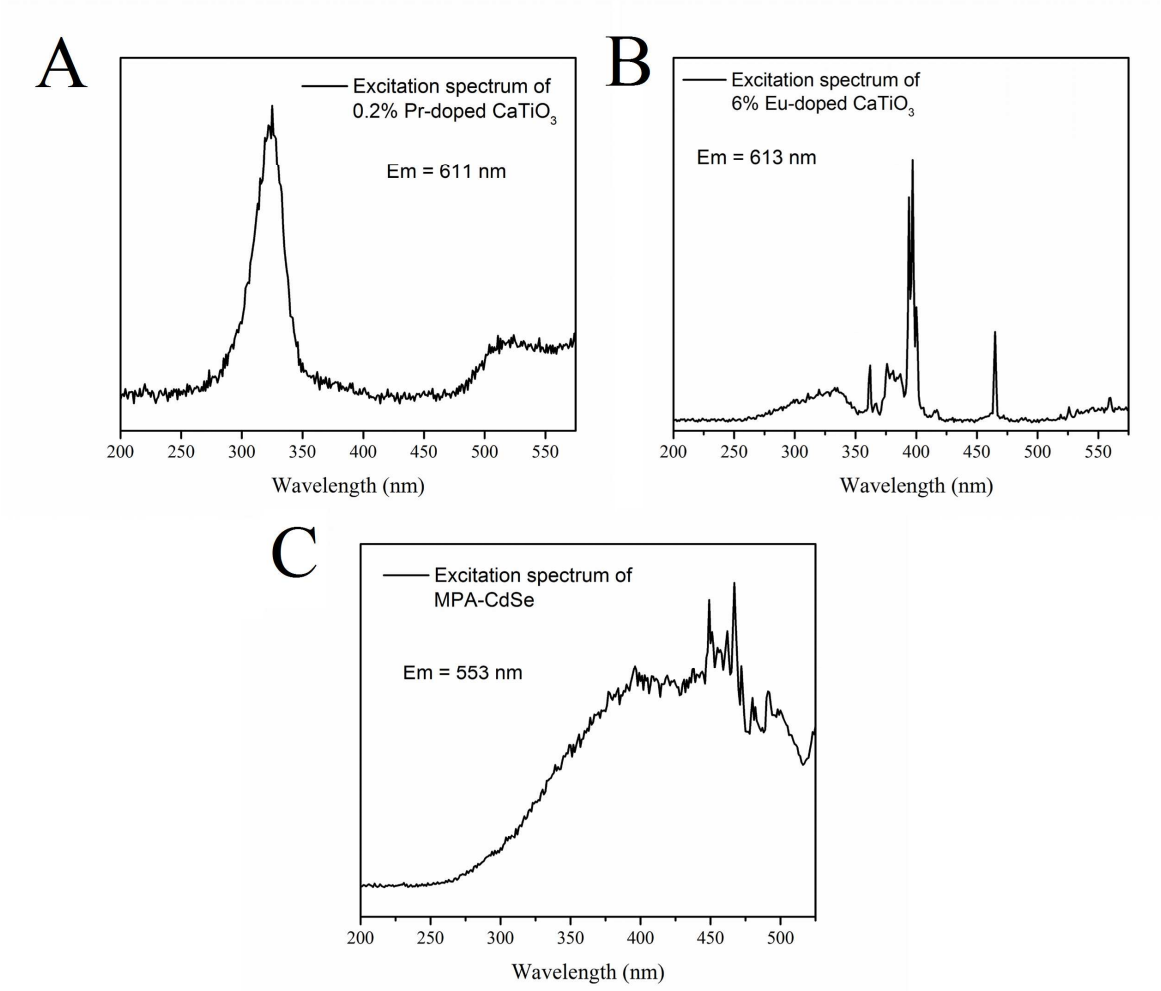

Figure 5.19. Excitation spectra of Pr-doped $CaTiO_3$, Eu-doped $CaTiO_3$, and MPA-capped CdSe QDs. Emission data were acquired at their respective emission peak positions. SI image reproduced from Ref. 74 with permission from The Royal Society of Chemistry.

5.3.5. Optical data collected on Eu-doped $CaTiO_3$ and Corresponding Heterostructures

PL emission spectra were collected on a complementary set of heterostructures, created from various molar percent concentrations (i.e. 'x' = 0, 2, 4, and 6) of a different dopant, i.e. Eu^{3+}, within $CaTiO_3$, using an excitation wavelength of 397 nm, as shown in Figure 5.20. The characteristic Eu^{3+} emission bands located at 547, 590, 623, 650, and 692 nm can be assigned to a number of *f-f* transitions of the RE^{3+} ion, specifically the

$^5D_1$-$^7F_1$, $^5D_0$-$^7F_1$, $^5D_0$-$^7F_2$, $^5D_0$-$^7F_3$, and $^5D_0$-$^7F_4$ transitions, respectively, of Eu^{3+}. By analogy, the PL intensity increased with increasing molar percent concentrations with a maximum observed with a 6 mol % material, i.e. yielding the highest PL red emission intensity observed. As a result, using this quantity as an 'optimal' composition, 6 mol % of Eu-doped $CaTiO_3$ was subsequently attached onto MPA-capped CdSe QDs in order to observe subsequent charge and energy transfer behavior.

Furthermore, this 'optimal' 6% Eu composition was taken as a 'standard' with which to draw comparisons with the optical properties of other perovskites including $SrTiO_3$, $BaTiO_3$, and $CaTiO_3$. For the PL spectra, the expected Eu^{3+} emission bands, corresponding to the *f-f* transitions, were observed for all of the perovskite titanate structures probed. However, from the collected PL spectra (Figure 5.21) of all of the various metal titanates analyzed, the Eu-doped $CaTiO_3$ evinced the highest measured PL red emission intensity.

From theoretical calculations, it has been postulated that this mid-sized rare earth metal undergoes an energetically favorable substitution with Ca, via a Ca oxygen vacancy within the $CaTiO_3$ host, whereas with $BaTiO_3$ and $SrTiO_3$, Eu can substitute at either the A or B sites.[20] Moreover, $BaTiO_3$ and $SrTiO_3$ appear to evince increasing binding energies for rare earth ion dopant cations of decreasing size.[20] Since Eu^{3+} is a medium-sized ion (~109 pm), it is plausible that the binding energy for Eu^{3+} is reduced within both Ba (~149 pm) and Sr (~118 pm) titanates with respect to $CaTiO_3$ (Ca^{2+} = ~132 pm and Ti^{4+} = 74.5 pm), and that therefore, the potential for Eu dopant incorporation is more favorable within the $CaTiO_3$ lattice. Hence, this phenomenon of an increased stabilization for Eu with the surrounding $CaTiO_3$ may possibly be due to not

only the increased Coulombic attraction but also the higher charge density associated with the Ca vacancy for Eu^{3+}.[20]

In terms of the corresponding MPA-capped CdSe QD-Eu-doped $CaTiO_3$ heterostructures (red curve), as indicated in Figures 5.22 and 5.24B, using an excitation wavelength of 399 nm, we noticed that the PL quenching of the $CaTiO_3$: Eu component is more significant and apparent, denoting behavior indicative of either (i) electron transfer occurring from Eu-doped $CaTiO_3$ to the CdSe QDs or (ii) a larger proportion of competing non-radiative decay processes. By contrast, the quenching of the CdSe QDs themselves is almost negligible, especially by comparison with the corresponding behavior of MPA-capped CdSe QD – Pr-doped $CaTiO_3$ heterostructures. Indeed, due to the higher redox potential of MPA as compared with CdSe QDs and therefore unfavorable band alignment present, it is reasonable to assert that both the photoinduced holes trapped within MPA and the holes and electrons confined in QDs are not likely to migrate into Eu-doped $CaTiO_3$, thereby explaining the minimal reduction of the PL output associated with the CdSe QDs incorporated within these heterostructures (Figure 5.23).

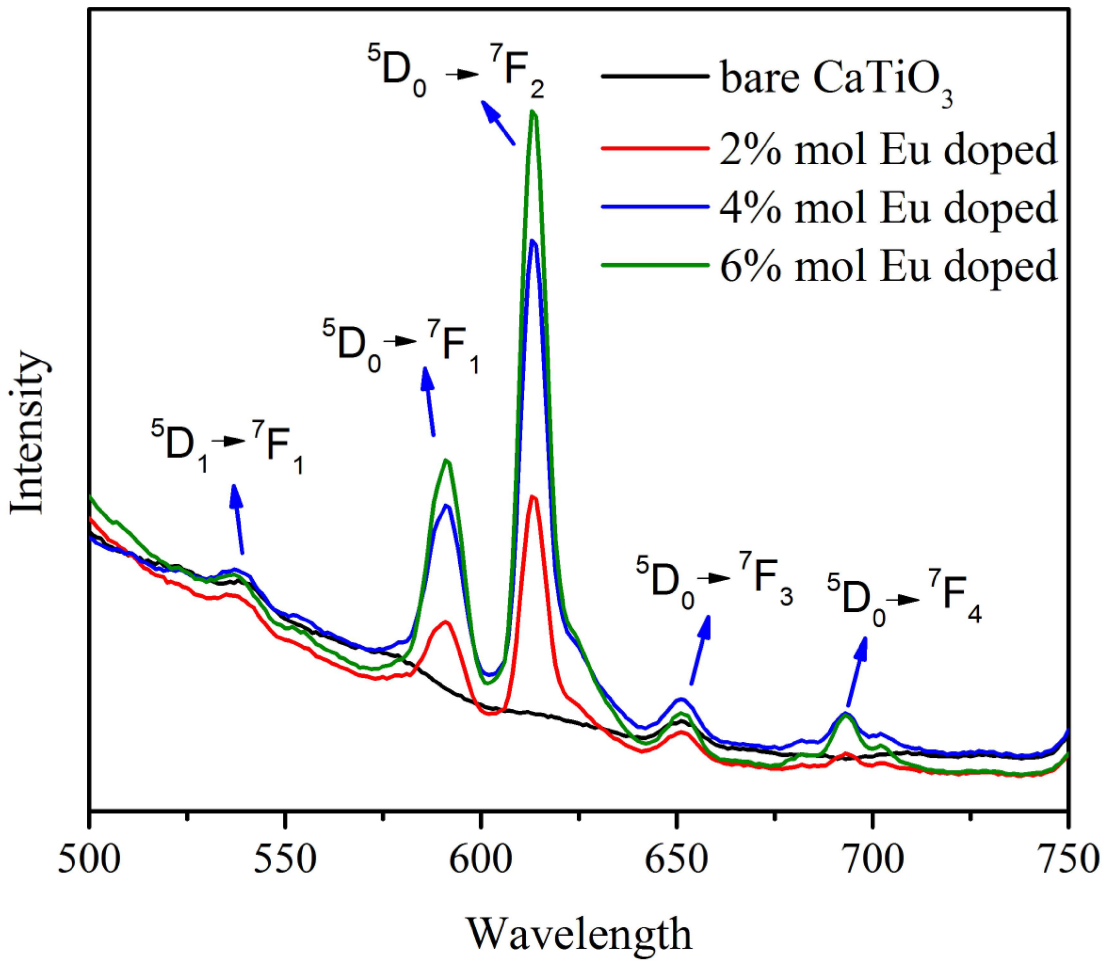

Figure 5.20. PL emission spectra of various molar % concentrations (i.e. 0, 2, 4, and 6%) of Eu-doped $CaTiO_3$, prepared using the molten salt method. Data were collected at an excitation wavelength of 399 nm. Image reproduced from Ref. 74 with permission from The Royal Society of Chemistry.

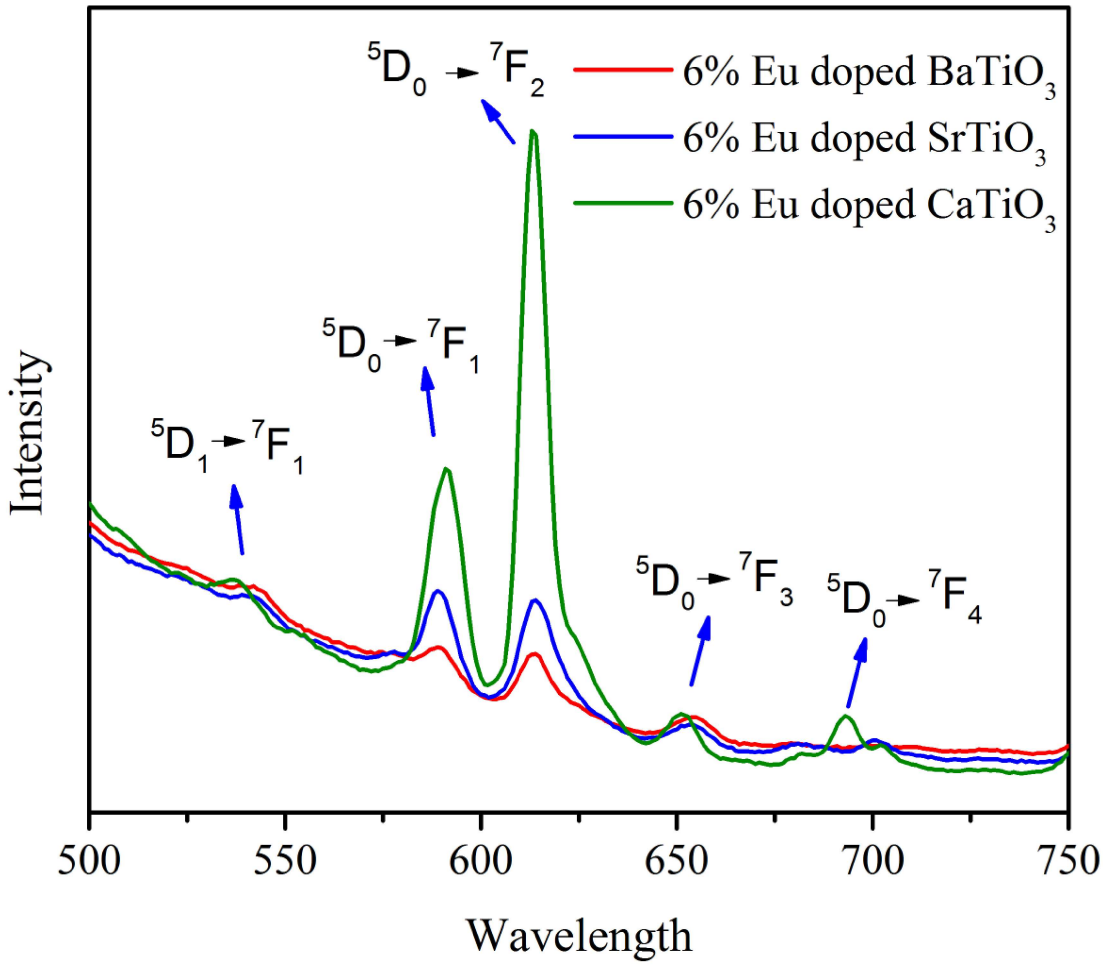

Figure 5.21. PL emission spectra obtained at 6 mol % concentrations of Eu-doped $CaTiO_3$, $BaTiO_3$, and $SrTiO_3$, prepared using the molten salt method. Data were collected at an excitation wavelength of 399 nm. Image reproduced from Ref. 74 with permission from The Royal Society of Chemistry.

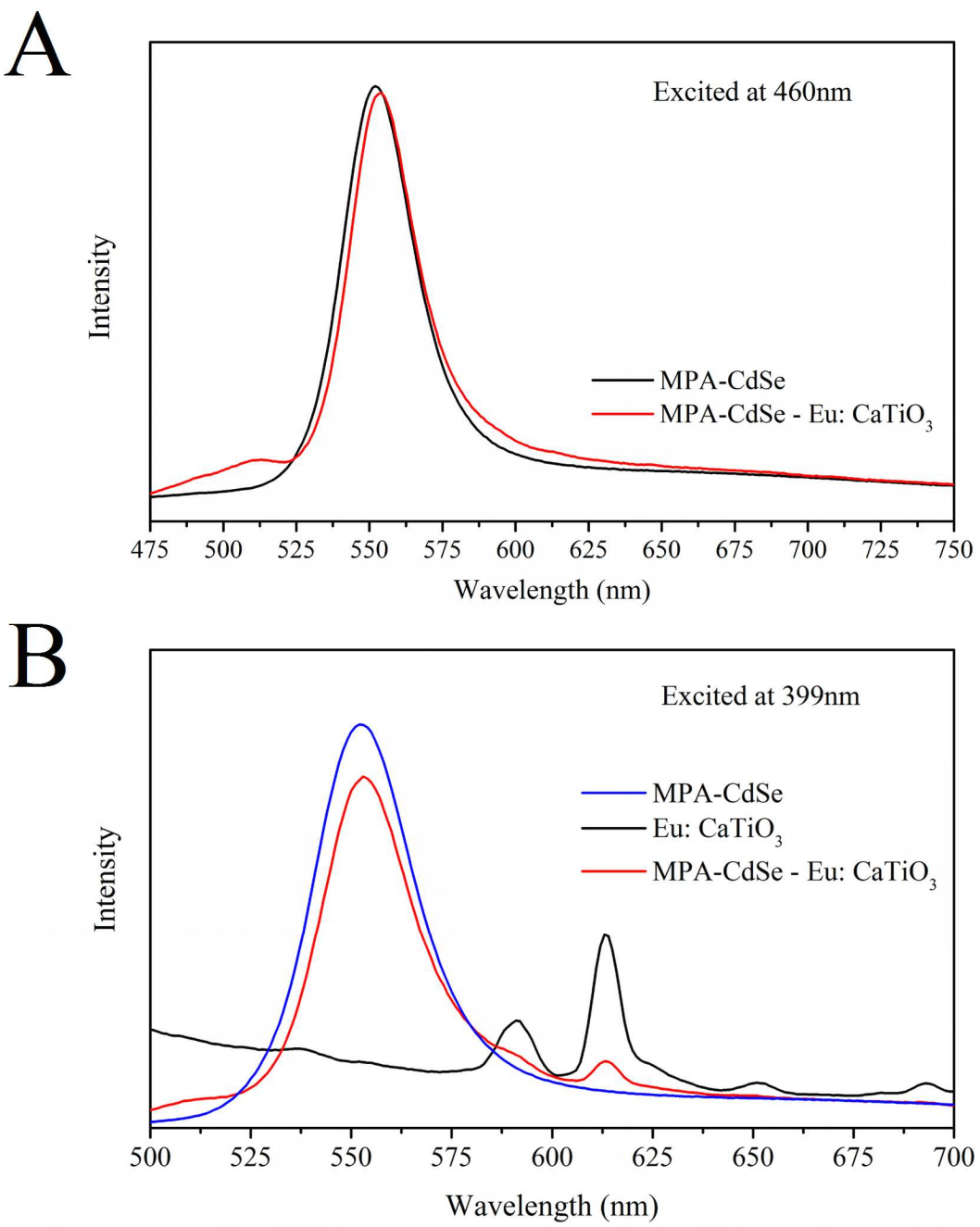

Figure 5.22. PL emission spectra of MPA-capped CdSe QDs, Eu-doped $CaTiO_3$, as well as MPA-capped CdSe-Eu-doped $CaTiO_3$ heterostructures under (A) 460 and (B) 399 nm excitation, respectively. Image reproduced from Ref. 74 with permission from The Royal Society of Chemistry.

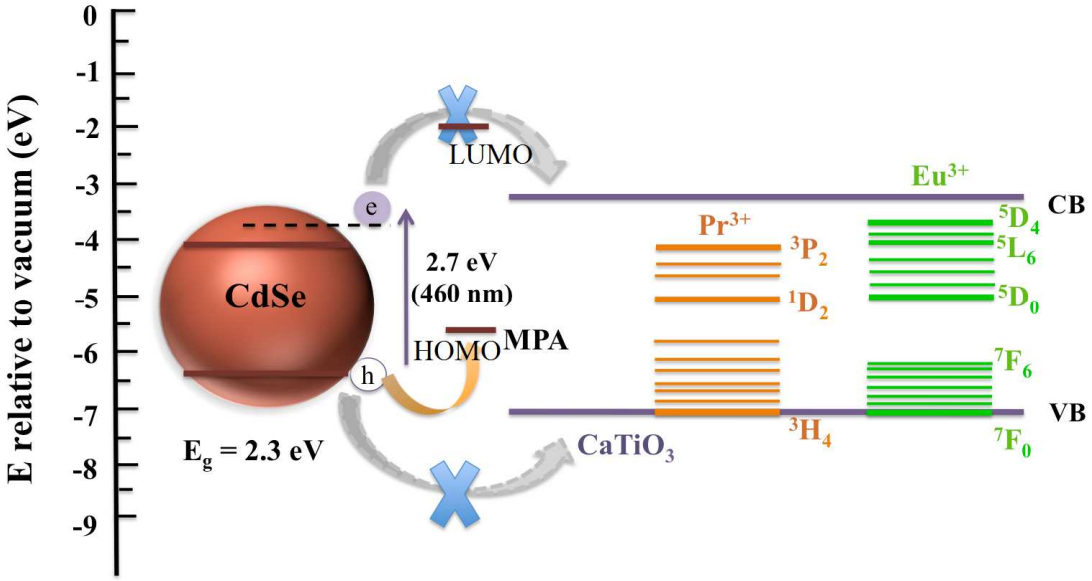

Figure 5.23. Potential electronic energy diagram, illustrating the energy band alignments associated with CdSe QDs anchored onto $CaTiO_3$ doped with Pr and with Eu, under an excitation of 460 nm incident light. CB = conduction band; VB = valence band; LUMO = lowest unoccupied molecular orbitals; and HOMO = highest occupied molecular orbitals. Image reproduced from Ref. 74 with permission from The Royal Society of Chemistry.

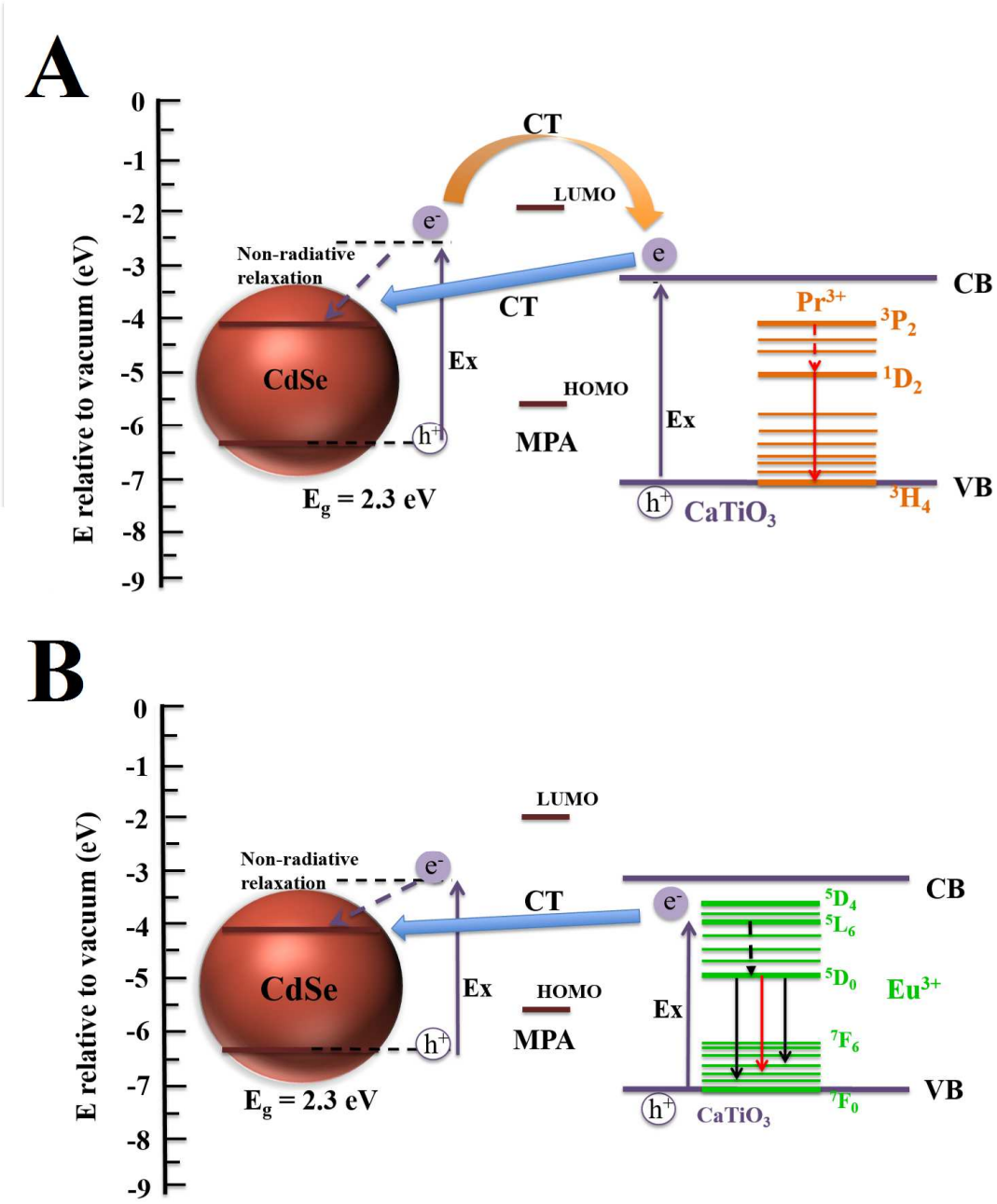

Figure 5.24. Potential electronic energy diagram, illustrating the energy band alignments associated with CdSe QDs anchored onto $CaTiO_3$ doped with Pr and with Eu, as well as the potential for corresponding charge transfer (CT), taking place within the heterostructure, under the excitation of 325 nm (panel A) and 399 nm (panel B), respectively. CB = conduction band; VB = valence band; LUMO = lowest unoccupied molecular orbitals; and HOMO = highest occupied molecular orbitals. Image reproduced from Ref. 74 with permission from The Royal Society of Chemistry.

5.4. Conclusions

Our work has elements of novelty in both synthesis and photophysics in an effort to predictively control optical behavior in nanoscale systems. Specifically, for the first time, a family of novel porous, crystalline, chemically pure, and micron-scale spherical motifs of RE-doped $CaTiO_3$, measuring ~200 to 350 nm in overall diameter and composed of individual constituent nanoparticles with diameters of ~30 to 40 nm, has been reliably prepared using both the molten salt as well as the hydrothermal methods. Based upon PL observations, our molten salt-derived samples evinced an increased red emission intensity possibly due to several factors, such as their slightly larger crystallite size, higher reaction temperature of formation, as well as greater surface area. Consequently, molten salt prepared samples of $CaTiO_3$ were generated with varying RE molar percentages in order to achieve the most 'optimized' photoluminescent material. Moreover, the optical behavior of Eu- doped $CaTiO_3$ was compared with that of their related perovskites, i.e. $BaTiO_3$ and $SrTiO_3$, in order to observe the efficiency of each perovskite as a host material for the dopant substituent Eu^{3+} ion.

Based upon PL measurements, amongst the samples tested, it was observed that $CaTiO_3$ served as the most appropriate host for Eu, due to an increased Coulombic attraction and a higher charge density for the dopant ion. As a result, 'optimized' concentrations of 0.2 and 6 mol % of Pr and Eu-doped $CaTiO_3$ structures, respectively, were decorated with CdSe QDs in order to observe and account for novel energy and charge transfer behaviors. In terms of the optical properties of the as-prepared heterostructures, enhancements of PL intensities were noted upon excitation under UV-visible light (i.e. 460 nm), owing to the surface passivation effect. Nevertheless, the

predominant storyline within the heterostructures themselves was the observation of effective charge transfer and/or non-radiative decay processes from CdSe to $CaTiO_3$ and vice versa, as verified by quenching effects of the PL profiles associated with the individual constituent components. In addition, due to the distinctive alignment of energy levels associated with the two discrete dopants, we found that the Pr-$CaTiO_3$ and Eu-$CaTiO_3$ yielded dissimilar but nevertheless fundamentally predictable quenching behaviors. In effect, the optical behavior of the heterostructures was effectively controlled by the luminescence properties of the activators, the host lattice, and the QDs as well as by their relative energy band level alignment.

5.5. Future Directions

5.5.1 Solar Water Splitting

Photoelectrochemical (PEC) water splitting has become an attractive candidate for H_2 production and storage. In principle, efficiencies greater than 30% can be achieved in a cost-effective and reasonably environmentally friendly fashion.[67] A typical PEC device consists of a photoanode and cathode immersed in water containing an electrolyte.

The photoanode is usually a semiconductor (i.e. a metal oxide) that absorbs light and subsequently generates electron-hole pairs. The electrons are then transported to a metal cathode (i.e. Pt), often aided by an external bias, and H_2 generation therefore occurs at the cathode as a result of the reduction of protons by electrons.[67] The holes left behind at the photoanode oxidize water molecules to O_2 and protons. To achieve photocatalytic water splitting using a single photocatalyst, the band gap of the semiconductor must straddle both the reduction and oxidation potentials of water, which are +0 and +1.23 V

vs. normal hydrogen electrode (NHE), respectively, when the reactant solution is set at a pH of 0.[68-73]

The demands for an effective PEC material are many, including the need for (i) effective light absorption and charge carrier generation in the solid, (ii) charge separation and transport in the solid and at the solid-liquid interface, as well as (iii) charge carrier extraction and electrochemical product formation at the solid-liquid interface.[67] Yet, nanomaterials do offer unique potential as possible catalysts for PEC applications.

From this study, we have observed efficient charge transfer between CdSe QDs and $CaTiO_3$.[74] Moreover, as previously mentioned, QDs associated with perovskite (i.e. $BaTiO_3$) materials for photoelectrochemical (PEC) water-splitting applications are only now being explored. As an extension of our prior work, we plan to systematically explore the relationship between the synthetic methodologies used (i.e. MS method & hydrothermal), the ligand effect, as well as their corresponding efficiency of our heterostructures for the water splitting process. Specifically for the ligand effect, various linkers such as MPA and mercaptohexanoic acid (MHA) will functionalize the surface of the QDs and attach to the surface of the metal oxide through electrostatic interactions. Additionally, to confirm the presence of ligand effects such as MPA and MHA, ligand free-controls will be incorporated within the PEC device.

5.5.2 PDF analysis

From a structural perspective, concerning RE-doped $CaTiO_3$, it has been observed that as the dopant concentration (i.e. 2-6 mol%) of Eu is increased, the measured photoluminescence also correspondingly increased. On the other hand, beyond a 0.2 mol

% Pr dopant level, the photoluminecent properties appeared to diminish.[75] However, these observations still lack a structural rationale as to understanding the nature of and possibly correlating the enhanced photoluminescence.

Therefore, in order to observe the overall spatial distribution of dopant ions, PDF analysis will be utilized in order to interrogate the crystalline structure of these nanomaterials as well as the local atomic environment of their respective dopant ions. Scenarios to account for dopant ion placement may involve either the creation of a vacancy or the replacement of A/B sites within the crystal lattice. Hence, PDF analysis should enable us to precisely spatially correlate dopant ion distribution and density with overall photoluminescence observed.

5.6 References

1. Y. Mao, S. Banerjee and S. S. Wong, *Journal of the American Chemical Society*, 2003, 125, 15718-15719.
2. J. Shi and L. Guo, *Progress in Natural Science: Materials International*, 2012, 22, 592-615.
3. S. Stolen, E. Bakken and C. E. Mohn, *Physical Chemistry Chemical Physics*, 2006, 8, 429-447.
4. F. A. Rabuffetti and R. L. Brutchey, *Dalton Transactions*, 2014, 43, 14499-14513.
5. J. Zhu, H. Li, L. Zhong, P. Xiao, X. Xu, X. Yang, Z. Zhao and J. Li, *ACS Catalysis*, 2014, 4, 2917-2940.
6. J. Kaur, V. Dubey, Y. Parganiha, D. Singh and N. S. Suryanarayana, *Research on Chemical Intermediates*, 2015, 41, 3597-3621.
7. X. Zhang, J. Zhang, Y. Jin, H. Zhao and X.-j. Wang, *Crystal Growth & Design*, 2008, 8, 779-781.
8. C. N. George, J. K. Thomas, R. Jose, H. P. Kumar, M. K. Suresh, V. R. Kumar, P. R. S. Wariar and J. Koshy, *Journal of Alloys and Compounds*, 2009, 486, 711-715.
9. D. Wang, Y. Liu, H. Hu, Z. Zeng, F. Zhou and W. Liu, *The Journal of Physical Chemistry C*, 2008, 112, 16123-16129.
10. A. L. Tiano, A. C. Santulli, C. Koenigsmann, M. Feygenson, M. C. Aronson, R. Harrington, J. B. Parise and S. S. Wong, *Chemistry of Materials*, 2011, 23, 3277-3288.
11. A. C. Santulli, H. Zhou, S. Berweger, M. B. Raschke, E. Sutter and S. S. Wong, *Crystal Engineering Communications*, 2010, 12, 2675-2678.
12. T.-J. Park, Y. Mao and S. S. Wong, *Chemical Communications*, 2004, 23, 2708-2709.
13. S. B. Yuanbing Mao, and Stanislaus S. Wong, *Journal of the American Chemical Society*, 2003, 125, 15718-15719.
14. Y. Mao, S. Banerjee and S. S. Wong, *Chemical Communications*, 2003, 3, 408-409.
15. K. Asami, K. Saito, N. Ohtsu, S. Nagata and T. Hanawa, *Surface and Interface Analysis*, 2003, 35, 483-488.
16. K. Asami, N. Ohtsu, K. Saito and T. Hanawa, *Surface and Coatings Technology*, 2005, 200, 1005-1008.
17. S. Som, A. K. Kunti, V. Kumar, V. Kumar, S. Dutta, M. Chowdhury, S. K. Sharma, J. J. Terblans and H. C. Swart, *Journal of Applied Physics*, 2014, 115, 193101/193101-193101/193114.
18. H. Takashima, K. Ueda and M. Itoh, *Applied Physics Letters*, 2006, 89, 261915/261911-261915/261913.
19. L. S. Cavalcantea, V. S. Marquesb, J. C. Sczancoskia, M. T. Escotec, M. R. Joyaa, J. A. Varelad, M. R. M. C. Santosb, P. S. Pizania and E. Longod, *Chemical Engineering Journal*, 2008, 143, 299-307.
20. J. A. Dawson, X. Li, C. L. Freeman, J. H. Harding and D. C. Sinclair, *Journal of Materials Chemistry C*, 2013, 1, 1574-1582.

21. V. V. Lemanov, A. V. Sotnikov, E. P. Smirnova and M. Weihnacht, *Applied Physics Letters*, 2002, 81, 886-888.
22. E. Korkmaz and N. O. Kalaycioglu, *Journal of the Chinese Chemical Society*, 2012, 59, 1390-1393.
23. K. Goto, Y. Nakachi and K. Ueda, *Thin Solid Films*, 2008, 516, 5885-5889.
24. M. Upadhyay Kahaly and U. Schwingenschlogl, *Journal of Materials Chemistry A: Materials for Energy and Sustainability*, 2014, 2, 10379-11383.
25. A. K. Levine and F. C. Palilla, *Applied Physics Letters*, 1964, 5, 118.
26. F. A. Rabuffetti, S. P. Culver, J. S. Lee and R. L. Brutchey, *Nanoscale*, 2014, 6, 2909-2914.
27. C. Peng, Z. Hou, C. Zhang, G. Li, H. Lian, Z. Cheng and J. Lin, *Optics Express*, 2010, 18, 7543-7551.
28. K. Minami, Y. Hakuta, M. Ohara, M. Aoki, K. Sue and H. Takashima, *Polymer Electrolyte Fuel Cells 10, Pts 1 and 2*, 2013, 50, 19-24.
29. A. Isobe, S. Takeshita and T. Isobe, *Langmuir*, 2015, 31, 1811-1819.
30. X. Peng, M. Y. Sfeir, F. Zhang, J. A. Misewich and S. S. Wong, *Journal of Physical Chemistry C*, 2010, 114, 8766-8773.
31. X. Peng, J. A. Misewich, S. S. Wong and M. Y. Sfeir, *Nano Letters*, 2011, 11, 4562-4568.
32. J. Han, L. Wang and S. S. Wong, *Rsc Advances*, 2014, 4, 34963-34980.
33. J. Han, L. Wang and S. S. Wong, *The Journal of Physical Chemistry C*, 2014, 118, 5671-5682.
34. S. Xiao, P. Liu, W. Zhu, G. Li, D. Zhang and H. Li, *Nano Letters*, 2015, 15, 4853-4858.
35. J. Han, C. McBean, L. Wang, C. Jaye, H. Liu, D. A. Fischer and S. S. Wong, *Journal of Physical Chemistry C*, 2015, 119, 3826-3842.
36. Z. Zhang, X. Li, C. Gao, F. Teng, Y. Wang, L. Chen, W. Han, Z. Zhang and E. Xie, *Journal of Materials Chemistry A: Materials for Energy and Sustainability*, 2015, 3, 12769-12776.
37. G. Sreedhar, A. Sivanantham, S. Venkateshwaran, S. K. Panda and M. Eashwar, *Journal of Materials Chemistry A: Materials for Energy and Sustainability*, 2015, 3, 13476-13482.
38. T. S. Malyy, V. V. Vistovskyy, Z. A. Khapko, A. S. Pushak, N. E. Mitina, A. S. Zaichenko, A. V. Gektin and A. S. Voloshinovskii, *Journal of Applied Physics*, 2013, 113, 224305/224301-224305/224307.
39. J. Zhang, N. Zhang, L. Zou and S. Gan, *Rsc Advances*, 2014, 4, 38455-38465.
40. T. Kimura, 2011.
41. J. Streit, L. C. Tran-Ho and E. Konigsberger, *Monatshefte Fur Chemie*, 1998, 129, 1225-1236.
42. G. J. Janz and N. P. Bansal, *Journal of Physical and Chemical Reference Data*, 1982, 11, 505-693.
43. B. F. Woodfield, J. L. Shapiro, R. Stevens and J. Boerio-Goates, *Journal of Chemical Thermodynamics*, 1999, 31, 1573-1583.
44. K. T. Jacob and K. P. Abraham, *Journal of Chemical Thermodynamics*, 2009, 41, 816-820.

45. J. A. Dean, *Lange's Handbook of Chemistry*, McGraw-Hill, New York, 14th edn., 1992.
46. H. Chang and P. J. Huang, *Anal Chem*, 1997, 69, 1485-1491.
47. J. Blazejowski and B. Zadykowicz, *Journal of Thermal Analysis and Calorimetry*, 2013, 113, 1497-1503.
48. X. C. Zhou and X. J. Wang, *Optik*, 2015, 126, 4800-4803.
49. H. T. Sun, M. Fujii, N. Nitta, F. Shimaoka, M. Mizuhata, H. Yasuda, S. Deki and S. Hayashiz, *Journal of the American Ceramic Society*, 2008, 91, 4158-4161.
50. V. V. Tatarchuk, A. P. Sergievskaya, T. M. Korda, I. A. Druzhinina and V. I. Zaikovsky, *Chemistry of Materials*, 2013, 25, 3570-3579.
51. X. Y. Yuan, K. Shen, M. X. Xu and Q. Y. Xu, *Journal of Superconductivity and Novel Magnetism*, 2012, 25, 2421-2424.
52. C. Y. Xu, J. Wu, P. Zhang, S. P. Hu, J. X. Cui, Z. Q. Wang, Y. D. Huang and L. Zhen, *Crystengcomm*, 2013, 15, 3448-3454.
53. J. Fu, Q. Zhang, Y. Li and H. Wang, *Journal of Luminescence*, 2009, 130, 231-235.
54. M. R. Mohammadi and D. J. Fray, *Journal of Sol-Gel Science and Technology*, 2013, 68, 324-333.
55. S. Fuentes, N. Barraza, E. Veloso, R. Villarroel and J. Llanos, *Journal of Alloys and Compounds*, 2013, 569, 52-57.
56. Z. Sun, G. Cao, Q. Zhang, Y. Li and H. Wang, *Materials Chemistry and Physics*, 2012, 132, 215-221.
57. G. Huang, W. Dong, L. Fang, F. Zheng and M. Shen, *Journal of Advanced Dielectrics*, 2011, 1, 215-221.
58. J. Han, C. McBean, L. Wang, J. Hoy, C. Jaye, H. Liu, Z.-Q. Li, M. Y. Sfeir, D. A. Fischer, G. T. Taylor, J. A. Misewich and S. S. Wong, *Chemistry of Materials*, 2015, 27, 778-792.
59. X. Zhang, J. Zhang, Y. Jin, H. Zhao and X.-j. Wang, *Crystal Growth & Design*, 2009, 8, 779-781.
60. X. Zhang, J. Zhang, X. Zhang, M. Wang, H. Zhao, S. Lu and X.-j. Wang, *Journal of Physical Chemistry C*, 2007, 111, 18044-18048.
61. A. Purwanto, D. Hidayat, Y. Terashi and K. Okuyama, *Chemistry of Materials*, 2008, 20, 7440-7446.
62. C. M. Lau, X. Wu and K. W. Kwok, *Journal of Applied Physics*, 2015, 118, 034107/034101-034107/034107.
63. M. L. Moreira, E. C. Paris, G. S. do Nascimento, V. M. Longo, J. R. Sambrano, V. R. Mastelaro, M. I. B. Bernardi, J. Andres, J. A. Varela and E. Longo, *Acta Materialia*, 2009, 57, 5174-5185.
64. J. Li, Y. C. Zhang, T. X. Wang and M. Zhang, *Materials Letters*, 2011, 65, 1556-1558.
65. B. Mari, K. C. Singh, P. Cembrero-Coca, I. Singh, D. Singh and S. Chand, *Displays*, 2013, 34, 346-351.
66. R. C. Somers, M. G. Bawendi and D. G. Nocera, *Chemical Society Reviews*, 2007, 36, 579-591.
67. J. Z. Zhang, *MRS Bulletin*, 2011, 36, 48-55.

68. T. Hisatomi, J. Kubota and K. Domen, *Chemical Society Reviews*, 2014, 43, 7520-7535.
69. Y. Ma, X. Wang, Y. Jia, X. Chen, H. Han and C. Li, *Chemical Reviews*, 2014, 114, 9987-10043.
70. M. S. Prevot and K. Sivula, *Journal of Physical Chemistry C*, 2013, 117, 17879-17893.
71. M. G. Walter, E. L. Warren, J. R. McKone, S. W. Boettcher, Q. Mi, E. A. Santori and N. S. Lewis, *Chemical Reviews*, 2010, 110, 6446-6473.
72. J. Sun, D. K. Zhong and D. R. Gamelin, *Energy & Environmental Science*, 2010, 3, 1252-1261.
73. N. Getoff, *International Journal of Hydrogen Energy*, 1990, 15, 407-417.
74. C. S. Lewis, H. Q. Liu, J. Y. Han, L. Wang, S. Y. Yue, N. A. Brennan and S. S. Wong, *Nanoscale*, 2016, 8, 2129-2142.
75. C. S. Lewis, H. Liu, J. Han, L. Wang, S. Yue, N. A. Brennan and S. S. Wong, *Nanoscale*, 2016, 8, 2129-2142.

Chapter 6- Absence of Cytotoxicity towards Microglia of Iron Oxide (α-Fe_2O_3) Nanorhombohedra

6.1 Introduction

6.1.1. Microglia

Microglia cells represent the first line of defense against disease or injury within the CNS.[1] As a result, microglia play key roles within neurodegenerative diseases (i.e. Parkinson's and Alzheimer's) and respond quickly to injury.[2] Specifically, studies have shown that microglia cells are constantly surveying the brain parenchyma, ready to respond to potential threats.[3] During this 'surveying' state, microglia cells may serve under both physiological as well as pathological conditions. Specifically, when the CNS is healthy, the microglia maintain homeostasis by supporting the formation of neural circuits and phagocytose apoptic cells, to name a few.[4, 5] However, under pathological conditions, the microglia transition from a resting state (i.e. long branched filaments) to an activated state (i.e. spherical shaped motifs without branched filaments), thereby initiating an inflammatory response. These responses include the upregulation of microglial receptors and cytokines as well as microglial proliferations.[2, 6]

Within minutes of an injury, microglia cells respond to adenosine triphosphate (ATP) through purinergic (P2) receptors.[7, 8] Subsequently, the microglia move quickly toward the site of injury, thereby releasing pro-inflammatory cytokines as well as removing cell debris.[6] Based upon previous studies, the first pro-inflammatory cytokines released within an hour, post-injury, are tumor necrosis factor alpha (TNFα), interleukin-1beta (IL-1β), and interleukin-6 (IL-6).[2, 9] When the release of cytokines takes place, the microglia's activated form is termed as a pro-inflammatory state (M1) as opposed to an anti-inflammatory state (M2), characterized by the production of interleukin-10 (IL-10).

Though there are two forms of activated states, M1 predominates within the site of injury for at least 28 days post-injury.[10] Herein, in this chapter, we aim to investigate the M1 activation of microglia cells upon engulfment of iron oxide nanostructures.

6.1.2. Relevance of Nanomaterials

Nanomaterials, comprising nanoscale structures measuring between 1 and 100 nm in size, have attracted significant research interest due to their unique structure-dependent physical properties. Recently, concerns have been raised over the potentially deleterious effects of these nanomaterials on human health and the environment.[11-13] From a toxicological perspective, nanoscale materials can induce different types of cellular responses, characterized by a variety of distinctive uptake mechanisms, such as endocytosis, mediated for example by receptor-specific target sites.[14-16]

For a given nanomaterial, morphology (e.g. in terms of its size and shape) is thought to be one of the key factors that can decisively determine the observed degree of its cytotoxicity and cellular uptake. Indeed, significant effort, including from one of our groups in particular, has been involved with systematically synthesizing novel motifs of diverse classes of nanomaterials, such as but not limited to derivatized carbon nanotubes (CNTs), rare earth ion-doped cerium phosphate ($CePO_4$) nanowires, silicon dioxide (SiO_2) nanotubes, titanium dioxide (TiO_2) nanostructures, and zinc oxide (ZnO) nanowires and nanoparticles, to analyze their potential for biomedical applications. The objective of that prior body of work had been to correlate size, shape, morphology, and chemical composition of nanomaterials with their corresponding uptake mechanisms in an effort to probe and understand their individual and collective impact upon cellular

toxicity, in general.[17-24] In effect, we had been interested in determining the factors that control nanoscale toxicity.

The model system we study herein is related to a family of magnetic iron oxide (Fe_3O_4) nanostructures that has already been well studied. Indeed, nanoparticulate magnetite have previously been extensively investigated for incorporation into diverse applications, including for biological fluids, tissue-specific release of therapeutic agents, anti-cancer drug delivery systems, hyperthermia, and contrast enhancement for magnetic resonance imaging (MRI).[25-28] In this context, the study of their potential toxicology to cells has served as a valuable means of gauging the viability, biocompatibility, and overall practicality of this magnetic iron oxide platform for ubiquitous use in these assorted contexts.[29] Nevertheless, the use of Fe_3O_4 for biomedical applications has been limited by issues associated not only with particle inhomogeneity and cost concerns but also with its inability to effectively differentiate between tumors and artifacts arising from bleeding, metal deposits, and/or calcification in T_2-weighted MRI images.[30]

A common, companion material to Fe_3O_4, i.e. hematite (Fe_2O_3), possesses a rhombohedral crystal structure with a *R3c* space group.[31] However unlike Fe_3O_4, hematite can exist in different crystallographic forms such as alpha-hematite (α-Fe_2O_3), beta-hematite (β-Fe_2O_3), gamma-hematite (γ-Fe_2O_3), and epsilon-hematite (ε-Fe_2O_3), with α-Fe_2O_3 and γ-Fe_2O_3 as the most familiar motifs. Particularly, α-Fe_2O_3 has been synthesized as different morphologies, including as particles, cubes, and rods, and has been incorporated as functional components of gas sensors, CO oxidation catalysts, lithium-ion batteries, and colloidal mediators for hyperthermia treatment.[32-36] In a number of these aforementioned applications,[37] the α-Fe_2O_3 nanoparticles have been employed as

particulate, aerosolized motifs. Therefore, it is imperative to understand the potential toxicological effect of exposure to nanoscale hematite, as manifested by different intake routes such as inhalation, ingestion, and injection.

Nevertheless, the intrinsic toxicity of Fe_2O_3 nanostructures still remains a matter of considerable controversy. For example, *in vitro* studies have shown that α-Fe_2O_3 nanoparticles larger than 90 nm in diameter (i.e. ~250 nm and ~1.2 μm) gave rise to little if any toxicity with respect to human lung epithelial cells (A549) and murine alveolar macrophages (MH-S).[38] Moreover, α-Fe_2O_3 nanotubes, characterized by ~200 nm diameters, were found to be compatible with rat adrenal medulla cells (PC12), and in fact served as a potential delivery vehicle for nerve growth factor (NGF) in order to convert these cells into neurons.[39] By contrast, animal studies using Fe_2O_3 nanoparticles have revealed that these nanostructures may detrimentally induce either airway inflammation in healthy mice or cellular reduction in alveolus and lymph nodes in allergic mice.[40]

According to Brunauer-Emmett-Teller (BET) analysis, nanoscale rhombohedra, normalized for geometric considerations, possess a higher surface area (~45 m^2/g) than either nanocubes (~13.5 m^2/g) or nanorods (~39 m^2/g), depending on their size.[32, 41] Therefore, since the surface area of α-Fe_2O_3 N-Rhomb is second only to that of spherical nanoparticles (~133 m^2/g), which have already been extensively explored in cytotoxic analysis, this observation provides us with a rationale to fully understand the shape dependence of α-Fe_2O_3 N-Rhomb's interaction with cells, especially when engulfed.[42] Moreover, with various reports on the shape-dependent cytotoxic behavior of nanowires versus nanoparticles under various cellular conditions,[43] it is therefore necessary to gain a similar insight into the analogous effects of rhombohedral α-Fe_2O_3 in a biological

context. In terms of a prior report with comparable objectives to our own, it is worth noting that studies involving $LiNbO_3$ nanorhombohedra have suggested that these nanostructures maintained cell viabilities of ~80% after 48 hours of incubation within mouse macrophage cells.[44]

Prior size and morphology-specific studies of various nanoparticles have indicated the ability of these nanoscale sized motifs to cross the blood brain barrier and thereby enter the central nervous system (CNS) of higher order biological organisms, such as mammals.[45, 46] In light of this result, many metal oxides such as Fe_2O_3 and TiO_2 have been previously probed for possible neurotoxic effects upon exposure.[47-49] With α-Fe_2O_3 N-Rhomb's small size (<100 nm), large surface area, and chemical stability, nanoscale hematite possesses significant potential to overcome the challenges associated with passage through the blood brain barrier. Therefore, it represents an excellent system with which to probe cytotoxic effects associated with exposure of the CNS to nanomaterials, particularly nanostructures that have been surface modified through the attachment of different specific and judiciously chosen moieties.[50]

In this work, herein, we have synthesized visually traceable, dye-conjugated nanostructures, i.e. Rhodamine B (RhB)-labeled α-Fe_2O_3 N-Rhomb. Subsequently, we tested their uptake and possible toxicity in a key model system, i.e. microglia, the immuno-competent cells associated with the CNS. These cells are implicated in the pathology of many CNS disorders, including Alzheimer's disease, spinal cord injury, multiple sclerosis, Parkinson's disease, and ischemia.[51-57] Hence, given the central function and critical biological importance of microglia, we aimed to understand the implication of their exposure to our iron oxide rhombohedral nanoparticles in order to

determine any potential cytotoxic effects. To the best of our knowledge, our use of iron oxide nanorhombohedra to assess the distinctive role of the rhombohedral shape (and associated surface area) in the context of cytotoxicity has not been previously demonstrated in the literature. Herein, we reveal that microglia successfully incorporate RhB-labeled α-Fe_2O_3 N-Rhomb under both *in vivo* and *in vitro* conditions. More importantly, we definitively demonstrate that these nanoscale metal oxides in fact do not induce either cellular toxicity or inflammatory reactions in cultured microglia at physiological concentrations.

6.2. Results

6.2.1. Investigation of the Reaction Mechanism

For the hydrothermal method, a stock solution of iron chloride ($FeCl_3$) was used as the iron precursor. The hydrothermal reaction for iron oxide production is rather simple, as shown in the following equation:

$$2\ FeCl_3 + 3\ H_2O \rightarrow Fe_2O_3 + 6\ HCl \qquad (6.1)$$

In this case, $FeCl_3$ initially forms iron oxyhydroxide (FeOOH) and ultimately undergoes a dehydration process, thereby forming hematite Fe_2O_3.[58] However, what is more interesting, yet generally unknown, is the role of CTAB in controlling the ultimate observed NRhomb structure.

From previous studies on this particular rhombohedral structure, it is clear that as the iron concentration increases, the Fe_2O_3 shape transitions from nanorhombohedra to nanorods and then ultimately to nanocubes (i.e. at higher iron concentrations). However, no concrete reasons were provided beyond the fact that at lower Fe concentrations, the

iron oxide chooses to assume a rhombohedral crystal structure.[59] Additional studies have shown that the halide ion of the surfactant has a strong influence upon the overall morphology. Specifically, bromide anions in CTAB are required for the generation of highly faceted materials such as cubes, nanorods, and so forth, as they bind strongly to particular facets.[60] In the case of gold (Au) nanorods, CTAB exhibits facet-selective binding onto the (100) surface, thereby directing anisotropic growth.[60]

6.2.2 Conjugation of RhB labeled-Fe_2O_3 N-Rhomb

The conjugation of RhB onto Fe_2O_3 N-Rhomb can be explained from the reaction scheme in Figure 6.1. First, the iron oxide nanoparticles are surface functionalized with amine-terminated groups, while separately, the RhB dye is deprotonated under basic conditions (i.e. NaOH). The RhB dyes are collected via centrifugation and dispersed in DMSO, containing the DCC catalyst. Upon exposure to the DCC catalyst, the RhB reacts with the catalyst, forming an imidate group with a good leaving group at the carbonyl carbon. Subsequently, the amine-functionalized Fe_2O_3 forms an amide bond with the carbonyl carbon site, ultimately displacing the DCC catalyst.[61] The presence of the fluorescent dye RhB incorporated within RhB-labeled Fe_2O_3 N-Rhomb was subsequently confirmed using UV-visible and IR spectroscopy (Figure 6.2), as well as with confocal microscopy.

It is noteworthy to state that competitive reactions such as the Pfitzner-Moffatt oxidation reaction can potentially take place, especially since the DCC catalyst initially dissolves in DMSO. Hence, it is possible that the protonated DCC would readily react with DMSO, thereby forming sulfonium species which might have possibly inhibited

RhB conjugation.[62] However, from UV-Visible and IR spectroscopy as well as confocal microscopy results, it is clear that the RhB dye is indeed covalently attached onto the Fe_2O_3 N-Rhomb.

For UV-visible data, the nanostructures gave rise to a maximum of ~565 nm, corresponding to the known absorption peak of the organic dye, RhB (Figure 6.2A). In terms of the IR analysis (Figure 6.2B), the RhB-conjugated Fe_2O_3 N-Rhomb were compared with both bare Fe_2O_3 and with APTES-functionalized Fe_2O_3, prior to covalent attachment. For bare Fe_2O_3 and APTES-functionalized Fe_2O_3, both materials exhibited OH stretching vibrations, located at ~3471 cm^{-1}. The amino-silanized Fe_2O_3 spectrum gave rise to peaks, located at ~972 cm^{-1} and ~1607 cm^{-1}, respectively, corresponding to a Fe-O-Si band and a primary NH_2 stretch, respectively. As for the RhB-conjugated Fe_2O_3 N-Rhomb (Figure 6.2B), stretching vibrations appeared at ~1547 cm^{-1} and 1689 cm^{-1}, respectively, which were associated with the expected vibrational signature of amide NH bonds. Additional peaks in the fingerprint region could be correlated with the known and expected structure of the RhB compound.

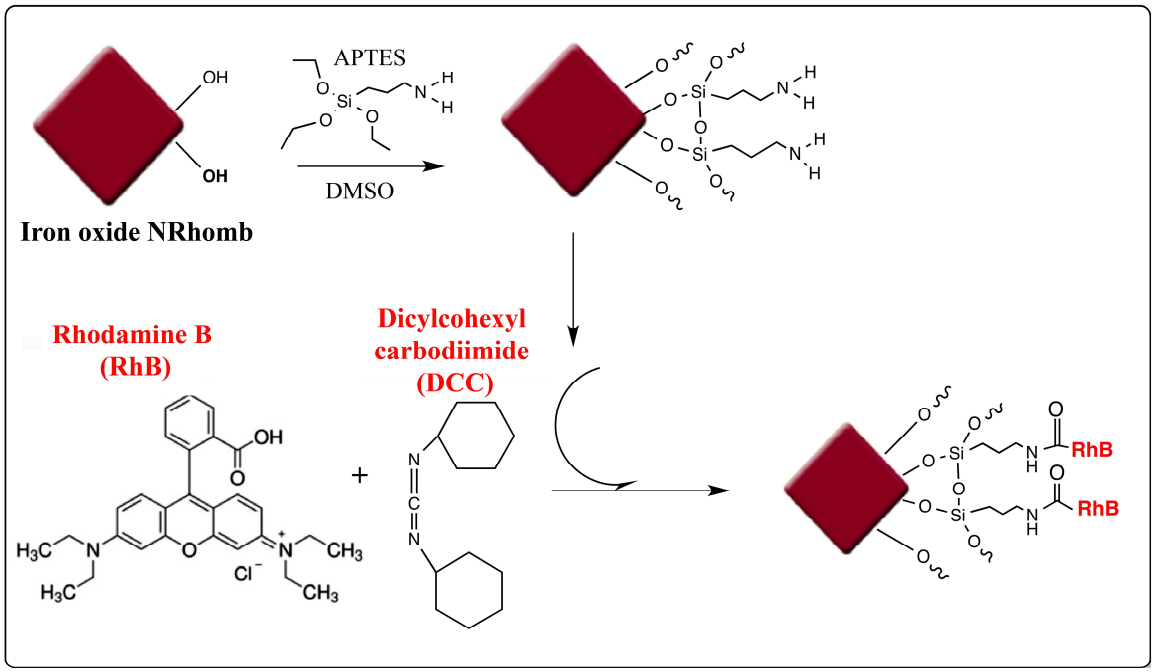

Figure 6.1: Reaction schematic for the conjugation of RhB dye onto α-Fe_2O_3 N-Rhomb. Supplementary image reproduced from Ref. 1 with permission from The Royal Society of Chemistry.

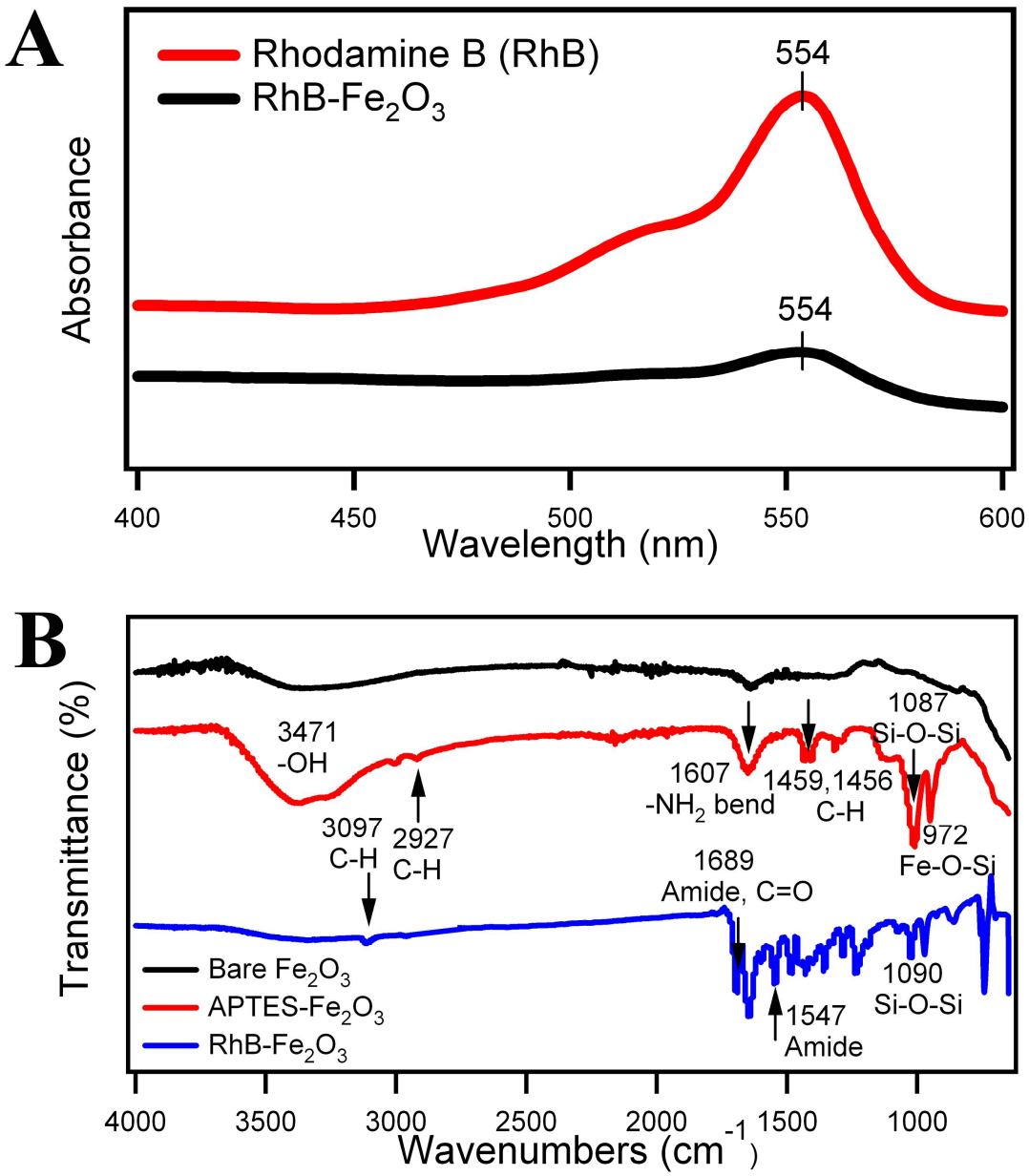

Figure 6.2. Characterization of RhB-labeled N-Rhomb. (A). UV-visible spectra of RhB organic dye (red line) and RhB-functionalized α-Fe_2O_3 N-Rhomb (black line). **(B).** Infrared spectra of bare α-Fe_2O_3 N-Rhomb (black line), APTES-functionalized Fe_2O_3 (red line), as well as RhB-labeled α-Fe_2O_3 N-Rhomb (blue line), respectively. Supplementary image reproduced from Ref. 1 with permission from The Royal Society of Chemistry.

6.2.3 Product Characterization of bare α-Fe_2O_3 N-Rhomb

We discuss the preparative protocols of our α-Fe_2O_3 N-Rhomb nanostructures in significant detail in the Supporting Information section. Specifically, using the hydrothermal technique at 120°C for 12 hours, we were able to generate both average-sized and small-sized α-Fe_2O_3 N-Rhomb, as determined by XRD (Figure 6.3C & D), with all of the expected diffraction peaks observed, corresponding to the standard JCPDS pattern for phase-pure hematite α-Fe_2O_3 (JCPDS #86-0550). Typical images associated with the SEM analysis of the smaller-sized and average-sized N-Rhomb, as shown in Figure 6.3A & B, revealed that the nanostructures possessed the correct morphology and were uniform in size, with associated measured lengths of 47 ± 10 nm and 75 ± 8 nm, and corresponding widths of 35 ± 8 nm and 50 ± 8 nm, respectively.

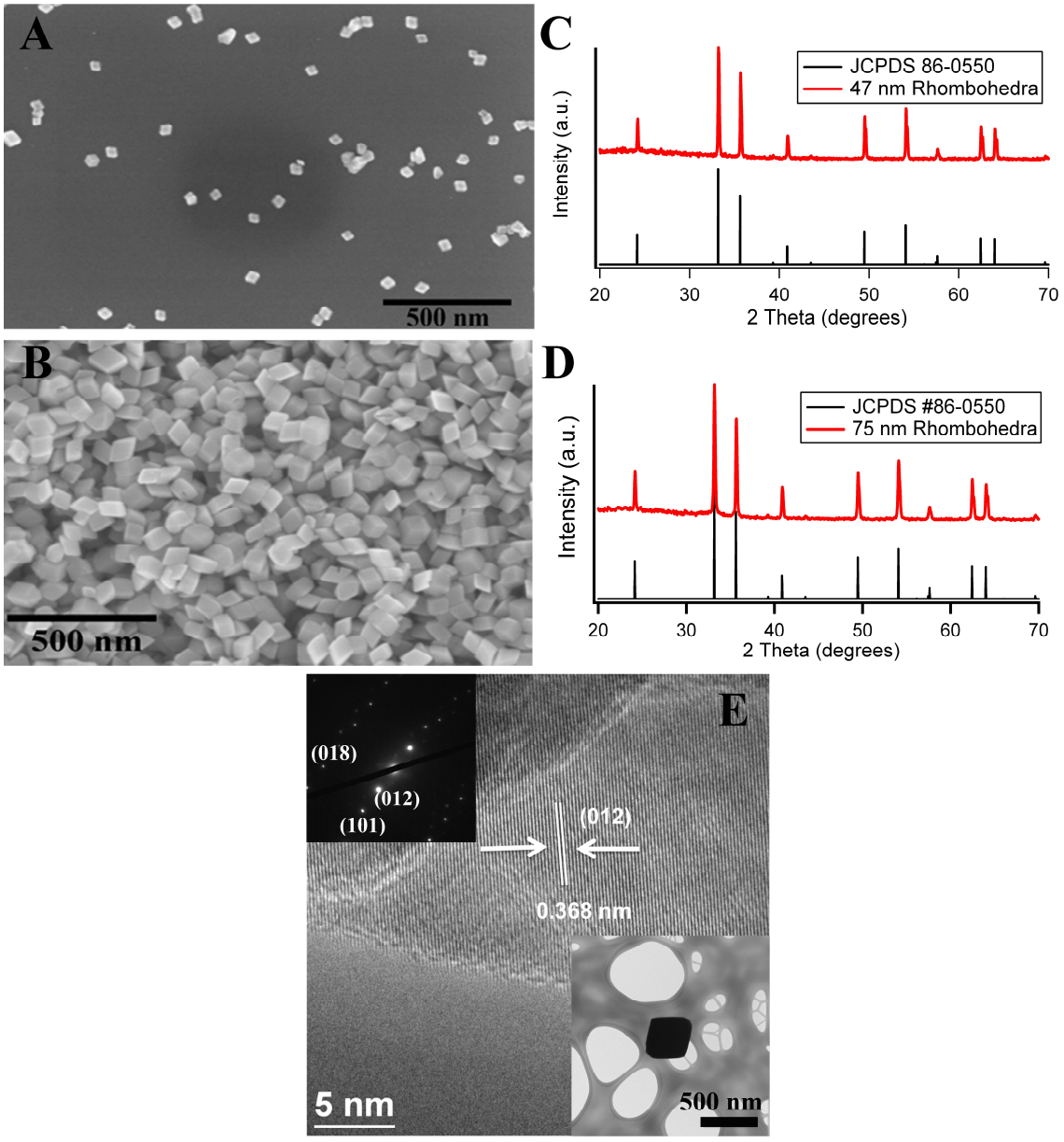

Figure 6.3. Characterization of small and average sized bare α-Fe_2O_3 N-Rhomb. (**A&C)** SEM and XRD images of small and average-sized (**B & D**) α-Fe_2O_3 N-Rhomb. (**E)**. High-resolution TEM image of bare α-Fe_2O_3 N-Rhomb. A low magnification image in the lower right-hand inset is shown. The upper left-hand inset highlights the electron diffraction pattern. Image reproduced from Ref. 1 with permission from The Royal Society of Chemistry.

6.2.4. Cultured Microglia Engulf bare α-Fe_2O_3 N-Rhomb

When the CNS undergoes either injury, infection, or disease, microglia, i.e. the immuno-competent cells of the CNS, act as the first line of defense. They migrate to the site of injury, assume antigen-presenting properties, secrete cytokines, and trigger phagocytosis of dead cells and cell debris.[63]

To test the ability of microglia to internalize nano-sized α-Fe_2O_3 particles, N9 immortalized microglia were exposed to increasing concentrations of the smaller sized bare α-Fe_2O_3 NRhomb (Figure 6.4A). The cells were imaged with a light microscope, approximately 24 hours after exposure (Figure 6.4A). The light microscopy images shows that N9 microglia did indeed internalize α-Fe_2O_3 N-Rhomb and consequentially, remained viable after treatment, as the structural integrity of the membranes of the microglia cells were maintained, even upon nanostructure incorporation (Figure 6.4A).

Electron microscopy images of primary C57BL6 microglia were also consistent with this observation. For each nanoparticulate concentration tested, these microglia cells were found to have incorporated ~47 nm α-Fe_2O_3 NRhomb primarily within the cellular vesicles as opposed to the nucleus (Figure 6.4B). In general, we found that the higher the initial incubation concentration, the greater the number of NRhomb particles observed within the microglia. Moreover, there was no sign of cytotoxicity, as the cells retained their resting state and shape (i.e. long branches with small cellular bodies). It is noteworthy that the larger-sized ~75 nm NRhomb were detected and incorporated to a lesser extent within the microglia cells as compared with the correspondingly smaller ~47 nm N-Rhomb (Figure 6.5). As a result, additional experiments were performed on the smaller-sized ~47 nm nanorhombohedra.

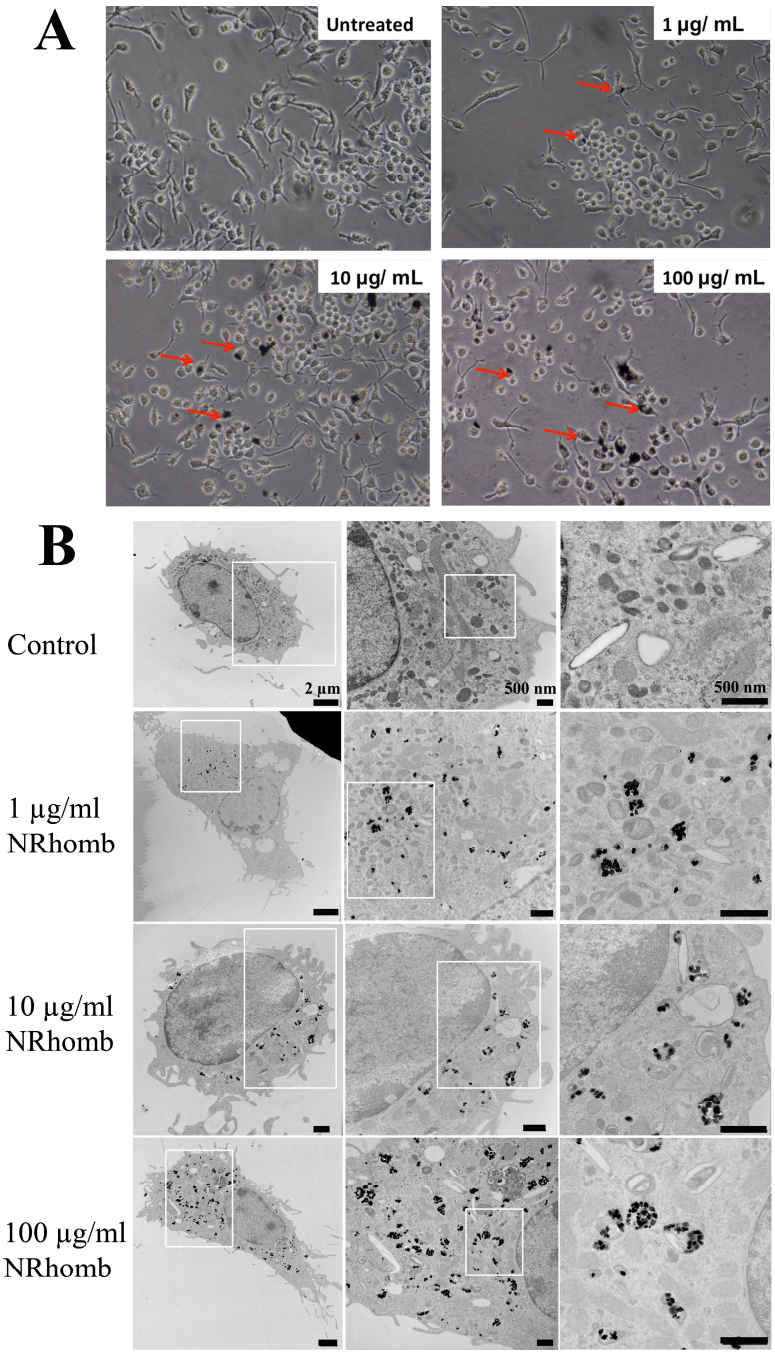

Figure 6.4. Cultured primary microglia engulf bare ~47 nm α-Fe_2O_3 N-Rhomb. Light microscopy images **(A)** of untreated cells and of cells exposed to 1, 10, and 100 µg/mL, respectively, of bare α-Fe_2O_3 N-Rhomb. Images were taken after 24 h after α-Fe_2O_3 N-Rhomb exposure. Red arrows point towards cells that have internalized α -Fe_2O_3 N-Rhomb. TEM images **(B)** of untreated cells and of cells exposed to 1, 10, and 100 µg/mL, respectively, of bare α-Fe_2O_3 N-Rhomb. High magnification images of control-treated microglia (RhB) and of 1 µg/mL α-Fe_2O_3 N-Rhomb (N-Rhomb)-treated microglia. Scale bars are either 2 µm or 500 nm. Image reproduced from Ref. 1 with permission from The Royal Society of Chemistry.

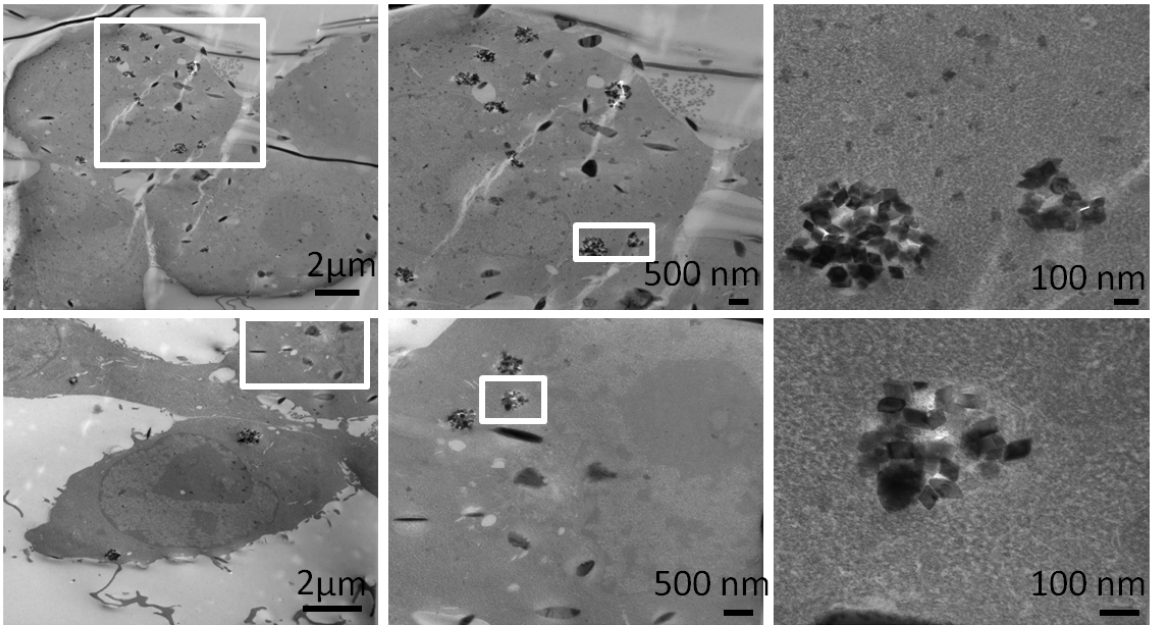

Figure 6.5. Cultured N9 microglia engulf bare α-Fe_2O_3 N-Rhomb. Electron microscopy images of untreated cells and of cells exposed to ~45 nm (top) and ~75 nm (bottom) bare α-Fe_2O_3 N-Rhomb. White squares surround areas chosen for magnification, which are shown in the subsequent images. Supplemental image reproduced from Ref. 1 with permission from The Royal Society of Chemistry.

To further confirm the presence of α-Fe_2O_3 NRhomb within the microglia cells themselves, chemically-sensitive EDX spectroscopy data were taken on two representative regions of the microglia (Figure 6.6). In one area, the hematite N-Rhomb structures appear to be clearly engulfed within the microglia cells (Free Draw 1), whereas in another area, no hematite nanorhombohedra are apparently visible (Free Draw 2). Based upon the EDX spectrum, the intensity of the N-Rhomb-containing area gave rise to significantly higher peak intensities for Fe, i.e. ~ 7x larger, than for the area without N-Rhomb present. Therefore, these data are consistent with the idea of the iron oxide nanostructures as being localized and engulfed within the microglia cells, as expected. Other peaks such as copper (Cu), lead (Pb), and osmium (Os) emanate from the TEM

copper grid as well as from the cross-sectional staining agents of lead citrate and osmium tetroxide, respectively.

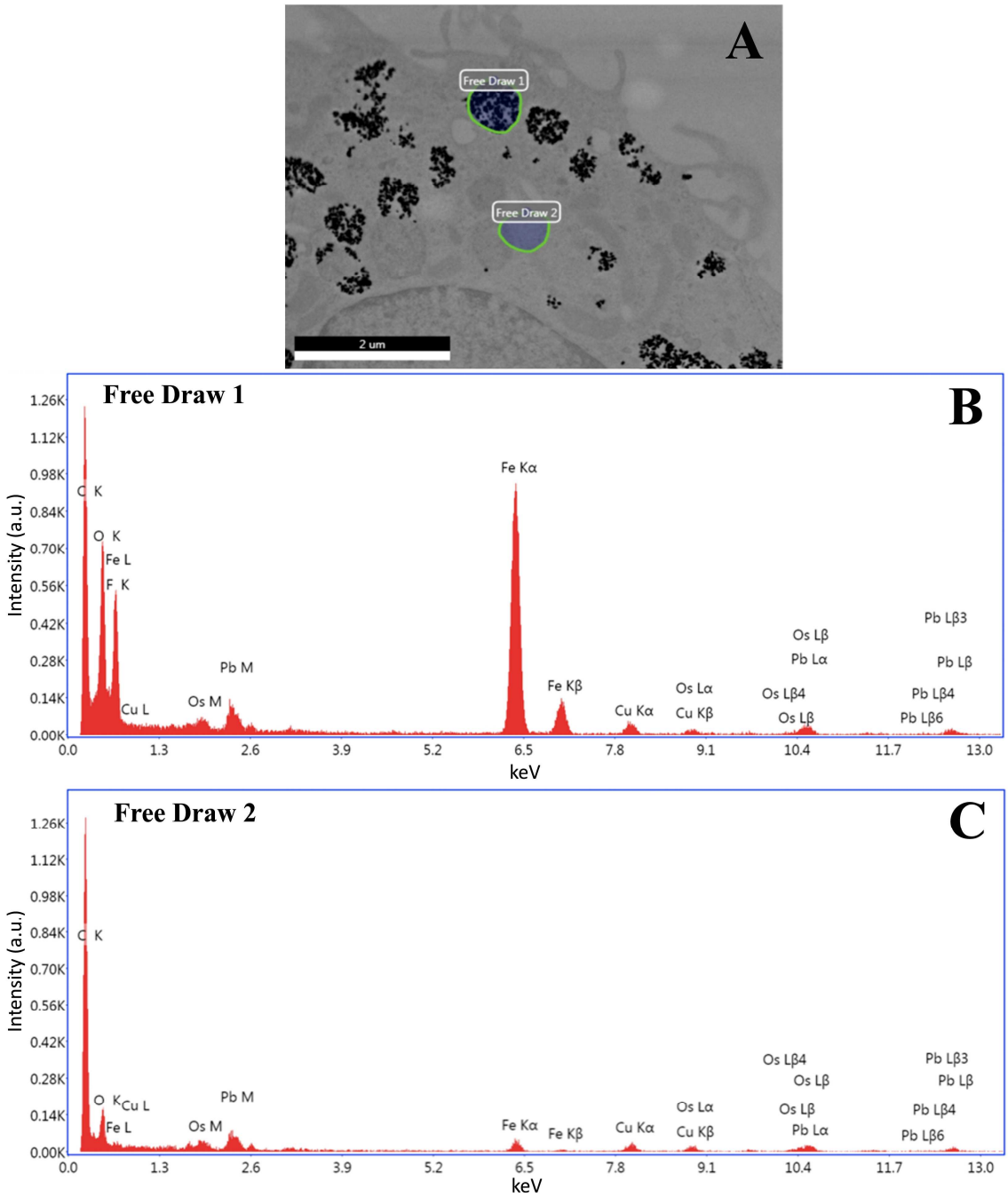

Figure 6.6. Energy-dispersive X-ray spectroscopy data on (A) Fe_2O_3 N-Rhomb-containing microglia cells in a region incorporating Fe_2O_3 N-Rhomb (B) and in an area without Fe_2O_3 N-Rhomb (C). Supplementary image reproduced from Ref. 1 with permission from The Royal Society of Chemistry.

To visualize the *in vitro* engulfment of the α-Fe_2O_3 NRhomb by microglia from an optical perspective, α-Fe_2O_3 NRhomb were labeled with the fluorescent dye RhB for easy detection (Figure 6.7A). We describe the chemical modification protocol used to conjugate α-Fe_2O_3 NRhomb with RhB, both in words as well as schematically (Figure 6.1) in the previous section. Spectroscopic confirmation of the successful attachment and binding of the dye onto the iron oxide surface was provided by UV-visible and IR spectroscopy data. The expected absorption and bond signatures noted in these results are consistent with the generation of RhB-labeled α-Fe_2O_3 NRhomb (Figure 6.2). Additionally, the engulfment behavior of RhB-labeled N-Rhomb by primary microglia was compared with that of a bare RhB control (Figure 6.8).

Primary microglia were obtained from neonatal MacGreen mice, which express eGFP under the control of the microglia/macrophage promoter CSF1R in the C57BL6 background.[64] MacGreen microglia were exposed to increasing concentrations of both RhB-labeled α-Fe_2O_3 NRhomb and bare RhB in separate runs for 24 hours. The cells were fixed, mounted on slides, and imaged using a confocal microscope. The fluorescence intensity, emanating from both the RhB-labeled α-Fe_2O_3 N-Rhomb and bare RhB contained within each cell, was quantified using ImageJ (Figure 6.7A & Figure 6.8).

Figure 6.7A is consistent with increasing fluorescence intensity correlated with increasing concentrations of RhB-labeled α-Fe_2O_3 NRhomb analyzed. Cells treated with 100 μg/mL of RhB-labeled α-Fe_2O_3 NRhomb possessed significantly higher total cell fluorescence especially when compared with untreated cells as well as with cells treated

with 1 μg/mL and 10 μg/mL of RhB-labeled α-Fe_2O_3 NRhomb, thereby indicating that microglia do successfully internalize these nanostructures (Figure 6.7A).

Upon comparison, the control RhB samples also substantiated a trend of increasing fluorescent intensity with increasing concentration (Figure 6.8). However, changes in the microglial morphology from the original resting to a more activated, amoeboid form were evident, when imaging cells treated with sample controls at concentrations of 10 μg/mL and higher. However, this did not appear to be true in the presence of RhB-labeled Fe_2O_3 NRhomb, as these microglia cells all maintained their inactive, ramified (i.e. long branched filaments) morphology.

6.2.5 Microglia engulf Rh-B-labeled α-Fe_2O_3 NRhomb in a clathrin-dependent manner

To investigate the mechanism underlying the internalization of RhB functionalized α-Fe_2O_3 NRhomb, we tested the effect of chlorpromazine (CPZ), a specific clathrin-mediated endocytosis inhibitor, on the ability of microglia to internalize RhB-labeled α-Fe_2O_3 NRhomb (Figure 6.7B).[65] Cultured MacGreen microglia were pre-treated with a high concentration (30 μM) of CPZ for 2 hours prior to RhB-labeled α-Fe_2O_3 NRhomb exposure, as previously described.[65] Approximately 24 hours later, the cells were fixed, mounted, and imaged under a confocal microscope. Microglia maintained their resting morphology after CPZ treatment, and in effect, we observed that the concentration of CPZ induced little if any apparent toxic effects (Figure 6.7B).

The localization of RhB labeled Fe_2O_3 NRhomb outside the cellular membrane of the microglia cells under confocal microscopy conditions suggested a lack of engulfment of the nanostructures (Figure 6.7B). Fluorescence quantification shows that treatment

with 30 µM CPZ significantly prevented as much as 96% of the potential uptake of RhB-labeled α-Fe_2O_3 NRhomb at all of the concentrations of nanoparticles tested from 1 µg/mL to 100 µg/mL, thereby supporting the idea that microglia primarily internalize these particles through a clathrin-dependent mechanism (Figure 6.7C).

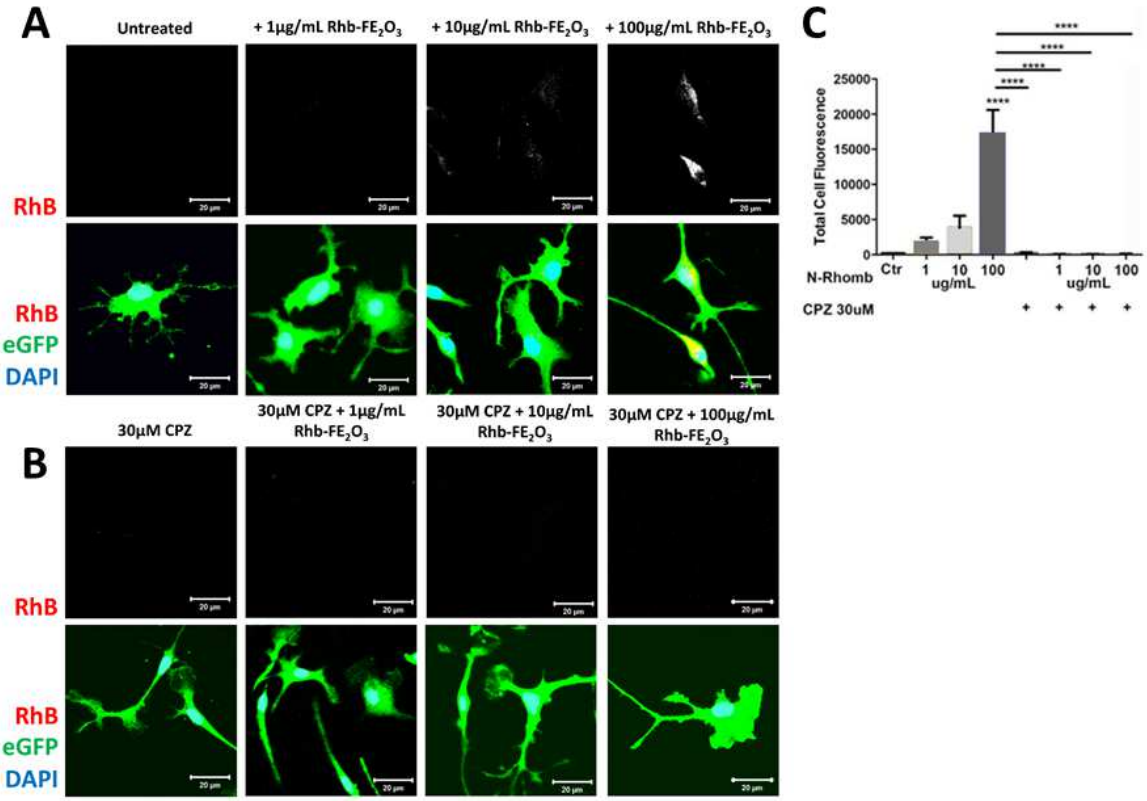

Figure 6.7. Primary microglia internalize RhB-labeled α-Fe_2O_3 N-Rhomb using a clathrin-dependent mechanism. (A). Confocal images of eGFP expressing microglia exposed to 1, 10, and 100 µg/mL, respectively, of RhB-labeled α-Fe_2O_3 N-Rhomb, stained with DAPI for nuclear staining. **(B).** Confocal images of cells exposed to 0, 1, 10, and 100 µg/mL, respectively, of RhB-labeled α-Fe_2O_3 N-Rhomb. Cells were pre-treated with 30 µM CPZ, 2 hours prior to nanoparticle exposure. Images were taken 24 hours after nanoparticle exposure. **(C).** Quantification of the RhB fluorescence of microglia treated either with or without 30 µM CPZ followed by incubation with RhB-labeled Fe_2O_3 N-Rhomb. Scale bars = 20 µm. Data are shown as mean ± SEM. **** $p<0.0001$. Image reproduced from Ref. 1 with permission from The Royal Society of Chemistry.

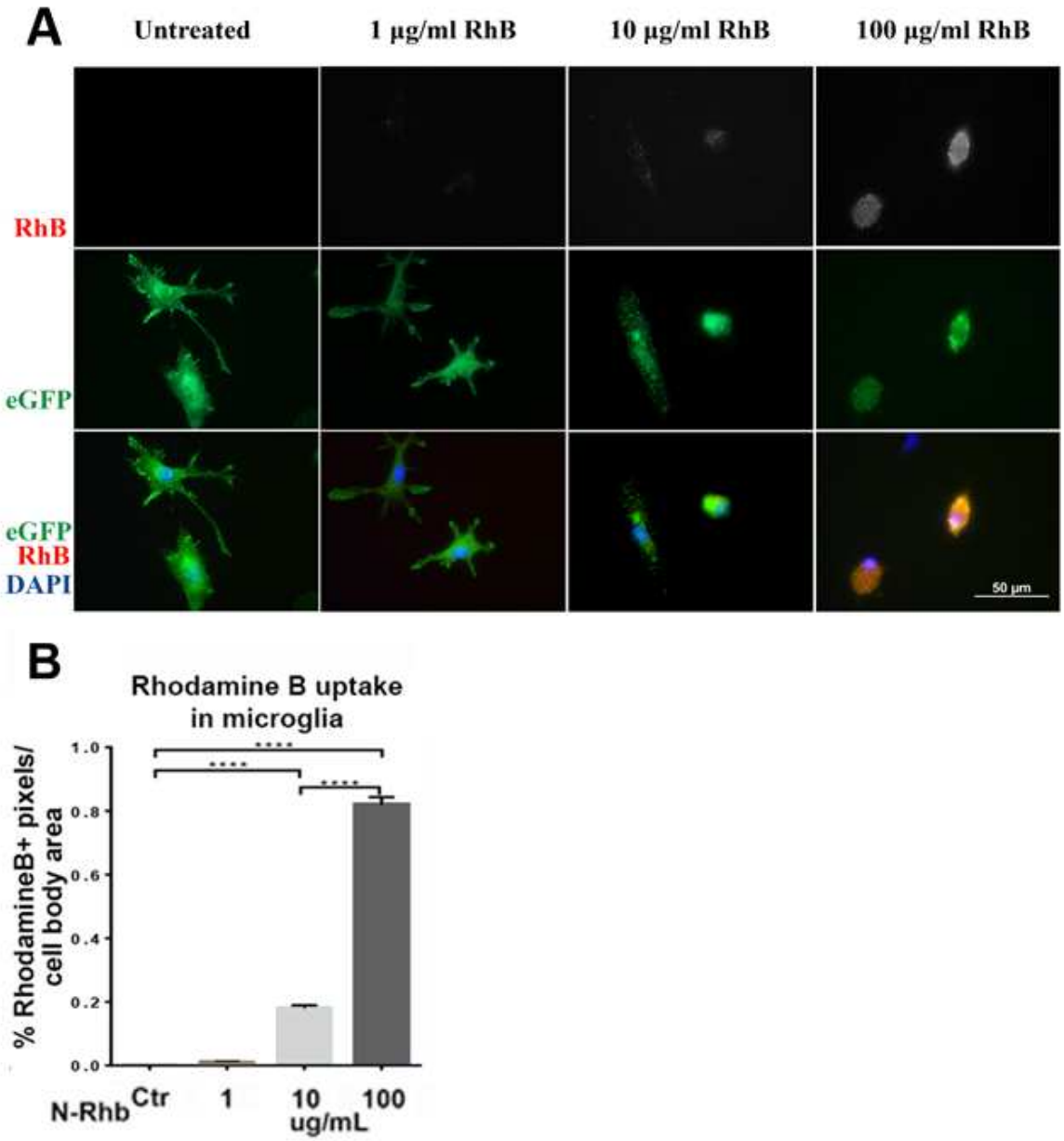

Figure 6.8. Uptake of bare Rhodamine B in microglia cells. (A). Confocal images of microglia exposed to 0 (Untreated), 1, 10, and 100 µg/mL, respectively, of bare RhB. DAPI was used to stain cell nuclei. Scale bar = 50µm. **(B).** Quantification of the RhB fluorescence of microglia treated with bare RhB at varying concentrations. Data are shown as mean ± SEM. **** $p<0.0001$. Supplementary image reproduced from Ref. 1 with permission from The Royal Society of Chemistry.

6.2.6 RhB-labeled α-Fe_2O_3 NRhomb are not toxic to Microglia at therapeutic concentrations

To test the potential cytotoxicity of the RhB functionalized α-Fe_2O_3 N-Rhomb on cultured microglia, a LDH assay was used. LDH is rapidly released when the membranes of cells rupture, and hence, the presence of LDH in the supernatant is indicative of cell death.[66] As such, primary microglia were treated with increasing concentrations of RhB-labeled α-Fe_2O_3 N-Rhomb (Figure 6.9A), and the media were collected 24 and 48 hours later so as to measure LDH release. As Figure 6.9A shows, both untreated and treated microglia exhibited similar levels of LDH release and displayed less than ~4% cytotoxicity at 24 hours. After 48 hours, a significant increase of ~30% cytotoxicity was noted in microglia treated with the highest concentration of NRhomb (i.e. 100 μg/mL). Furthermore, it should be noted that this concentration is approximately 626μM, which far exceeds a normal therapeutic dose. All of the other concentrations tested exhibited no apparent cytotoxicity over the period of time tested.

6.2.7 RhB-labeled α-Fe_2O_3 N-Rhomb do not cause in vitro microglial activation

Microglia can give rise to at least two different activation states, depending on the signals they receive: the pro-inflammatory M1 state and the anti-inflammatory M2 state. In the M1 state, microglia secrete tumor necrosis factor alpha (TNFα), interleukin-1 beta (IL1β), and other pro-inflammatory cytokines, while in the M2 state, microglia produce IL-10, IL-4, TGF-β, as well as other anti-inflammatory factors. In several injury models, M2 microglia have been deemed to be beneficial for tissue regeneration,[67, 68] whereas M1 microglia are considered to inhibit tissue healing and repair. Upregulation of TNFα has

been found in previous literature to be implicated as a factor in various ailments such as Alzheimer's disease, cancer, major depression, and inflammatory bowel disease.[69-73]

To evaluate whether RhB-labeled α-Fe_2O_3 N-Rhomb result in microglial release of pro-inflammatory factors, ELISAs were performed to quantify the levels of the pro-inflammatory cytokines TNFα and IL1β. Primary microglia were treated with increasing concentrations of RhB-labeled α-Fe_2O_3 N-Rhomb, and the media were collected approximately 24 hours later to measure corresponding levels of TNFα and IL1β (Figure 6.9B & C).

Exposure to lipopolysaccharide (LPS) was used as a positive control since it is a potent inducer of pro-inflammatory cytokines in microglia.[74] After 24 hours, there was no significant increase in the levels of either TNFα or IL1β produced by microglia that had been treated with systematically greater concentrations (i.e. 1, 10, or 100 μg/mL) of RhB-labeled α-Fe_2O_3 N-Rhomb, relative to the control. As expected, the levels of TNFα and IL1β released by LPS-treated cells were significantly higher than those produced by both untreated cells (i.e. control) as well as the cells treated with RhB-labeled α-Fe_2O_3 N-Rhomb, thereby confirming that the presence of these nanoparticles does not necessarily give rise to the expression of pro-inflammatory agents.

6.2.8 RhB-labeled α-Fe_2O_3 N-Rhomb do not trigger either nitric oxide or ROS production in vitro

It is well known that nitric oxide (NO) is associated with various key functions within the CNS, such as regulation of synaptic plasticity, the sleep-wake cycle, and hormone secretion.[75, 76] However, when produced in excess, NO can undergo oxidation reduction reactions through the formation of reactive oxygen species (ROS), thereby

generating reactive nitrogen-containing species that can result in nitrosative stress and cellular damage.[75, 76] Nitrite production by microglia after engulfment of N-Rhomb remained low, suggesting that the presence of varying concentrations of N-Rhomb did not result in the production of NO by microglia (Figure 6.9D). All concentrations of RhB-labeled N-Rhomb particles tested gave rise to insignificant changes in NO production by microglia, relative to untreated, control cells. Moreover, their NO production was significantly lower than that of a positive LPS control. Hence, it can be concluded that the presence of RhB labeled N-Rhomb alone does not induce noticeable NO production in microglia.

The production of ROS by microglia was also assessed using a DCFDA assay. DCFDA is esterified and oxidized by cells in the presence of ROS, giving rise to the fluorescent compound, DCF. Microglia treated with LPS served as a positive control for the production of ROS and, by extension, the intracellular accumulation of DCF. Cells treated with increasing concentrations of N-Rhomb showed no significant elevation in DCF accumulation relative to that of control samples, i.e. untreated cells, a finding indicative of negligible production of ROS (Figure 6.9E). Thus, it was determined that concentrations of NRhomb of up to 100 μg/mL did not induce ROS production in microglia *in vitro*.

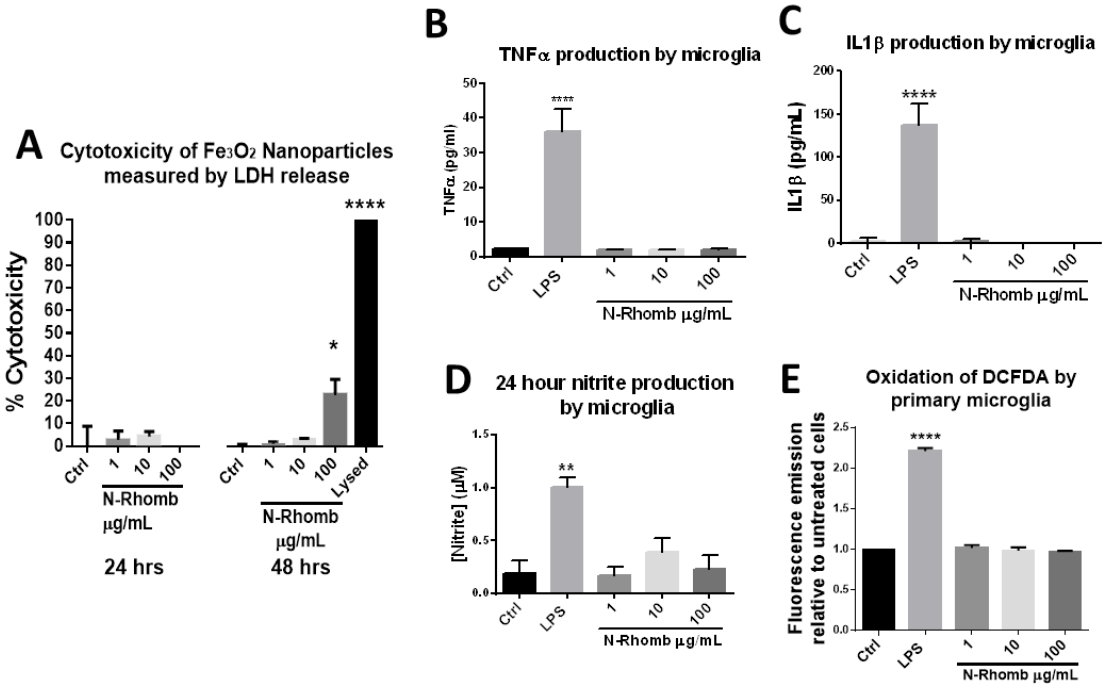

Figure 6.9. RhB-labeled α -Fe_2O_3 N-Rhomb are minimally cytotoxic and do not result in either the upregulation of pro-inflammatory factors or nitrite production within cultured microglia. (**A**)**.** Conditioned media from primary microglia, treated with 1, 10, and 100 µg/mL, respectively, of α-Fe_2O_3 N-Rhomb were collected, and levels of LDH were measured at 24 and 48 hours. Untreated cells (Ctrl) served as a negative control and lysed cells served as a positive control for LDH release. **(B-C).** Primary microglia were treated with either 0 (Ctrl), 1, 10, or 100 µg/mL, respectively, of α-Fe_2O_3 N-Rhomb, or with 100 ng/mL LPS (LPS). Approximately 24 hours after treatment, media isolated from the cells were used for the detection of TNFα **(B).** or IL1β (**C**)**.** (**D**)**.** Nitrite production by primary microglia after 24 hours of incubation with 0 (Ctrl), 1, 10, or 100 µg/mL of α-Fe_2O_3 N-Rhomb, or with 100 ng/mL LPS. **(E).** Oxidation of DCFDA by microglia after a 24 hour incubation with 0 (Ctrl), 1, 10, or 100 µg/mL of α-Fe_2O_3 N-Rhomb, or with 100 ng/mL LPS. Data are shown as mean ± SEM. * $p<0.05$, ** $p<0.01$, **** $p<0.0001$. Image reproduced from Ref. 1 with permission from The Royal Society of Chemistry.

6.2.9 Microglia internalize RhB-labeled α-Fe_2O_3 N-Rhomb in vivo

To test whether microglia can internalize RhB-labeled α-Fe_2O_3 N-Rhomb *in vivo*, MacGreen mice were injected with 100 µg/mL of RhB-labeled α-Fe_2O_3 N-Rhomb bilaterally into the dorsal hippocampus. Approximately 24 hours after the injection, the mice were transcardially perfused with 4% PFA; the brains were then collected, cryo-protected, sectioned into 40-µm thick slices, mounted, and imaged under a confocal microscope. White arrows in Figure 6.10 point towards microglia that have internalized RhB-labeled α-Fe_2O_3 N-Rhomb. Taken together, these data indicate that microglia can engulf α-Fe_2O_3 nanostructures under both *in vitro* and *in vivo* conditions in a clathrin-dependent manner without causing microglia to release pro-inflammatory factors which might have thereby compromised the viability of the cells.

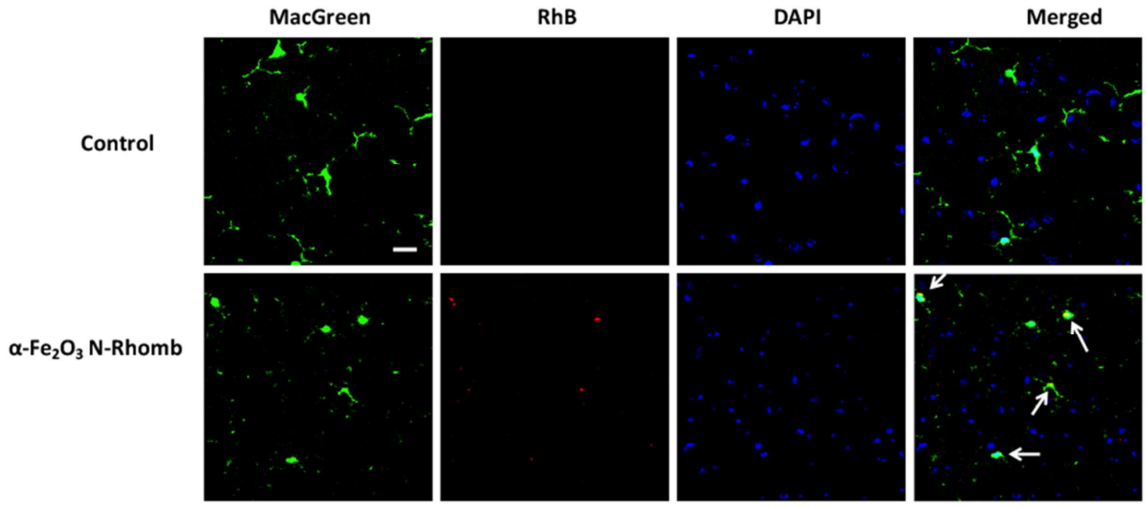

Figure 6.10. Microglia engulf RhB-labeled α -Fe_2O_3 N-Rhomb in vivo. Confocal images of brain sections from MacGreen mice treated with 100 µg/mL RhB-labeled α-Fe_2O_3 N-Rhomb. White arrows point towards microglia that have internalized the RhB-labeled α-Fe_2O_3 N-Rhomb. Scale = 20 µm. Image reproduced from Ref. 1 with permission from The Royal Society of Chemistry.

6.3. Discussion & Conclusions

We have synthesized RhB labeled α-Fe_2O_3 N-Rhomb, and tested the ability of microglia to internalize them. These cells appear to efficiently engulf the RhB functionalized α-Fe_2O_3 N-Rhomb without any noticeable membrane damage, as suggested by electron and confocal microscopy. In terms of addressing potential shape-dependent toxicity, RhB-labeled α-Fe_2O_3 N-Rhomb are non-inflammatory and non-cytotoxic at therapeutic concentrations, suggesting that α-Fe_2O_3 N-Rhomb have the potential to be used as drug carriers. Drugs that either reduce M1 activation or induce M2 activation such as minocycline, tuftsin (TKPR), or microglia inhibitory factor (MIF/TKP)[77] could be conjugated onto nanoparticles in order to alter the phenotype of microglia. For instance, Papa et al. showed that nanostructures conjugated onto minocycline are engulfed by microglia and reduce inflammation in a model of spinal cord injury.[77]

Our results thus show promise for future studies involving the conjugation of anti-inflammatory compounds onto nanostructures that can be engulfed by microglia as well as for the tracking of cell behavior using imaging techniques such as confocal microscopy and MRI, for example. This point has been demonstrated by some of our unpublished work (data not shown), in which we have observed that α-Fe_2O_3 N-Rhomb can be detected within a mouse brain by using T_2-weighted MRI scans.

We have been able to demonstrate that microglia can internalize both bare and RhB labeled N-Rhomb. Particle aggregation is expected due to the direct mutual attraction between nanostructures occurring via either van der Waals forces or chemical bonding.[78, 79] Sonication of the RhB labeled N-Rhomb prior to exposure to microglia

reduced the degree of particle aggregation, although it did not completely prevent clustering. Due to the low TNFα, IL-1β, ROS, and nitrite levels in microglia after the RhB-labeled N-Rhomb treatment, it is unlikely that microglia themselves became over-activated, thereby resulting in an engulfment of a large amount of particles. The particle clusters observed in Figure 6.4 are more likely the result of aggregation, due to strong mutual attraction between these nanostructures.

Microglia are highly phagocytic and can clear away dead cells and debris using a variety of endocytic mechanisms, including receptor-mediated endocytosis, pinocytosis, and phagocytosis.[77] Indeed, microglia play key roles in several neurological diseases and can quickly respond to either infection or injury.[77] Chemically modified nanostructures that can be easily engulfed by microglia represent therefore a potentially viable strategy with which to manipulate the functional properties of the microglia themselves.

Specifically, we have shown that microglia used a clathrin-dependent endocytic pathway to internalize RhB-labeled α-Fe_2O_3 N-Rhomb, as evidenced by the lack of nanoparticle uptake even at varying concentration levels, in the presence of the endocytosis inhibitor, CPZ. This observation is in agreement with other studies that have successfully demonstrated internalization of other types of nanostructures by microglia.[77] Additionally, we have highlighted that internalization does not cause aberrant activation in cultured microglia, i.e. in the presence of RhB labeled-α-Fe_2O_3 N-Rhomb maintaining concentrations of up to 100 μg/mL, and that microglia in the mouse brain are equally efficient at internalizing hematite nanostructures, thereby indicating that α-Fe_2O_3 N-Rhomb may be suitable for coupling anti-inflammatory agents as a form of drug therapy.

6.4 Future Directions

As previously mentioned, microglia also possess an M2 active state where this species can promote neuronal regeneration by releasing anti-inflammatory cytokines such as IL-10. Tuftsin, a tetrapeptide (Thr-Lys-Pro-Arg), stimulates such a response within microphages and microglia.[80] Tuftsin also binds to cell-surface receptors such as neuropinil-1 (Nrp1) which mediates axonal guidance and immune responses.[81] As a result, this tetrapeptide is generally considered for use in immunotherapy.

As an extension of our work, we propose to use Fe_2O_3 as a carrier to deliver tuftsin to the lesioned and damaged area in order to enhance the anti-inflammatory mechanistic response of the cells and to ultimately and favorably redress problems at the site of injury. Initially, in order to conjugate tuftsin onto the iron oxide surface, a similar carbodiimide chemistry protocol would be employed. However, steric hindrance could prevent conjugation at the carbonyl carbon. As a result, other crosslinking methods, particularly amine-reactive crosslinkers (i.e. NHS-ester species), may be utilized to activate the amine groups of the tuftsin compound.

Subsequently, the Fe_2O_3 can easily be functionalized with a carboxyl group for amide formation between the two entities (i.e. Tuftsin-Fe_2O_3). These microglia will be introduced to the Tuftsin-Fe_2O_3 NRhomb and tested to determine whether these remain in a 'resting' state. Changes in the level of activity will be observed over time by immunostaining F-actin and vimentin filament networks as markers to detect alterations in the microglia morphology.[82] The levels of pro-inflammatory cytokines (i.e. TNFα, IL-1β, and etc.) will be quantified, using their respective assays, to confirm M1 activation; to

complement this work, the appearance of IL10 secretions would serve as indicators for M2 activation.

6.5. References

1. C. S. Lewis, L. Torres, J. T. Miyauchi, C. Rastegar, J. M. Patete, J. M. Smith, S. S. Wong and S. E. Tsirka, *Toxicology Research*, 2016, 5, 2129-2142.
2. C. A. Colton and D. M. Wilcock, *CNS & Neurological Disorder - Drug Targets*, 2010, 9, 174-191.
3. A. Nimmerjahn, F. Kirchhoff and F. Helmchen, *Science*, 2005, 308, 1314-1318.
4. M. Ueno, *Nature Neuroscience*, 2013, 16, 543-551.
5. R. C. Paolicelli, *Science*, 2011, 333, 1456-1458.
6. U. K. Hanisch, *Glia*, 2002, 40, 140-155.
7. D. Davalos, *Nature Neuroscience*, 2005, 8, 752-758.
8. C. A. Colton, *Journal of NeuroImmune Pharmacology*, 2009, 4, 399-418.
9. J. Z. Pan, *Journal of Neuroscience Research*, 2002, 68, 315-322.
10. K. A. Kigerl, *The Journal of Neuroscience*, 2009, 29, 13435-13444.
11. V. Colvin, *Nat. Biotech.*, 2003, 21, 1166-1170.
12. C. S. S. R. Kumar, ed., *Nanomaterials: toxicity, health and environmental issues*, Wiley-VCH, Weinheim, 2006.
13. N. Lewinski, V. Colvin and R. Drezek, *Small*, 2008, 4, 26-49.
14. W. Li, C. Chen, C. Ye, T. Wei, Y. Zhao, F. Lao, Z. Chen, H. Meng, Y. Gao, H. Yuan, G. Xing, F. Zhao, Z. Chai, X. Zhang, F. Yang, D. Han, X. Tang and Y. Zhang, *Nanotechnology*, 2008, 19, 145102.
15. J. Sudimack and R. J. Lee, *Advanced Drug Delivery Review*, 2000, 41, 147-162.
16. W. H. Suh, K. S. Suslick, G. D. Stucky and Y.-H. Suh, *Progress in Neurobiology*, 2009, 87, 133-170.
17. S. Chen, X. Zhao, J. Chen, J. Chen, S. S. Wong and I. Ojima, *Bioconjugate Chemistry*, 2010, 21, 979-987.
18. F. Zhang and S. S. Wong, *American Chemistry Society Nano*, 2010, 4, 99-112.
19. H. Zhou, J. Chen, E. Sutter, M. Feygenson, M. C. Aronson and S. S. Wong, *Small*, 2010, 6, 412-420.
20. J. Chen, H. Zhou, A. C. Santulli and S. S. Wong, *Chemical Research in Toxicology*, 2010, 23, 871-879.
21. B. J. Panessa-Warren, J. Warren, S. S. Wong and J. A. Misewich, *Journal of Physics: Condensed Matter*, 2006, 18, S2185-S2201.
22. A. Magrez, L. Horváth, R. Smajda, V. Salicio, N. Pasquier, L. Forró and B. Schwaller, *ACS Nanoscience & Nanotechnology*, 2009, 3, 2274-2280.
23. C. Jin, Y. Tang, F. Yang, X. Li, S. Xu, X. Fan, Y. Huang and Y. Yang, *Biological Trace Element Research*, 2011, 141, 3-15.
24. G. Tejral, N. R. Panyala and J. Havel, *Journal of Applied Biomedicine*, 2009, 7, 1-13.
25. Z. Q. Samra, S. Shabir, Z. Rehmat, M. Zaman, A. Nazir, N. Dar and M. A. Athar, *Applied Biochemistry and Biotechnology*, 2010, 162, 671-686.
26. Y. Ling, K. Wei, Y. Luo, X. Gao and S. Zhong, *Biomaterials*, 2011, 32, 7139-7150.
27. B. Polyak and G. Friedman, *Expert Opinion on Drug Delivery*, 2009, 6, 53-70.
28. Y. Wang, *Quantitative Imaging in Medicine and Surgery*, 2011, 1, 35-40.

29. S. Xu, F. Yang, X. Zhou, Y. Zhuang, B. Liu, Y. Mu, X. Wang, H. Shen, G. Zhi and D. Wu, *ACS Appl Mater Interfaces*, 2015, 7, 20460-20468.
30. M. Z. Iqbal, X. Ma, T. Chen, L. e. Zhang, W. Ren, L. Xiang and A. Wu, *Journal of Materials Chemistry B: Materials for Biology and Medicine*, 2015, 3, 5172-5181.
31. M. Catti, G. Valerio and R. Dovesi, *Physical Review B: Condensed Matter*, 1995, 51, 7441-7450.
32. H. Liang, X. Jiang, Z. Qi, W. Chen, Z. Wu, B. Xu, Z. Wang, J. Mi and Q. Li, *Nanoscale*, 2014, 6, 7199-7203.
33. G. Wang, W. Li, K. Jia, B. Spliethoff, F. Schüth and A. Lu, *Applied Catalysis A: General*, 2009, 364, 42-47.
34. S. Xu, C. M. Hessel, H. Ren, R. Yu, Q. Jin, M. Yang, H. Zhao and D. Wang, *Energy & Environmental Science*, 2014, 7, 632-637.
35. G. Tong, J. Guan and Q. Zhang, *Materials Chemistry and Physics*, 2011, 127, 371-378.
36. P. Basnet, G. K. Larsen, R. P. Jadeja, Y.-C. Hung and Y. Zhao, *Applied Materials & Interfaces*, 2013, 5, 2085-2095.
37. J. M. Berg, S. Ho, W. Hwang, R. Zebda, K. Cummins, M. P. Soriaga, R. Taylor, B. Guo and C. M. Sayes, *Chemical Research in Toxicology*, 2010, 23, 1874-1882.
38. F. S. Freyria, B. Bonelli, M. Tomatis, M. Ghiazza, E. Gazzano, D. Ghigo, E. Garrone and B. Fubini, *Chemical Research in Toxicology*, 2012, 25, 850-861.
39. L. Chen, J. Xie, J. Yancey, M. Srivatsan and V. K. Varadan, *Journal of Nanotechnology in Engineering and Medicine*, 2010, 1, 041014/041011-041014/041015.
40. Å. Gustafsson, U. Bergström, L. Ågren, L. Österlund, T. Sandström and A. Buchta, *Toxicology and Applied Pharmacology*, 2015, 288, 1-11.
41. Y. Zhao, F. Pan, H. Li, T. Niu, G. Xu and W. Chen, *Journal of Materials Chemistry A*, 2013, 1, 7242-7246.
42. L. E. Barton, A. N. Quicksall and P. A. Maurice, *Geomicrobiology Journal*, 2012, 29, 314-322.
43. A. Adili, S. Crowe, M. F. Beaux, T. Cantrell, P. J. Shapiro, D. N. McIlroy and K. E. Gustin, *Nanotoxicology*, 2008, 2, 1-8.
44. Y. Wang, X. Y. Zhou, Z. Chen, B. Cai, Z. Z. Ye, C. Y. Gao and J. Y. Huang, *Applied Physics a-Materials Science & Processing*, 2014, 117, 2121-2126.
45. P. R. Lockman, M. O. Oyewumi, J. M. Koziara, K. E. Roder, R. J. Mumper and D. D. Allen, *Journal of Controlled Release*, 2003, 93, 271-282.
46. B. T. Farrell, B. E. Hamilton, E. Dósa, E. Rimely, M. Nasseri, S. Gahramanov, C. A. Lacy, E. P. Frenkel, N. D. Doolittle, P. M. Jacobs and E. A. Neuwelt, *Neurology*, 2013, 81, 256-263.
47. Y. Wang, B. Wang, M. T. Zhu, M. Li, H. J. Wang, M. Wang, H. Ouyang, Z. F. Chai, W. Y. Feng and Y. L. Zhao, *Toxicology Letters*, 2011, 205, 26-37.
48. B. Wang, W. Y. Feng, M. T. Zhu, Y. Wang, M. Wang, Y. Q. Gu, H. Ouyang, H. J. Wang, M. Li, Y. L. Zhao, Z. F. Chai and H. F. Wang, *Journal of Nanoparticle Research*, 2009, 11, 41-53.

49. J. X. Wang, C. Y. Chen, Y. Liu, F. Jiao, W. Li, F. Lao, Y. F. Li, B. Li, C. C. Ge, G. Q. Zhou, Y. X. Gao, Y. L. Zhao and Z. F. Chai, *Toxicology Letters*, 2008, 183, 72-80.
50. M. Mahmoudi, S. Sant, B. Wang, S. Laurent and T. Sen, *Advanced Drug Delivery Reviews*, 2011, 63, 24-46.
51. L. J. Chew, P. Fusar-Poli and T. Schmitz, *Dev Neurosci*, 2013, 35, 102-129.
52. Y. Deng, J. Lu, V. Sivakumar, E. A. Ling and C. Kaur, *Brain Pathol*, 2008, 18, 387-400.
53. J. E. Merrill and N. J. Scolding, *Neuropathol Appl Neurobiol*, 1999, 25, 435-458.
54. L. Peferoen, M. Kipp, P. van der Valk, J. M. van Noort and S. Amor, *Immunology*, 2014, 141, 302-313.
55. M. Domercq, A. Perez-Samartin, D. Aparicio, E. Alberdi, O. Pampliega and C. Matute, *Glia*, 2010, 58, 730-740.
56. M. M. Varnum and T. Ikezu, *Arch Immunol Ther Exp (Warsz)*, 2012, 60, 251-266.
57. Z. Gao and S. E. Tsirka, *Neurol Res Int*, 2011, 2011, 383087.
58. Y. Wang, J. Cao, S. Wang, X. Guo, J. Zhang, H. Xia, S. Zhang and S. Wu, *Journal of Physical Chemistry C*, 2008, 112, 17804-17808.
59. Z. Pu, M. Cao, J. Yang, K. Huang and C. Hu, *Nanotechnology*, 2006, 17, 799-804.
60. S. E. Lohse, N. D. Burrows, L. Scarabelli, L. M. Liz-Marzan and C. J. Murphy, *Chemistry of Materials*, 2014, 26, 34-43.
61. J. J. Monagle, *Journal of Organic Chemistry*, 1962, 27, 3851–3855.
62. K. E. Pfitzner and J. G. Moffatt, *Journal of American Chemical Society*, 1963, 85, 3027-3028.
63. K. Nakajima and S. Kohsaka, *The Journal of Biochemistry*, 2001, 130, 169-175.
64. R. T. Sasmono, A. Ehrnsperger, S. L. Cronau, T. Ravasi, R. Kandane, M. J. Hickey, A. D. Cook, S. R. Himes, J. A. Hamilton and D. A. Hume, *J Leukoc Biol*, 2007, 82, 111-123.
65. S. Papa, F. Rossi, R. Ferrari, A. Mariani, M. De Paola, I. Caron, F. Fiordaliso, C. Bisighini, E. Sammali, C. Colombo, M. Gobbi, M. Canovi, J. Lucchetti, M. Peviani, M. Morbidelli, G. Forloni, G. Perale, D. Moscatelli and P. Veglianese, *ACS Nano*, 2013, 7, 9881-9895.
66. F. K. Chan, K. Moriwaki and M. J. De Rosa, *Methods Mol Biol*, 2013, 979, 65-70.
67. K. A. Kigerl, J. C. Gensel, D. P. Ankeny, J. K. Alexander, D. J. Donnelly and P. G. Popovich, *J Neurosci*, 2009, 29, 13435-13444.
68. V. E. Miron, A. Boyd, J. W. Zhao, T. J. Yuen, J. M. Ruckh, J. L. Shadrach, P. van Wijngaarden, A. J. Wagers, A. Williams, R. J. Franklin and C. ffrench-Constant, *Nat Neurosci*, 2013, 16, 1211-1218.
69. D. Brenner, H. Blaser and T. W. Mak, *Nat Rev Immunol*, 2015, 15, 362-374.
70. R. M. Locksley, N. Killeen and M. J. Lenardo, *Cell*, 2001, 104, 487-501.
71. W. Swardfager, K. Lanctot, L. Rothenburg, A. Wong, J. Cappell and N. Herrmann, *Biol Psychiatry*, 2010, 68, 930-941.
72. Y. Dowlati, N. Herrmann, W. Swardfager, H. Liu, L. Sham, E. K. Reim and K. L. Lanctot, *Biol Psychiatry*, 2010, 67, 446-457.

73. J. Brynskov, P. Foegh, G. Pedersen, C. Ellervik, T. Kirkegaard, A. Bingham and T. Saermark, *Gut*, 2002, 51, 37-43.
74. Y. Nakamura, Q. S. Si and K. Kataoka, *Neurosci Res*, 1999, 35, 95-100.
75. P. Pacher, J. S. Beckman and L. Liaudet, *Physiological Reviews*, 2007, 87, 315-424.
76. V. Calabrese, C. Mancuso, M. Calvani, E. Rizzarelli, D. A. Butterfield and A. M. Stella, *Nature Reviews Neuroscience*, 2007, 8, 766-775.
77. J. C. Nissen, D. L. Selwood and S. E. Tsirka, *J Neurochem*, 2013, DOI: 10.1111/jnc.12404.
78. R. J. Hunter, *Foundations of Colloid Science*, Oxford University Press, New York, 1987.
79. D. Li and R. B. Kaner, *Journal of the American Chemical Society*, 2006, 128, 968-975.
80. V. A. Najjar and K. Nishioka, *Nature*, 1970, 228, 672-673.
81. N. J. Bump, J. Lee, M. Wleklik, J. Reichler and V. A. Najjar, *Proceedings of the National Academy of Sciences of the United States of America*, 1986, 83, 7187-7191.
82. V. Pierre, B. Veronique, M. Michel, D. Philippe, D. Laura, F. Kristian, F. Jean-Michel and B.-S. Anne-Karine, *Frontiers in Neuroenergetics*, 2010, 2, 131.

Chapter 7- Conclusions

7.1. Conclusions

The experiments described within this thesis, represents a straightforward and cost effective approach for synthesizing various nanomaterials. In addition to controlling the size, morphology, and chemical composition, various parameters were employed to optimize their photocatalytic, magnetic, charge transfer as well as cytotoxic properties. These nanomaterials were all produced using reasonably mild synthetic conditions without either the use of toxic precursors or the creation of toxic by-products within the chemical reactions, thereby minimizing the overall environmental impacts while maintaining high crystallinity and purity.

Specifically, in Chapter 3, the synthesis and characterization of elemental Cu and Ni nanowires were investigated for their enhanced photocatalytic activity. These elemental nanowires were prepared using a facile, ambient, and surfactantless U-tube double diffusion method upholding at least 3 principles concerning green chemistry. Moreover when the Cu and Ni nanowires were coupled with TiO_2, enhanced photocatalytic activity with rate constants of ~ 3.6×10^{-2} min^{-1} and 7.7×10^{-3} min^{-1}, respectively were observed. Moreover, these Cu and Ni-based heterostructures displayed faster kinetics as compared with both bulk and commercial TiO_2 counterparts in the presence of two distinctive dyes such as Methyl Orange and Methylene Blue, respectively.

In Chapter 4, a different synthetic technique was employed for the synthesis of metal ferrite nanoparticles and nanowires. Specifically, the hydrothermal method was utilized under slightly basic conditions. These nanomaterials were investigated for any

correlations between chemical composition and their superparamagnetic behavior via XRD, PDF, and SQUID analyses. Through a thorough time-dependent and temperature dependent study coupled with control experiments, it was found that the morphology was indeed controlled not only with APTES functioning as both a surfactant and templating agent but also NaOH in stabilizing the APTES. As for the chemical composition, it was confirmed through XPS and PDF to be metal ferrite impregnated with metal silicates (MFe_2O_4@$MSiO_4$). In addition, it is clear that the composition rather than the morphology drives the superparamagnetic behavior.

In Chapter 5, both hydrothermal and molten salt methods were used to synthesize rare earth ion doped calcium titanate (RE-$CaTiO_3$) microspheres measuring ~200 to 350 nm in overall diameter. Both synthetic protocols utilized non-toxic solvents as well as reduced the production of toxic by-products. PL measurements showed ~3x greater emission for the molten salt-prepared sample by comparison with the hydrothermally prepared perovskite, possibly due to the reduced surface area prohibiting unfavorable PL quenching. Moreover, optical properties of various perovskite materials such as $BaTiO_3$, $SrTiO_3$, and $CaTiO_3$ were compared with that of Eu-$CaTiO_3$ microsphere. The Eu-$CaTiO_3$ displaying the highest red emission intensity with respect to its doped perovskite counterparts due to favorable synergistic interaction between Eu with the surrounding $CaTiO_3$ matrix. The molten salt samples (i.e. Pr-doped $CaTiO_3$ & Eu-doped $CaTiO_3$) were subsequently coupled with CdSe QDs and displayed efficient charge transfer properties via PL measurements.

In Chapter 6, hematite (α-Fe_2O_3) nanorhombohedra (NRhomb) of various sizes, ~75 and 47 nm, were synthesized using a CTAB-assisted hydrothermal method. These

nanorhombohedra were subsequently conjugated to the Rhodamine B (RhB) and were observed within microglia cells. We were able to confirm that microglia used a clathrin-dependent endocytic pathway to internalize RhB-labled Fe_2O_3 NRhomb, maintaining concentrations up to 100 μg/mL. Upon internalization, microglia cells preserved their resting state as well as conserved their healthy status, due to the lack of tangible evidence for any inflammatory response, reactive oxygen species, and nitric oxide release.

7.2 Future Directions

Throughout the thesis, we have demonstrated our ability to utilize green, cost effective methodologies to control the size, morphology, and composition but to also acquire the basic understanding of their photocatalytic, magnetic, energy transfer, and non-toxic properties. These methodologies uphold at least two of the 12 principles of green chemistry. Moreover, these as-synthesized nanomaterials show promise as potential catalysts for fuel cells, solar water splitting as well as drug carriers for biomedical applications.

In the field of fuel cells, it is commonly known that Pt is the most efficient metal for most fuel cells reactions but also expensive. As a result in utilizing an ambient, surfactantless U-tube technique to produce Cu/Ni nanowires, the amount of expensive Pt metal can ultimately be reduced. The goal herein, is to utilize the U-tube method to synthesize M (M=Cu, Ni, Co, and Fe) NWs, and subsequently deposit Pt NPs to create heterostructured motifs and tested for their applications as catalysts for the ORR fuel cell reaction for PEMFCs and HOR fuel cells reactions for AFCs.[1] The goal here would be to investigate whether either a core shell configuration or an alloyed composition would

generate the highest activity. Once the activities are observed, the aim would be to understand the underlying mechanistic interactions that are responsible for enhancing the activity.

Additionally, these elemental nanowires, particularly Cu NWs, may be used as surface-enhanced Raman spectroscopic (SERS) substrates to detect biomolecules such as DNA, for instance. This is possible, since Cu NWs display optical properties with small imaginary dielectric constants over a wide range of wavelengths in order to ultimately facilitate surface plasmon resonance (SPR) upon visible light irradiation.[2] In an effort to manipulate these properties, in future studies, template-derived Cu NWs will be used to facilitate the signal amplification of not only organic dyes but also DNA molecules. Specifically, these molecules would be absorbed onto the surfaces of our as-prepared Cu NWs and subsequently excited at 532 nm. As a result, we would expect enhancements in the overall peak intensitities, corresponding to either R6G or DNA molecules.[3] Consequently, this Cu metal nanowire substrate may serve as a potential substitute for the more expensive and less abundant Ag SER substrate.

As for the solar water splitting applications, due to the efficient charge transfer effects of CdSe QDs-RE-$CaTiO_3$ microspheres, these heterostructures will be utilized as catalysts. Specifically, relationships between synthetic morphology, ligand effect, and their corresponding efficiency will be systematically explored. Concerning the ligand effect, ligands such as MPA and MHA will act as linkers between the host ($CaTiO_3$) and the sensitizer (QDs) and observe the effect of electrostatic interactions with the overall conversion efficiency. Moreover, the overall efficiency of heterostructures in the absence of linkers will be used as a control. From a structural perspective, PDF analysis will be

used to observe the overall spatial distributions of the rare earth ions (i.e. Pr and Eu) within the perovskite structure. Moreover, creation of vacancies as well as replacement of the rare earth ions will also be accounted for via PDF analysis.

As for nanomaterials for biomedical applications, in this thesis we were able to confirm the biocompatibility of Fe_2O_3 NRhombs within microglia cells. As a result, Fe_2O_3 will be functionalized with an immunotherapeutic drug, for example, i.e. a tetrapeptide commonly known as Tuftsin, and will be subsequently tested to determine whether the microglia remains in either its resting or active state. The adsorption of this peptide onto the surface of nanoparticles can lead to conformational changes as well as a modification in the biological activity of the protein, which can subsequently affect both *in vitro* and *in vivo* responses. Hence, we intend to initiate an investigation with respect to protein interaction with nanoparticles and how conjugation onto the nanoparticle surface improves upon nanoscale iron oxide's delivery within microglia cells. Specifically, Tuftsin's binding strength onto the surfaces of iron oxide nanorhombohedra as well as induced conformational changes will be explored using isothermal titration calorimetry (ITC) and molecular dynamic (MD) simulations, respectively.[4, 5] Additionally, in an effort to gain an understanding of the physicochemical structure of dye-labeled-Fe_2O_3, characteristic features such as the core shell composition as well as the hydrodynamic size will be observed using both XPS and dynamic light scattering (DLS).

The introduction to Tuftsin within the microglia cells, both *in vivo* and *in vitro,* should enhance M2 activation, and thus levels of pro-inflammatory cytokines such as interleukin-10 (IL10) will be quantified in future assay studies. After tuftsin treatment, this cytokine will be further probed for indications of mRNA changes using the

polymerase chain reaction (PCR), as M2 activation is an important element in mitigating against neurodegenerative diseases, such as Parkinson's and Alzheimer's.[6]

7.3 References

1. M. E. Scofield, H. Q. Liu and S. S. Wong, *Chemical Society Reviews*, 2015, 44, 5836-5860.
2. A. I. Henry, J. M. Bingham, E. Ringe, L. D. Marks, G. C. Schatz and R. P. Van Duyne, *Journal of Physical Chemistry C*, 2011, 115, 9291-9305.
3. Q. Gao, A. Zhao, Z. Gan, W. Tao, D. Li, M. Zhang, H. Guo, D. Wang, H. Sun, R. Mao and E. Liu, *Crystengcomm*, 2012, 14, 4834-4842.
4. E. Freire, O. L. Mayorga and M. Straume, *Anal Chem*, 1990, 62, 950A-959A.
5. H. Joshi, P. S. Shirude, V. Bansal, K. N. Ganesh and M. Sastry, *The Journal of Physical Chemistry B*, 2004, 108, 11535-11540.
6. M. Wu, J. C. Nissen, E. I. Chen and S. E. Tsirka, *Plos One*, 2012, 7, 1-13.

Chapter 8- Full List of References

8.1 Full Reference List

1. J. M. Patete, X. H. Peng, C. Koenigsmann, Y. Xu, B. Karn and S. S. Wong, *Green Chemistry*, 2011, 13, 482-519.
2. I. Freestone, N. Meeks, M. Sax and C. Higgitt, *Gold Bulletin*, 2007, 40, 270-277.
3. M. Reibold, P. Paufler, A. A. Levin, W. Kochmann, N. Patzke and D. C. Meyer, *Nature*, 2006, 444, 286-286.
4. R. Feynman, *Engineering and Science*, 1960, 23, 22-36.
5. M. C. Roco, *Journal of Nanoparticle Research*, 2011, 13, 427-445.
6. National Science and Technology Council, ed. N. N. Initiative, 2016, pp. 1-112.
7. Interagency Working Group on Nanoscience Engineering and Technology, ed. N. N. Initiative, Washington, D.C. , 2000.
8. Z.-Y. Zhou, N. Tian, J.-T. Li, I. Broadwell and S.-G. Sun, *Chemical Society Reviews*, 2011, 40, 4167-4185.
9. P. G. Bruce, B. Scrosati and J.-M. Tarascon, *Angewandte Chemie*, 2008, 47, 2930-2946.
10. H. Flynn, Nanotechnology Update: Corporations Up Their Spending as Revenues for Nano-enabled Products Increase, https://portal.luxresearchinc.com/research/report_excerpt/16215, Accessed February 17, 2014, 2014.
11. W. W. I. C. f. Scholars, Project on Emerging Nanotechnologies, Inventories: Consumer Products, http://www.nanotechproject.org/, Accessed January 20, 2010, 2010.
12. H. H. Duan, D. S. Wang and Y. D. Li, *Chemical Society Reviews*, 2015, 44, 5778-5792.
13. T. J. Collins, Simon and Schuser Macmillan, New York, 1997.
14. P. T. Anastas and J. C. Warner, *Green Chemistry: Theory and Practice*, Oxford University Press, New York, 1998.
15. R. S. Varma, *Pure and Applied Chemistry*, 2013, 85, 1703-1710.
16. J. Shi and L. Guo, *Progress in Natural Science: Materials International*, 2012, 22, 592-615.
17. M. U. Din Sheikh, G. A. Naikoo, M. Thomas, M. Bano, D. Ahirwar, U. J. Pandit and F. Khan, *Rsc Advances*, 2016, 6, 42807-42818.
18. S. B. Warren, S. Vernick, E. Romano and K. L. Shepard, *Nano Lett*, 2016, 16, 2674-2679.
19. A. Aijaz, J. Masa, C. Rosler, W. Xia, P. Weide, A. J. R. Botz, R. A. Fischer, W. Schuhmann and M. Muhler, *Angewandte Chemie-International Edition*, 2016, 55, 4087-4091.
20. D. L. Feldheim and C. A. Foss, *Metal Nanoparticles: Synthesis, Characterization, and Applications*, Marcel Dekker, Inc, New York, NY, 2002.
21. S. A. Maiera and H. A. Atwater, *Journal of Applied Physics*, 2005, 98, 011101-011101 - 011101-011110.
22. A. Kudo and Y. Miseki, *Chemical Society Reviews*, 2009, 38, 253-278.

23. Y. Ma, X. Wang, Y. Jia, X. Chen, H. Han and C. Li, *Chemical Reviews*, 2014, 114, 9987-10043.
24. G. Chen, J. Seo, C. Yang and P. N. Prasad, *Chemical Society Reviews*, 2013, 42, 8304-8338.
25. A. Kongkanand, K. Tvrdy, K. Takechi, M. Kuno and P. V. Kamat, *J Am Chem Soc*, 2008, 130, 4007-4015.
26. J. M. Luther, M. Law, M. C. Beard, Q. Song, M. O. Reese, R. J. Ellingson and A. J. Nozik, *Nano Lett*, 2008, 8, 3488-3492.
27. J. Seo, M. J. Cho, D. Lee, A. N. Cartwright and P. N. Prasad, *Adv Mater*, 2011, 23, 3984-3988.
28. Y. Sun, C. J. Takacs, S. R. Cowan, J. H. Seo, X. Gong, A. Roy and A. J. Heeger, *Adv Mater*, 2011, 23, 2226-2230.
29. A. P. Alivisatos, *Science*, 1996, 271, 933-937.
30. C. B. Murray, D. J. Norris and M. G. Bawendi, *Journal of American Chemical Society*, 1993, 115, 8706-8715.
31. R. J. Ellingson, M. C. Beard, J. C. Johnson, P. Yu, O. I. Micic, A. J. Nozik, A. Shabaev and A. L. Efros, *Nano Letters*, 2005, 5, 865-871.
32. M. C. Beard, K. P. Knutsen, P. Yu, J. M. Luther, Q. Song, W. K. Metzger, R. J. Ellingson and A. J. Nozik, *Nano Letters*, 2007, 7, 2506-2512.
33. T. R. Fadel, D. F. Farrell, L. E. Friedersdorf, M. H. Griep, M. D. Hoover, M. A. Meador and M. Meyyappan, *ACS Sensors*, 2016, 1, 207-216.
34. P. Zijlstra, P. M. R. Paulo and M. Orrit, *Nature Nanotechnology*, 2012, 7, 379-382.
35. S. Y. Tee, P. T. Choon and E. Ye, *Materials Science and Engineering: C*, 2016, In Press.
36. R. Long, H. Huang, Y. P. Li, L. Song and Y. J. Xiong, *Advanced Materials*, 2015, 27, 7025-7042.
37. C. Koenigsmann, M. E. Scofield, H. Q. Liu and S. S. Wong, *Journal of Physical Chemistry Letters*, 2012, 3, 3385-3398.
38. Z. W. Quan, Y. X. Wang and J. Y. Fang, *Acc Chem Res*, 2013, 46, 191-202.
39. C.-C. Wang, J.-R. Li, X.-L. Lv, Y.-Q. Zhang and G. Guo, *Energy & Environmental Science*, 2014, 7, 2831-2867.
40. D. Lin, Q. Zhao, L. Hu and B. Xing, *Chemosphere*, 2014, 103, 188-196.
41. E. Y. Kim, D. Kumar, G. Khang and D. K. Lim, *Journal of Materials Chemistry B*, 2015, 3, 8433-8444.
42. H. Dong, S.-R. Du, X.-Y. Zheng, G.-M. Lyu, L.-D. Sun, L.-D. Li, P.-Z. Zhang, C. Zhang and C.-H. Yan, *Chem Rev*, 2015, 115, 10725-10815.
43. N. Lee, D. Yoo, D. Ling, M. H. Cho, T. Hyeon and J. Cheon, *Chem Rev*, 2015, 115, 10637-10689.
44. T. J. Kim, K. S. Chae, Y. Chang and G. H. Lee, *Current Topics in Medicinal Chemistry*, 2013, 13, 422-433.
45. H. M. Joshi, *Journal of Nanoparticle Research*, 2013, 15, 1235-(1-19).
46. P. Chevallier, A. Walter, A. Garofalo, I. Veksler, J. Lagueux, S. Begin-Colin, D. Felder-Flesch and M. A. Fortin, *Journal of Materials Chemistry B*, 2014, 2, 1779-1790.

47. T. H. Shin, Y. Choi, S. Kim and J. Cheon, *Chemical Society Reviews*, 2015, 44, 4501-4516.
48. P. Bouziotis, D. Psimadas, T. Tsotakos, D. Stamopoulos and C. Tsoukalas, *Current Topics in Medicinal Chemistry*, 2012, 12, 2694-2702.
49. N. Venkatesha, Y. Qurishi, H. S. Atreya and C. Srivastava, *Rsc Advances*, 2016, 6, 18843-18851.
50. N. Kamaly, B. Yameen, J. Wu and O. C. Farokhzad, *Chem Rev*, 2016, 116, 2602-2663.
51. Z. W. Mao, X. Y. Zhou and C. Y. Gao, *Biomaterials Science*, 2013, 1, 896-911.
52. J. M. Herrmann and A. Spang, *Methods Mol Biol*, 2015, 1270, 1-12.
53. B. D. Chithrani, A. A. Ghazani and W. C. W. Chan, *Nano Letters*, 2006, 6, 662-668.
54. H. Y. Yuan, J. Li, G. Bao and S. L. Zhang, *Phys Rev Lett*, 2010, 105.
55. M. T. Zhu, G. J. Nie, H. Meng, T. Xia, A. Nel and Y. L. Zhao, *Acc Chem Res*, 2013, 46, 622-631.
56. K. Takei and V. Haucke, *Trends Cell Biol*, 2001, 11, 385-391.
57. M. Bohdanowicz and S. Grinstein, *Physiological Reviews*, 2013, 93, 69-106.
58. T. Kirchhausen, *Trends Cell Biol*, 2009, 19, 596-605.
59. M. A. Edeling, C. Smith and D. Owen, *Nat Rev Mol Cell Biol*, 2006, 7, 32-44.
60. K. O. Schubert, M. Focking, J. H. Prehn and D. R. Cotter, *Mol Psychiatry*, 2012, 17, 669-681.
61. H. T. McMahon and E. Boucrot, *Nat Rev Mol Cell Biol*, 2011, 12, 517-533.
62. B. T. Kelly, S. C. Graham, N. Liska, P. N. Dannhauser, S. Honing, E. J. Ungewickell and D. J. Owen, *Science*, 2014, 345, 459-463.
63. M. Kaksonen, C. P. Toret and D. G. Drubin, *Cell*, 2005, 123, 305-320.
64. S. M. Smith, M. B. Wunder, D. A. Norris and Y. G. Shellman, *Plos One*, 2011, 6.
65. S. K. Choudhari, M. Chaudhary, S. Bagde, A. R. Gadbail and V. Joshi, *World Journal of Surgical Oncology*, 2013, 11.
66. C. S. Lewis, L. Wang, H. Q. Liu, J. K. Han and S. S. Wong, *Crystal Growth & Design*, 2014, 14, 3825-3838.
67. C. S. Lewis, H. Q. Liu, J. Y. Han, L. Wang, S. Y. Yue, N. A. Brennan and S. S. Wong, *Nanoscale*, 2016, 8, 2129-2142.
68. C. S. Lewis, L. Torres, J. T. Miyauchi, C. Rastegar, J. M. Patete, J. M. Smith, S. S. Wong and S. E. Tsirka, *Toxicology Research*, 2016, 5, 2129-2142.
69. P. Iqbal, J. A. Preece and P. M. Mendes, *Supramolecular Chemistry: From Molecules to Nanomaterials*, 2012, 8, 3589-3602.
70. S. Diodati, P. Dolcet, M. Casarin and S. Gross, *Chem Rev*, 2015, 115, 11449-11502.
71. A. Betke and G. Kickelbick, *Inorganics*, 2014, 2, 1-15.
72. H. Kawasaki, *Nanotechnology Reviews*, 2013, 2, 5-25.
73. K. Esumi, T. Tano and K. Meguro, *Langmuir*, 1989, 5, 268-270.
74. M. I. Dar, S. Sampath and S. A. Shivashankar, *Journal of Materials Chemistry*, 2012, 22, 22418-22423.
75. I. Pastoriza-Santos and L. M. Liz-Marzan, *Advanced Functional Materials*, 2009, 19, 679-688.

76. S. P. Xie, M. C. Paau, Y. Zhang, S. M. Shuang, W. Chan and M. M. F. Choi, *Nanoscale*, 2012, 4, 5325-5332.
77. Y. Wang, J. W. Ren, K. Deng, L. L. Gui and Y. Q. Tang, *Chemistry of Materials*, 2000, 12, 1622-1627.
78. M. Niederberger, M. H. Bartl and G. D. Stucky, *Chemistry of Materials*, 2002, 14, 4364-4370.
79. A. H. Jadhav, A. C. Lim, G. M. Thorat, H. S. Jadhav and J. G. Seo, *Rsc Advances*, 2016, 6, 31675-31686.
80. L. H. Qu and X. G. Peng, *Journal of the American Chemical Society*, 2002, 124, 2049-2055.
81. P. Lv, W. Y. Fu, Y. N. Mu, H. R. Sun, T. Liu, J. Wang, J. S. Niu, X. Li, L. Liu and H. B. Yang, *Journal of Materials Chemistry A*, 2015, 3, 16089-16096.
82. G. Ennas, G. Marongiu, A. Musinu, A. Falqui, P. Ballirano and R. Caminiti, *Journal of Materials Research*, 1999, 14, 1570-1575.
83. S. Jana, S. Pande, A. K. Sinha, S. Sarkar, M. Pradhan, M. Basu, S. Saha and T. Pal, *Journal of Physical Chemistry C*, 2009, 113, 1386-1392.
84. A. Phuruangrat, S. Thongtem and T. Thongtem, *Chalcogenide Letters*, 2013, 10, 359-365.
85. S. Xiao, P. Liu, W. Zhu, G. Li, D. Zhang and H. Li, *Nano Letters*, 2015, 15, 4853-4858.
86. C. Yan, C. M. Raghavan and D. J. Kang, *Materials Letters*, 2014, 116, 341-344.
87. T. Kita, S. Nishimoto, Y. Kameshima and M. Miyake, *Journal of the American Ceramic Society*, 2010, 93, 2427-2429.
88. D. Ding, Y. Huang, C. Zhou, Z. Liu, J. Ren, R. Zhang, J. Wang, Y. Zhang, Z. Lei, Z. Zhang and C. Zhi, *ACS Appl Mater Interfaces*, 2016, 8, 142-151.
89. P. Mukherjee, S. K. Misra, M. C. Gryka, H. H. Chang, S. Tiwari, W. L. Wilson, J. W. Scott, R. Bhargava and D. Pan, *Small*, 2015, 11, 4691-4703.
90. C. Wu, J. Cai, Q. Zhang, X. Zhou, Y. Zhu, P. K. Shen and K. Zhang, *ACS Appl Mater Interfaces*, 2015, 7, 26512-26521.
91. E. Dertli, S. Coskun and E. N. Esenturk, *Journal of Materials Research*, 2013, 28, 250-260.
92. C. Sikalidis, *Advances in Ceramics,* InTech, 2011, DOI: 10.52772/985.
93. X. Zhao, M. V. Reddy, H. X. Liu, S. Ramakrishna, G. V. S. Rao and B. V. R. Chowdari, *Rsc Advances*, 2012, 2, 7462-7469.
94. D. Wang, J. L. Chu, Y. H. Liu, J. Li, T. Y. Xue, W. J. Wang and T. Qi, *Industrial & Engineering Chemistry Research*, 2013, 52, 15756-15762.
95. P. Nithyadharseni, M. V. Reddy, H. Fanny, S. Adams and B. V. R. Chowdari, *Rsc Advances*, 2015, 5, 60552-60561.
96. K. H. Yoon, Y. S. Cho and D. H. Kang, *Journal of Materials Science*, 1998, 33, 2977-2984.
97. M. N. Rahaman, in *Kirk-Othmer Encyclopedia of Chemical Technology*, John Wiley & Sons, Inc., 2000, DOI: 10.1002/0471238961.0305180105231921.a01.pub2.
98. A. L. Tiano, C. Koenigsmann, A. C. Santulli and S. S. Wong, *Chemical Communications*, 2010, 46, 8093-8130.
99. X. Y. Li and Y. Q. Qu, *Crystal Growth & Design*, 2016, 16, 34-41.

100. R. E. Rojas-Hernandez, F. Rubio-Marcos, R. H. Goncalves, M. A. Rodriguez, E. Veron, M. Allix, C. Bessada and J. F. Fernandez, *Inorg Chem*, 2015, 54, 9896-9907.
101. T.-J. Park, Y. Mao and S. S. Wong, *Chemical Communications*, 2004, 23, 2708-2709.
102. S. B. Yuanbing Mao, and Stanislaus S. Wong, *Journal of the American Chemical Society*, 2003, 125, 15718-15719.
103. A. L. Tiano, A. C. Santulli, C. Koenigsmann, M. Feygenson, M. C. Aronson, R. Harrington, J. B. Parise and S. S. Wong, *Chemistry of Materials*, 2011, 23, 3277-3288.
104. G. Huang, X. C. Du, F. F. Zhang, D. M. Yin and L. M. Wang, *Chemistry-a European Journal*, 2015, 21, 14140-14145.
105. R. D. Farahani, K. Chizari and D. Therriault, *Nanoscale*, 2014, 6, 10470-10485.
106. H. Zhou and S. Wong, *American Chemistry Society Nano*, 2008, 2, 944-958.
107. H. Zhou and S. S. Wong, *ACS Nanoscience & Nanotechnology*, 2008, 2, 944-958.
108. F. Zhang and S. S. Wong, *ACS Nano*, 2010, 4, 99-112.
109. C. Koenigsmann, D. B. Semple, E. Sutter, S. E. Tobierre and S. S. Wong, *ACS Appl Mater Interfaces*, 2013, 5, 5518-5530.
110. F. Zhang and S. S. Wong, *Chemistry of Materials*, 2009, 21, 4541-4554.
111. J. Doshi and D. H. Reneker, *Journal of Electrostatics*, 1995, 35, 151-160.
112. S. De Vrieze, T. Van Camp, A. Nelvig, B. Hagstrom, P. Westbroek and K. De Clerck, *Journal of Materials Science*, 2009, 44, 1357-1362.
113. Z. Li and C. Wang, *One-Dimensional Nanostructures: Electrospinning Techniqe and Unique Nanofibers*, Springer, New York, 2013.
114. P. Peh, N. S. J. Lim, A. Blocki, S. M. L. Chee, H. C. Park, S. Liao, C. Chan and M. Raghunath, *Bioconjugate Chemistry*, 2015, 26, 1348-1358.
115. A. GhavamiNejad, A. R. K. Sasikala, A. R. Unnithan, R. G. Thomas, Y. Y. Jeong, M. Vatankhah-Varnoosfaderani, F. J. Stadler, C. H. Park and C. S. Kim, *Advanced Functional Materials*, 2015, 25, 2867-2875.
116. J. Xiao, C. Shi, H. Zheng, Z. Shi, D. Jiang, Y. Li and Q. Huang, *J Agric Food Chem*, 2016, 64, 3226-3233.
117. S. Padmakumar, J. Joseph, M. H. Neppalli, S. E. Mathew, S. V. Nair, S. A. Shankarappa and D. Menon, *ACS Appl Mater Interfaces*, 2016, 8, 6925-6934.
118. X. Zhao, Z. M. Yuan, L. Yildirimer, J. W. Zhao, Z. Y. Lin, Z. Cao, G. Q. Pan and W. G. Cui, *Small*, 2015, 11, 4284-4291.
119. J. J. Alcaraz-Espinoza, A. E. Chavez-Guajardo, J. C. Medina-Llamas, C. A. S. Andrade and C. P. de Melo, *ACS Appl Mater Interfaces*, 2015, 7, 7231-7240.
120. T. Krishnamoorthy, V. Thavasi, M. Subodh G and S. Ramakrishna, *Energy & Environmental Science*, 2011, 4, 2807-2812.
121. L. Xu, H. Song, B. Dong, Y. Wang, J. Chen and X. Bai, *Inorg Chem*, 2010, 49, 10590-10597.
122. O. Yildiz, K. Stano, S. Faraji, C. Stone, C. Willis, X. W. Zhang, J. S. Jur and P. D. Bradford, *Nanoscale*, 2015, 7, 16744-16754.
123. F. Y. Zhai, W. Huang, G. Wu, X. K. Jing, M. J. Wang, S. C. Chen, Y. Z. Wang, I. J. Chin and Y. Liu, *ACS Nano*, 2013, 7, 4892-4901.

124. M. Li, Y. P. Xiong, X. T. Liu, X. J. Bo, Y. F. Zhang, C. Han and L. P. Guo, *Nanoscale*, 2015, 7, 8920-8930.
125. L. J. Chen, C. R. Lee, Y. J. Chuang, Z. H. Wu and C. Y. Chen, *Crystengcomm*, 2015, 17, 4434-4438.
126. Y. Liu and L. Guo, *J Nanosci Nanotechnol*, 2013, 13, 843-847.
127. M. A. Alamein, S. Stephens, Q. Liu, S. Skabo and P. H. Warnke, *Tissue Eng Part C Methods*, 2013, 19, 458-472.
128. T. Proffen, S. J. L. Billinge, T. Egami and D. Louca, *Zeitschrift Fur Kristallographie*, 2003, 218, 132-143.
129. S. J. L. Billinge, R. G. DiFrancesco, G. H. Kwei, J. J. Neumeier and J. D. Thompson, *Physical Review Letters*, 1996, 77, 715-718.
130. P. Juhas, T. Davis, C. L. Farrow and S. J. L. Billinge, *Journal of Applied Crystallography*, 2013, 46, 560-566.
131. T. Egami and S. J. L. Billinge, *Underneath the Bragg peaks: structural analysis of complex materials*, Elsevier, Amsterdam, 2nd. edn., 2012.
132. T. Proffen and S. J. L. Billinge, *Journal of Applied Crystallography*, 1999, 32, 572-575.
133. C. L. Farrow, P. Juhas, J. Liu, D. Bryndin, E. S. Bozin, J. Bloch, T. Pro and S. J. L. Billinge, *Journal of Physics: Condensed Matter*, 2007, 19, 335219.
134. J.-A. Conchello and J. W. Lichtman, *Nature Methods*, 2005, 2, 920-931.
135. J. H. Liu, L. Cao, G. E. LeCroy, P. Wang, M. J. Meziani, Y. Y. Dong, Y. F. Liu, P. J. G. Luo and Y. P. Sun, *ACS Appl Mater Interfaces*, 2015, 7, 19439-19445.
136. R. F. Egerton, *Electron energy-loss spectroscopy in the electron microscope*, Springer, New York-Dordrecht-Heidelberg-London, 3rd edn., 2011.
137. R. F. Egerton, *Reports on Progress in Physics*, 2009, 72, 016502-(1-25).
138. J. Ma, F. Yu, L. Zhou, L. Jin, M. Yang, J. Luan, Y. Tang, H. Fan, Z. Yuan and J. Chen, *ACS Appl Mater Interfaces*, 2012, 4, 5749-5760.
139. A. Houas, H. Lachheb, M. Ksibi, E. Elaloui, C. Guillard and J.-M. Herrmann, *Applied Catalysis, B: Environmental*, 2001, 31, 145-157.
140. M. C. Das, H. Xu, Z. Wang, G. Srinivas, W. Zhou, Y.-F. Yue, V. N. Nesterov, G. Qian and B. Chen, *Chemical Communications*, 2011, 47, 11715-11717.
141. P. R. Griffiths and J. A. De Haseth, *Fourier Transform Infrared Spectrometry*, A John Wiley & Sons, Inc., Hoboken, New Jersey, 2nd edn., 2007.
142. B. Ketterer, M. Heiss, M. J. Livrozet, A. Rudolph, E. Reiger and A. F. I. Morral, *Physical Review B*, 2011, 83.
143. D. L. Dexter and J. H. Schulman, *Journal of Chemical Physics*, 1954, 22, 1063-1070.
144. Z. Burshtein, *Optical Engineering*, 2010, 49, 091005/091001-091005/091019.
145. M. S. Mehata, *Applied Physics Letters*, 2012, 100.
146. S. Brunauer, P. H. Emmett and E. Teller, *Journal of the American Chemical Society*, 1938, 60, 309-319.
147. K. S. Walton and R. Q. Snurr, *Journal of the American Chemical Society*, 2007, 129, 8552-8556.
148. A. G. Kolhatkar, A. C. Jamison, D. Litvinov, R. C. Willson and T. R. Lee, *International Journal of Molecular Sciences*, 2013, 14, 15977-16009.
149. G. C. Papaefthymiou, *Nano Today*, 2009, 4, 438-447.

150. K. L. Cox, V. Devanarayan, A. Kriauciunas, J. Manetta, C. Montrose and S. Sittampalam, in *Assay Guidance Manual*, eds. G. S. Sittampalam, N. P. Coussens, H. Nelson, M. Arkin, D. Auld, C. Austin, B. Bejcek, M. Glicksman, J. Inglese, P. W. Iversen, Z. Li, J. McGee, O. McManus, L. Minor, A. Napper, J. M. Peltier, T. Riss, O. J. Trask, Jr. and J. Weidner, Bethesda (MD), 2004.
151. N. S. Bryan and M. B. Grisham, *Free Radic Biol Med*, 2007, 43, 645-657.
152. M. M. Tarpey, D. A. Wink and M. B. Grisham, *American Journal of Physiology-Regulatory Integrative and Comparative Physiology*, 2004, 286, R431-R444.
153. T. J. Guzik, R. Korbut and T. Adamek-Guzik, *Journal of Physiology and Pharmacology*, 2003, 54, 469-487.
154. W. Droge, *Physiological Reviews*, 2002, 82, 47-95.
155. X. Guo, F. Zheng, M. Guo, M. Zhang and K.-C. Chou, *Rare Metals (Beijing, China)*, 2013, 32, 179-185.
156. J. Wang, Q. Chen, B. Hou and Z. Peng, *European Journal of Inorganic Chemistry*, 2004, 2004, 1165-1168.
157. A. L. Tiano, G. C. Papaefthymiou, C. S. Lewis, J. Han, C. Zhang, Q. Li, C. Shi, A. M. M. Abeykoon, S. J. L. Billinge, E. Stach, J. Thomas, K. Guerrero, P. Munayco, J. Munayco, R. B. Scorzelli, P. Burnham, A. J. Viescas and S. S. Wong, *Chemistry of Materials*, 2015, 27, 3572–3592.
158. L. Qu and X. Peng, *Journal of the American Chemical Society*, 2002, 124, 2049-2055.
159. Z. Pu, M. Cao, J. Yang, K. Huang and C. Hu, *Nanotechnology*, 2006, 17, 799-804.
160. L. Ye, R. Pelton and M. A. Brook, *Langmuir*, 2007, 23, 5630-5637.
161. S. Chen, Z. Wei, L. Guo, W. Ding, L. Dong, P. Shen, X. Qi and L. Li, *Chem Commun (Camb)*, 2011, 47, 10984-10986.
162. Y. Zhang, M. Huang, F. Li, H. Zhao and Z. Wen, *Journal of Materials Science*, 2013, 48, 6728-6736.
163. Y. Mao and S. S. Wong, *Journal of the American Chemical Society*, 2006, 128, 8217-8226.
164. G. G. Nakhate, V. S. Nikam, K. G. Kanade, S. Arbuj, B. B. Kale and J. O. Baeg, *Materials Chemistry and Physics*, 2010, 124, 976-981.
165. R. T. Sasmono, A. Ehrnsperger, S. L. Cronau, T. Ravasi, R. Kandane, M. J. Hickey, A. D. Cook, S. R. Himes, J. A. Hamilton and D. A. Hume, *J Leukoc Biol*, 2007, 82, 111-123.
166. R. Bronstein, L. Torres, J. C. Nissen and S. E. Tsirka, *J Vis Exp*, 2013, DOI: 10.3791/50647.
167. R. J. Hunter, *Foundations of Colloid Science*, Oxford University Press, New York, 1987.
168. D. Li and R. B. Kaner, *Journal of the American Chemical Society*, 2006, 128, 968-975.
169. A. D. Harrington, S. E. Tsirka and M. A. A. Schoonen, *Chemosphere*, 2013, 93, 1216-1221.
170. M. A. Mahmoud, R. Narayanan and M. A. El-Sayed, *Acc Chem Res*, 2013, 46, 1795-1805.

171. A. I. Henry, J. M. Bingham, E. Ringe, L. D. Marks, G. C. Schatz and R. P. Van Duyne, *Journal of Physical Chemistry C*, 2011, 115, 9291-9305.
172. T. M. D. Dang, T. T. T. Le, E. Fribourg-Blanc and M. C. Dang, *Advances in Natural Sciences: Nanoscience and Nanotechnology*, 2011, 2, 150091-150096.
173. Y. Wang, A. V. Biradar, G. Wang, K. K. Sharma, C. Duncan, S. Rangan and T. Asefa, *Chemistry - A European Journal*, 2010, 16, 10735-107343.
174. S. Kuld, M. Thorhauge, H. Falsig, C. F. Elkjaer, S. Helveg, I. Chorkendorff and J. Sehested, *Science*, 2016, 352, 969-974.
175. S. D. Senanayake, P. J. Ramirez, I. Waluyo, S. Kundu, K. Mudiyanselage, Z. Y. Liu, Z. Liu, S. Axnanda, D. J. Stacchiola, J. Evans and J. A. Rodriguez, *Journal of Physical Chemistry C*, 2016, 120, 1778-1784.
176. M. Zhu, T. C. R. Rocha, T. Lunkenbein, A. Knop-Gericke, R. Schlögl and I. E. Wachs, *ACS Catalysis*, 2016, DOI: 10.1021/acscatal.6b00698, 4455-4464.
177. Y. Cao, Y. Yang, Y. Shan and Z. Huang, *ACS Appl Mater Interfaces*, 2016, 8, 5998-6003.
178. A. R. Rathmell, S. M. Bergin, Y.-L. Hua, Z.-Y. Li and B. J. Wiley, *Advanced Materials*, 2010, 22, 3558-3563.
179. H. Wu, D. Kong, Z. Ruan, P.-C. Hsu, S. Wang, Z. Yu, T. J. Carney, L. F. Hu, S. an and Y. Cui, *Nature Nanotechnology*, 2013, 8, 421-425.
180. Y. Zhao, Y. Zhang, Y. Li, Z. He and Z. Yan, *RSC Adv.*, 2012, 2, 11544-11551.
181. M.-G. Kang, H. J. Park, S. H. Ahn and L. J. Guo, *Sol. Energy Mater. Sol. Cells*, 2010, 94, 1179-1184.
182. S. Ye, A. R. Rathmell, I. E. Stewart, Y.-C. Ha, A. R. Wilson and Z. Chen, *Chemical Communications*, 2014, 50, 2562-2564.
183. O. Lupan, T. Pauporte, B. Viana and P. Aschehoug, *Electrochim. Acta*, 2011, 56, 10543-10549.
184. I. Halaciuga, S. LaPlante and D. Goia, *Rapid Communications*, 2009, 24, 3237-3240.
185. Y. Zhao, Y. Zhang, Y. Li, Z. He and Z. Yan, *Royal Society of Chemistry Advances*, 2012, 2, 11544-11551.
186. M. Cempel and G. Nikel, *Polish Journal of Environmental Studies*, 2006, 15, 375-382.
187. S. B. Sapkal, K. F. Shelke, B. B. Shingate and M. S. Shingare, *Bulletin of the Korean Chemical Society*, 2010, 31, 351-354.
188. D. Ai and S. Kang, *Materials Transactions*, 2006, 47, 1056-2059.
189. A. K. Shukla, S. Venugopalan and B. Hariprakash, *Journal of Power Sources*, 2001, 100, 125-148.
190. V. Pokropivny, R. Lohmus, I. Hussainova, A. Pokropivny and S. Vlassov, *Introduction to Nanomaterials and Nanotechnology*, Tartu University Press, Ukraine, 2007.
191. K. Hasegawa, M. Ohnishi, M. Oshitani, K. Takeshima, Y. Matsumaru and K. Tamura, *Zeitschrift für Physikalische Chemie*, 1994, 183, 325-331.
192. M. N. Ou, T. J. Yang, S. R. Harutyunyan, Y. Y. Chen and C. D. Chen, *Applied Physics Letters*, 2008, 92, 63101-63104.
193. H.-W. Liang, J.-W. Liu, H.-S. Qian and S.-H. Yu, *Acc Chem Res*, 2013, 46, 1450-1461.

194. Q.-c. Chen, *Jingxi Huagong*, 2005, 22, 417-419.
195. A. Khalil, R. Hashaikeh and M. Jouiad, *J. Mater. Sci.*, 2014, 49, 3052-3065.
196. X.-h. Wang, G. Chen, C.-y. Li, L. Yang, H. Cao and W.-m. Zhou, *Cailiao Gongcheng*, 2010, 20-23.
197. X. Sun and F. Xu, *Adv. Mater. Res. (Durnten-Zurich, Switz.)*, 2011, 335-336, 429-432.
198. X. Liu, X. She, G. Song, X. Sun and S. Wang, *Dianzi Yuanjian Yu Cailiao*, 2008, 27, 51-53.
199. L. Qingming, Z. Debi, Y. Yamamoto, R. Ichino and M. Okido, *Transactions of Nonferrous Metals Society of China*, 2012, 22, 117-123.
200. H. Choi and S.-H. Park, *Journal of American Chemistry Society*, 2004, 126, 6248-6249.
201. G. Yue, Q. Xu, G. Meng, X. He, F. Han and L. Zhang, *Journal of Alloys and Compounds*, 2009, 477, L30-L34.
202. N. V. Surmawar, S. R. Thakare and N. T. Khaty, *International Journal of Green Nanotechnology*, 2011, 3, 302-308.
203. X. Li, Y. Wang, G. Song, X. She, Z. Peng, S. Wang and J. Li, *J. Nanosci. Nanotechnol.*, 2010, 10, 4363-4367.
204. Y.-Q Liu, M. Zheng, F.-X. Wang, and G.-B. Pan, *RSC Advances*, 2012, 2, 11235-11237.
205. Y. Zhao, Y. Zhang, Y. Li and Z. Yan, *New Journal of Chemistry*, 2012, 36, 130-138.
206. A. Roy, V. Srinivas, S. Ram, J. A. De Toro and U. Mizutani, *Physical Review B*, 2005, 71.
207. M. R. Knecht, J. C. Garcia-Martinez and R. M. Crooks, *Chemical Materials*, 2006, 18, 5039-5044.
208. Y. Chang, M. L. Lye and H. C. Zeng, *Langmuir*, 2005, 21, 3746-3748.
209. A. R. Rathmell and B. J. Wiley, *Advanced Materials*, 2011, 23, 4798-4803.
210. D. Zhang, R. Wang, M. Wen, D. Weng, X. Cui, J. Sun, H. Li and Y. Lu, *Journal of American Chemical Society*, 2012, 134, 14283-14286.
211. K. R. Krishnadas, P. R. Sajanlal and T. Pradeep, *journal of Physical Chemistry C*, 2011, 115, 4483-4490.
212. F. Zhang, Y. Yiu, M. Aronson and S. Wong, *Journal of Physical Chemistry C*, 2008, 38, 14816-14824.
213. C. Koenigsmann, E. Sutter, T. A. Chiesa, R. R. Adzic and S. S. Wong, *Nano Letters*, 2012, 12, 2013-2020.
214. C. Koenigsmann, Z. Tan, H. Peng, E. Sutter, J. Jacobskind and S. Wong, *Israel Journal of Chemistry*, 2012, 52, 1090-1103.
215. C. Koenigsmann, A. Santulli, E. Sutter and S. Wong, *American Chemistry Society Nano*, 2011, 5, 7471-7487.
216. F. Zhang and S. S. Wong, *American Chemistry Society Nano*, 2010, 4, 99-112.
217. Y. Mao, F. Zhang and S. S. Wong, *Advanced Materials*, 2006, 18, 1895-1899.
218. H. Zhou, W.-p. Zhou, R. R. Adzic and S. S. Wong, *Journal of Physical Chemistry C*, 2009, 113, 5460-5466.
219. D. Bu and H. Zhuang, *Appl. Surf. Sci.*, 2013, 265, 677-685.

220. P. K. Khanna, S. Gaikwad, P. V. Adhyapak, N. Singh and R. Marimuthu, *Materials Letters*, 2007, 61, 4711-4714.
221. H. Ikeda, Y. Qi, T. Cagin, K. Samwer, W. L. Johnson and W. A. Goddard, *Phys Rev Lett*, 1999, 82, 2900-2903.
222. K. Rajagopal, *Engineering Physics*, PHI Learning Private Limited, New Dehli, Second Edition edn., 2011.
223. M. Salavati-Niasari and F. Davar, *Materials Letters*, 2009, 63, 441-443.
224. J. L. Cuya Huaman, K. Sato, S. Kurita, T. Matsumoto and B. Jeyadevan, *Journal of Materials Chemistry*, 2011, 21, 7062-7069.
225. A. Ghaddar, J. Gieraltowski and F. Gloaguen, *J. Appl. Electrochem.*, 2009, 39, 719-725.
226. P. Pootawang, N. Saito and S. Lee, *Nanotechnology*, 2013, 24, 55604-55613.
227. J.-L. Duan, J. Liu, H.-J. Yao, D. Mo, M.-D. Hou, Y.-M. Sun, Y.-F. Chen and L. Zhang, *Mater. Sci. Eng., B*, 2008, 147, 57-62.
228. M. Vishlaghi, M. Tabriz and O. Moradi, *Materials Research Bulletin*, 2012, 47, 1666-1669.
229. Y. Su, Y. Yang, H. Zhang, Y. Xie, Z. Wu, Y. Jiang, N. Fukata, Y. Bando and Z. L. Wang, *Nanotechnology*, 2013, 24, 295401: 295401-295406.
230. X. H. Wang, J.-G. Li, H. Kamiyama, Y. Moriyoshi and T. Ishigaki, *Journal of Physical Chemistry B*, 2006, 110, 6804-6809.
231. A. Zaleska, *Recent Patents on Engineering*, 2008, 2, 157-164.
232. K.-i. Yamanaka, T. Ohwaki and T. Morikawa, *Journal of Physical Chemistry C*, 2013, 117, 16448-165456.
233. K. Song, J. Zhou, J. Bao and Y. Feng, *Journal of the American Ceramic Society*, 2008, 91, 1369-1371.
234. B. Xin, P. Wang, D. Ding, J. Liu, Z. Ren and H. Fu, *Applied Surface Science*, 2008, 254, 2569-2574.
235. M. Sahu, B. Wu, L. Zhu, C. Jacobson, W.-N. Wang, K. Jones, Y. Goyal, Y. J. Tang and P. Biswas, *Nanotechnology*, 2011, 22, 415704- (415701-415709).
236. G. Mele, R. Del Sole, G. Vasapollo, E. Garcia-Lopez, L. Palmisano and M. Schiavello, *Journal of Catalysis*, 2003, 217, 334-342.
237. M. Zeng, *Bulletin of the Korean Chemical Society*, 2013, 34, 953-956.
238. M. Kemmell, V. Pore, J. Tupala, M. Ritala and M. Leskela, *Chemistry of Materials*, 2007, 19, 1816-1820.
239. G. N. Glavee, K. J. Klabunde, C. M. Sorensen and G. C. Hadjipanayis, *Langmuir*, 1994, 10, 4726-4730.
240. Z. Ding, W. Wang, S. Z. Wu and J. P. Liu, *Ieee Transactions on Magnetics*, 2015, 51.
241. K. J. Ziegler, R. C. Doty, K. P. Johnston and B. A. Korgel, *Journal of the American Chemical Society*, 2001, 123, 7797-7803.
242. Q. M. Liu, D. B. Zhou, Y. Yamamoto, R. Ichino and M. Okido, *Transactions of Nonferrous Metals Society of China*, 2012, 22, 117-123.
243. A. K. Singh and Q. Xu, *International Journal of Hydrogen Energy*, 2014, 39, 9128-9134.
244. N. Sahiner, S. Butun, O. Ozay and B. Dibek, *Journal of Colloid and Interface Science*, 2012, 373, 122-128.

245. M. B. B. Guerra, R. Carapelli, K. Miranda, A. R. A. Nogueira and E. R. Pereira-Filho, *Analytical Methods*, 2011, 3, 599-605.
246. A. Ghaddar, J. Gieraltowski and F. Gloaguen, *J. Appl. Electrochem.*, 2009, 39, 719-725.
247. W.-r. Lee, Y. S. Lim, S. Kim, J. Jung, Y.-K. Han, S. Yoon, L. Piao and S.-H. Kim, *Journal of Materials Chemistry*, 2011, 21, 6928-6933.
248. S. E. Allen, R. R. Walvoord, R. Padilla-Salinas and M. C. Kozlowski, *Chem Rev*, 2013, 113, 6234-6458.
249. T. Punniyamurthy, S. Velusamy and J. Iqbal, *Chem Rev*, 2005, 105, 2329-2363.
250. Y. Liao, G. Yu, Y. Zhang, T. T. Guo, F. F. Chang and C. J. Zhong, *Journal of Physical Chemistry C*, 2016, 120, 10476-10484.
251. K. W. Lux and K. J. Rodriguez, *Nano Letters*, 2006, 6, 288-295.
252. K. Jayasayee, J. A. R. Van Veen, T. G. Manivasagam, S. Celebi, E. J. M. Hensen and F. A. de Bruijn, *Applied Catalysis B-Environmental*, 2012, 111, 515-526.
253. M. Oezaslan, F. Hasche and P. Strasser, *Polymer Electrolyte Fuel Cells 10, Pts 1 and 2*, 2010, 33, 333-341.
254. X. W. Du, S. P. Luo, H. Y. Du, M. Tang, X. D. Huang and P. K. Shen, *Journal of Materials Chemistry A*, 2016, 4, 1579-1585.
255. M. E. Scofield, H. Q. Liu and S. S. Wong, *Chemical Society Reviews*, 2015, 44, 5836-5860.
256. M. T. Koper, *Nat Chem*, 2013, 5, 255-256.
257. E. Antolini and E. R. Gonzalez, *Journal of Power Sources*, 2010, 195, 3431-3450.
258. J. Durst, A. Siebel, C. Simon, F. Hasche, J. Herranz and H. A. Gasteiger, *Energy & Environmental Science*, 2014, 7, 2255-2260.
259. W. C. Sheng, H. A. Gasteiger and Y. Shao-Horn, *Journal of the Electrochemical Society*, 2010, 157, B1529-B1536.
260. E. G. Mahoney, W. C. Sheng, Y. S. Yan and J. G. G. Chen, *Chemelectrochem*, 2014, 1, 2058-2063.
261. Y. Wang, G. W. Wang, G. W. Li, B. Huang, J. Pan, Q. Liu, J. J. Han, L. Xiao, J. T. Lu and L. Zhuang, *Energy & Environmental Science*, 2015, 8, 177-181.
262. M. A. Montero, M. R. G. de Chialvo and A. C. Chialvo, *International Journal of Hydrogen Energy*, 2011, 36, 3811-3816.
263. S. M. Alia, B. S. Pivovar and Y. S. Yan, *Journal of the American Chemical Society*, 2013, 135, 13473-13478.
264. S. J. L. Billinge and I. Levin, *Science*, 2007, 316, 561-565.
265. R. E. Dinnebier and S. J. L. Billinge, *Powder Diffraction: Theory and Practice*, Royal Society of Chemistry Cambridge, UK, 1 edn., 2008.
266. S. Tripathi, V. Petkov, S. M. Selbach, K. Bergum, M.-A. Einarsrud, T. Grande and Y. Ren, *Physical Review B*, 2012, 86, 094101/094101-094101/094108.
267. A. S. Masadeh, E. S. Bozin, C. L. Farrow, G. Paglia, P. Juhas, A. Karkamkar, M. G. Kanatzidis and S. J. L. Billinge, *Physical Review B*, 2007, 76, 115413/115411 - 115413/115411.
268. N. G. Jovic, A. S. Masadeh, A. S. Kremenovic, B. V. Antic, J. L. Blanusa, N. D. Cvjeticanin, G. F. Goya, M. V. Antisari and E. S. Bozin, *Journal of Physical Chemistry C*, 2009, 113, 20559-20567.

269. L. Kumar, P. Kumar, A. Narayan and M. Kar, *International Nano Letters*, 2013, 3, 8(1)-(8)12.
270. M. Gateshki, V. Petkov, S. K. Pradhan and T. Vogt, *Journal of Applied Crystallography*, 2005, 38, 772-779.
271. J. L. Moran-Lopez, R. A. Guirado-Lopez, J. M. Montejano-Carrizalez, F. Aguilera-Granja, R. Rodriguez-Alba, J. Mejia-Lopez, A. H. Romero and M. E. Garcia, *Current Science*, 2008, 95, 1177-1201.
272. A. K. M. Bantu, J. Rivas, G. Zaragoza, M. A. López-Quintela and M. C. Blanco, *Journal of Applied Physics*, 2001, 89, 3393-3397.
273. J. P. Pierce, E. W. Plummer and J. Shen, *Journal of Applied Physics Letters*, 2002, 81, 1890-1892.
274. M. Ravichandran, G. Oza, S. Velumani, J. T. Ramirez, F. Garcia-Sierra, N. B. Andrade, M. A. Garza-Navarro, D. I. Garcia-Gutierrez, R. Lara-Estrada, E. Sacristán-Rockf and J. Yig, *RSC Advances*, 2015, 5, 17223-17227.
275. S. Zeng, D. Baillargeat, H.-P. Ho and K.-T. Yong, *Chemical Society Reviews*, 2014, 43, 3426-3452.
276. Z. Wang, X. Liu, M. Lv, P. Chai, Y. Liu, X. Zhou and J. Meng, *The Journal of Physical Chemistry C*, 2008, 112, 15171-15175.
277. D. A. Allwood, G. Xiong, M. D. Cooke, C. C. Faulkner, D. Atkinson, N. Vernier and R. P. Cowburn, *Science*, 2002, 296, 2003-2006.
278. J. M. Patete, J. Han, A. L. Tiano, H. Liu, M.-G. Han, J. W. Simonson, Y. Li, A. C. Santulli, M. C. Aronson, A. I. Frenkel, Y. Zhu and S. S. Wong, *Journal of Physical Chemistry C*, 2014, 118, 21695-21705.
279. T.-J. Park, G. C. Papaefthymiou, A. J. Viescas, A. R. Moodenbaugh and S. S. Wong, 2007, 7, 766-772.
280. T.-J. Park and S. S. Wong, 2006, 18, 5289-5296.
281. E.-K. Lim, Y.-M. Huh, J. Yang, K. Lee, J.-S. Suh and S. Haam, *Advanced Materials*, 2011, 23, 2436-2442.
282. J.-T. Jang, H. Nah, J.-H. Lee, S. H. Moon, M. G. Kim and J. Cheon, *Angewandte Chemie*, 2009, 121, 1260-1264.
283. T. Yamashita and P. Hayes, *Applied Surface Science*, 2008, 254, 2441-2449.
284. R. D. Desautels, M. P. Rowe, M. Jones, A. Whallen and J. van Lierop, *Langmuir*, 2015, 31, 2879-2884.
285. P. S. Guo and C. X. Wang, *RSC Advances*, 2015, 5, 70661-70667.
286. R. D. Desautels, J. W. Freeland, M. P. Rowe and J. van Lierop, *Journal of Applied Physics*, 2015, 117.
287. T. Tago, T. Hatsuta, K. Miyajima, M. Kishida, S. Tashiro and K. Wakabayashi, *Journal of American Ceramics Society*, 2002, 85, 2188-2194.
288. A. Casu, M. F. Casula, A. Corrias, A. Falqui, D. Loche and S. Marras, *The Journal of Physical Chemistry C*, 2007, 111, 916-922.
289. A. L. Tiano, G. C. Papaefthymiou, C. S. Lewis, J. Han, C. Zhang, Q. Li, C. Shi, A. M. M. Abeykoon, S. J. L. Billinge, E. Stach, J. Thomas, K. Guerrero, P. Munayco, J. Munayco, R. B. Scorzelli, P. Burnham, A. J. Viescas and S. S. Wong, *Chemistry of Materials*, 2015, 27, 3572-3592.
290. Z. Liu, X. Duan, G. Qian, X. Zhou and W. Yuan, 2013, 24, 045609/045601-045609/045606.

291. C. Manjunatha, B. M. Nagabhushana, H. Nagabhushana and R. P. S. Chakradhar, *Journal of Materials Chemistry*, 2012, 22, 22392-22397.
292. B. Miao, W. Zeng, S. Hussain, Q. Mei, S. Xu, H. Zhang, Y. Li and T. Li, *Materials Letters*, 2015, 147, 12-15.
293. Z.-x. Yang, W. Zhong, Y.-x. Yin, X. Du, Y. Deng, C. Au and Y.-w. Du, *Nanoscale Research Letters*, 2010, 5, 961-965.
294. L. Hou, H. Hua, S. Liu, G. Pang and C. Yuan, *New J. Chem.*, 2015, 39, 5507-5512.
295. L. Liu, H. Z. Kou, W. Mo, H. Liu and Y. Wang, *Journal of Physical Chemistry B*, 2006, 110, 15218-15223.
296. D. Qin, J. Zhou, C. Luo, Y. Liu, L. Han and Y. Cao, *Nanotechnology*, 2006, 17, 674-679.
297. C. Bao, M. Jin, R. Lu, P. Xue, Q. Zhang, D. Wang and Y. Zhao, *Journal of Solid State Chemistry*, 2003, 175, 322-327.
298. X. Shi, M. Li, H. Yang, S. Chen, L. Yuan, K. Zhang and J. Sun, *Materials Research Bulletin*, 2007, 42, 1649-1656.
299. R. Liu, Y. Jiang, H. Fan, Q. Lu, W. Du and F. Gao, *Chemistry*, 2012, 18, 8957-8963.
300. C. Z. Wen, H. B. Jiang, S. Z. Qiao, H. G. Yang and G. Q. Lu, *Journal of Materials Chemistry*, 2011, 21, 7052.
301. X. Han, M. Jin, S. Xie, Q. Kuang, Z. Jiang, Y. Jiang, Z. Xie and L. Zheng, *Angew Chem Int Ed Engl*, 2009, 48, 9180-9183.
302. Q. Zhang, L. Han, H. Jing, D. A. Blom, Y. Lin, H. L. Xin and H. Wang, *ACS Nano*, 2016, 10, 2960-2974.
303. M. Mohapatra, D. Behera, S. Layek, S. Anand, H. C. Verma and B. K. Mishra, *Crystal Growth & Design*, 2012, 12, 18-28.
304. Y. Mao, S. Banerjee and S. S. Wong, *Journal of the American Chemical Society*, 2003, 125, 15718-15719.
305. S. Stolen, E. Bakken and C. E. Mohn, *Physical Chemistry Chemical Physics*, 2006, 8, 429-447.
306. F. A. Rabuffetti and R. L. Brutchey, *Dalton Transactions*, 2014, 43, 14499-14513.
307. J. Zhu, H. Li, L. Zhong, P. Xiao, X. Xu, X. Yang, Z. Zhao and J. Li, *ACS Catalysis*, 2014, 4, 2917-2940.
308. J. Kaur, V. Dubey, Y. Parganiha, D. Singh and N. S. Suryanarayana, *Research on Chemical Intermediates*, 2015, 41, 3597-3621.
309. X. Zhang, J. Zhang, Y. Jin, H. Zhao and X.-j. Wang, *Crystal Growth & Design*, 2008, 8, 779-781.
310. C. N. George, J. K. Thomas, R. Jose, H. P. Kumar, M. K. Suresh, V. R. Kumar, P. R. S. Wariar and J. Koshy, *Journal of Alloys and Compounds*, 2009, 486, 711-715.
311. D. Wang, Y. Liu, H. Hu, Z. Zeng, F. Zhou and W. Liu, *The Journal of Physical Chemistry C*, 2008, 112, 16123-16129.
312. A. C. Santulli, H. Zhou, S. Berweger, M. B. Raschke, E. Sutter and S. S. Wong, *Crystal Engineering Communications*, 2010, 12, 2675-2678.

313. Y. Mao, S. Banerjee and S. S. Wong, *Chemical Communications*, 2003, 3, 408-409.
314. K. Asami, K. Saito, N. Ohtsu, S. Nagata and T. Hanawa, *Surface and Interface Analysis*, 2003, 35, 483-488.
315. K. Asami, N. Ohtsu, K. Saito and T. Hanawa, *Surface and Coatings Technology*, 2005, 200, 1005-1008.
316. S. Som, A. K. Kunti, V. Kumar, V. Kumar, S. Dutta, M. Chowdhury, S. K. Sharma, J. J. Terblans and H. C. Swart, *Journal of Applied Physics*, 2014, 115, 193101/193101-193101/193114.
317. H. Takashima, K. Ueda and M. Itoh, *Applied Physics Letters*, 2006, 89, 261915/261911-261915/261913.
318. L. S. Cavalcantea, V. S. Marquesb, J. C. Sczancoskia, M. T. Escotec, M. R. Joyaa, J. A. Varelad, M. R. M. C. Santosb, P. S. Pizania and E. Longod, *Chemical Engineering Journal*, 2008, 143, 299-307.
319. J. A. Dawson, X. Li, C. L. Freeman, J. H. Harding and D. C. Sinclair, *Journal of Materials Chemistry C*, 2013, 1, 1574-1582.
320. V. V. Lemanov, A. V. Sotnikov, E. P. Smirnova and M. Weihnacht, *Applied Physics Letters*, 2002, 81, 886-888.
321. E. Korkmaz and N. O. Kalaycioglu, *Journal of the Chinese Chemical Society*, 2012, 59, 1390-1393.
322. K. Goto, Y. Nakachi and K. Ueda, *Thin Solid Films*, 2008, 516, 5885-5889.
323. M. Upadhyay Kahaly and U. Schwingenschlogl, *Journal of Materials Chemistry A: Materials for Energy and Sustainability*, 2014, 2, 10379-11383.
324. A. K. Levine and F. C. Palilla, *Applied Physics Letters*, 1964, 5, 118.
325. F. A. Rabuffetti, S. P. Culver, J. S. Lee and R. L. Brutchey, *Nanoscale*, 2014, 6, 2909-2914.
326. C. Peng, Z. Hou, C. Zhang, G. Li, H. Lian, Z. Cheng and J. Lin, *Optics Express*, 2010, 18, 7543-7551.
327. K. Minami, Y. Hakuta, M. Ohara, M. Aoki, K. Sue and H. Takashima, *Polymer Electrolyte Fuel Cells 10, Pts 1 and 2*, 2013, 50, 19-24.
328. A. Isobe, S. Takeshita and T. Isobe, *Langmuir*, 2015, 31, 1811-1819.
329. X. Peng, M. Y. Sfeir, F. Zhang, J. A. Misewich and S. S. Wong, *Journal of Physical Chemistry C*, 2010, 114, 8766-8773.
330. X. Peng, J. A. Misewich, S. S. Wong and M. Y. Sfeir, *Nano Letters*, 2011, 11, 4562-4568.
331. J. Han, L. Wang and S. S. Wong, *Rsc Advances*, 2014, 4, 34963-34980.
332. J. Han, L. Wang and S. S. Wong, *The Journal of Physical Chemistry C*, 2014, 118, 5671-5682.
333. J. Han, C. McBean, L. Wang, C. Jaye, H. Liu, D. A. Fischer and S. S. Wong, *Journal of Physical Chemistry C*, 2015, 119, 3826-3842.
334. Z. Zhang, X. Li, C. Gao, F. Teng, Y. Wang, L. Chen, W. Han, Z. Zhang and E. Xie, *Journal of Materials Chemistry A: Materials for Energy and Sustainability*, 2015, 3, 12769-12776.
335. G. Sreedhar, A. Sivanantham, S. Venkateshwaran, S. K. Panda and M. Eashwar, *Journal of Materials Chemistry A: Materials for Energy and Sustainability*, 2015, 3, 13476-13482.

336. T. S. Malyy, V. V. Vistovskyy, Z. A. Khapko, A. S. Pushak, N. E. Mitina, A. S. Zaichenko, A. V. Gektin and A. S. Voloshinovskii, *Journal of Applied Physics*, 2013, 113, 224305/224301-224305/224307.
337. J. Zhang, N. Zhang, L. Zou and S. Gan, *Rsc Advances*, 2014, 4, 38455-38465.
338. J. Streit, L. C. Tran-Ho and E. Konigsberger, *Monatshefte Fur Chemie*, 1998, 129, 1225-1236.
339. G. J. Janz and N. P. Bansal, *Journal of Physical and Chemical Reference Data*, 1982, 11, 505-693.
340. B. F. Woodfield, J. L. Shapiro, R. Stevens and J. Boerio-Goates, *Journal of Chemical Thermodynamics*, 1999, 31, 1573-1583.
341. H. Chang and P. J. Huang, *Anal Chem*, 1997, 69, 1485-1491.
342. J. Blazejowski and B. Zadykowicz, *Journal of Thermal Analysis and Calorimetry*, 2013, 113, 1497-1503.
343. X. C. Zhou and X. J. Wang, *Optik*, 2015, 126, 4800-4803.
344. H. T. Sun, M. Fujii, N. Nitta, F. Shimaoka, M. Mizuhata, H. Yasuda, S. Deki and S. Hayashiz, *Journal of the American Ceramic Society*, 2008, 91, 4158-4161.
345. V. V. Tatarchuk, A. P. Sergievskaya, T. M. Korda, I. A. Druzhinina and V. I. Zaikovsky, *Chemistry of Materials*, 2013, 25, 3570-3579.
346. X. Y. Yuan, K. Shen, M. X. Xu and Q. Y. Xu, *Journal of Superconductivity and Novel Magnetism*, 2012, 25, 2421-2424.
347. C. Y. Xu, J. Wu, P. Zhang, S. P. Hu, J. X. Cui, Z. Q. Wang, Y. D. Huang and L. Zhen, *Crystengcomm*, 2013, 15, 3448-3454.
348. J. Fu, Q. Zhang, Y. Li and H. Wang, *Journal of Luminescence*, 2009, 130, 231-235.
349. M. R. Mohammadi and D. J. Fray, *Journal of Sol-Gel Science and Technology*, 2013, 68, 324-333.
350. S. Fuentes, N. Barraza, E. Veloso, R. Villarroel and J. Llanos, *Journal of Alloys and Compounds*, 2013, 569, 52-57.
351. Z. Sun, G. Cao, Q. Zhang, Y. Li and H. Wang, *Materials Chemistry and Physics*, 2012, 132, 215-221.
352. G. Huang, W. Dong, L. Fang, F. Zheng and M. Shen, *Journal of Advanced Dielectrics*, 2011, 1, 215-221.
353. J. Han, C. McBean, L. Wang, J. Hoy, C. Jaye, H. Liu, Z.-Q. Li, M. Y. Sfeir, D. A. Fischer, G. T. Taylor, J. A. Misewich and S. S. Wong, *Chemistry of Materials*, 2015, 27, 778-792.
354. X. Zhang, J. Zhang, Y. Jin, H. Zhao and X.-j. Wang, *Crystal Growth & Design*, 2009, 8, 779-781.
355. X. Zhang, J. Zhang, X. Zhang, M. Wang, H. Zhao, S. Lu and X.-j. Wang, *Journal of Physical Chemistry C*, 2007, 111, 18044-18048.
356. A. Purwanto, D. Hidayat, Y. Terashi and K. Okuyama, *Chemistry of Materials*, 2008, 20, 7440-7446.
357. C. M. Lau, X. Wu and K. W. Kwok, *Journal of Applied Physics*, 2015, 118, 034107/034101-034107/034107.
358. M. L. Moreira, E. C. Paris, G. S. do Nascimento, V. M. Longo, J. R. Sambrano, V. R. Mastelaro, M. I. B. Bernardi, J. Andres, J. A. Varela and E. Longo, *Acta Materialia*, 2009, 57, 5174-5185.

359. J. Li, Y. C. Zhang, T. X. Wang and M. Zhang, *Materials Letters*, 2011, 65, 1556-1558.
360. B. Mari, K. C. Singh, P. Cembrero-Coca, I. Singh, D. Singh and S. Chand, *Displays*, 2013, 34, 346-351.
361. R. C. Somers, M. G. Bawendi and D. G. Nocera, *Chemical Society Reviews*, 2007, 36, 579-591.
362. J. Z. Zhang, *MRS Bulletin*, 2011, 36, 48-55.
363. T. Hisatomi, J. Kubota and K. Domen, *Chemical Society Reviews*, 2014, 43, 7520-7535.
364. M. S. Prevot and K. Sivula, *Journal of Physical Chemistry C*, 2013, 117, 17879-17893.
365. M. G. Walter, E. L. Warren, J. R. McKone, S. W. Boettcher, Q. Mi, E. A. Santori and N. S. Lewis, *Chemical Reviews*, 2010, 110, 6446-6473.
366. J. Sun, D. K. Zhong and D. R. Gamelin, *Energy & Environmental Science*, 2010, 3, 1252-1261.
367. N. Getoff, *International Journal of Hydrogen Energy*, 1990, 15, 407-417.
368. C. S. Lewis, H. Liu, J. Han, L. Wang, S. Yue, N. A. Brennan and S. S. Wong, *Nanoscale*, 2016, 8, 2129-2142.
369. C. A. Colton and D. M. Wilcock, *CNS & Neurological Disorder - Drug Targets*, 2010, 9, 174-191.
370. A. Nimmerjahn, F. Kirchhoff and F. Helmchen, *Science*, 2005, 308, 1314-1318.
371. M. Ueno, *Nature Neuroscience*, 2013, 16, 543-551.
372. R. C. Paolicelli, *Science*, 2011, 333, 1456-1458.
373. U. K. Hanisch, *Glia*, 2002, 40, 140-155.
374. D. Davalos, *Nature Neuroscience*, 2005, 8, 752-758.
375. C. A. Colton, *Journal of NeuroImmune Pharmacology*, 2009, 4, 399-418.
376. J. Z. Pan, *Journal of Neuroscience Research*, 2002, 68, 315-322.
377. K. A. Kigerl, *The Journal of Neuroscience*, 2009, 29, 13435-13444.
378. V. Colvin, *Nat. Biotech.*, 2003, 21, 1166-1170.
379. C. S. S. R. Kumar, ed., *Nanomaterials: toxicity, health and environmental issues*, Wiley-VCH, Weinheim, 2006.
380. N. Lewinski, V. Colvin and R. Drezek, *Small*, 2008, 4, 26-49.
381. W. Li, C. Chen, C. Ye, T. Wei, Y. Zhao, F. Lao, Z. Chen, H. Meng, Y. Gao, H. Yuan, G. Xing, F. Zhao, Z. Chai, X. Zhang, F. Yang, D. Han, X. Tang and Y. Zhang, *Nanotechnology*, 2008, 19, 145102.
382. J. Sudimack and R. J. Lee, *Advanced Drug Delivery Review*, 2000, 41, 147-162.
383. W. H. Suh, K. S. Suslick, G. D. Stucky and Y.-H. Suh, *Progress in Neurobiology*, 2009, 87, 133-170.
384. S. Chen, X. Zhao, J. Chen, J. Chen, S. S. Wong and I. Ojima, *Bioconjugate Chemistry*, 2010, 21, 979-987.
385. H. Zhou, J. Chen, E. Sutter, M. Feygenson, M. C. Aronson and S. S. Wong, *Small*, 2010, 6, 412-420.
386. J. Chen, H. Zhou, A. C. Santulli and S. S. Wong, *Chemical Research in Toxicology*, 2010, 23, 871-879.
387. B. J. Panessa-Warren, J. Warren, S. S. Wong and J. A. Misewich, *Journal of Physics: Condensed Matter*, 2006, 18, S2185-S2201.

388. A. Magrez, L. Horváth, R. Smajda, V. Salicio, N. Pasquier, L. Forró and B. Schwaller, *ACS Nanoscience & Nanotechnology*, 2009, 3, 2274-2280.
389. C. Jin, Y. Tang, F. Yang, X. Li, S. Xu, X. Fan, Y. Huang and Y. Yang, *Biological Trace Element Research*, 2011, 141, 3-15.
390. G. Tejral, N. R. Panyala and J. Havel, *Journal of Applied Biomedicine*, 2009, 7, 1-13.
391. Z. Q. Samra, S. Shabir, Z. Rehmat, M. Zaman, A. Nazir, N. Dar and M. A. Athar, *Applied Biochemistry and Biotechnology*, 2010, 162, 671-686.
392. Y. Ling, K. Wei, Y. Luo, X. Gao and S. Zhong, *Biomaterials*, 2011, 32, 7139-7150.
393. B. Polyak and G. Friedman, *Expert Opinion on Drug Delivery*, 2009, 6, 53-70.
394. Y. Wang, *Quantitative Imaging in Medicine and Surgery*, 2011, 1, 35-40.
395. S. Xu, F. Yang, X. Zhou, Y. Zhuang, B. Liu, Y. Mu, X. Wang, H. Shen, G. Zhi and D. Wu, *ACS Appl Mater Interfaces*, 2015, 7, 20460-20468.
396. M. Z. Iqbal, X. Ma, T. Chen, L. e. Zhang, W. Ren, L. Xiang and A. Wu, *Journal of Materials Chemistry B: Materials for Biology and Medicine*, 2015, 3, 5172-5181.
397. M. Catti, G. Valerio and R. Dovesi, *Physical Review B: Condensed Matter*, 1995, 51, 7441-7450.
398. H. Liang, X. Jiang, Z. Qi, W. Chen, Z. Wu, B. Xu, Z. Wang, J. Mi and Q. Li, *Nanoscale*, 2014, 6, 7199-7203.
399. G. Wang, W. Li, K. Jia, B. Spliethoff, F. Schüth and A. Lu, *Applied Catalysis A: General*, 2009, 364, 42-47.
400. S. Xu, C. M. Hessel, H. Ren, R. Yu, Q. Jin, M. Yang, H. Zhao and D. Wang, *Energy & Environmental Science*, 2014, 7, 632-637.
401. G. Tong, J. Guan and Q. Zhang, *Materials Chemistry and Physics*, 2011, 127, 371-378.
402. P. Basnet, G. K. Larsen, R. P. Jadeja, Y.-C. Hung and Y. Zhao, *Applied Materials & Interfaces*, 2013, 5, 2085-2095.
403. J. M. Berg, S. Ho, W. Hwang, R. Zebda, K. Cummins, M. P. Soriaga, R. Taylor, B. Guo and C. M. Sayes, *Chemical Research in Toxicology*, 2010, 23, 1874-1882.
404. F. S. Freyria, B. Bonelli, M. Tomatis, M. Ghiazza, E. Gazzano, D. Ghigo, E. Garrone and B. Fubini, *Chemical Research in Toxicology*, 2012, 25, 850-861.
405. L. Chen, J. Xie, J. Yancey, M. Srivatsan and V. K. Varadan, *Journal of Nanotechnology in Engineering and Medicine*, 2010, 1, 041014/041011-041014/041015.
406. Å. Gustafsson, U. Bergström, L. Ågren, L. Österlund, T. Sandström and A. Buchta, *Toxicology and Applied Pharmacology*, 2015, 288, 1-11.
407. Y. Zhao, F. Pan, H. Li, T. Niu, G. Xu and W. Chen, *Journal of Materials Chemistry A*, 2013, 1, 7242-7246.
408. L. E. Barton, A. N. Quicksall and P. A. Maurice, *Geomicrobiology Journal*, 2012, 29, 314-322.
409. A. Adili, S. Crowe, M. F. Beaux, T. Cantrell, P. J. Shapiro, D. N. McIlroy and K. E. Gustin, *Nanotoxicology*, 2008, 2, 1-8.
410. Y. Wang, X. Y. Zhou, Z. Chen, B. Cai, Z. Z. Ye, C. Y. Gao and J. Y. Huang, *Applied Physics a-Materials Science & Processing*, 2014, 117, 2121-2126.

411. P. R. Lockman, M. O. Oyewumi, J. M. Koziara, K. E. Roder, R. J. Mumper and D. D. Allen, *Journal of Controlled Release*, 2003, 93, 271-282.
412. B. T. Farrell, B. E. Hamilton, E. Dósa, E. Rimely, M. Nasseri, S. Gahramanov, C. A. Lacy, E. P. Frenkel, N. D. Doolittle, P. M. Jacobs and E. A. Neuwelt, *Neurology*, 2013, 81, 256-263.
413. Y. Wang, B. Wang, M. T. Zhu, M. Li, H. J. Wang, M. Wang, H. Ouyang, Z. F. Chai, W. Y. Feng and Y. L. Zhao, *Toxicology Letters*, 2011, 205, 26-37.
414. B. Wang, W. Y. Feng, M. T. Zhu, Y. Wang, M. Wang, Y. Q. Gu, H. Ouyang, H. J. Wang, M. Li, Y. L. Zhao, Z. F. Chai and H. F. Wang, *Journal of Nanoparticle Research*, 2009, 11, 41-53.
415. J. X. Wang, C. Y. Chen, Y. Liu, F. Jiao, W. Li, F. Lao, Y. F. Li, B. Li, C. C. Ge, G. Q. Zhou, Y. X. Gao, Y. L. Zhao and Z. F. Chai, *Toxicology Letters*, 2008, 183, 72-80.
416. M. Mahmoudi, S. Sant, B. Wang, S. Laurent and T. Sen, *Advanced Drug Delivery Reviews*, 2011, 63, 24-46.
417. L. J. Chew, P. Fusar-Poli and T. Schmitz, *Dev Neurosci*, 2013, 35, 102-129.
418. Y. Deng, J. Lu, V. Sivakumar, E. A. Ling and C. Kaur, *Brain Pathol*, 2008, 18, 387-400.
419. J. E. Merrill and N. J. Scolding, *Neuropathol Appl Neurobiol*, 1999, 25, 435-458.
420. L. Peferoen, M. Kipp, P. van der Valk, J. M. van Noort and S. Amor, *Immunology*, 2014, 141, 302-313.
421. M. Domercq, A. Perez-Samartin, D. Aparicio, E. Alberdi, O. Pampliega and C. Matute, *Glia*, 2010, 58, 730-740.
422. M. M. Varnum and T. Ikezu, *Arch Immunol Ther Exp (Warsz)*, 2012, 60, 251-266.
423. Z. Gao and S. E. Tsirka, *Neurol Res Int*, 2011, 2011, 383087.
424. Y. Wang, J. Cao, S. Wang, X. Guo, J. Zhang, H. Xia, S. Zhang and S. Wu, *Journal of Physical Chemistry C*, 2008, 112, 17804-17808.
425. Z. Pu, M. Cao, J. Yang, K. Huang and C. Hu, *Nanotechnology*, 2006, 17, 799-804.
426. S. E. Lohse, N. D. Burrows, L. Scarabelli, L. M. Liz-Marzan and C. J. Murphy, *Chemistry of Materials*, 2014, 26, 34-43.
427. J. J. Monagle, *Journal of Organic Chemistry*, 1962, 27, 3851–3855.
428. K. E. Pfitzner and J. G. Moffatt, *Journal of American Chemical Society*, 1963, 85, 3027-3028.
429. K. Nakajima and S. Kohsaka, *The Journal of Biochemistry*, 2001, 130, 169-175.
430. S. Papa, F. Rossi, R. Ferrari, A. Mariani, M. De Paola, I. Caron, F. Fiordaliso, C. Bisighini, E. Sammali, C. Colombo, M. Gobbi, M. Canovi, J. Lucchetti, M. Peviani, M. Morbidelli, G. Forloni, G. Perale, D. Moscatelli and P. Veglianese, *ACS Nano*, 2013, 7, 9881-9895.
431. F. K. Chan, K. Moriwaki and M. J. De Rosa, *Methods Mol Biol*, 2013, 979, 65-70.
432. K. A. Kigerl, J. C. Gensel, D. P. Ankeny, J. K. Alexander, D. J. Donnelly and P. G. Popovich, *J Neurosci*, 2009, 29, 13435-13444.
433. V. E. Miron, A. Boyd, J. W. Zhao, T. J. Yuen, J. M. Ruckh, J. L. Shadrach, P. van Wijngaarden, A. J. Wagers, A. Williams, R. J. Franklin and C. ffrench-Constant, *Nat Neurosci*, 2013, 16, 1211-1218.

434. D. Brenner, H. Blaser and T. W. Mak, *Nat Rev Immunol*, 2015, 15, 362-374.
435. R. M. Locksley, N. Killeen and M. J. Lenardo, *Cell*, 2001, 104, 487-501.
436. W. Swardfager, K. Lanctot, L. Rothenburg, A. Wong, J. Cappell and N. Herrmann, *Biol Psychiatry*, 2010, 68, 930-941.
437. Y. Dowlati, N. Herrmann, W. Swardfager, H. Liu, L. Sham, E. K. Reim and K. L. Lanctot, *Biol Psychiatry*, 2010, 67, 446-457.
438. J. Brynskov, P. Foegh, G. Pedersen, C. Ellervik, T. Kirkegaard, A. Bingham and T. Saermark, *Gut*, 2002, 51, 37-43.
439. Y. Nakamura, Q. S. Si and K. Kataoka, *Neurosci Res*, 1999, 35, 95-100.
440. P. Pacher, J. S. Beckman and L. Liaudet, *Physiological Reviews*, 2007, 87, 315-424.
441. V. Calabrese, C. Mancuso, M. Calvani, E. Rizzarelli, D. A. Butterfield and A. M. Stella, *Nature Reviews Neuroscience*, 2007, 8, 766-775.
442. J. C. Nissen, D. L. Selwood and S. E. Tsirka, *J Neurochem*, 2013, DOI: 10.1111/jnc.12404.
443. V. A. Najjar and K. Nishioka, *Nature*, 1970, 228, 672-673.
444. N. J. Bump, J. Lee, M. Wleklik, J. Reichler and V. A. Najjar, *Proceedings of the National Academy of Sciences of the United States of America*, 1986, 83, 7187-7191.
445. V. Pierre, B. Veronique, M. Michel, D. Philippe, D. Laura, F. Kristian, F. Jean-Michel and B.-S. Anne-Karine, *Frontiers in Neuroenergetics*, 2010, 2, 131.